Contributions to the Development of Cured-in-Place Pipe Composite Liners for Pressure Water Pipes Rehabilitation

Ferran Gras Travesset

http://hdl.handle.net/10803/689834

Data de defensa: 12-01-2024

UNIVERSITAT RAMON LLULL

DOCTORAL THESIS

Title	Contributions to the Development of Cured-in-Place Pipe Composite Liners for Pressure Water Pipes Rehabilitation
Presented by	Ferran Gras Travesset
Centre	IQS School of Engineering
Department	Department of Industrial Engineering
Directed by	Dr. Marco Antonio Pérez Martínez Dr. Antoni Andreu Torras

"*Keep your face always toward the sunshine,*
and shadows will fall behind you."

Walt Whitman
(1819-1892)

This doctoral thesis was supported and funded by the Agència de Gestió d'Ajuts Universitaris i de Recerca and the Pla de Doctorats Industrials del Department de Recerca i Universitats de la Generalitat de Catalunya with reference project 2019 DI45 (2019-2023).

Acknowledgements

La consecució d'una tesi doctoral és fruit d'un llarg camí ple d'entrebancs. Per sort un no acaba d'estar mai sol del tot, hi ha una sèrie de persones que de manera més directa o indirecta t'acompanyen en el procés. A aquestes persones m'agradaria agrair el seu granet de sorra aportat en un moment o altre de la tesi doctoral.

En primer lloc, m'agradaria donar les gràcies a l'Institut Químic de Sarrià (IQS), a l'empresa Aigües de Barcelona (AB) i al Pla de doctorats Industrials de la Generalitat de Catalunya per brindar-me l'oportunitat de realitzar estudis de doctorat. L'IQS, a més, ha estat el centre universitari que m'ha format tots aquests anys des de que vaig començar el grau tot il·lusionat amb la carrera que de ben petit havia somiat realitzar. També m'agradaria fer menció als directors d'IQS, Dr. Salvador Borrós i en especial a l'exdirector Dr. Pedro Regull pels savis consells proporcionats a l'inici de la meva etapa com a estudiant de doctorat. D'altra banda, agrair el suport i el tracte rebut per Aigües de Barcelona i en especial al departament d'Enginyeria que m'ha proporcionat recursos, contactes, col·laboradors i accés a informació primordial per al desenvolupament de la tesi i totalment fora de l'abast del món universitari. Entre els col·laboradors, m'agradaria destacar al Sr. Ludwing Felipe Libreros d'Aquatec S.A. per la seva implicació en el full-scale test realitzat a obra i el bon tracte rebut, i al Sr. Timo Münstermann de SAERTEX multiCom Group. No hauria sigut possible sense les seves aportacions.

En segon lloc, dono les gràcies als directors de tesi Dr. Marco A. Pérez (IQS) i Antoni Andreu Torras (AB), i al tutor d'empresa Francesc Flos (AB) per confiar-me aquesta nova línia d'investigació dins d'IQS a més de l'acompanyament i indicacions donades, i vetllar per tal de que la tesi arribés a bon port.

Per altra banda, agrair també al grup d'investigació i en especial al Dr. Giovanni Gómez qui ha seguit de més a prop l'evolució de la tesi. També vull mencionar a la resta de membres del departament d'Enginyeria Industrial de l'IQS que m'han format tots aquests anys i que sempre han estat oberts a atendrem i ajudar-me en el que fos necessari entre els quals m'agradaria destacar al Sr. César Alquézar, cap de taller de l'IQS amb qui he compartit un gran nombre d'hores de fabricació d'utillatges, peces i mostres per la tesi doctoral.

També vull fer una menció especial als doctorands amb qui he passat moltes hores junts tant dins i fora del laboratori, a la universitat i en ambients d'oci més distrets: Ariadna, Albert, Daniel, Ricard, Guillermo, Josep i Héctor. Tot i treballar en temàtiques diferents, junts ens hem recolzat i ajudat a superar les dificultats sorgides al llarg de la tesi. M'enorgulleix veure com alguns d'ells ja han assolit la fita de doctors! Molts ànims per aquells qui segueixen lluitant per aconseguir-ho.

Els meus amics enginyers que m'han recolzat en moments difícils també es mereixen ser mencionats així com el meu company de pis l'Albert Forés i la seva xicota, que m'han acompanyat durant tots aquests anys i amb qui he passat molts moments productius i d'esbarjo.

Finalment, agraeixo a la meva família per ser-hi sempre i la formació proporcionada que m'ha permès arribar a assolir la titulació de Doctor. Gràcies pel suport rebut i per confiar pacientment en les meves capacitats.

Ferran Gras Travesset

A la meva família

Abstract

The aging of pipelines in most developed countries has become a reality in recent decades, primarily due to insufficient renovation rates. Widespread pipeline deterioration has led to frequent leaks and failures, resulting in significant daily potable water losses. Additionally, the rise in droughts and periods of water scarcity, attributed to the consequences of climate change, has aggravated the situation. Consequently, governments and authorities have intensified efforts to minimize water loss during transportation.

The vast network of pipelines poses a considerable challenge for their replacement. It is not only a costly endeavor, but it also demands significant time and resources. Trenchless technologies have emerged as a viable alternative to replacing damaged pipes, offering reduced costs and shorter installation times. Among these methods, Cured-In-Place Pipe (CIPP) technology has witnessed a surge in demand in recent years, especially in sewer pipes. However, challenges have arisen in some pressure pipe projects involving higher pressures. Even minor installation defects can significantly impact the performance of the rehabilitated pipe, leading to failures. Hence, there is a need to increase the level of knowledge of the CIPP technology.

This thesis aims to contribute to developing the CIPP technique, mainly in its application to pressure pipes. The contributions focus on detecting and surpassing the uncertainties that arise during the design and after installing a CIPP liner.

Particularly, this research established a robust quality control protocol for CIPP liners installed on pressure pipes. Secondly, a novel testing method, the IBPT, is introduced, addressing existing limitations in assessing hoop tensile performance and ensuring alignment with results from flat sample tensile tests. The research further provides experimental evidence from a full-scale test on a severely damaged reinforced concrete pressure pipe. A sophisticated mathematical model is also developed, optimizing semi-structural liner designs for pressure pipes by accommodating irregular and circular host pipe holes.

Resum

En les darreres dècades, l'envelliment de les canonades s'ha convertit en una realitat en la majoria dels països desenvolupats principalment degut a les insuficients taxes de renovació. El deteriorament generalitzat de les canonades ha provocat fuites i avaries freqüents i per tant importants pèrdues diàries d'aigua potable. A més, l'augment de les sequeres i dels períodes d'escassetat d'aigua atribuïts a les conseqüències del canvi climàtic ha empitjorat la situació. Com a resultat, governs i autoritats han intensificat els esforços per minimitzar la pèrdua d'aigua durant el transport.

La immensa extensió de la xarxa de canonades presenta un desafiament considerable en quant a la seva substitució. No només és una solució costosa a nivell econòmic, sinó que també es requereix temps i recursos significatius. Tot i això, les tecnologies sense rasa han sorgit com una alternativa viable per a la rehabilitació de canonades deteriorades, oferint reduïts costos i temps d'instal·lació més curts. Entre aquests mètodes, en els darrers anys, el Cured-In-Place Pipe (CIPP) ha experimentat un augment de la demanda, especialment en les canonades de clavegueram. No obstant, en alguns projectes de canonades de pressió han sorgit problemes a causa de les elevades pressions de treball. En aquests casos, fins i tot el mínim defecte durant la instal·lació pot tenir un impacte significatiu en el rendiment de la canonada rehabilitada generant avaries. Així doncs, és necessari ampliar el nivell de coneixement de la tecnologia CIPP.

Aquesta tesi té com a objectiu contribuir al desenvolupament de la tècnica CIPP, especialment en la seva aplicació a canonades de pressió. Les aportacions es focalitzen en detectar i superar les incerteses que sorgeixen tant en el disseny com després de la instal·lació de la mànega CIPP.

Concretament, en aquesta tesi s'estableix un protocol de control de qualitat robust per a mànegues de CIPP instal·lades en canonades de pressió. En segon lloc, es proposa un nou mètode d'assaig, l'IBPT, que aborda les limitacions existents per avaluar les propietats mecàniques de tracció d'una mànega en la direcció circumferencial. A més, garanteix la coherència amb els resultats dels assajos de mostres planes. D'altra banda, també s'aporten dades experimentals d'un assaig a escala real a camp realitzat en una canonada de pressió deteriorada de formigó armat. Finalment, s'ha desenvolupat un model matemàtic sofisticat per optimitzar els dissenys de mànegues semi-estructurals per a canonades de pressió que considera orificis en la canonada amfitriona tant circulars com irregulars.

Resumen

En las últimas décadas, en la mayoría de los países desarrollados, el envejecimiento de las tuberías se ha convertido en una realidad debido principalmente a unas tasas de renovación insuficientes. El deterioro generalizado de las tuberías ha provocado frecuentes fugas y fallos, resultando en pérdidas significativas diarias de agua potable. Además, el aumento de las sequías y los períodos de escasez de agua, atribuidos a las consecuencias del cambio climático, ha empeorado la situación. En consecuencia, gobiernos y autoridades han intensificado los esfuerzos para minimizar la pérdida de agua durante el transporte.

La gran extensión de la red de tuberías presenta un desafío considerable para su reemplazo. No solo es una solución costosa a nivel económico, sino que también requiere de tiempo y recursos significativos. Sin embargo, las tecnologías sin zanja han surgido como una alternativa viable para rehabilitar tuberías deterioradas, ofreciendo costes reducidos y tiempos de instalación más cortos. Entre estos métodos, en los últimos años, el Cured-In-Place Pipe (CIPP) ha experimentado un aumento de la demanda, especialmente en las tuberías de alcantarillado. Sin embargo, en algunos proyectos de tuberías de presión han surgido problemas debido a las elevadas presiones de trabajo. En estos casos, incluso el mínimo defecto en la instalación puede tener un impacto significativo en el rendimiento de la tubería rehabilitada, generando averías. Así pues, resulta necesario ampliar el nivel de conocimiento de la tecnología CIPP.

Esta tesis tiene como objetivo contribuir al desarrollo de la técnica CIPP, especialmente en su aplicación a tuberías de presión. Las aportaciones se focalizan en detectar y superar las incertidumbres que surgen tanto en el diseño como después de la instalación de la manga CIPP.

Concretamente, en esta tesis se establece un protocolo de control de calidad robusto para mangas de CIPP instaladas en tuberías de presión. En segundo lugar, se propone un nuevo método de ensayo, el IBPT, que aborda las limitaciones existentes para evaluar las propiedades mecánicas de tracción en la dirección circunferencial. Además, garantiza la coherencia con los resultados de los ensayos de muestras planas. Por otra parte, se aportan también datos experimentales de un ensayo a escala real a campo realizado en una tubería de presión de hormigón armado deteriorada. Finalmente, se ha desarrollado un sofisticado modelo matemático para optimizar los diseños de mangas semi-estructurales para tuberías a presión que considera orificios en la tubería huésped irregulares y circulares.

Compendium of publications

Journal articles

- **Gras-Travesset, F.**, Andreu Torras, A. & Pérez, M. A., A novel test procedure to assess the performance of composite cured-in-place-pipe liners for rehabilitation of water pressure pipes. *Case Stud. Constr.* 19, e02381. JCR Impact factor 2022: 6.2 (Q1 in *Engineering Civil and Construction & Building Technology*), doi: 10.1016/j.cscm.2023.e02381 (2023).
- **Gras-Travesset, F.**, Andreu Torras, A. & Pérez, M. A., Optimizing thickness for semi-structural CIPP liners in pressure pipes : A mathematical modeling approach. *Tunn. Undergr. Space Technol.*. JCR Impact factor 2022: 6.9 (Q1 in *Engineering Civil and Construction & Building Technology*), Preprint submitted on June 14th, 2023.

Comunications in conferences

- **Gras-Travesset, F.**, Andreu Torras, A. & Pérez, M. A., Rehabilitació avançada d'una canonada d'aigua potable mitjançant materials compostos, 14ns Debats de recerca, Andorra, October 18-19, 2021. p205-220, ISBN: 978-99920-61-65-7. Oral presentation and Conference proceeding.
- **Gras-Travesset, F.**, Andreu Torras, A. & Pérez, M. A., Full-scale validation test of a pressure pipeline rehabilitated with CIPP, 17th Pipeline Technology Conference, No dig, Berlin (Germany), March 7-10, 2022. Oral presentation and Conference proceeding.
- **Gras-Travesset, F.**, Andreu Torras, A. & Pérez, M. A., Experimental study for the rehabilitation of pressure drinking water pipes using Glass Fiber Reinforced Polymer, 25th International Conference on Composite Structures (ICCS25), Porto (Portugal), July 19-22, 2022. Oral presentation.

Other contributions

- **Gras-Travesset, F.**, Andreu Torras, A. & Pérez, M. A., Protocol per a projecte i execució d'obres de rehabilitació amb mànegues de canonades d'abastament. Internal document Aigües de Barcelona
- Comité técnico CTN 53 Plásticos y caucho, UNE 53929 [1]. Plásticos. Rehabilitación de conducciones de abastecimiento y alcantarillado con tubos continuos curados in situ (CIPP). Diseño, cálculo e instalación, URL www.une.org (2022).

- **Gras-Travesset, F.**, Andreu Torras, A. & Pérez, M. A., Estudi per a la rehabilitació sostenible i costo efectiva de les canonades de subministrament d'aigua potable, Premis impacte 2022 del Pla de doctorats industrials, Barcelona (Spain), 2022. Poster and extended abstract

Contents

List of figures

List of tables

List of abbreviations

3D	**T**hree-**D**imensional
AOR	**A**llowable **O**versizing **R**atio
ASCE	**A**merican **S**ociety of **C**ivil **E**ngineers
ASTM	**A**merican **S**ociety for **T**esting and **M**aterials
AWWA	**A**merican **W**ater **W**orks **A**ssociation
CIPP	**C**ured-**I**n-**P**lace **P**ipe
CTN	**C**omité **T**écnico de **N**ormalización
DIC	**D**igital **I**mage **C**orrelation
DN	**D**iameter **N**ominal
DSC	**D**ifferential **S**canning **C**alorimetry
FE	**F**inite **E**lements
HAP	**H**azardous **A**ir **P**ollutants
HEA	**H**-shaped cross-section beam
IBPT	**I**nner **B**alloon **P**ressure **T**est
ISO	**I**nternational **O**rganization for **S**tandardization
LED	**L**ight-**E**mitting **D**iode
LS	**L**imit **S**tate
MAE	**M**ean **A**bsolut **E**rror
MDP	**M**aximum **D**esign **P**ressure
MSE	**M**ean **S**quared **E**rror
N_2	**N**itrogen
PE	**P**olyethylene
PVC	**P**olyvinyl **C**hloride
QC	**Q**uality **C**ontrol
SEM	**S**canning **E**lectron **M**icroscope
SDR	**S**tandard **D**imension **R**atio
STP	**S**upported **T**est **P**ressure
TGA	**T**hermogravimetric **A**nalysis
TV	**T**elevision
UNE	**U**na **N**orma **E**spañola
USA	**U**nited **S**tates of **A**merica
UV	**U**ltraviolet
VOC	**V**olatile **O**rganic **C**ompounds

List of symbols

Latin symbols

A	Area	mm^2
a_1	Hole's longitudinal dimension	mm
a_H	Hall's equation polynomial	(-)
A_H	Host pipe hole length	mm
A_m	Cross sectional area of a curved beam	mm^2
b	Sample's width (bending test)	mm
$b1$	Hole's hoop dimension	mm
B_H	Host pipe hole width	mm
C	Ovality reduction factor	(-)
c_B	Coefficient of a logarithmic interpolation from the Boot's charts	(-)
C_E	Young Modulus correction coefficient	(-)
C_σ	Stress correction coefficient	(-)
d	Host pipe hole diameter	mm
D	Host pipe diameter	mm
dA	Differential of Area	mm^2
d_g	Annular gap amplitude	mm
dM	Differential of bending moment	N·m
d_n	Diameter of the sample at half of the sample's thickness (cruved sample)	mm
$d\theta$	Differential of angle	°
DR	Outer diameter to thickness ratio	(-)
dx	Differential of length	mm
E	Young modulus	MPa
F	Force	N
$F(xi)$	Previous model (mathematical model)	(-)
$F_0(x)$	Base model (mathematical model)	(-)
g	Annular gap (Thépot's equation)	mm
h	Sample's thickness (bending test)	mm
$h_m(xi)$	Decision tree made on residuals	(-)
h_{Th}	Liner's ovality (Thépot's equation)	%
I	Second moment of area	mm^4
IDM	Maximum inside host pipe's diameter	mm

IDx	Host pipe's mean inside diameter	mm
K	Enhancement factor	(-)
$K_{GR,\nu}$	Local wavy imperfection reduction factor (ATV-M 127-2)	(-)
K_ν	Annular gap reduction factor (ATV-M 127-2)	(-)
K_s	Ovality reduction factor (ATV-M 127-2)	(-)
L	Distance between supports	mm
L_2	Distance between the sample's contact points	mm
L_3	Total length of the chord of a curved sample	mm
L_s	Loss function	(-)
M	Bending moment	N·m
m_B	Coefficient of a logarithmic interpolation from the Boot's charts	(-)
m_H	Hall's equation polynomial	(-)
N	Safety factor	(-)
N_1	Axial force	N
O	Center of curvature	(-)
P	Pressure	MPa
P_{Cr}	Critical buckling pressure	MPa
$\overline{P}_{Cr}$	Levy's critical buckling pressure	MPa
P_{Cr}^{Gl}	Glock's critical buckling pressure	MPa
P_{Cr}^{T}	Timoshenko's critical buckling pressure	MPa
Per_{HP}	Host pipe's perimeter	mm
Per_{liner}	Liner's perimeter	mm
P_I	Inner pressure	MPa
q	Liner's ovality (Moore's equation)	%
r	Support's radius (bending test)	mm
R	Inside host pipe radius	mm
r_1	Distance from the center of curvature to the differential of area (curved beams)	mm
R_1	Distance from the center of curvature to the center of mass (curved beams)	mm
R_{1n}	Distance from the center of curvature to the neutral axis (curved beams)	mm
R^2	Coefficient of determination	(-)
R_2	Radius of curvature at half of the thickness of a curved sample	mm
R_{d_g}	Annular gap reduction factor (Moore's equation)	(-)
R_{Δ_w}	Local wavy imperfection reduction factor (Moore's equation)	(-)
r_{im}	Pseudo residuals errors	(-)
R_q	Ovality reduction factor (Moore's equation)	(-)
s	Displacement of the surface of the sample at the load application from its initial position	mm
SDR	Standard Dimension ratio (IDx/t)	(-)

t	Liner's thickness	mm
T	Temperature	°C
V	Shear force	N
y	Distance from the neutral axis	mm

Greek symbols

α	Angular groove host pipe hole angle	°
β	Host pipe hole orientation respect the longitudinal direction	°
β_k	Buckling factor (Thépot's equation)	(-)
δ	Vertical displacement	mm
Δ	Host pipe ovality	%
δ_g	Annular gap coefficient (Thépot's equation)	(-)
δ_h	Ovality coefficient (Thépot's equation)	(-)
Δ_w	Wrinkle depth	mm
ε	Strain	mm/mm
ϕ	Half-angle of an unloaded sample between the sample's contact point	°
γ	Predicted value (mathematical model)	(-)
$\Gamma_{p,g}$	Annular gap reduction factor (Thépot's equation)	(-)
$\Gamma_{p,gxh}$	Reduction factor for the combination of annular gap and ovality together (Thépot's equation)	(-)
$\Gamma_{p,h}$	Ovality reduction factor (Thépot's equation)	(-)
λ	Wrinkle wavelength	mm
μ	Friction coefficient	(-)
μ_d	Dynamic viscosity	Pa·s
ν	Poisson's ratio	(-)
ν_m	Previous prediction (mathematical model)	(-)
θ	Wrinkle angle	°
ρ	Radius of curvature	mm
σ	Tensile stress	MPa
σ_{rh}	Shear stress of a curved beam	MPa
τ	Shear stress	MPa
ω	Weight used to switch from quadratic to a linear error function	(-)

Subscripts

$_0$	Initial point	(-)
c	Flexural property	(-)
fL	Long-term flexural property	(-)
fm	Maximum point flexural test	(-)
fy	Yield point, flexural property	(-)
h	Hoop direction	(-)

l	Longitudinal direction	(-)
L	Long-term property	(-)
m	Number of distribution tree	(-)
min	Minimum	(-)
n	Neutral axis	(-)
r	Radial direction	(-)
TL	Long-term tensile property	(-)
u	Ultimate	(-)
uh	Ultimate hoop property	(-)
ul	Ultimate longitudinal property	(-)
x	x-direction	(-)
y	Yield point	(-)
y	y-direction	(-)
z	z-direction	(-)

1 Introduction

The initial chapter presents the research topic and the motivation of the present doctoral thesis. The chapter includes the main research hypotheses and objectives. Moreover, a concise overview of the document's structure is delivered to serve as a guide for the reader.

1.1 Motivation

A vast pipeline network is responsible of providing drinking water to most world's population. In most developed countries, the pipeline was built between 1920 and 1970. The life expectancy of pipes depend on the materials and manufacturing techniques. In concrete pipes it can be set around fifty years. During this period, regular inspections must be performed to check the degree of deterioration of the pipe due to aging. Some times, a small reparation can extend the life of a whole pipe section. Nevertheless, a completely renovation may be needed in the case of advanced states of deterioration or severe damage. Otherwise, constant leaks and failures may often occur even in the same section of the pipeline. Some of these leaks on buried pipes are difficult to detect when no third parties are affected. However, a pressure pipe failure can led to catastrophic consequences as shown in Figure 1.1.

Figure 1.1: Example of real pressure pipe failure causing important damage to the road and third parties.

On the other hand, the water stress and drought periods have motivated the public administrations to focus on pipe's leaks and water lost during its transportation. It should be noted that a huge amount of water is lost daily. For example, the American Society of Civil Engineers (ASCE), estimated that in the US 22.7 hm^3 of potable water is lost daily. Moreover, a ratio of one leak every 2 minutes was estimated to happen [2]. Furthermore, increasingly city floods generated by pipe's bursts have uncovered the advance damaged state of the pipeline network. The appearance of these pipe bursts on the news during water stress periods have even caught the attention of the population.

The renovation of pipelines must be performed progressively to ensure the whole network is updated and free of leaks. However, the annual renovation ratios of most countries are far from the recommended 2% set by experts. For example, in Spain [3] in 2020 only a 0.46% was reached. Moreover, the 26% of the drinking water network was over 40 years old. Even worst statistics can be found from the sewer network where the 44% of pipes have surpass their life expectancy. Therefore, the renovation of the pipeline have become an urgent problem to address.

The extensive mileage of the network makes its renovation a challenge. As a reference to pressure water pipes, in Spain in 2020, there was 248,245 km [3], in France 875,000 km [4], and in the United States, $3.54 \cdot 10^6$ km [3]. Not only the costs of the pipe's replacement are high, but also it is a very time consuming operation. Moreover, the substitution of a pipe also have a high impact to its surroundings. For instance, in the case of a city, the substitution of buried pipes may imply direct consequences on the city's life, traffic, other essential services and neighborhood. In addition permission must be requested to the respective authorities which is often a slow process.

In recent years, several countries have glanced the trenchless technologies as a solution to speed up the process with also lower costs [5]. Rehabilitation by trenchless technologies take advantage of the existing old pipe to create a new pipe inside. Thus, only two access points are needed; at the beginning and at the end of the section to be rehabilitated. Consequently, it is considered a more environmentally friendly technique than the traditional substitution operation. Furthermore, it significantly reduces inconveniences to the city's activity.

Each trenchless technology have its own market. In particular, the Cured-In-Place Pipe (CIPP) has expanded considerably and caught the attention of some countries [6]. For example, in Germany in 2020, the use of CIPP liners accounted for 17.9% of the repair and renovation sector [5]. Looking ahead to 2028, the worldwide investment in CIPP projected to reach approximately 3800 million dollars [7].

CIPP liners have been first used to rehabilitate sewer pipes and then migrated to pressure water pipes. Despite the success in the sewer market, some problems have arise in pressure pipes where high pressures (over 10 bar) are often reached. These high pressure make the installation of CIPP liners more complex. Furthermore, the impact of a minor imperfections during the installation process is magnified in pressure pipes and even can leave the whole pipeline out of service. Therefore, robust quality control procedures are required to detect installation defects. A few procedures mainly based on bending tests are stated in current CIPP standards such as ASTM F1216 [8], ISO 11296-4 [9], and ISO 11298-4 [10]. However, deficiencies detected in some CIPP rehabilitation projects suggest further investigation should be performed to develop new quality control tests to accurately asses the mechanical performance of an installed CIPP liner.

Besides quality control practices, the optimization of the design of CIPP liners can also contribute to avoid installation defects. It should be noted that lighter liners may facilitate the rehabilitation as the maneuverability of the liner is increased. However, the uncertainty around CIPP applied to pressure pipes have led to conservative designs with unnecessary high safety coefficients.

1.2 Hypotheses and research objectives

According to the motivation behind this research, the following hypotheses are formulated.

- The uncertainties in the design of CIPP liners have been identified as a potential source of failures. Therefore, increasing the level of knowledge on the mechanical performance of the

raw and the installed liner could contribute to reducing these possible misalignments. Moreover, understanding the complex interaction between the composite and the host pipe under inner pressure conditions, including the host pipe deterioration, could contribute to the development of new design strategies and novel liner's configurations.

- The installation defects are also considered as one of the main factors to cause rehabilitated pipe's failures. Hence, a thoroughly analysis of the uncertainties that often arise in pressure pipe's projects along the complex installation process, could help to reduce the number of defects. Moreover, quantifying its impact on the mechanical performance of the rehabilitated pipe could contribute to create acceptance rates of success.
- Different procedures and parties are involved in a CIPP rehabilitation project. Thus, a comprehensive understanding of all processes can be a guarantee of success. Detailed technical data and information in every installation step could contribute on minimizing risks and maximize the overall operation's effectiveness.
- In the past, the absence of specific protocols for the mechanical characterization of these liners led to the adoption of generalized tests from the composite materials industry. However, the conditions that samples are subjected to in these standardized tests may not be representative of real on-site operating CIPP conditions. Therefore, developing specific testing procedures could contribute to broadening the knowledge of the mechanical performance of CIPP liners.
- The relative lack of knowledge about some aspects of the CIPP technology has led to conservative sizing practices, resulting in unnecessarily high safety factors. Thus, contributions that help to accurately understand the mechanical performance of a CIPP liner could aid in design strategies, allowing for more precise sizing, lower safety factors, cost-saving designs, and assuring high installation success.

Based on the above hypotheses, this thesis aims to contribute to developing the Cured-in-Place Pipe technique, particularly in its application to pressure pipes. These contributions focus on detecting and surpassing the uncertainties that arise after installing a CIPP liner. Improvements in the liner's design, new tests to assess the mechanical performance of an on-site installed liner, and the implementation of robust quality control procedures specific for CIPP, can help to reduce the uncertainty surrounding the water pressure pipe's rehabilitation.

The main objective is addressed by the achievement of the following specific objectives:

1. Define a control protocol to assess the parameters that may influence the installation process. The proposed procedures should consider the whole process from the analysis of the constituent materials to the on-site installation and post-installation testing.
2. Define a new test capable of reproducing the on-site operational conditions supported by a CIPP liner. The validation of the test will be done by a comparison with the already existing standard procedures used in CIPP testing.

3. Examine the existing analytical approaches aiming to optimize the design procedures to achieve cost savings, simplify the installation process, and reduce the likelihood of installation defects while keeping the structural performance.

1.3 Thesis outline

This document is organized into seven chapters structured as follows.

First, in **Chapter 1**, the motivation, the hypotheses and research objectives, and the document structure are presented.

Chapter 2 encompass the fundamentals of CIPP and covers a comprehensive review of the state of the art of the CIPP technique. The chapter is structured into five subsections. First, an overview of relevant trenchless technologies is set. Second, the CIPP technique is presented followed by an examination of the installation procedure. Then, the buckling approaches for the design of CIPP liners is revised as well as the liner's design and the installation challenges. Finally, the literature gaps identified are exposed.

Chapter 3 presents the quality control protocol developed for CIPP rehabilitation addressing the first specific objective. Moreover, the chapter delves into an example of implementation of the protocol showing the viability of the procedures proposed.

Chapter 4 encompasses the development of a new quality control test named the inner balloon pressure test to assess the hoop performance of an installed liner. Thus, the second specific objective is addressed. The test is presented as an alternative to the current bending test of curved samples and other tests proposed by authors sharing the same aim.

Chapter 5 addresses the third specific objective. The design equations of CIPP liners are thoroughly analyzed, and a new procedure based on a mathematical model is proposed to optimize the semi-structural liner's design in presence of irregular host pipe holes. The results of the full-scale test performed and numerical models are also presented.

Chapter 6 summarizes the points discussed in the previous chapters and aimed at provide precise responses to the thesis hypotheses and objectives in the form of conclusions. Moreover, this chapter also encompasses the scientific contributions derived from the present doctoral thesis and outlines recommendations for future research.

Finally, **Chapter 7** presents the journal publications derived from the present doctoral thesis.

2

Fundamentals and literature review

A comprehensive review of the CIPP trenchless technology is presented in this chapter. The most relevant findings concerning the liner's design and performance, installation challenges, and quality control tests on water pressure pipes are exposed. Finally, weaknesses detected in current standards on CIPP pressure pipes and literature gaps are highlighted.

2.1 Trenchless technologies

In recent years, sewer and water pipeline aging has proven to be a reality in most developed countries. Consequently, constant leaks occur every day, and a huge quantity of water is lost daily. The vast mileage concerning the pipeline and the number of pipes to renovate is also a challenge that has surpassed most countries in terms of time, capacity, and costs. However, rehabilitation trenchless technologies have appeared in the last decades with outstanding time and cost-saving performances. These technologies take advantage of the existing gallery provided by the damaged pipe. Hence, the deployment of large machinery like excavators and bulldozers is minimized, as they are only needed for establishing access points at the start and end of the pipe's section to be rehabilitated. Thus, the associated noise of these machines is minimal. In addition, there is no need to close the whole street, which makes trenchless technologies interesting for crowded cities. The operating time is also further reduced compared to the traditional pipe replacement, making trenchless technologies less intrusive to society.

Furthermore, the slight excavation makes these technologies environmentally friendly with minimal impact. On the other hand, the important cost-saving feature makes trenchless technologies also attractive to enterprises and customers. The main trenchless technologies used for pipe rehabilitation are listed below:

- **Sliplining**: a smaller new pipe diameter than the host pipe is inserted by slipping in it. However, it is limited to straight sections (see Figure 2.1a).
- **Pipe bursting**: a new pipe of the same or slightly higher diameter is inserted into the old damaged pipe. The old damaged pipe breaks when the new pipe is introduced during the process. It is also limited to straight sections (see Figure 2.1b).
- **Spray lining**: a rotating spray head is introduced in the host pipe. When using a polymeric spray, a thin coating layer is generated. It is especially useful to avoid corrosion. However, no structural contribution is expected from polymeric spray linings (see Figure 2.1c).
- **Cured-In-Place Pipe**: an initially soft liner is introduced in the host pipe. Then, the liner is pressurized and fitted snugly to the host pipe. After a curing process, the liner solidifies, and a new pipe is created. It should be noted that some CIPP liners can surpass 45° elbows (see Figure 2.1d).
- **Fold and form**: it consists of a thermoformed pipe lining process where a polymeric (PE or PVC) folded liner is introduced in the host pipe by the pulling method. Then, pressurized steam is used to unfold the liner, which will perfectly fit the host pipe (see Figure 2.1e).

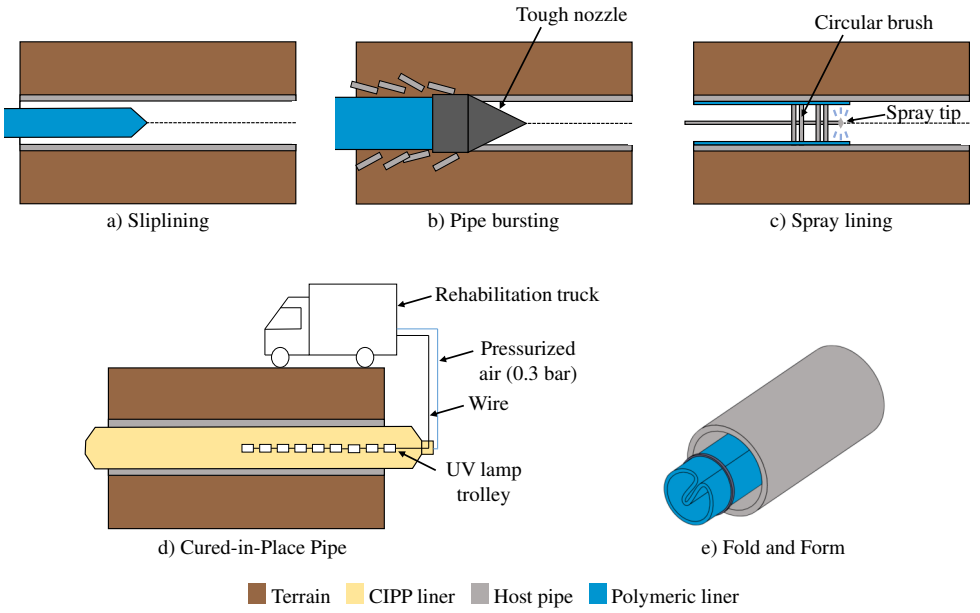

Figure 2.1: Main trenchless technologies used in pipe rehabilitation.

2.2 CIPP Fundamentals

2.2.1 Origin of the CIPP

The CIPP rehabilitation technique was invented by the agricultural engineer Eric Wood while thinking of a solution to repair a leaky pipe in the home garage. The access to the pipe was not easy, and its substitution was expensive. Hence, Mr. Wood came up with a trenchless technique solution to address the problem: the CIPP.

Later on, Brian Holmes, a member of the Greater London Council, introduced Wood to the pipe issues of Thames Water. An alternative approach to the traditional cement mortar lining was required. In 1971, the first CIPP liner was installed in Hackney (London). A felt tube impregnated with polyester resin wrapped in a plastic sheet was used to rehabilitate seventy meters of a 1160×609 mm diameter egg-shaped brick sewer pipe. Only the first liner installed has met the CIPP liner life expectancy. No available data confirms that the first installed liner has not experienced considerable damage over the years. However, tests conducted on liner samples after 20, 25, and 30 years published in the Trenchless International journal show satisfactory results.

The first CIPP company, Insituform Technologies, was founded during the early 1970s by Wood in the United Kingdom and later moved to Missouri (USA). Insituform Technologies exploited CIPP patents. Nevertheless, nowadays, all the original CIPP patents have expired, and a significant global market has been established, which is in a phase of continuous growth.

2.2.2 The Cured-in-Place Pipe technique

The CIPP is a worldwide trenchless technology technique to rehabilitate damaged old pipes. The process consists of creating a new pipe inside the host pipe, taking advantage of the already existing grout. The initially soft CIPP liner is first introduced in the host pipe. After a pressurized and curing process, the liner perfectly fits the host pipe and solidifies, creating a new pipe. It should be noted that the host pipe's nominal diameter is reduced by only a few millimeters while the friction coefficient is also reduced. Hence, there is no increase in the pipe's working pressure.

The liner is a composite material made of resin, fiber, and a polymeric coating (see Figure 2.2). The structural component, the fiber layers, is embedded into a resin matrix. Finally, a polymeric coating prevents fiber migration to the water. A wide variety of CIPP liners and different installation techniques can be adjusted to the host pipe requirement (see Figure 2.3).

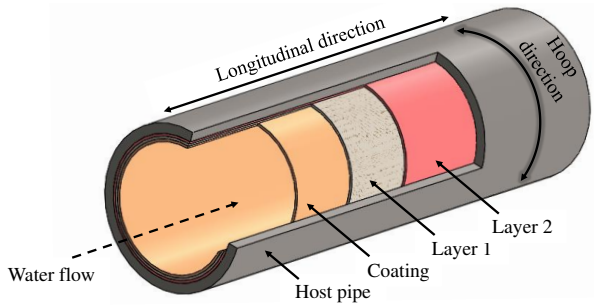

Figure 2.2: Representative scheme of a pipeline rehabilitated by the CIPP technology.

Three types of resins are used: polyester, vinyl ester, and epoxy resins. Polyester resins are mainly used in sewer pipelines, and it is the main resin employed as the CIPP sewer market is consolidated, while potable water pressure pipes are still in the minority due to issues experienced. On the other hand, epoxy resin is used in potable water pipelines as it is the only resin that meets the potable water certification requirements. Moreover, it does not contain hazardous air pollutants (HAP) and causes very low volatile organic compounds (VOC) emissions.

Regarding the structural component, there are two main types of fibers in the market: polyester and glass fiber. The polyester fabric meets the minimum mechanical strength required by CIPP standards at a very competitive price compared to other materials. Hence, it is the main fabric used in CIPP liners. However, glass fiber is preferred in CIPP liners with a UV curing process, and it is starting to emerge as the sewer rehabilitation market is migrating to UV technology rather than thermal curing.

According to the liner's design, there is no consensus between manufacturers. Every brand has its own liner's design composition. Therefore, non-woven, woven, and other types of liners can be found. The fiber's layers disposal also depends on the manufacturer's choice and the liner's final application. There are liners that allow considerable expansion, contain more or less fiber, and are more or less prepared to withstand the pulling installation forces. Nevertheless, current CIPP standards have classified the

liner's design depending on its mechanical performance, regardless of its inner composition. According to ASTM F1216 [8] and UNE 53929 [1] CIPP liners have been classified into:

- **Non-structural**: the liner is not able to withstand external or internal loads, and therefore, the host pipe must be structurally sound. Non-structural liners are used in gravity sewer pipes that have experienced inner corrosion and minor damage.
- **Semi-structural**: the liner can withstand external and internal loads at host pipe holes. However, the structural capacity remains on the host pipe. Therefore, the host pipe may have a maximum of three longitudinal cracks at the same cross-section and less than 10% of ovality. Semi-structural liners should perfectly fit the host pipe and usually present excellent expansion features. Moreover, they contain a medium amount of fiber, which makes them lighter than structural liners, and they present a higher maneuverability, contributing to the installation success.
- **Structural**: the liner can withstand full internal and external loads. The host pipe has no structural contribution, which may have experienced severe damage, losing its structural function.

On the other hand, an even more detailed liner's classification is presented in AWWA M28 [11] and ISO 11295:2020 Table 16 [12]:

- **Class I**: non-structural liners used to protect the host pipe from corrosion (class D according to ISO 11295 [12]).
- **Class II**: the liner is used to improve the hydraulic capacity of the host pipe and is classified as semi-structural. The liner may be used to avoid leaks due to corrosion pits or leaking joints, and it should be able to withstand inner loads at these points (class C according to ISO 11295 [12]).
- **Class III**: it is also a semi-structural liner with the mechanical properties of class II liners improved. Class III liner should be able to have a reduced ring stiffness to withstand reduced vacuum (class B according to ISO 11295 [12]).
- **Class IV**: the liner should withstand full internal and external loads. Therefore, it is considered structural, and the host pipe has no structural capacity (class A according to ISO 11295 [12]).

2.3 Installation procedure

There are two CIPP installation methodologies: the inversion and the pulling procedure. In both, a common set of fundamental steps are followed. The general procedure involves the host pipe's assessment, the liner's design, the impregnation of the liner with resin, and the liner's installation by either the inversion or the pulling procedure followed by the final steps: sealing the ends and quality control tasks.

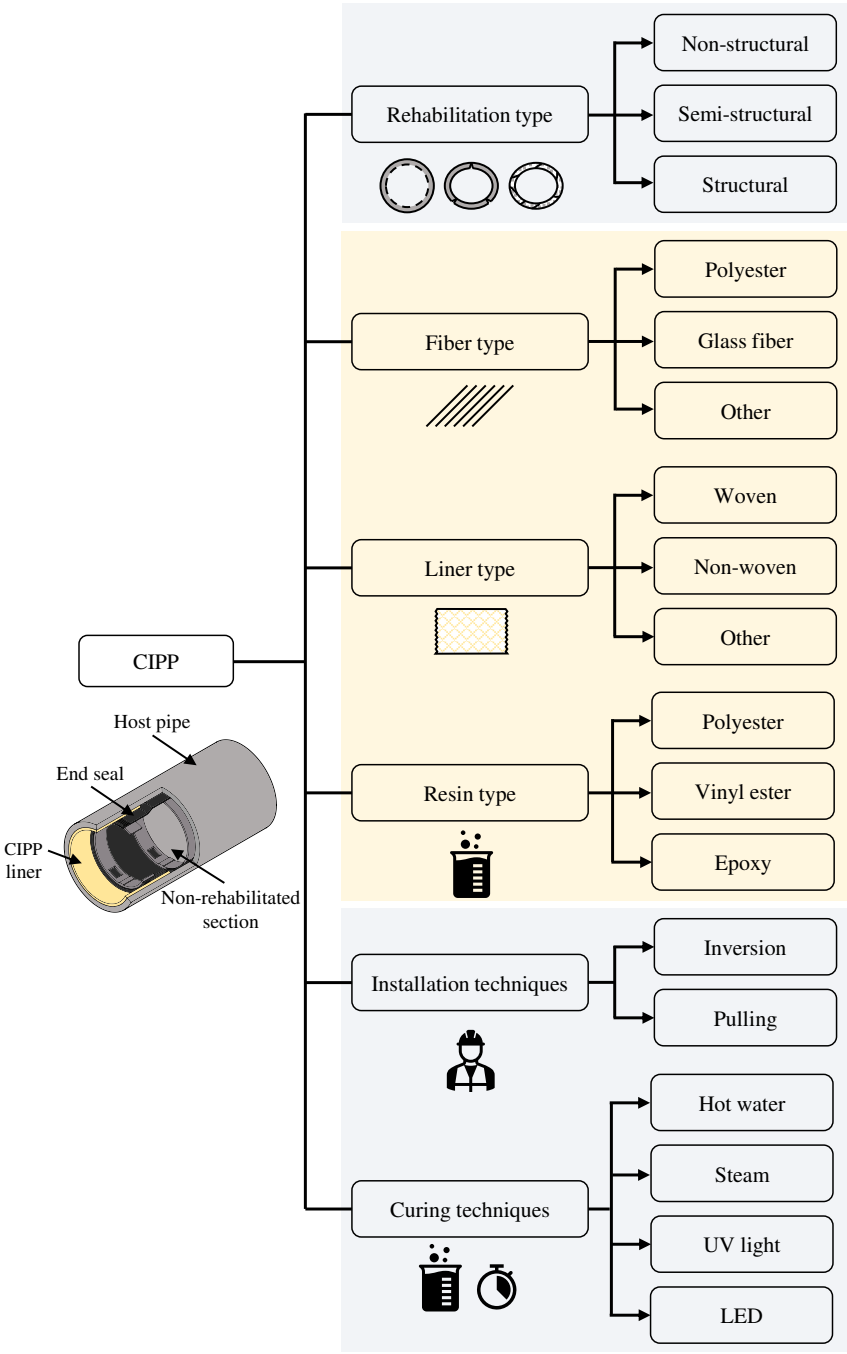

Figure 2.3: Overview of the available Cured-In-Place Pipe liners and installation techniques.

2.3.1 Pre-installation

a) Evaluation and conditioning of the host pipe

The level of damage that has experienced the host pipe over the years will directly influence the liner's design. Therefore, before thinking of a liner's design, an inspection of the host pipe to be rehabilitated is performed. Then, a non-structural, semi-structural, or structural liner's design is defined. Moreover, this inspection is also used to obtain the host pipe morphology used in the liner's design step.

On the other hand, pipelines, especially sewer pipes, may present tuberculations (small mounds of corrosion) or incrustations. However, the host pipe must be clean and smooth without protuberances to be rehabilitated with a CIPP liner. Otherwise, installation defects such as wrinkles or folds will appear. In addition, it is also necessary to remove sand or pebbles that are often found in pressure pipes. High-pressure water jets, brushes, and even milling procedures are used in the cleaning procedure.

b) Liner's design

The mechanical performance and thickness of the liner are defined by the design equations presented in current CIPP standards as ASTM F1216 [8] and UNE 53929 [1]. A custom liner is designed depending on the host pipe's degree of deterioration. The liner may be prepared or not to face hydraulic groundwater loads, host pipe ovality, host pipe holes, negative pressure, and external loads.

c) Liner's impregnation: the wet-out process

Depending on the manufacturer and curing process used (thermal or UV), the impregnation of the liner is performed on-site or at the manufacturer's factory. UV liners are usually impregnated at the factory. The liner is then wrapped with an opaque cover to prevent the curing process from starting due to ambient light exposure.

On the other hand, thermal curing liners are often impregnated a few hours before the liner's installation takes place under a controlled atmosphere. These resins are usually made of two or more components. When mixed, a limited gel time is established, and the liner must be installed before it starts to solidify. Some manufacturers have tried to perform an on-site impregnation of liners with a reduced gel time. However, predicting the on-site temperature conditions is challenging as sometimes delays in the working plan or unexpected events happen. Moreover, the impregnation is often performed at night to have the liner prepared to be introduced early in the morning. Consequently, the impregnation is often performed under lower predicted temperatures, decreasing the resin's viscosity. In some cases, where the resin's viscosity is heavily influenced by the temperature, low ambient temperatures may create difficulties in the liner's impregnation, generating a lack of resin in some regions of the liner. For that reason, most manufacturers prefer to impregnate the liner at the factory under controlled conditions.

Furthermore, the impregnation of the liner is performed under vacuum conditions to avoid the generation of bubbles that will result in an impregnation defect. It should be noted that a liner must be thoroughly impregnated with resin for its best performance. Therefore, every single fiber must be surrounded by resin to create the best interphase interaction between the binder (resin) and the reinforcement (fiber) to take full advantage of the composite mechanical properties.

2.3.2 Installation

a) Installation technologies

Over the years, the CIPP industry has developed and improved the CIPP installation technologies. The first liners were installed by the pulling method described in ASTM F1743 [13]. Later, the inversion technology described in ASTM F1216 [8] was developed. The features of both installation methods are described below.

- **Pulling**: a soft liner impregnated with resin is inserted into the host pipe by pulling it using a winch. Then, a calibration liner made of a thin polymeric layer is also introduced and then inflated with air to proceed with the curing process. Depending on the curing process, the calibration liner can be installed by the inversion or the pulling method. The inversion methodology is preferred in thermal curing processes, while the UV curing process requires pulling the calibration liner to allow the UV lamps trolley path (see Figure 2.4).

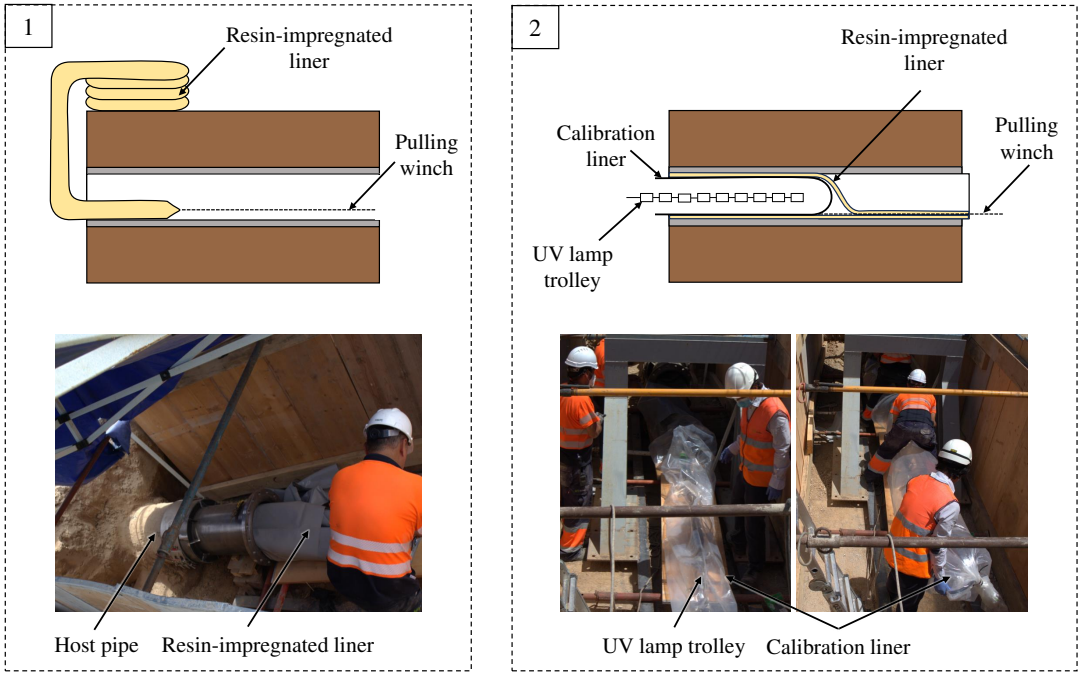

a) Step 1: liner introduction

b) Step 2: introduction of the pressurized calibration liner

Figure 2.4: CIPP liner's installation by the pulling technique.

- **Inversion**: in the inversion methodology, the soft resin-impregnated liner is first placed into the inversion drum. Then, the liner is introduced through the host pipe by inverting itself again using compressed air. The liner must withstand forces due to the inversion and the internal air pressure used in the installation procedure.

  The inversion technique prevents the generation of airbags between the liner and the host pipe. The absence of friction between the host pipe and the liner during its installation prevents damaging the liner. Furthermore, it is possible to rehabilitate pipelines with 45° elbows.

  However, heavy liners with a considerable amount of fiber such as structural liners and large thicknesses, are challenging to install by the inversion methodology as higher inversion pressures are required. Moreover, the equipment cost may be further increased and thereby avoided by the installation enterprise.

b) The curing process

The curing process is the procedure where the resin solidifies, generating the new pipe inside the host pipe. It exists different curing technologies based on thermal or wavelength curing processes. Thermal curing can be performed by hot water or steam, while wavelength curing is mainly based on UV or LED wavelengths. Although thermal curing is dominant in the market, it has been an important growth of UV curing liners in recent years, especially in the sewer industry. The LED curing technology is the last that has appeared, and it is still very new and rarely used. However, all the curing processes require a minimum air pressure to keep the liner fitted to the host pipe.

- **Thermal curing**: hot water or steam is introduced in the pressurized liner. The temperature and curing time are crucial factors to control.

- **Wavelength curing**: a trolley of lamps is introduced in the pressurized liner. The curing speed is controlled by the trolley speed and the intensity of the lamps. The trolley also incorporates temperature sensors. Therefore, failures in any lamp can be easily detected as the lamps also emit considerable heat due to the Joule effect. A UV curing lamp control station is shown in Figure 2.5 and Figure 2.6. Moreover, the power and intensity of each lamp are also shown in the control station panel. The exposure time is crucial. A low exposure time will cause the resin not to cure in its totality. However, a high exposure time can damage the liner, causing deterioration or small burns.

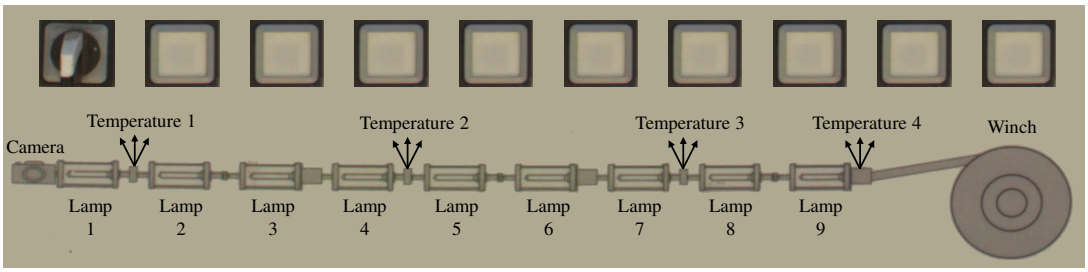

Figure 2.5: UV lamp trolley configuration. Panel from a UV lamp control station.

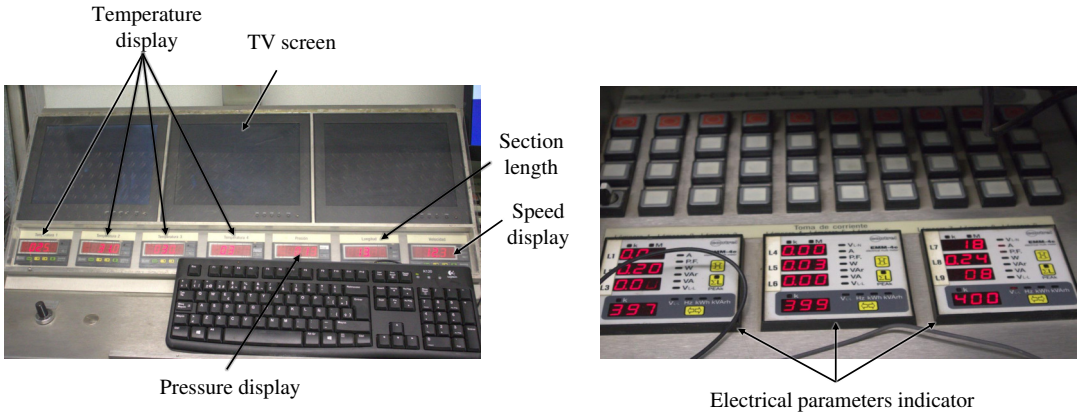

Figure 2.6: Control center of a UV lamp station to monitor the curing process.

2.3.3 Post-installation

After the curing process, seals at the ends must be installed to avoid the introduction of water between the host pipe and the liner. The seals are made of rubber and steel rings. Moreover, lateral derivations (if any) must be opened using a TV-controlled cutting robot.

Then, a visual TV inspection is conducted to identify any installation defects. Furthermore, pressure and leakage tests are performed on-site to evaluate the mechanical strength of the liner installed. In addition, ring liner samples are extracted from the cured on-site liner for laboratory testing.

2.4 Buckling of CIPP liners: analytical approaches

In the nineteenth century, Levy [14] presented the critical buckling pressure (P_{Cr}) equation for an unsupported circular ring subjected to external pressure (see Eq. 2.1).

$$\overline{P}_{Cr} = \frac{3EI}{R^3} \tag{2.1}$$

Where E is the Young's modulus, I the moment of inertia and R is the ring's radius.

The buckling of a cylindrical pipe can be seen as a plane strain problem when an infinitely long pipe is considered. Consequently, Timoshenko [15] implemented the theory of elasticity in the ring case by adjusting the elastic Young's modulus ($E' = E/(1-\nu^2)$) and the moment of inertia $I = bt^3/12$ with b being one (see Eq. 2.2).

$$P_{Cr}^{T} = \frac{E}{4(1-\nu^2)}\left(\frac{t}{R}\right)^3 = \frac{2E}{1-\nu^2}\left(\frac{t}{D}\right)^3 = \frac{2E}{1-\nu^2}\left(\frac{1}{(DR-1)^3}\right) \tag{2.2}$$

Where t is the liner's thickness, ν is the Poisson's ratio, DR is the outer diameter to thickness ratio, and D is the pipe diameter.

The equations exposed above explain the buckling behavior of an unsupported free liner (see Figure 2.8a). However, rehabilitation liners are placed inside a host pipe with expansion limitations. Hence, a fitted liner would collapse at a higher pressure than an unsupported free liner. Therefore, many researchers have focused their studies on the case of a ring or a cylindrical liner encased in a rigid cavity.

The existing buckling equations for liner's design subjected to external pressure can be classified as a contribution of two main procedures: Timoshenko's [15] and Glock's [16] approaches (see Figure 2.9). The main difference between both approaches is how the liner's imperfections are considered. In Timoshenko's approach [15], global and local imperfections are treated together and evaluated under an enhancement factor K, while in Glock's approach, imperfections are treated separately as reduction factors. However, although Glock's derivative equations may find more optimized and accurate design thicknesses than Timoshenko's equation, difficulties in quantifying and measuring the imperfections on the field have led to implementing Timoshenko's formulation in the current design CIPP standards ASTM F1216 [8] and UNE 53929 [1].

Imperfections are present in most CIPP rehabilitations. Moreover, a liner with imperfections presents lower critical buckling pressures than tight-fit circular liners. Imperfections are classified as global and local.

Global imperfections

- **Ovality**: the liner is installed in a host pipe that presents ovality due to severe damage or low manufacturing tolerances of old pipes. Then, the liner takes the oval shape (see Figure 2.7a).
- **Loose-fit**: a gap between the liner and the host pipe may be generated during its installation due to polymerization shrinkage of the resin or a wrong inner pressure applied in the curing process (see Figure 2.7b).
- **Longitudinal wrinkle**: longitudinal wrinkles may appear when the outer diameter of the liner is bigger than the inner diameter of the host pipe (see Figure 2.7c).
- **Variable thickness**: small cavities may be formed in the inner face of host pipes due to corrosive liquids or gases in service. During a rehabilitation procedure by a CIPP liner, the extra resin may fill these random cavities. Consequently, the liner may present significant thickness differences in the same ring section (see Figure 2.7d).

Local imperfections

- **Wavy imperfections**: localized intrusions or debris on the host pipe may cause a local wavy imperfection. Broken segments of the damaged host pipe are also responsible for this type of imperfection (see Figure 2.7e).
- **Grouting voids**: sometimes, the host pipe presents local voids or inner corrosion pits responsible for creating local bumps or extrusions of the liner, losing its perfectly circular shape (see Figure 2.7d).

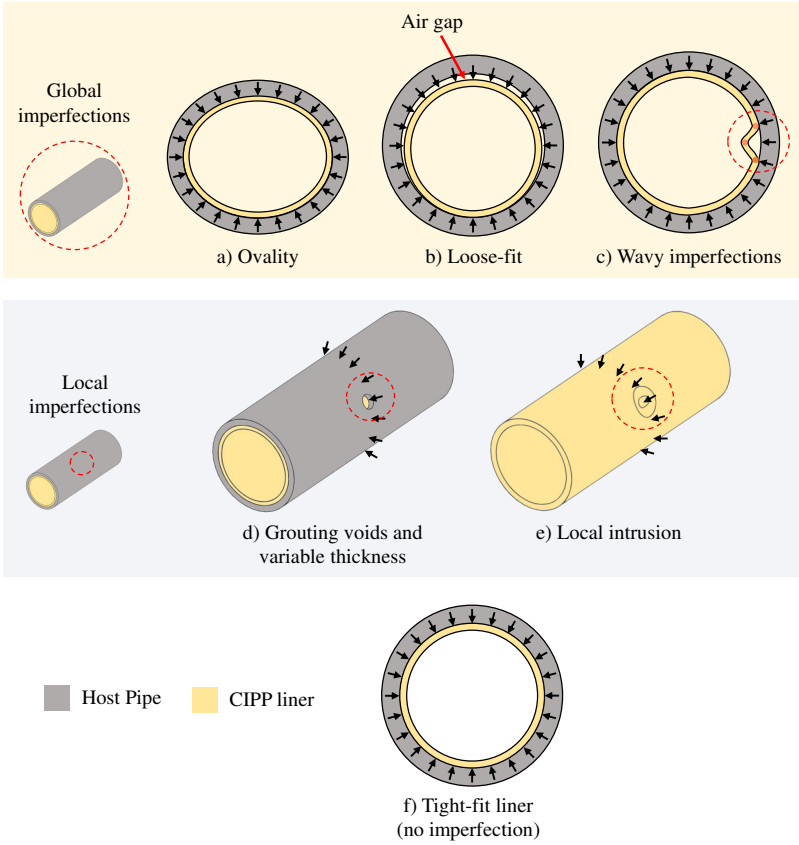

Figure 2.7: Classification of liner's imperfections subjected to buckling due to external pressure identified and studied by authors. Global imperfections: ovality (a), loose-fit (b), and wavy imperfection (longitudinal wrinkles) (c). Local imperfections: grouting voids and variable thickness (d), and local wavy imperfection (local intrusion) (e). No imperfection: tight-fit liner (f).

2.4.1 Timoshenko's approach

Timoshenko's equation (Eq. 2.2) was developed for unsupported liners. However, an experimental enhancement factor K was added to define the critical buckling pressure of an encased liner (see Eq. 2.3). This factor was experimentally defined by comparing the buckling pressures for unsupported and encased liners. Local and global imperfections (except ovality) were implemented in the experimental tests. Aggarwal and Cooper established an enhancement factor of $K = 7$ in 1984 [17].

It should be noted that some current CIPP standards as ASTM F1216 [8] and UNE 53929 [1] have implemented Timoshenko's approach with the enhancement factor $K = 7$.

$$P_{Cr} = P_{Cr}^{T} K \tag{2.3}$$

ASTM F1216 and UNE 53929

ASTM F1216 [8] and UNE 53929 [1] use a conservative model derived from Timoshenko's approach to

prevent buckling due to hydrostatic pressure. Moreover, an ovality reduction factor was added (see Eq. 2.4).

$$P_{Cr} = \left(\frac{2KE_L}{1-\nu^2}\right)\left(\frac{1}{(DR-1)^3}\right)\frac{C}{N} \tag{2.4}$$

Where E_L is the long-term Young's modulus, DR is the outer diameter to thickness ratio, C is the ovality reduction factor, and N is the safety factor.

2.4.2 Glock's approach

The Glock's approach [16] originated the non-linear theory based on the minimum potential energy principle (see Eq. 2.5).

$$P_{Cr}^{Gl} = \frac{E}{1-\nu^2}\left(\frac{t}{D}\right)^{2.2} \tag{2.5}$$

Where D is the diameter of the thin liner.

Two main patterns of fundamental buckling were identified in encased liners: single-lobe mode and the two-lobe mode (see Figure 2.8b-c). Glock's theory assumes that in a perfectly circular encased liner, single-lobe mode will take place as the potential energy balance of the liner system indicates that the single-lobe mode yields a lower critical pressure. However, an initial gap between the liner and the host pipe may induce an elliptical deformation tendency on the liner following the two-lobe mode until failure occurs. Therefore, identifying and quantifying the imperfections is crucial as the buckling mechanism and critical buckling pressure may change. Some authors have extended Glock's equation by considering the effect of global and local imperfections. The main contributions are listed below.

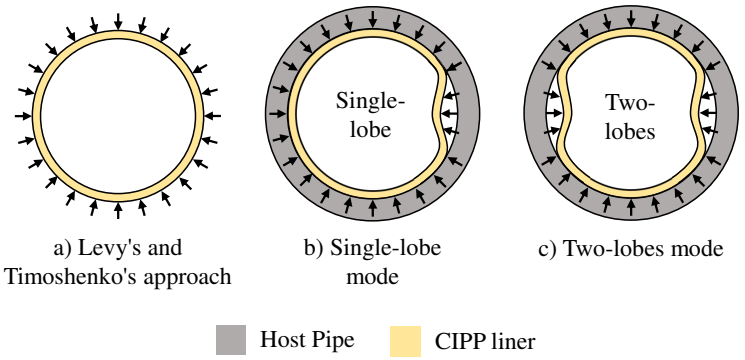

Figure 2.8: Buckling modes of liners subjected to external pressure. Unsupported free liner: Levy's and Timoshenko's approach (a). Encased liner: single-lobe mode (b) and two-lobes mode (c).

Hall's equation

Hall's equation (see Eq. 2.6), developed in the USA, is based on the one-lobe Glock's approach. The annular gap (x), ovality (y), and local wavy imperfections (z) are considered [18, 19].

$$P_{Cr} = \left(\frac{a_H E_L}{1-\nu^2}\right)\left(\frac{1}{(DR-1)^{m_H}}\right)\frac{1}{N}$$
$$a_H = b_{ijk}x^i y^j z^k \tag{2.6}$$
$$m_H = c_{ijk}x^i y^j z^k$$

Where a_H and m_H are polynomials with three variables. The 27 (3^3) coefficients were adjusted using numerical FE results.

Boot's equation

In the UK, Boot [20] considered the loose-fit and ovality imperfections. Thus, the effect of a gap between the liner and the host pipe was considered on the liner's buckling pressure, leading to a two-lobe mode. The following extended Glock's equation was presented:

$$log_{10}\left(\frac{P_{Cr}}{E}\right) = m_B log_{10}\left(\frac{D}{t}\right) + log_{10}(c_B) \tag{2.7}$$

Where m_B and c_B are the coefficients of a logarithmic interpolation from Boot's charts obtained by numerical FE analysis or by directly solving Glock's equation considering ovality and the initial annular gap.

ATV-M 127-2

The ATV-M 127-2 [21] Germany's standard is based on the one-lobe Glock's equation. Moreover, reduction factors for annular gap (K_s), ovality ($K_{GR,v}$), and local wavy imperfection (K_v) are considered. The reduction factors were adjusted by numerical FE results (see Eq. 2.8).

$$P_{Cr} = K_v K_{GR,v} K_s \alpha_D t$$
$$\alpha_D = 2.62\left(\frac{R}{t}\right)^{0.8} \tag{2.8}$$
$$t = \frac{EI}{R^3}$$

Where t is the liner's thickness.

Moore's equation

In Canada, the one-lobe Glock's equation was adjusted by Moore [22]. Three reduction factors for

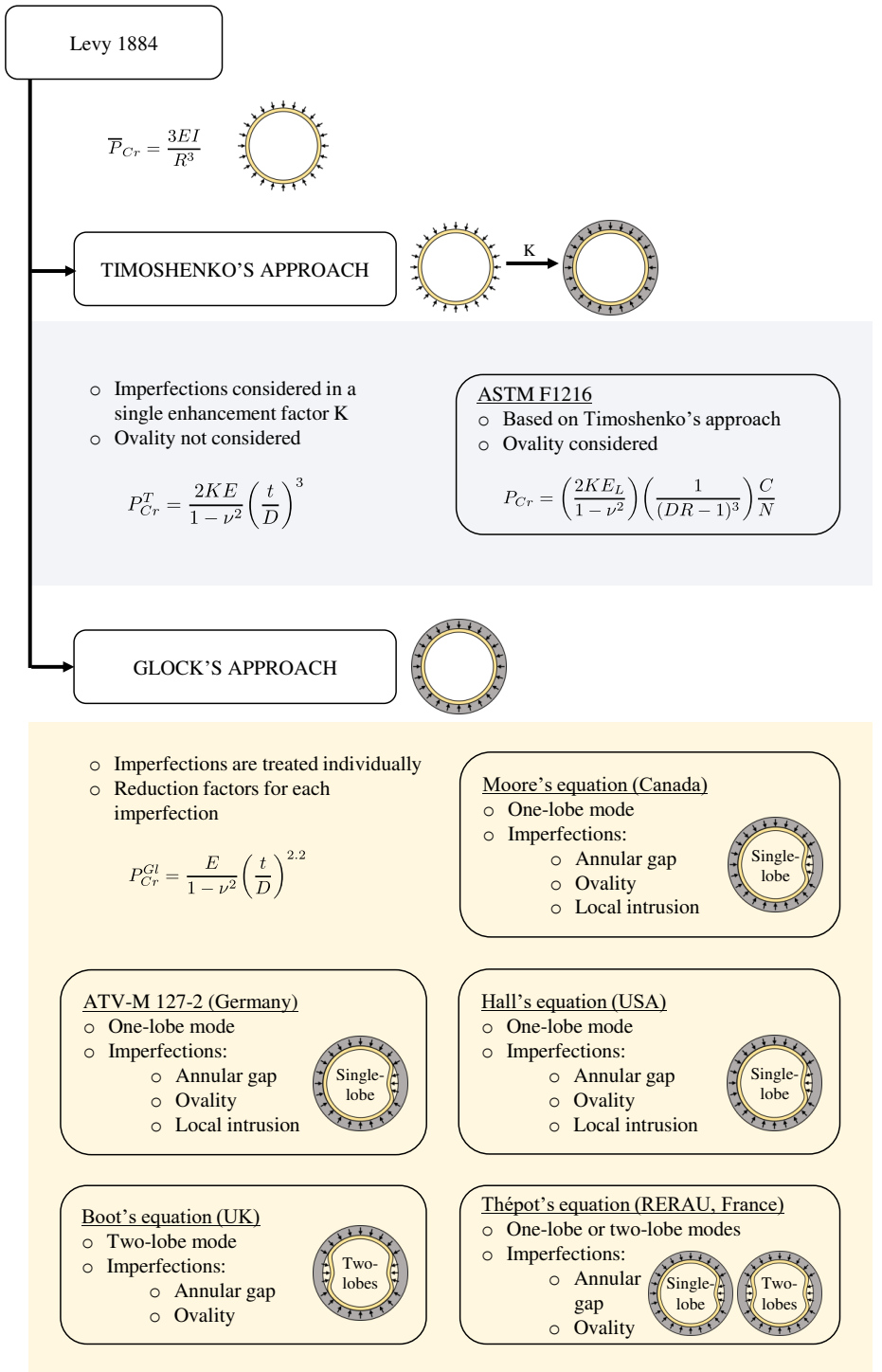

Figure 2.9: Development of the buckling theory of encased liners subjected to buckling due to external pressure.

ovality (R_q), local wavy imperfection (R_{Δ_w}) and annular gap (R_{d_g}) were implemented (see Eq. 2.9).

$$P_{Cr} = \left(\frac{E_L}{1-\nu^2}\right)\left(\frac{t}{D}\right)^{2.2} R_q R_{\Delta_w} R_{d_g}$$

$$\begin{aligned} R_q &= e^{-q/10} \\ R_{\Delta_w} &= e^{-0.56\Delta_w/t} \\ R_{d_g} &= e^{-d_g/t} \end{aligned} \tag{2.9}$$

Where q is the ovality (%), Δ_w is the intrusion of the local wavy imperfection, and d_g is the amplitude of the annular gap (mm).

Thépot's equation

Thépot [23], in the national research project RERAU (France) about the rehabilitation of urban sewers, also employed the Glock's equation, featuring either a one-lobe or two-lobe design, incorporating reduction factors for annular gap ($\Gamma_{p,g}$) and ovality ($\Gamma_{p,h}$) imperfections (see Eq. 2.10).

$$P_{Cr} = \Gamma_{p,h}\Gamma_{p,g}\beta_k \frac{EI}{R^3}$$

$$\begin{aligned} \beta_k &= 2.02\left[k\left(\frac{EA}{Per_{liner}}\right)\left(\frac{R^3}{EI}\right)\right]^{0.4} \\ \Gamma_{p,h} &= \frac{1}{1+0.41\delta_h - 0.006\delta_h^2} \\ \Gamma_{p,g} &= \frac{1}{1+0.41\delta_g - 0.006\delta_g^2} \end{aligned} \tag{2.10}$$

Where Per_{liner} is the perimeter of the liner, β_k is the buckling factor, $k = 1$ for one-lobe mode and $k = 2$ for two-lobe mode, δ_h is the ovality and δ_g is the annular gap and are calculated according Eq. 2.11.

$$\begin{aligned} \delta_g &= 2.94\frac{g}{t}\left(\frac{R}{t}\right)^{0.2} \\ \delta_h &= 0.515 h_{Th}\left(\frac{R}{t}\right)^{0.4} \end{aligned} \tag{2.11}$$

Where g is the annular gap and h_{Th} the ovality.

For solid and homogeneous materials ($EI/EA = t^2/12$) and a circular shape liner ($Per_{liner} = 2\pi R$), the buckling factor (β_k) can be calculated according Eq. 2.12

$$\beta_k = 2.62k^{0.4}\left(\frac{R}{t}\right)^{0.8} \tag{2.12}$$

Finally, a global reduction factor was also developed that combines both imperfections: annular gap and ovality (see Eq. 2.13).

$$\Gamma_{p,gxh} = \frac{1 - 4\delta_h + 4.9\delta_h^2}{1 + 0.4\delta_g - 0.6\delta_g\delta_h} \tag{2.13}$$

2.4.3 Other contributions to liners buckling

Extensive literature can be found on Glock's buckling and derivates formulation. Authors have considered circular, oval, and egg-shaped liners, although only a few have focused on non-circular liners [24–28]. Analytical formulation and numerical FE models have led the buckling model design rather than experimental data. Only a handful of authors have succeeded in performing experimental buckling tests [17, 29–31]. On the other hand, elastic buckling was mainly considered by authors, while a reduced literature can be found on inelastic buckling [30, 32–35]. Finally, global and local imperfections, as well as tight-fit liners, have been deeply studied by many authors. Table 2.1 lists a selection of the most relevant studies that have contributed to the encased liner's buckling theory.

Table 2.1: References of contributions to liner's buckling theory. *Light gray*: experimental solution. *White*: analytical and numerical FE solutions.

Reference	Buckling type	Liner geometry	Imperfection	Solution	Aim of study
Levy, 1884 [14]	Elastic	Circular ring	Tight-fit	Analytical	Development of the formulation of buckling of an unsupported circular ring subjected to external pressure.
Glock, 1977 [16]	Elastic	Fitted circular liner	Tight-fit	Analytical	Development of non-linear equations for CIPP liner's buckling theory based on the principle of minimum potential energy. Single lobe mode vs two-lobe mode.
Aggarwal & Cooper, 1984 [17]	Elastic	Circular	Tight-fit	Experimental	Experimental finding of the enhancement factor of the soil and the existing pipe adjacent to the new pipe (K = 7).
Boot, 1997 [20]	Elastic	Circular	Loose-fit (gap)	Analytical	New equations are presented to extend the range of application of Glock's formulation covering symmetrical and asymmetrical annular gaps.
El-Sawy & Moore, 1997, 1998 [22, 36]	Elastic	Circular	Tight-fit, Loose-fit (gap), ovality, and longitudinal wrinkle	Numerical FE	Effect of local imperfections (folds) and global imperfections (ovality and gap between the host pipe and the liner) studied to the liner stability. New design buckling equations for liners.
Omara *et al.*, 2000 [29]	Elastic	Oval	Ovality	Experimental and analytical	A new model for predicting the buckling pressure of thin circular pipes encased in rigid oval host pipes is presented.

*Full-scale test

Continued on next page

Table 2.1 – continued from previous page

Reference	Buckling type	Liner geometry	Imperfection	Solution	Aim of study
Thépot, 2000 [25]	Elastic	Circular and non-circular	Tight-fit (no imperfection)	Analytical	New design method based on Glock's formulation for non-circular sewer linings. Safety factors to prevent buckling are given.
Thépot, 2001 [26]	Elastic	Oval	Loose-fit (gap)	Analytical	New design equations for oval-shaped sewer linings (buckling based).
El-Sawy, 2001 [32]	Elastic and inelastic	Circular	Tight-fit	Numerical FE	Evaluation of Jacobsen solution of thick cylindrical liners by a numerical FE model.
El-Sawy, 2002 [33]	Elastic and inelastic	Circular	Loose-fit (gap)	Numerical FE	Evaluation of Jacobsen solution of thick cylindrical liners with loose-fit imperfection by a numerical FE model.
Madryas & Szot, 2003 [37]	Elastic	Circular	Loose-fit (gap), ovality and wavy imperfections	Numerical FE	The study proposed a general formula for elastic critical pressure of liners with combined imperfections (gap, ovality and wavy imperfections).
Jeyapalan, 2004 [38]	Elastic	Circular	Tight-fit, ovality, and longitudinal wrinkle	Analytical	A unified design method is proposed for most no-dig rehabilitation methods including CIPP.
El-Sawy & Sweedan, 2010 [39]	Elastic	Circular	Local wavy imperfections	Numerical FE	Numerical study that investigates the effect of various geometric parameters of local wavy imperfections on the elastic buckling pressure of cylindrical liners. New equations are presented.
El-Sawy & Sweedan, 2010 [40]	Elastic	Circular	Loose-fit (gap)	Numerical FE	A simplified procedure based on FE results is proposed for calculating buckling pressure of thin liners. The model asses the non-linearity effects of large deformations and geometric imperfections.
Li *et al.*, 2012 [41]	Elastic	Circular	Tight-fit with variable thickness	Analytical and numerical FE	Analytical solution for the elastic buckling of cylindrical pipe linings with variable thickness subjected to external hydrostatic pressure.
El-Sawy, 2013 [34]	Inelastic	Circular	Local wavy imperfections	Numerical FE	Inelastic buckling of liners with local imperfections. First paper to assess inelastic buckling and local imperfections.
Boot *et al.*, 2014 [27]	Elastic	Egg-shaped	Tight-fit	Analytical	A new design method is proposed for egg-shaped liners to optimize actual designs calculated by the French and UK procedures.
Wang & Koizumi, 2017 [30]	Inelastic	Circular	Tight-fit, Loose-fit (gap)	Experimental	Experimental data that clarify some of the buckling formulation (El-Sawy) and buckling mechanisms of liners encased in a rigid host pipe.
Li & Huang, 2019 [35]	Elastic and inelastic	Circular	Loose-fit (non-uniform gap)	Numerical FE and analytical	Effect of temperature rise to the buckling performance of a liner with a non-uniform gap.

*Full-scale test

Continued on next page

Table 2.1 – continued from previous page

Reference	Buckling type	Liner geometry	Imperfection	Solution	Aim of study
Li *et al.*, 2019 [28]	Elastic	Circular and egg-shaped	Grouting voids	Numerical FE and analytical	The contribution of small, medium and large grouting voids (host pipe damage) to the buckling of thin-walled confined liners were studied.
Thépot, 2021 [42]	Elastic	Circular and non-circular (elliptical and egg-shaped)	Close-fit (gap)	Analytical and numerical FE	Correction factors for close-fit liners encased in fractured rigid circular and non-circular host pipes are presented.
*Wang *et al.*, 2023 [31]	Elastic	Circular	Ovality, loose-fit (gap)	Experimental and analytical	The current analytical equations to calculate the critical buckling pressure of liners with imperfections under the influence of an annular gap, were improved based on experimental results.

*Full-scale test

2.5 Liner's design and installation challenges

The design of CIPP liners is defined by the equations set in current CIPP standards (ASTM F1216 [8], UNE 53929 [1]). The liner's design is adjusted to the host pipe structural capacity. Therefore, a non-structural, semi-structural, or structural liner must be designed. However, significant issues with CIPP liners in pressure pipes have led to the use of structural liners in most projects. Oversizing has been a usual practice to overcome CIPP uncertainty [43, 44]. However, in the case of CIPP liners, oversizing may negatively affect the safety of the rehabilitation. A liner with wider thicknesses and a higher amount of fiber may produce a heavier liner with reduced maneuverability. Hence, the installation process became more challenging, as stated in section 7.5.2.3 of UNE 53929 [1]. Therefore, the likelihood of having installation defects that will negatively affect the performance of the liner is increased. In most cases, when installation defects cannot be rectified, the rehabilitated pipe must be replaced. Therefore, in addition to the costs of rehabilitation, there is an additional cost of replacing the pipe that was initially intended to be avoided using CIPP. Consequently, some authors have proposed the optimization of CIPP liners [45–48]. Short and long-term tests have demonstrated the viability of reducing the liner's thicknesses [46]. Moreover, thickness reductions of about 20% were proposed in [47] with current CIPP liners.

On the other hand, Allouche et al. [49] identified six limit states of CIPP liners that can cause instabilities due to internal pressure and uneven ground movements:

- **LS1**: hoop stress due to internal pressure (see Figure 2.10a).
- **LS2**: longitudinal bending due to a liner's change on section, from a broken host pipe section to a structurally sound one (see Figure 2.10b).

- **LS3**: longitudinal bending due to the liner passing through a clamped, fractured, or joined section (see Figure 2.10c).
- **LS4**: global or local bending moment and wall stretching of the liner at a ring fracture or joint (see Figure 2.10d).
- **LS5**: liner spanning through a host pipe hole (local bending) (see Figure 2.10e).
- **LS6**: local liner stresses due to a re-opened lateral connection (see Figure 2.10f).

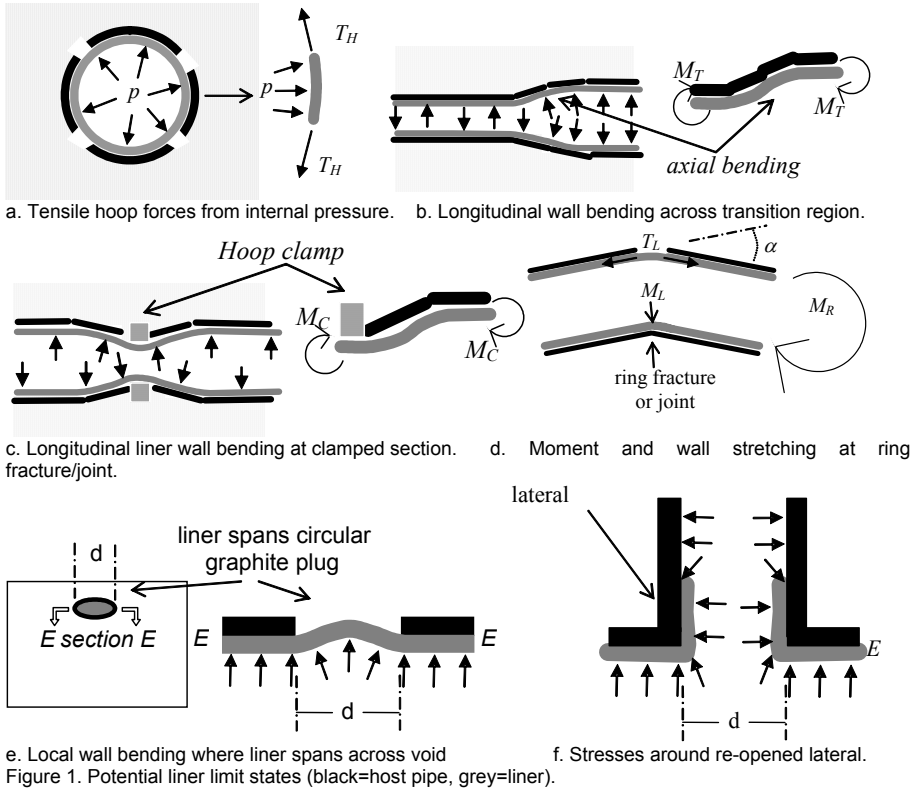

Figure 2.10: The six limit states a CIPP liner can be subjected to due to internal water pressure and non-uniform ground movements. Adapted from [49].

Several authors have studied the above liner's instabilities and provided valuable data and approaches. These authors have paid particular interest in investigating the liner's performance in front of wrinkles, host pipe damage (corrosion pits, fractures, and holes), joints, and lateral openings, among others.

2.5.1 Wrinkles and longitudinal folds

Current CIPP design regulations do not include procedures to prevent the appearance of wrinkles during the installation of a liner. The structural consequences that can cause the appearance of wrinkles should be mentioned in ASTM F1216 [8]. Moreover, an acceptance wrinkle criterion should be defined.

The structural integrity of a liner can be significantly reduced when hoop or longitudinal wrinkles appear. Buckling theories considered longitudinal wrinkles due to hydrostatic pressure. However, pressure pipes may be governed by inner pressure rather than external loading conditions. Numerical and experimental analysis on CIPP liners with longitudinal wrinkles subjected to inner pressure also showed a significant reduction of the mechanical properties of the liner [49–52].

To date, few published scientific articles about the effect of longitudinal folds on structural liners in pressure pipes are available in the literature. In a pioneering study, a combination of limit states (LS5 with liner folds) was suggested to be considered by [50] as a new potentially critical limit state. The negative impact of the longitudinal wrinkle was demonstrated to be increased when it passes through a host pipe hole [50]. The study included experimental pressure tests on old pipes from the city of Hamilton (Canada), a numerical model, and a parametric study. The pressure rates of a liner with a longitudinal wrinkle passing through a rectangular host pipe hole and the same wrinkle-free liner passing through a circular hole were experimentally compared. These results were used to validate the numerical 3D solid model created in which it was demonstrated that longitudinal wrinkles have a very negative effect on the mechanical properties of the liner.

Moreover, a wrinkle was defined by two parameters: the depth (amplitude, Δ_w) and an angle θ [50] (see Figure 2.14). The mechanical properties of the liner are reduced with higher wrinkle depths (Δ_w). In addition, the 90° wrinkle is considered the worst case [50, 51].

Longitudinal wrinkles are generated when the outer liner's diameter exceeds the host pipe's inner diameter. Therefore, the dimensions of the liner in the design process became crucial. Nevertheless, as stated in [51], the damaged pipes to rehabilitate were manufactured between 1920 and 1970. Consequently, these pipes were manufactured according to poor tolerances and with less robust quality controls than nowadays. As a result, old pipes can have significant variations in diameter with considerable ovality coefficients. Therefore, it is difficult to accurately identify the real inner diameter of the host pipe at each section point since usually only the nominal diameter is annotated on the technical drawings of the project. Hence, an oversize of the CIPP liner is usually performed to absorb the variations in the host pipe's inner diameter. Although longitudinal wrinkles can be generated, no gaps between the host pipe and the liner should appear. However, a threshold for liner's oversizing was defined to avoid the liner being over-weakened by the longitudinal wrinkles due to buckling and wrinkle stress concentration phenomena [50]. The Allowable Oversizing Ratio (AOR) (see Eq. 2.14) defines the maximum wrinkles depth (Δ_w) that can appear in the installed liner for a given liner and host pipe perimeter.

Then, numerical FE calculations can be performed to identify the maximum allowable depth permitted for a specific pipe's burst pressure.

$$\left[\frac{Per_{liner} - Per_{HP}}{Per_{HP}}\right]100 = \left[\frac{\Delta_w}{\pi R}\right]100 \tag{2.14}$$

Where Per_{liner} is the liner's perimeter, Per_{HP} is the inner host pipe perimeter, Δ_w is the wrinkle's depth and R is the inner host pipe radius.

On the other hand, CIPP longitudinal wrinkles were classified based on their geometry pattern [51] in SW, IW, and LW (see Figure 2.11). Moreover, the failure mechanism of each wrinkle pattern tested according to the split disk test (ASTM D2290 [53]) was described in [52].

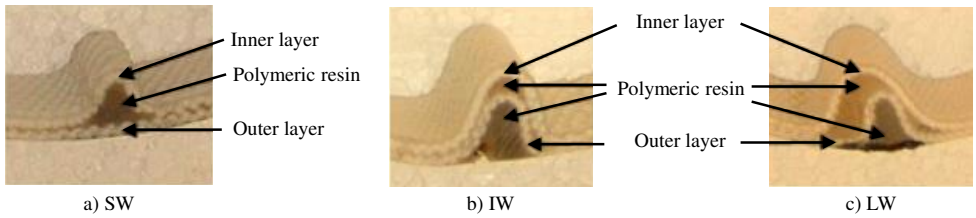

Figure 2.11: Geometry-based wrinkles classification. a) SW: only the inner layer lifts, b) IW: symmetrical wrinkle, and c) LW: non-symmetrical wrinkle. Adapted from [51].

- **SW**: the inner layer, which is in contact with the fluid, lifts. However, contact between the liner outermost layer and the host pipe remains intact (see Figure 2.11a). Two failure mechanisms were identified. First, the LW failure system was identified (from outside to inside). Second, the failure begins in the outermost layer (in contact with the host pipe). Then, the resin between the two layers is detached (does not break), and finally, the liner's inner layer (smaller diameter layer) is broken (see Figure 2.12).

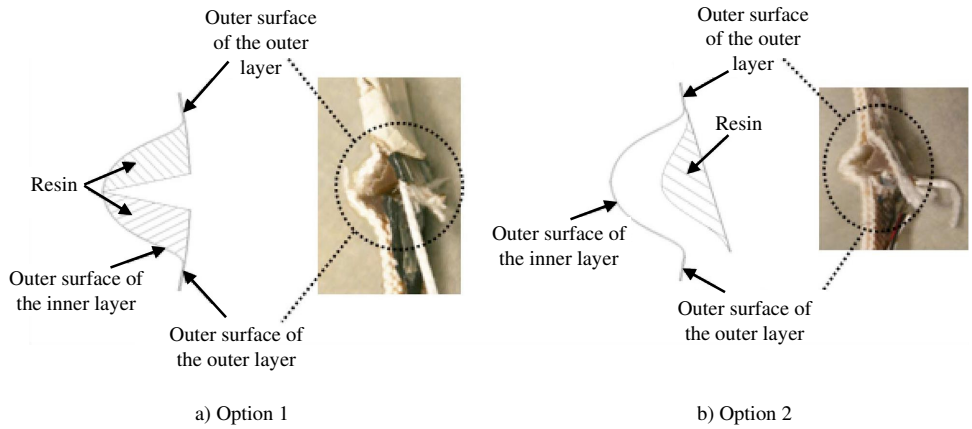

Figure 2.12: SW failure mechanisms identified. Adapted from [52].

- **IW**: all the layers of the liner are folded, generating a symmetrical wrinkle (see Figure 2.11b). Regarding the failure mechanism, first, it breaks the outer resin, followed by the resin between the two layers. Finally, the outermost layer fails before the most folded layer due to the test features (see Figure 2.13).

Figure 2.13: IW failure mechanism. Adapted from [52].

- **LW**: all the layers of the liner are folded, generating a non-symmetrical wrinkle (see Figure 2.11c). Regarding the failure mechanism, a crack is propagated from outside to inwards. For example, the crack will start at the outer resin between the outer liner's layer and the host pipe's inner face in a two-layer liner. Then, the crack will propagate through the outermost liner's layer, followed by the interlayer resin, and finally, the inner layer of the liner.

The effect of wrinkle size, shape, and pattern was experimentally studied in [51]. The wrinkle size was defined by its amplitude (Δ_w) and the wavelength (λ) parameters (see Figure 2.14a). The wrinkle shape was defined by its amplitude (Δ_w) and angle (θ) as reported in [50] (see Figure 2.14b). Experimental split disk tests (ASTM D2290 [53]) up to the first cracking load revealed that IW (θ=90°) is the worst possible scenario. Moreover, the LW has a larger section than the IW, allowing it to withstand higher loads. The section of the wrinkle is calculated as the area of a triangle of the same wrinkle's dimensions (Δ_w and λ). However, the best results were obtained with the SW pattern due to their reduced amplitude (Δ_w) compared to IW and LW. Therefore, the wrinkle's amplitude is a crucial parameter as mentioned in [50–52].

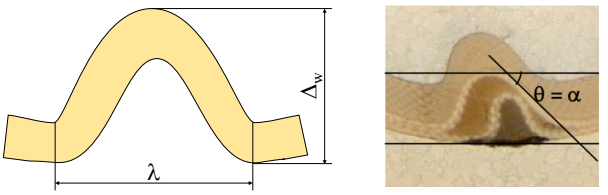

a) Wrinkle shape b) Wrinkle size

Figure 2.14: Wrinkle definition. Adapted from [51].

2.5.2 Host pipe condition: corrosion pits and holes

Several authors have investigated the impact of host pipe holes corresponding to limit state LS5 [49, 54–59]. Internal loads in pressure pipes may induce severe stresses in the hole's or pits area [60, 61]. Two procedures have been identified as host pipe hole generators.

- **Cracks**: sometimes, small cracks appear in the host pipe's outer face. At first glance, these small cracks may look harmless. However, air bubbles may sneak through them, corroding the pipe's structure until it collapses, generating a hole (see Figure 2.15). Moreover, external water can also sink in the small cracks. In winter, this water may turn into ice. Then, the expansion of the ice may widen the crack or even generate a hole.

- **Corrosion pits**: some pipes are placed near high corrosive environments. Consequently, small corrosion pits start to appear in the outer face of the pipe. Over time, the pits became deeper and wider. Thus, they begin to unify, generating a host pipe hole. Some corrosion pits patterns reported in [56] are depicted in Figure 2.16.

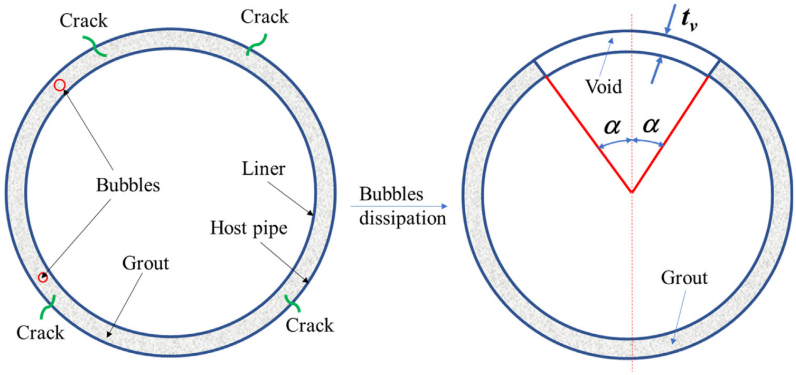

Figure 2.15: Generation mechanism of host pipe holes. Adapted from [28].

Figure 2.16: Pitting corrosion patterns that have generated host pipe holes. Adapted from [56].

The current CIPP standards present analytical equations to consider the impact of a host pipe hole in the liner's design. Different approaches can be found in the CIPP standards. However, the procedures presented in ASTM F1216 [8] and ASTM F2207 [62] (see Figure 2.17) have caught the attention of some authors.

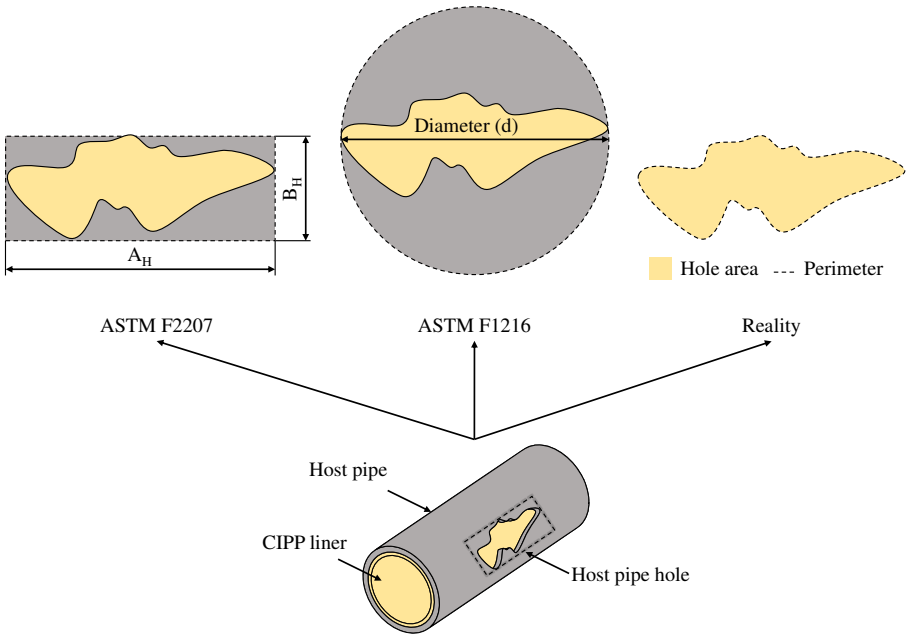

Figure 2.17: Host pipe hole consideration by current CIPP standards.

ASTM F1216 approach

The ASTM F1216 [8] procedure considers circular host pipe holes. Two equations are presented for small voids and larger holes. When Eq. 2.15 is satisfied, the small voids equation must be used.

$$\frac{d}{IDx} \leq 1.83\left(\frac{t}{IDx}\right)^{0.5} \tag{2.15}$$

Where d is the host pipe hole diameter (mm), t is the liner thickness (mm), and IDx is the mean inside diameter of the host pipe (mm)

- **Small voids**: the liner spanning through a host pipe hole is assumed to behave as an edge-fixed circular flat plate subjected only to transverse pressure (see Figure 2.18a).
- **Large holes**: the liner spanning through a host pipe hole is assumed to behave as a ring-in-tension. Hence, the structural contribution of the host pipe is disregarded (see Figure 2.18b).

However, although the flat plate model for small voids has proven to be an accurate simplification providing consistent results [59], some numerical studies [57, 58] revealed that the analytical equation of the ring-in-tension model does not precisely govern larger holes. According to He and Shawn's findings in 2019 [57], when the ratio of the aperture diameter (d) to the inner diameter of the host pipe (D) exceeds 0.4, there is a reduction in hoop stress. These findings contrast with the conventional ring-in-tension model, as the liner is observed to expand freely in the radial direction.

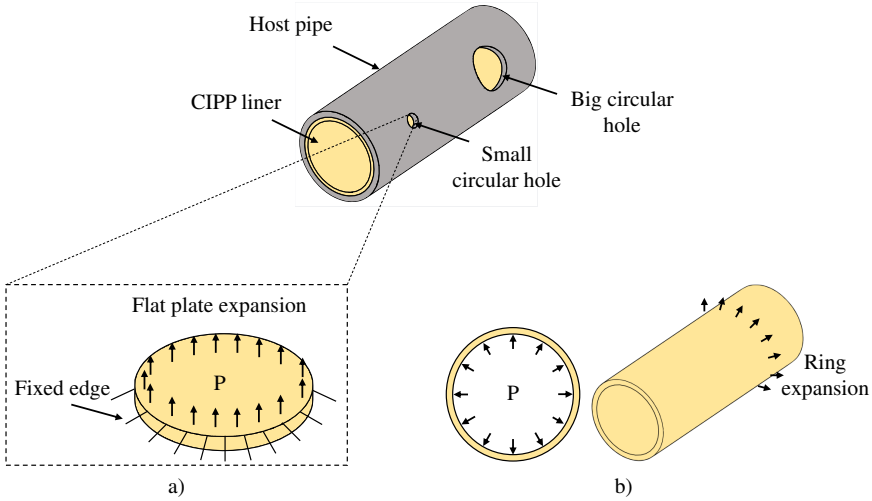

Figure 2.18: Hole's consideration according to ASTM F1216 [8]. a) Small holes: flat plate assumption. b) Big holes: ring-in-tension assumption.

In addition, the ASTM F1216 [8] only considers perfectly circular holes. Although the circular shape is the worst-case scenario, it is difficult to find perfectly circular holes in damaged pipes (see Figure 2.19). Some of them have a completely irregular shape. Nevertheless, ASTM F1216 [8] equations consider these non-circular holes as perfectly circular as the irregular-shape holes were inscribed into a circumference (see Figure 2.17). Consequently, the liner's thickness is heavily oversized.

Nevertheless, many projects have demonstrated that oversizing a CIPP liner does not necessarily enhance rehabilitation safety. An oversized liner contains a greater amount of fiber, increasing its cost and weight and making it more challenging to handle, as stated in section 7.5.2.3 of UNE 53929 [1] (2022). Consequently, the installation became more complex, and the likelihood of installation defects that can negatively affect the mechanical properties of the liner is also increased. Moreover, in most cases where installation defects cannot be rectified, the rehabilitated pipe must be replaced. This procedure incurs additional costs and contradicts the initial intention of the CIPP: avoid the pipe replacement. Therefore, the advantage of using a lighter CIPP liner lies not only in potential material and cost savings, as noted in [46], but also in the fact that the installation procedure is simplified.

On the other hand, the contribution of friction between the liner and a host pipe with holes was numerically studied in [58]. It was revealed that friction reduces the liner stress in the host pipe hole area. Hence, in the absence of experimental data, the usage of minimum friction conditions was recommended to generate conservative models.

ASTM F2207 approach

Some authors [54] highlighted the importance of exploring hole configurations that are not circular. The ASTM F2207 [62] standard presents a mathematical model to consider non-circular holes as rectangular (see Figure 2.17).

Figure 2.19: Holes typology reported in real host pipes. Circular-like holes (f-g, i), longitudinal grooves (a-b), hoop grooves (c), angular grooves (d) and completely irregular shapes (e, h).

However, it is a standard limited to steel gas pipes and orthotropic elastomer-fabric type liners where the shear stiffness is non-existent or very small compared to the hoop and longitudinal stiffness of the liner. The model presented is based on analytical equations, and it assumes that a liner through a hole deforms as a perfectly circular arc. Moreover, two failure criteria are defined.

- **Maximum stress criterion**: failure occurs when the liner reaches its maximum admissible stress in the longitudinal or hoop direction.
- **Interactive stress criterion**: failure can occur before the hoop or longitudinal ultimate stresses are reached. Thus, the liner fails due to the interaction between longitudinal and hoop stresses.

Few authors [54, 55, 58] have numerically investigated the ASTM F2207 [62] hole criterion in CIPP liners. Although it is a standard that considers non-circular holes, most authors have successfully used it to study the liner's spanning through circular holes [54, 58]. Only in [54] elliptical, rectangular, and squared holes were numerically considered. The study revealed that holes oriented in the hoop direction had higher stresses and were suggested to be treated as squared when ASTM F2207 [62] is used to reduce the liner's burst pressure over-estimation.

On the other hand, the circular hole's criterion calculation of ASTM F1216 [8] was intended to be improved in [58] by using the ASTM F2207 [62] approach. As mentioned above, for big holes, the ring-in-tension model can be further improved [63]. The orthotropic numerical model used in [58] revealed that small holes (according to ASTM F1216 [8], see Eq. 2.15) are governed by the interactive stress criterion. In contrast, larger holes are governed by the maximum stress criterion in the hoop direction.

The ASTM F2207 [62] hole criterion was also suggested to calculate a liner spanning through a host pipe section that has lost its structural integrity (limit states LS2 and LS3) [55]. It was concluded that the liner was governed by the maximum stress criterion from ASTM F2207 [62] and especially the hoop stress.

2.5.3 Joints and multi-field coupling effects

CIPP liners were designed to rehabilitate damaged pipelines. However, some authors have considered this trenchless technique for retrofitting pipelines for earthquakes or ground movements [64–77]. The studies have focused on the effect of multi-field coupling effects that induce transient ground deformations near a weak joint or hoop crack. The pipeline can be subjected to six deformation modes due to transient ground deformation: longitudinal, transverse vertical and horizontal displacement, vertical and horizontal rotation, and torsion (see Figure 2.20). However, as stated in [65], a pipeline subjected to multi-coupling loads may be governed by the effect of transient ground deformations in the longitudinal direction. Hence, authors have focused on developing numerical models based on full-scale experimental tests considering longitudinal strains. The effect of repetitive external loads such as traffic, temperature changes, and ground movements due to adjacent parallel trench construction in ductile iron host pipe crack was analyzed in [64]. In addition, full-scale tests on a DN 150 mm ductile iron pipe were performed at Cornell University by some authors [66–71]. It was concluded that CIPP liners can manage ground movements and are suitable for pipe retrofitting.

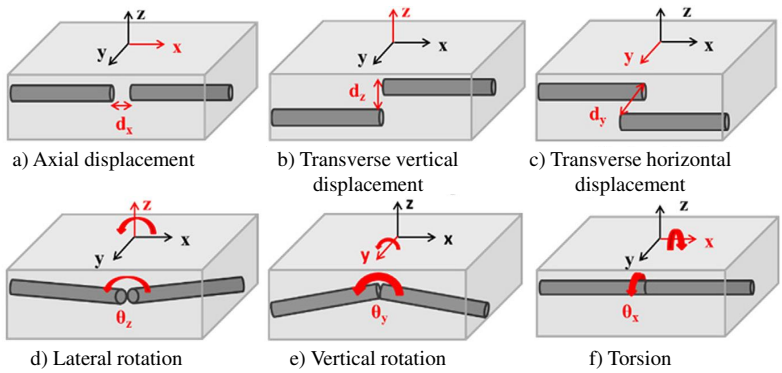

Figure 2.20: Deformation modes that a weak joint or hoop crack can be subjected to. Adapted from [70].

2.5.4 Lateral openings

Opening the lateral connections (see Figure 2.21) is one of the last steps of rehabilitation by CIPP. A lathe robot is sent into the rehabilitated pipe to open and seal the lateral connections. However, it is considered a critical step, especially in pressure pipes. Water leakage between the liner and the host pipe must be avoided. In addition, lateral openings are just mentioned in current standards ASTM F1216 [8] and UNE 53929 [1], but no limitations or specifications are set. Consequently, CIPP installers avoid rehabilitating sections with lateral openings as they are a source of problems. Any damage to the liner or sealing issues may result in using dig-and-replace procedures, causing economic losses. Accordingly, even when a straight section with a lateral opening needs to be rehabilitated, the section is divided into two sections: the section before and the section after the lateral connection. Thus, the lateral connection is replaced by the traditional open-trench method.

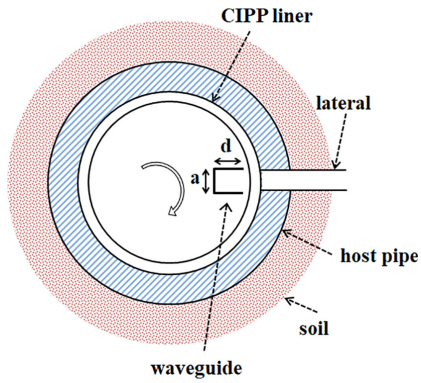

Figure 2.21: Representative scheme of the procedure followed to detect lateral connections after the CIPP liner installation. Adapted from [78].

Although the uncertainty of lateral openings, only a handful of authors have mentioned and investigated them [49, 78]. There are two main steps in lateral openings:

- **Location**: it is a complex task to accurately locate the lateral openings since there is no GPS signal inside the pipe. In addition, cutting the liner in a bad location or causing damage to the liner may result in replacing the installed CIPP liner.

  On the other hand, considering the lateral connection before the installation by cutting the liner or manufacturing a "T" may result in disaster as then it is difficult to match it with the real lateral connection. Consequently, lateral opening studies have focused on developing new methods to accurately detect a lateral connection when a liner is installed to give precise instructions to the cutter robot. For example, a low-cost sensor based on the open-ended rectangular waveguide was numerically developed and experimentally tested in [78].

- **Sealing**: after the cutter robot has opened the lateral connection, the liner's perimeter must be sealed to avoid leaks between the liner and the host pipe.

2.5.5 Quality control tests

A CIPP rehabilitation is a complex task. It consists of the host pipe diagnosis, the correct sizing and design of the liner, a proper installation, and post-installation tasks. In pressure pipes, a slight imperfection can leave them out of service. Consequently, a quantitative evaluation is proposed by some authors to verify that the CIPP liner installed preserves the design mechanical properties [79–83]. A review of North America's main quality control practices in sewer pipes was presented in [79]. Furthermore, laboratory tests were proposed in a pilot study with liners from Denver, CO, and Columbus OH [80]. The tests included thickness, annular gap, ovality, density, specific gravity, porosity, flexural strength, tensile strength, surface hardness, glass transition temperature, and Raman spectroscopy.

The hoop tensile performance of an installed liner is one of the main parameters to control. Nevertheless, due to the curved geometry of a pipe's sample, flat tensile tests are not possible to perform. Consequently, bending tests of curved samples are proposed in current standards ASTM F1216 [8], UNE 53929 [1], ISO 11296-4 [9], and ISO 11298-4 [10]. However, some authors have reported difficulties in evaluating the correct ultimate stress from the bending test when testing CIPP samples. Due to the polymeric coating of CIPP liners, the sample's section in the bending test is complex to measure, as reported in [81]. Therefore, the bending test may induce a wrong assessment of the liner's hoop performance, compromising the rehabilitation's safety.

For that reason, some authors have suggested using the split disk test from ASTM D2290 [53] to evaluate the hoop tensile behavior of a liner [84, 85]. However, the ASTM D2290 [53] split disk test's weaknesses were shown in [86]. It was found that bending stresses were generated during the test, causing premature failure (see Figure 2.22).

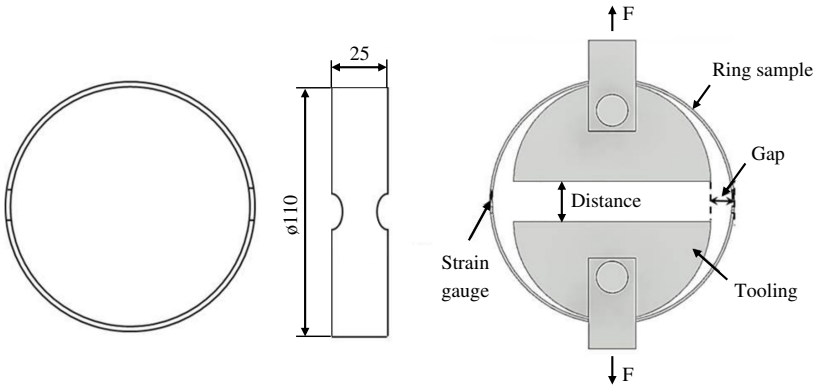

Figure 2.22: Evaluation of the hoop tensile properties by the ASTM D2290 [53] split disk test. Adapted from [86].

2.6 Literature gaps

A wide range of CIPP topics have been investigated by authors (see Table 2.2). However, there are still literature gaps that have been identified and addressed in this doctoral thesis.

- **Deficiencies detected in current CIPP standards for pressure pipes**
  Detailed design equations are presented in ASTM F1216 [8] and UNE 53929 [1]. However, few details of procedures to verify the correct installation of the liner are provided. Recently, UNE 53929 [1] have incorporated quality assurance procedures due to the contribution of this doctoral thesis. Although some authors have delved into CIPP quality control practices in sewer pipes, further research is needed on water pressure pipes. Moreover, an exhaustive quality control protocol may be developed considering the previous procedures of a CIPP rehabilitation, the verification of the materials prior to the installation, the installation procedure, and the post-installation verification tests.

  On the other hand, the effect of imperfections such as wrinkles, cracks, or damaged joints is not considered in current CIPP standards. The author's findings, such as the AOR on longitudinal wrinkles, should be included in CIPP standards to create an acceptance criterion when installation defects appear. Moreover, further research based on experimental full-scale testing on pressure pipes (DN>400) to establish an acceptance criterion for hoop wrinkles, longitudinal and hoop cracks, impregnation deficiencies, folds, swollen areas, and gaps between the host pipe and a semi-structural CIPP liner should be developed.

  Furthermore, only isotropic liners and circular holes are considered in ASTM F1216 [8] while rectangular holes and anisotropic liners are considered in ASTM F2207 [62].

- **Host pipe holes consideration for liner's design**
  Host pipe holes have been investigated by some authors, and there is even a design criterion in ASTM F1216 [8] where they are considered. However, only perfectly circular holes were considered by authors and ASTM F1216 [8]. Only an author has superficially and numerically considered elliptical, rectangular, and squared holes based on ASTM F2207 [62] host pipe holes approach. Nevertheless, host pipe's holes in pipelines are not circular at all, nor have regular geometrical shapes. Consequently, a liner's design procedure should be developed considering irregular host pipe hole shapes with random orientation.

- **Semi-structural liner's design optimization**
  The oversizing of CIPP liners has been a hidden source of problems reported by some authors. The increase of liner's performance by adding structural material in the CIPP liner has been proven to be a wrong practice in pressure pipes. The installation process of a CIPP liner is complex; thereby, the liner's design should contribute to the correct liner's installation. A lighter liner may help in the installation process due to its higher maneuverability; therefore, installation defects may be avoided.

  Consequently, further research may focus on optimizing liner design in pressure pipes. Semi-structural liners should be a proper option for most CIPP pressure pipe rehabilitation projects. Moreover, design equations of current CIPP standards should be revised as high conservative coefficients are applied for buckling and host pipe holes. For example, current host pipe hole design equations are based on analytical expressions deducted from simple approaches.

Big holes equation from ASTM F1216 [8] has been proven to be excessively conservative as the host pipe holes are calculated as a free-liner under the ring-in-tension assumption rather than considering the residual structural capacity of the damaged host pipe.

- **Development of a tensile test to evaluate the hoop stress of an installed CIPP liner** Although the hoop performance of the liner is one of the most important parameters in pressure pipes, few authors have considered alternatives to the bending test of curved samples. It should be noted that the bending test of curved samples presented in ISO 11296-4 [9] and suggested in ASTM F1216 [8] and UNE 53929 [1], has been proven to over-estimate the CIPP liner's hoop performance.

  On the other hand, the split-disk test from ASTM F2207 [62] suggested by some authors has also been proven a wrong alternative as bending stresses are induced in the sample. Hence, further investigation on new tests to assess the hoop tensile performance of an installed liner is required to correctly verify its mechanical properties.

Table 2.2: Most relevant contributions to CIPP liners for water pressure pipes and sewer systems. *Light gray*: full-scale tests (<DN400). *Light blue*: full-scale tests (≥DN400). *White*: analytical, laboratory tests and numerical FE solutions.

Reference	Topic	Solution	Aim of study
Jaganathan *et al.*, 2007 [50]	Longitudinal wrinkles	Numerical FE and laboratory tests	Wrinkle crossing a host pipe hole. Development of the liner's AOR (maximum Allowable Oversizing Ratio) to control longitudinal wrinkles.
Ampiah *et al.*, 2008 [51]	Longitudinal wrinkles	Laboratory tests	Impact of wrinkle's size, shape, and pattern to the mechanical properties of the liner.
Ampiah *et al.*, 2010 [52]	Longitudinal wrinkles	Laboratory tests	Failure procedure of SW, IW, and LW wrinkles. Fatigue testing.
Allouche *et al.*, 2005 [49]	Limit states, circular holes, wrinkles, and lateral openings	Numerical FE and laboratory tests	Definition of the 6 CIPP limit states (LS1-LS6).
Allouche *et al.*, 2008 [54]	Non-circular holes, and creep	Numerical FE and laboratory tests	Study of the effect of the shape of the hole (circular and square (experimental), rectangular-elliptical (numerical) using ASTM F2207 model calculation. The effect of primary and secondary creep was also studied around the holes.
Rajeev *et al.*, 2014 [56]	Holes: corrosion pits	Field pipes	Study of 5 Australian utilities (pipelines) to analyze the factors contributing to failure (example of real holes).
Brown *et al.*, 2014 [55]	Holes: clamped section	Numerical FE	Liner spanning through a host pipe section without structural integrity. Limit states LS2 and LS3. The limiting factor is the maximum stress criterion (hoop stress) from ASTM F2207.
Shou & Chen, 2018 [60]	Circular holes: corrosion pits	Numerical FE	CIPP liner repair significantly reduced the stress concentration around the void.

Continued on next page

Table 2.2 – continued from previous page

Reference	Topic	Solution	Aim of study
He & Shawn, 2019 [57]	Circular holes	Numerical FE	ASTM F1216 equations. Simulation of host pipe circular holes. Influence of 4 parameters: D/t, d/D, σ_h/σ_y, and μ. ring-in-tension stress decreases at d/D = 0.4.
Brown *et al.*, 2020 [58]	Circular holes	Numerical FE	Orthotropic numerical model. The interactive stress criterion governs small holes (ASTM F1216 criterion). The maximum stress criterion in the hoop direction governs big holes.
Shou & Huang, 2020 [61]	Circular holes: corrosion pits	Numerical FE	Analysis of corrosion pits in straight and curved pipelines.
Adebola *et al.*, 2021 [59]	Circular holes	Full-scale test (DN150)	Use of fiber optic strain sensors to monitor the strain in CIPP pressure liners at small diameter void locations and compares it to an analytical solution based on flat plate theory. Demonstration of the validity of the design method in ASTM F1216 standard).
Jeon *et al.*, 2004 [64]	Repetitive external loads	Analytical and laboratory tests (DN150)	Effect of repetitive external loads (traffic, temperature changes, ground movements) on a hoop host pipe crack.
Bouziou *et al.*, 2012 [65]	Joints: earthquake	Full-scale test (DN150)	Use of CIPP for seismic retrofit.
Zhong *et al.*, 2014 [66]	Joints: earthquake	Full-scale test (DN150)	Full-scale experimental tests with twin shake tables. Retrofitted pipelines subjected to quasi-static and seismic ground motions were capable to withstand high-intensity transient ground motions.
Zhong *et al.*, 2015 [67]	Joints: earthquake	Full-scale test and numerical FE (DN150)	CIPP subjected to severe earthquakes (ground movements) and cyclic loading.
Zhong *et al.*, 2017 [69]	Joints: earthquake	Full-scale test (DN150)	Experimental evaluation of ductile iron pipelines under seismic response.
Zhong *et al.*, 2017 [68]	Joints: earthquake	Numerical FE	Development of an experimentally validated hysteretic numerical model on ductile iron push-on joints.
Argyrou *et al.*, 2018 [70]	Joints: earthquake	Full-scale test (DN150)	Evaluation of weak joints and hoop cracks. Transient ground deformations mainly affect pipelines in the longitudinal direction.
Argyrou *et al.*, 2019 [71]	Joints: earthquake	Full-scale test (DN150)	Experimentally characterization of debonding, longitudinal elongation, and bending performance of a CIPP liner subjected to weak joints and hoop cracks.
Fang *et al.*, 2020 [72]	Corrosion and multi-field coupling effects	Numerical FE	Multifield coupling effects of soil, pressure, and traffic loads of a pipeline with inner corrosion.
Yang *et al.*, 2021 [73]	Joints: multi-field loads	Full-scale test (DN1200)	Effect of multi-field loads (traffic, surcharge, and fluid) on a semi-structural liner installed on a corroded concrete pipe. Bell and spigot joints.

Continued on next page

Table 2.2 – continued from previous page

Reference	Topic	Solution	Aim of study
Hsu & Shou, 2022 [74]	Joints	Numerical FE	Host pipe separated joints rehabilitated by CIPP. Backfill and interface factors were studied.
Yang *et al.*, 2022 [75]	Joints: multi-field loads	Numerical FE	Effect of multi-field loads (traffic, surcharge, and fluid) on a semi-structural liner on a corroded concrete pipe. Bell and spigot joints.
Kiriella *et al.*, 2023 [76]	Joints: traffic loads	Numerical FE and full-scale test (DN300)	Numerical analysis validated with full-scale tests. Effect of joints subjected to lateral bending.
Zhai & Moore, 2023 [77]	Joints: initial gap or ring fracture on pressure pipes.	Numerical FE	Development of a new equation based on a parametric analysis using a numerical model to predict maximum axial stress as a function of initial gap width, liner diameter, inner pressure, friction coefficient, and the liner thickness.
Jaganathan & Kodali, 2019 [78]	Lateral openings	Numerical FE and laboratory test	Accurate location of lateral openings using a new electromagnetic sensor.
Hudson *et al.*, 2023 [87]	External loads	Numerical FE	Effect of external loads to a rehabilitated corrugated metal pipe culvert.
Das *et al.*, 2016 [44]	CIPP challenges	-	Issues and challenges observed in rehabilitated pipes of sewer mains, water mains, and service laterals.
Li *et al.*, 2023 [88]	Trenchless technologies challenges	-	A review of trenchless rehabilitation technologies for sewage pipelines.
Ji *et al.*, 2018 [45]	Liner's design: material	Laboratory tests	A new liner composition is proposed.
Ji *et al.*, 2020 [46]	Liner's design: thickness reduction	Laboratory tests	Short and long-term bending tests demonstrate a CIPP liner can be optimized.
Yahong *et al.*, 2023 [47]	Liner's design: thickness reduction	Laboratory tests	New design model to achieve a 20% reduction in liner's thickness.
Gras-Travesset *et al.*, 2024 [48]	Liner's design: thickness reduction, non-circular holes, and machine learning	Full-scale test (DN400), numerical FE, and mathematical model	Design optimization of semi-structural liners subjected to irregular host pipe holes.
Selvakumar *et al.*, 2012 [79]	Quality control	-	Overview of how QC issues in trenchless technologies have been handled in North America.
Allouche *et al.*, 2014 [80]	Quality control	Laboratory tests	A quality assurance protocol was applied to 4 liners.
Cigler *et al.*, 2015 [81]	Quality control	Laboratory tests	Quality control tests. Bending test weakness: the correct sample's thickness measurement.
Suresh & Jayakumari, 2016 [84]	Hoop tensile properties	Laboratory tests and numerical FE	Evaluation of hoop strength by the split disk procedure from ASTM D2290.

Continued on next page

Table 2.2 – continued from previous page

Reference	Topic	Solution	Aim of study
Adebola *et al.*, 2020 [82]	Hoop tensile properties	Laboratory tests	Measurement of tensile properties through tensile and bending tests using distributed optical fiber sensing.
Gras-Travesset *et al.*, 2023 [83]	Hoop tensile properties	Numerical FE and laboratory tests	Development of a new tensile test to assess the hoop tensile performance of a CIPP installed liner: the IBPT.
El-Sawy & Elshafei, 2003 [89]	Machine learning	Numerical FE and mathematical model	Feed-forward neural network to predict buckling of loose-fit liners.
Xia *et al.*, 2022 [90]	Machine learning	Laboratory tests and mathematical model	Model to predict the flexural properties of UV-CIPP liners. Inputs: curing time, UV lamp irradiation intensity, curing distance, and material thickness.
Xia *et al.*, 2023 [91]	Machine learning	Mathematical model	Influence of some parameters on UV-CIPP liner's bending performance. Parameters: UV lamp power, temperature at the illuminated side, curing time, temperature at the back side, curing distance, and material thickness.

3

Quality control of CIPP pressure pipe liners

This chapter presents a quality control protocol designed to prevent and detect irregularities during the rehabilitation of pipes using the CIPP technology. The protocol is structured into four main stages, aligned with the work timings: previous procedures, materials verification, installation process, and post-installation verification. Furthermore, a practical implementation of the protocol is presented to further clarify the procedures proposed and verify its application in the field of CIPP.

3.1 CIPP challenges

The CIPP liners design is defined by some standards developed by different countries. Above all, the ASTM F1216[8] is considered the regulation of reference, and most of the standards later developed are based on this standard. The installation procedure is also described in ASTM F1216[8], although it is widely open to the installer or manufacturer criterion. Moreover, a few quality control tests are recommended to be performed after the installation of the liner. Thus, the design equations presented in ASTM F1216[8] are highly developed and restricted to a solid design procedure, while the installation and post-installation processes are open to the installer and manufacturer agreement. Consequently, some CIPP projects are subjected to a more or less robust quality control test.

Although the design of a liner is crucial, the installation process is also a very important step. Liner can be correctly designed, but it will only work if the installation is well performed, especially in pressure pipes. The installation process may not be as important in the sewerage market as gravity pipes are subjected to low pressures of around 1 bar. Hence, the liner has no structural behavior and is not subjected to big internal loads. In contrast, pressures over 10 bar are registered in most drinking water pipes. Consequently, problems may arise if the liner is not perfectly installed, as the minimum installation defect is magnified due to high inner pressures.

Several authors have reported problems due to installation defects [44] although the liner was designed according to ASTM F1216[8] standard. Most installation defects can be visually identified as cracks, wrinkles, swollen areas, a lack of expansion of the liner, impregnation deficiencies, or buckling of the liner. All of them have a negative and severe repercussion to the mechanical performance of the installed liner. In a few cases where there is a minor installation defect, it can be corrected or even accepted as pressure pipe liners are intended to be far oversized. However, a badly installed liner must be usually extracted and replaced. It should be noted that extracting a liner is a complex procedure and sometimes even not feasible without producing severe damage to the host pipe. The liner is semi-bonded to the host pipe due to the curing process. In addition, the inversion installation technique allows to surpass 45° elbows, and thereby, the installed liner cannot be extracted by just pulling it out as it does have any more flexible behavior.

Two solutions are generally performed when installation defects appear. On the one hand, a second liner can be installed onto the poorly installed liner. Previously, the protuberances of liner one must be milled, and the surface must be kept constant and smooth. However, although this solution is cheaper than replacing the whole host pipe, it is usually discarded because the interaction between both liners is complex to predict, and the inner diameter of the rehabilitated pipe is reduced more than expected in the design process. On the other hand, the traditional replacement of the host pipe is the solution performed in most of the cases. Undoubtedly, it is the most expensive and time-consuming option. Apart from the liner cost, the traditional replacement of the damaged pipe is now added, which was intended to be avoided by the CIPP trenchless technique.

For this reason, rigorous quality control procedures are intended to be performed not only during

the installation of a liner but also during the pre-installation time to avoid installing a liner that will probably induce installation defects. Furthermore, a post-installation control is also important to be performed to ensure the liner was correctly installed and prevent possible future issues before connecting the rehabilitated pipe to the pipeline. It should be highlighted that a liner's failure can induce heavy leaks and considerable damage to third parties.

According to current standards such as ASTM F1216 [8], ISO 11296-4 [9] and ISO 11298-4 [10], these quality control tests are mainly based on bending tests of curved samples (discussed on the next chapter) of the liner after being installed. However, problems detected in some CIPP projects suggested that more procedures must be performed to ensure the liner was correctly designed and installed. Moreover, these standards do not mention preliminary tests of the raw materials (resin and fiber). Consequently, there is a need to establish a robust quality control protocol that covers the pre-installation, the installation, and the post-installation of the liner. Furthermore, in front of this scenario of uncertainty [92], enterprises of the CIPP market have developed their own quality control procedures. However, a general consensus on a universal quality control protocol has yet to be reached. Recently, some organizations have begun to centralize, unify, and standardize these quality control procedures. For example, standards ISO 11298-4 [93] and UNE 53929 [1] have been recently developed.

3.2 Installation defects

Some installation defects were identified in this research and classified according to their origin into pre-installation, installation, and post-installation defects.

The pre-installation defects are usually caused by sizing errors in the design process. For example, longitudinal wrinkles (see Figure 3.1b) are generated when the installed liner has a greater outside diameter than the inside host pipe diameter. In contrast, two installation defects can appear when the outside liner's diameter is smaller than the host pipe's inside diameter, and the liner's expansion is insufficient to fit the host pipe. The liner's failure occurs if the compressor used in the curing process is powerful enough. Longitudinal cracks (see Figure 3.1c) are generated while a lack of contact between the host pipe and the liner will be registered if the compressor is not that powerful (see Figure 3.1a). Nevertheless, the lack of contact between both bodies is only considered an installation defect in gravity or semi-structural liners. It should be noted that the correct sizing of the liner also depends on having good accuracy when measuring the host pipe inside diameter and its ovality. However, the damaged old pipes were built some decades ago with poor tolerances. Consequently, the ovality and inside diameter of the host pipe can considerably vary along the pipe's length.

On the other hand, impregnation defects are also classified as pre-installation defects. There are many types of resin with different curing technologies in the market. However, most are colored to visually identify a lack of resin in the impregnation process. In Figure 3.1d, the resin used had a red pigment. Hence, the regions without resin (the white stripes) can clearly be identified.

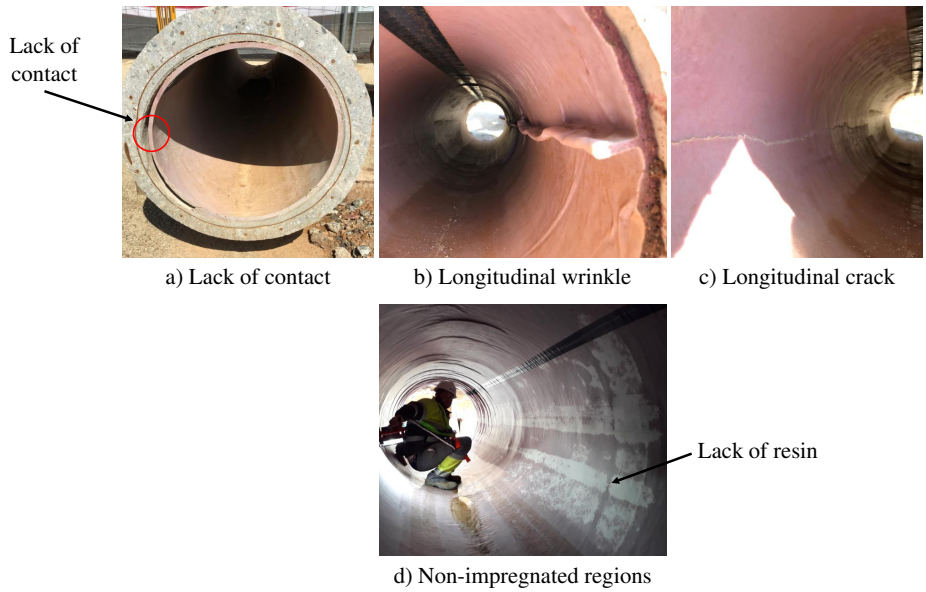

Figure 3.1: Pre-installation defects caused by a bad sizing of the liner or problems with the impregnation process: lack of contact between the host pipe and a semi-structural liner (a), longitudinal wrinkles (b), longitudinal cracks (c), and identification of regions without resin (d).

The installation defects usually originate due to problems inserting the liner into the host pipe or bad execution of the curing process. For example, hoop wrinkles (see Figure 3.2a) are generated when the liner has difficulty moving along the host pipe or even gets stacked at some point. It is important to note that the liner has a specific gel time before being solidified. Especially in resins subjected to a temperature curing process, in the time it takes to clear the liner, the resin begins to cure, solidifying the liner while forming a hoop wrinkle.

On the other hand, swollen areas were also identified as an installation defect (see Figure 3.2b). These protuberances are caused by the presence of pressurized water between the installed liner and the host pipe. They are potentially risky as they can cause the liner to buckle when the pipe is depressurized for maintenance tasks. Furthermore, the buckling of the liner (see Figure 3.2c) can also be caused by a reduction in the curing time. If the liner is not completely cured, its stiffness is heavily reduced, and thereby the liner collapses.

Finally, some irregular protuberances were also identified in some projects. However, they are mainly caused by objects or remnants of the pipe preparation process that have been kept between the host pipe and the liner.

The post-installation defects originate after the liner is cured and are generally caused by problems with the end seals. The end seals are rubber pieces with steel rings placed at the end of the rehabilitated section (see Figure 3.3). The end seals are placed in such a way that half of the piece is in contact with the host pipe wall while the other part leans directly onto the installed liner. Multiple steel rings maintain a uniform pressure against the rubber to guarantee tightness. However, the ovality of the

a) Hoop wrinkle b) Swollen areas c) Buckling of the liner

Figure 3.2: Defects caused by difficulties in the installation of the liner: hoop wrinkles (a), swollen areas [94] (b), and the buckling of the liner [94] (c).

pipe increases the complexity of the tightening system of the steel rings. When a uniform pressure is not reached, water drains between the host pipe and the installed liner, generating the swollen areas shown in Figure 3.2.

It should be noted that lateral derivations are still a challenge, especially in pressure pipes where high pressures make sealing a complex task. Although some enterprises have successfully installed "T packers" in domestic low-pressure pipes, placing a liner with a "T" derivation is more complex to install. The complexity of the liner increases with the number of lateral derivations as it is difficult to exactly match the lateral derivation of the host pipe with the lateral derivation of the liner. Consequently, installers prefer to install liners in sections without lateral derivations. If a section containing lateral derivations must be rehabilitated, it is usually divided into small sections, avoiding the lateral derivations and replacing them with new pieces instead of a liner.

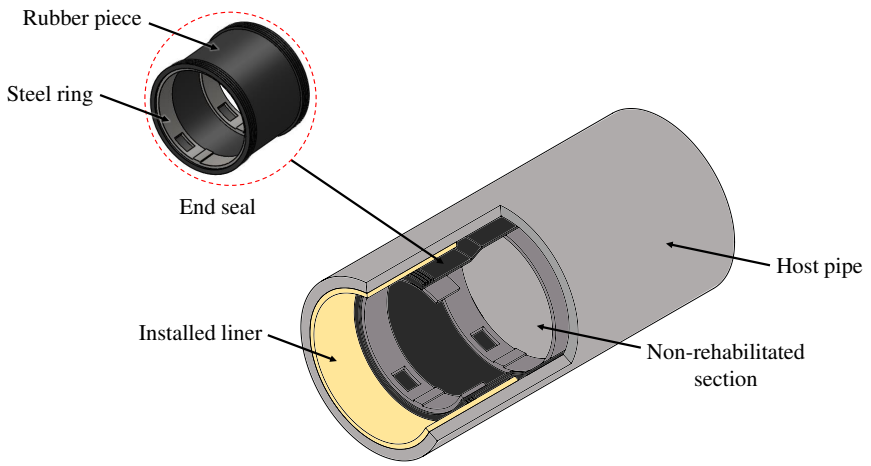

Figure 3.3: Schematic representation of the placement of an end seal after the installation of the liner.

3.3 Proposed quality control protocol

A quality control protocol to assess the installation of a CIPP liner was developed to prevent the defects commented above. The premature detection of these defects may help to save time and costs. For instance, when there is a problem with the liner sizing, it is important to detect it before the liner installation. Otherwise, cracks, folds, or wrinkles will be generated, and then removing the liner is a complex task and often not feasible.

The protocol was divided into four stages according to the work timings (see Figure 3.5 and Figure 3.6).

I. Previous procedures.

II. Materials verification.

III. Installation process.

IV. Post-installation verification.

3.3.1 Previous procedures

In pipe rehabilitation, the first step is to evaluate the degree of damage of the pipe. Then, the trenchless technique to be employed is selected. It should be noted that every trenchless technique has its own application. Thereby, there is not a unique solution. In case the CIPP technique is selected, then the type of liner to use is chosen (see Section 2.2.2) according to the host pipes states defined in UNE 53929 [1] (see Figure 3.4). In the host pipe states classification, the ovality, the degree of damage, the tightness, and the pressure of the pipe are considered. However, the standard UNE 53929 [1] is conservative and defines the state III for all pressure pipes except if there is only a tightness problem. Afterward, considering the state of the host pipe, the liner design is defined according to ASTM F1216 [8] or UNE 53929 [1].

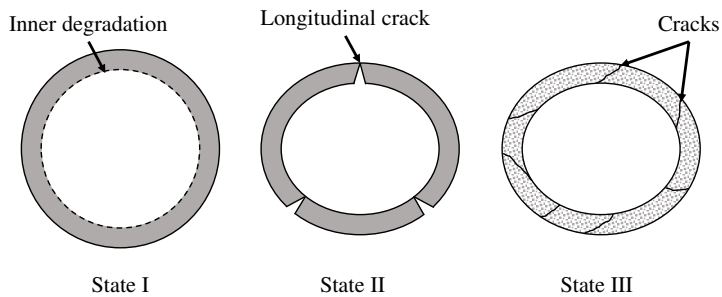

Figure 3.4: Host pipe condition based on the degree of damage.

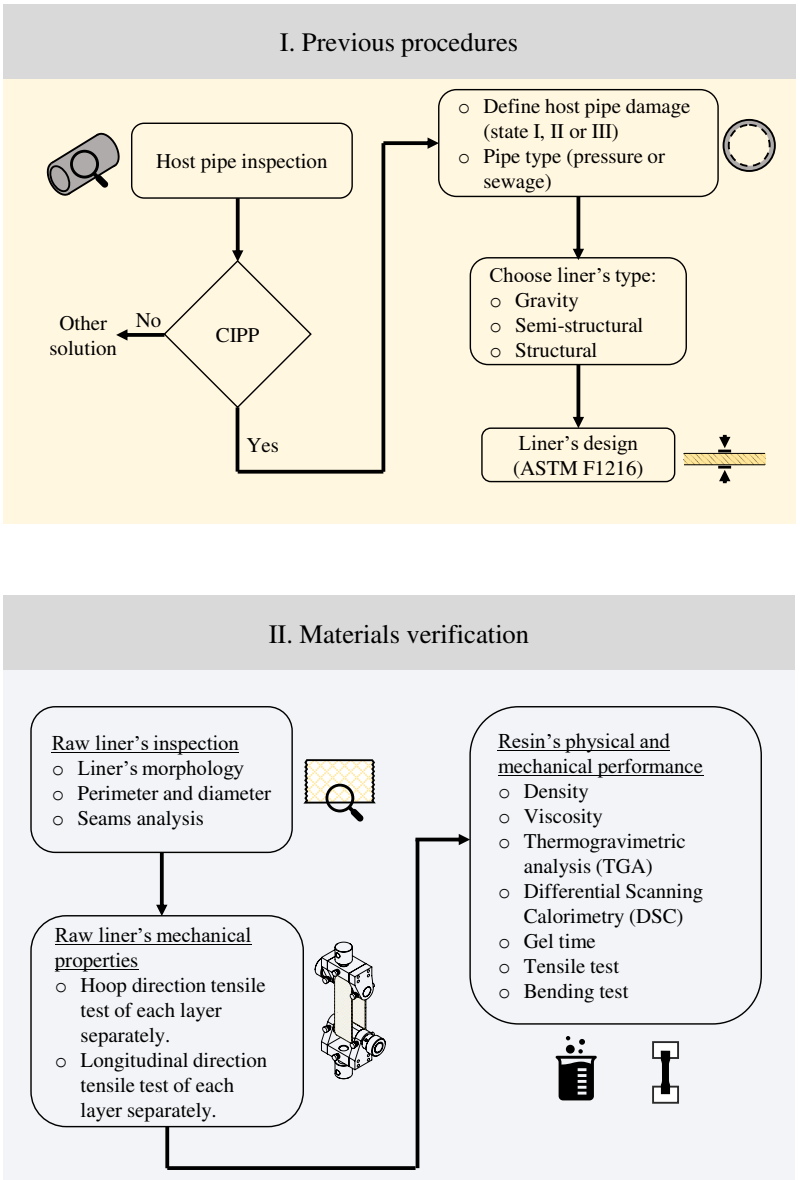

Figure 3.5: Schematic representation of the proposed quality control protocol - Part 1.

3.3.2 Materials verification

The material verification is an important stage to detect any irregularity in the raw materials before installing the liner. For instance, an error of the supplier sending the wrong liner to the work can be detected. Moreover, in this stage, the mechanical properties of the raw liner and resin are evaluated to verify that the raw materials properties agree with the manufacturer's specifications.

Consequently, three main groups are proposed:

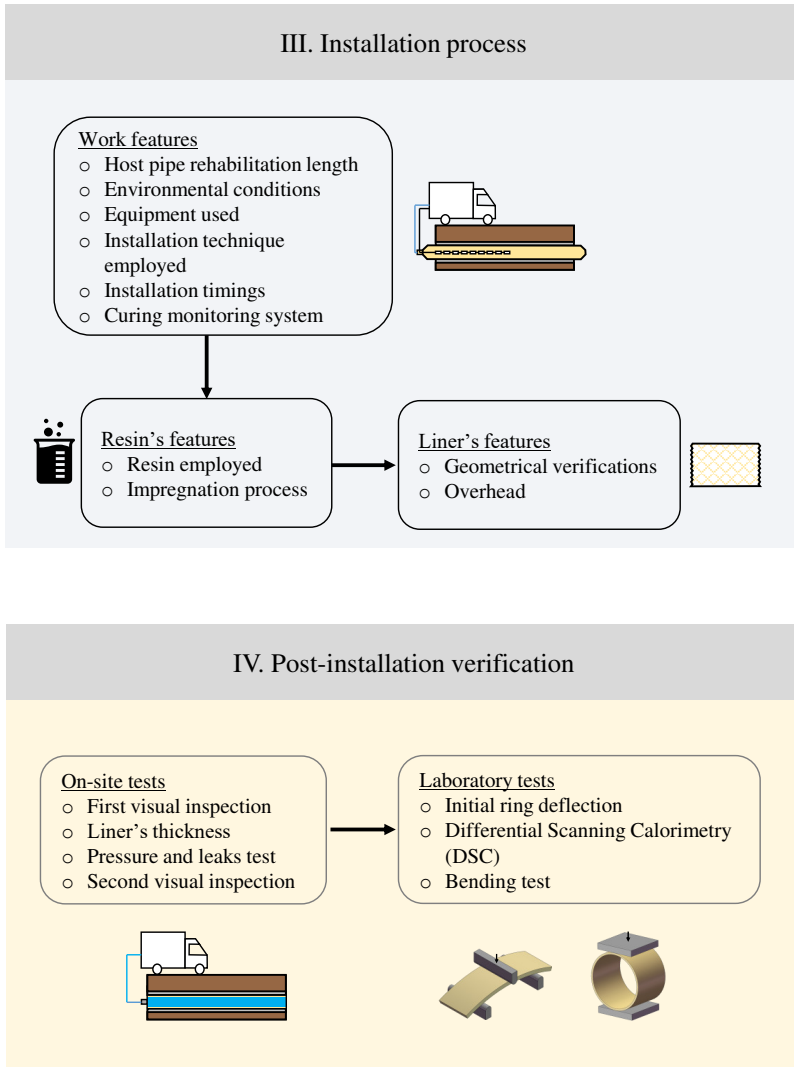

Figure 3.6: Schematic representation of the proposed quality control protocol - Part 2.

a) Raw liner inspection

- **Liner's morphology**: the geometrical features and morphology of the liner prior to the resin impregnation process are analyzed to identify the role of each layer as well as its constitution. Layer n is defined as the layer in contact with the host pipe, while layer 0 is in contact with the water. Samples of 150×150 mm are cut, avoiding possible seams to obtain the amount of glass fiber in each direction (see Figure 3.7). Then, the glass fiber in each direction is separated and weighed. Moreover, each layer's thickness is measured according to ISO 5084 [95].

- **Perimeter and diameter**: the perimeter and diameter of each layer are measured. It is important to note that interlaminar wrinkles will be generated if an inside layer is longer than the outer

layers. To obtain the perimeter of each layer, a ring sample of 150 mm to 200 mm width is cut and opened in the longitudinal direction, avoiding any seam (see Figure 3.7). Then, the layers are separated and stretched on a flat surface, eliminating any kind of wrinkle or fold. The placement of weights onto the layers may help. Then, three measures of the layer perimeter are taken, and the mean and standard deviation are given.

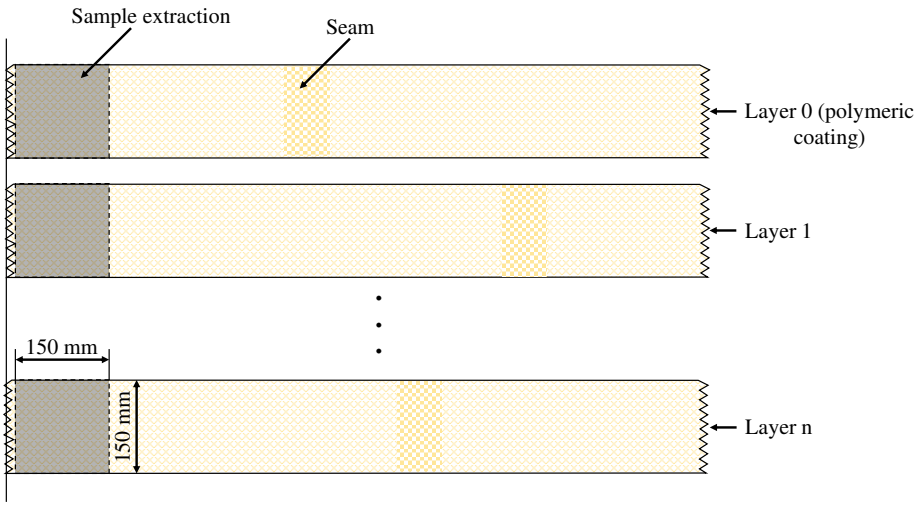

Figure 3.7: Perimeter and diameter measurement operation of each layer and sample extraction for the liner's morphology analysis.

- **Seams analysis**: the analysis of the seams of each layer is performed, indicating the separation between seams if there is more than one and its composition. The location of the seam in each layer must also be reported.

b) Raw liner tests

Tensile tests of each layer of the raw liner must be performed in both directions (hoop and longitudinal) according to ASTM D6775 [96] (see Figure 3.8) or the novel hoop test proposed (see Figure 3.9) to evaluate the tensile performance of a liner. Moreover, the expansion of the raw liner is also a feature that can be deducted from tensile tests. The maximum expansion of the liner is crucial, especially in semi-structural liners, as the liner must perfectly fit the host pipe. Thus, from tensile tests, the pressure that might be applied can be deducted in the case of liners installed by the inversion technique.

Tensile test ASTM D6775

There still needs to be a specific standard to evaluate the tensile properties of a raw CIPP liner. However, some authors have successfully used the ASTM D6775 [96] to evaluate the tensile properties of textiles, and thereby, it was considered for CIPP raw liners assessment although it is a test used to obtain the tensile properties of textile webbing, tape, and braided materials rather than non-woven materials.

Nevertheless, the sample fixation system of this test is considered optimum to avoid heavy stress concentration due to the grip effects. The sample is passed through the split shaft and rolled (see Figure 3.8).

However, a sample slide during the test was detected in glass fiber samples. The problem could be potentially solved by rolling a longer sample. In CIPP liners, obtaining a longer sample in the longitudinal direction is possible, but in the hoop direction, samples are limited to the liner's perimeter. Hence, the "hoop test" was proposed to assess the tensile performance of a liner in the hoop direction.

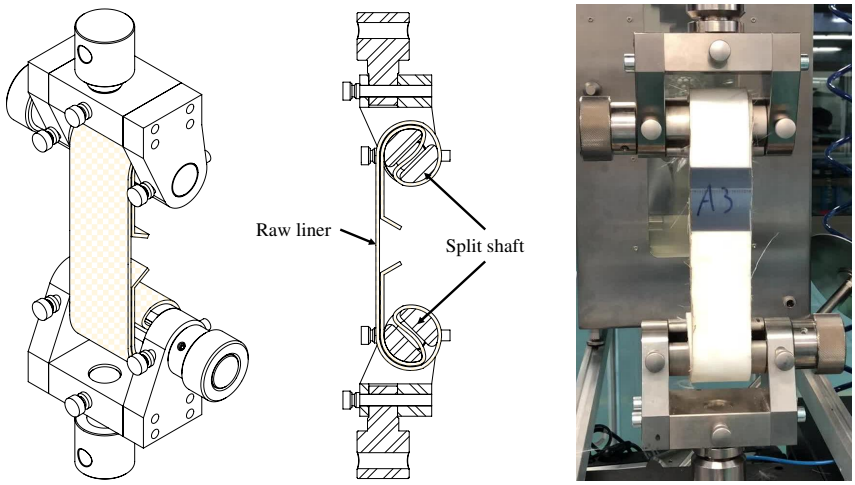

Figure 3.8: Operational scheme and sample placement of the tensile test ASTM D6775 [96].

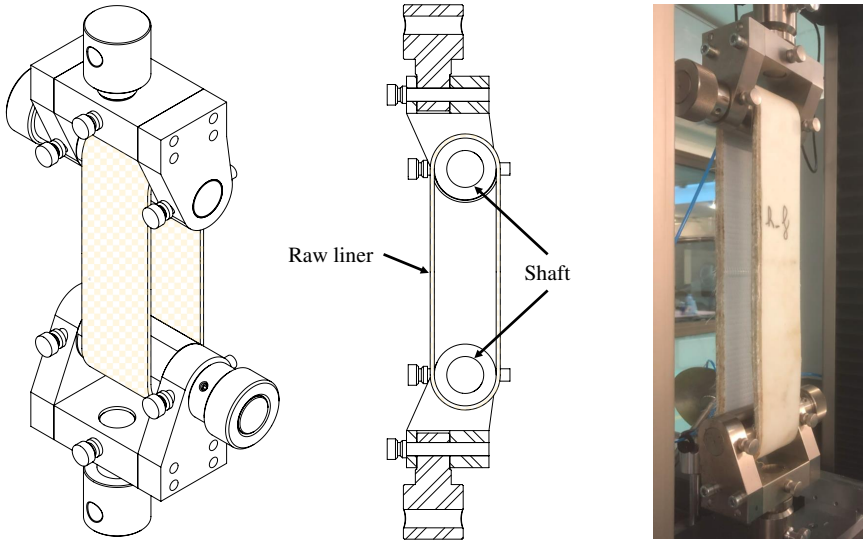

Figure 3.9: Operational scheme and sample placement of the hoop test proposed.

The hoop test

A modification of the tooling of ASTM D6775 [96] was performed to create the hoop test. A new fixing system was proposed to avoid the samples sliding during the test. In this test, the grips are shafts rather than split shafts. Consequently, the sample is not rolled anymore. The ring sample is passed through both shafts (see Figure 3.9) and loaded until failure.

The stress-strain curve of samples from the same liner using both tests is represented in Figure 3.10a. Although the tested liner had a high capacity of elongation due to its constitution, the liner's slip can be appreciated in the ASTM D6775 [96] curves as an incredibly high elongation (140% to 170%) was obtained. Moreover, a considerable strain deviation was observed in the ASTM D6775 [96] curves. In contrast, the strain deviation in the hoop test is minimal (around 70%). Thereby, the slip of the liner problem is solved in the hoop test.

On the other hand, the hoop test is also useful to obtain the necessary inversion pressure that must be applied to the liner to achieve an "x" diameter corresponding to the inside host pipe's diameter. For example, Figure 3.10b indicates that a pressure above 1 bar must be applied to this liner in the curing process if a diameter of 400 mm is pretended to be achieved.

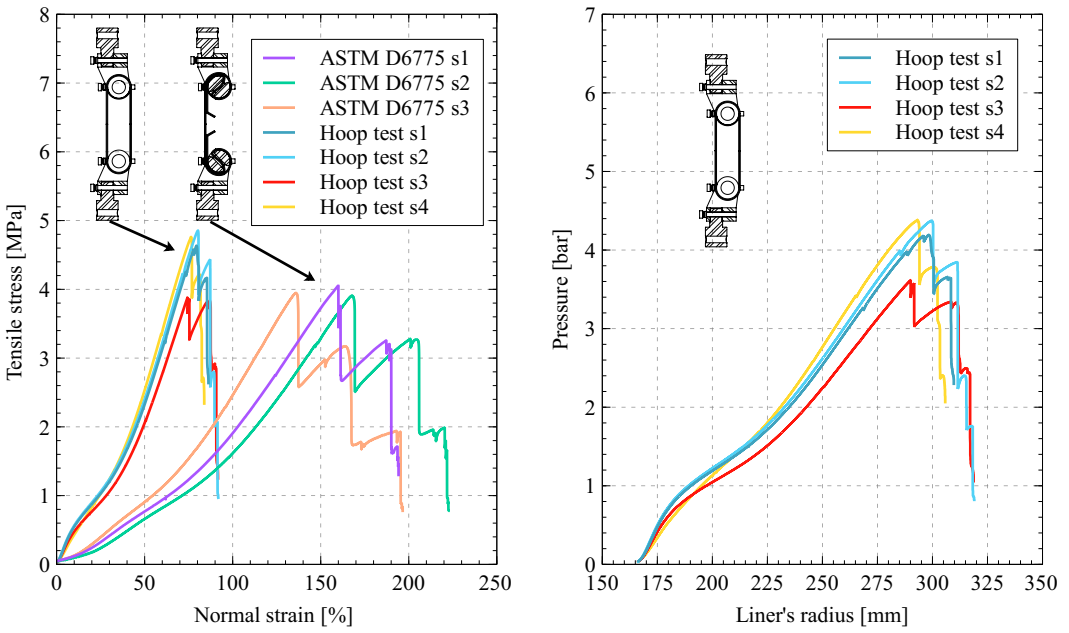

Figure 3.10: Assessment of the tensile properties of the raw liner. Hoop test and ASTM D6775 [96] comparison (a). Required installation pressure deducted from the hoop test (b).

Assessment of the longitudinal tensile performance of the liner

Five longitudinal samples of 60×1400 mm are cut, avoiding possible seams (see Figure 3.11). Then, the sample is placed in the tooling with a distance between grips of 250 mm. The test speed must be set to 75 mm/min.

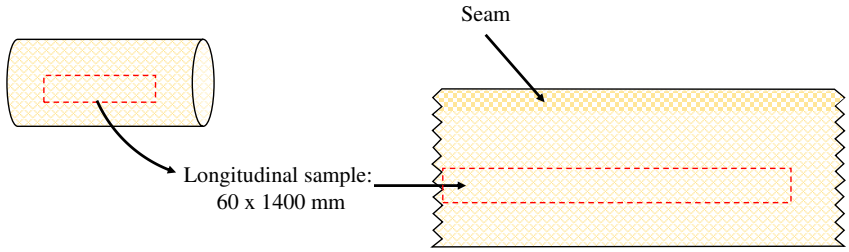

Figure 3.11: Extraction of raw liner samples in the longitudinal direction.

Assessment of the hoop tensile performance of the liner

Two different procedures (ASTM D6775 test [96] and the novel hoop test) were established above. It should be highlighted that the hoop test must be preferably performed as the first option. The same operation parameters (test speed and distance between grips) defined in ASTM D6775 [96] are employed in the hoop test.

However, for raw liners that do not have seams and are longitudinally open (see Figure 3.12), ASTM D6775 [96] must be performed. Hence, five hoop samples of 60 mm in width must be cut. The sample must contain the maximum number of possible seams. Rectangular samples of 1400 mm in length are supposed to be obtained (see Figure 3.13). However, if the liner's perimeters are smaller than this value, the whole perimeter of the liner must be taken. Again, the distance between grips is fixed to 250 mm, and the test speed is kept to 75 mm/min.

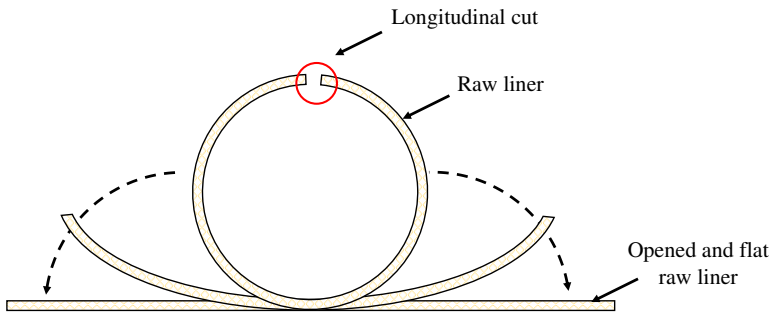

Figure 3.12: Opening operation of a longitudinally open raw liner.

c) Resin tests

Some tests are proposed to evaluate the physical and mechanical properties of the resin.

- **Density of the resin**: the resin's density is measured according to ASTM D1475 standard [97], and it must agree with the value declared by the manufacturer.

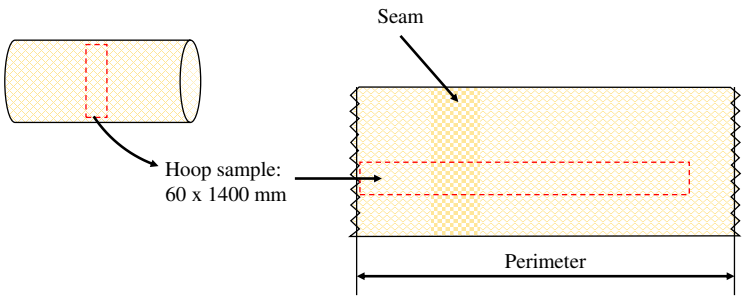

Figure 3.13: Extraction of raw liner samples in the hoop direction.

- **Resin's viscosity**: the viscosity of the liner is important, especially in the impregnation procedure of the liner. A low viscosity contributes to perfectly embed liner fibers but can also easily move away with the transport and manipulation of the impregnated liner. In contrast, a high-viscosity resin complicates the impregnation process, and thereby, there is a high probability that the resin did not reach some fibers and then impregnation defects arise. Hence, it is crucial to perfectly know the ideal viscosity of the resin for the impregnation process.

  The viscosity analysis is performed with a rheometer for a range of temperatures from 0°C to 45°C and a fixed shear stress. The temperature speed must be set to 5°C/min, and the initial gap between plates must be 300 μm.

- **Thermogravimetric analysis (TGA)**: the TGA is proposed to mainly evaluate the Volatile Organic Compounds (VOC) and the fillers of the resin. The test must be performed according to ASTM E1131 [98].

- **Differential Scanning Calorimetry (DSC)**: the DSC test is proposed for resins that cure with temperature. The aim is to identify the ideal curing temperature window. Moreover, the decomposition temperature can also be obtained. The DSC test must be performed according to ISO 11357-1 [99].

- **Gel time test**: it is important to know the gel time of the resin at a specific temperature as it is the maximum time available for the installer to introduce the liner into the host pipe and pressurize it against the host pipe's walls before it solidifies. The gel time test must be performed according to ISO 15040 [100].

- **Tensile test**: the tensile properties of the resin are also assessed according ASTM D638 [101]. Five samples type I must be manufactured and then tested. First, the resin is poured into a mold and then cured to obtain the dog-bone type I samples. Second, the samples are tested using a 5 mm/min test speed. The Young Modulus has to be measured by the regression method between the strain range of 0.05% and 0.25%. Finally, the stress-strain curves, the Young Modulus, and the ultimate stress and strain must be reported.

- **Bending test**: the three-point bending test is proposed to evaluate the flexural properties of the resin. The test can be performed according to ASTM D790 [102] or ISO 178 [103]. Again, first, the resin is prepared and poured into a mold. After the curing process, five rectangular samples are obtained. The recommended sample dimensions are 80×10×4 mm (length, width, and thickness). In addition, a distance between supports of 16 times the thickness must be established. Finally, the stress-strain curves and the mean Young Modulus, mean ultimate stress, and strain are reported.

3.3.3 Installation process

The installation process stage consists of a collection of data of different parameters. In this stage, installation defects can also be prevented until the liner is completely cured. This stage is also divided into three main groups.

a) Work features

Some information concerning the overall work should be checked.

- **Host pipe rehabilitation length**: the exact length of the section to rehabilitate must be checked before the liner placement.
- **Environmental conditions**: the environmental temperature can significantly impact the resin impregnation or the curing process in resins cured with temperature. Thus, the gel time can vary a lot from winter to summer. Moreover, in some cases where the water table is close to or above the host pipe, heavy rain can also be a source of problems.
- **Equipment used**: a description of the equipment used with technical details is required. For example, the pressure applied by the compressor in the curing process must be reported and agree with the result obtained in the tensile test of the raw liner.
- **Installation technique**: the installation technique (pulling or inversion) must be reported, as well as the curing process system (temperature, UV, LED).
- **Installation timings**: the initial and final timing of the installation process are crucial. Both UV and temperature-cured liners have a specific gel time. Hence, the control of the installation time is mandatory. It is better to stop the installation process and remove a liner before it is solidified than to have a semi-placed liner cured inside the host pipe.
- **Curing monitoring system**: the curing process requires thorough control. The pressure in the curing process must be reported. Then, in the case of temperature curing liners, the steam or hot water temperature must be reported, as well as the total curing time. On the other hand, in UV liners, the speed of the trolley lamps and the exposure time must also be reported.

b) Liner's features

- **Geometrical verification**: some geometrical features of the liner must be checked before the liner solidifies. For example, the installed liner's length and diameter must be reported.
- **Overhead**: the overhead of the liner is stipulated by the manufacturer to ensure the liner is perfectly installed without wrinkles or folds. Moreover, an overhead must be planned to extract samples of the cured liner for the post-installation laboratory tests. Thus, the overhead length must be reported.

c) Resin's features

- **Resin employed**: the exact amount of resin used to impregnate the liner must be reported, as well as the overhead obtained.
- **Impregnation**: some manufacturers perform the impregnation process in the work rather than in the factory. However, the resin temperature in the impregnation process is important to be reported in the case of temperature-curing liners.

3.3.4 Post-installation verification

After the liner installation is finished, some tests are proposed to verify that the installed liner is free of installation defects. Moreover, the structural and tightness capacities are also checked by work and laboratory tests.

a) Field tests

- **First visual inspection**: a TV robot inspection of the rehabilitated pipe is proposed to detect any visual installation defect before connecting the rehabilitated pipe to the pipeline.
- **Liner's thickness**: the liner's thickness must be defined according to one of the following standards: ASTM F1216 [8], ASTM D3567 [104], ASTM D5813 [105] or ISO 3126 [106]. To properly measure the liner's thickness, a total of eight measurements equally separated along the liner's diameter must be performed (see Figure 3.14). Then, the mean value and the standard deviation must be reported.
- **Pressure and leaks test**: a pressure and leak test according to UNE-EN 805 [107] must be performed after the first visual inspection to evaluate the tightness of the rehabilitated pipe. The pipe is filled with water using a bleeding valve to avoid air bubbles or air gaps. Then, a 24-hour break must be respected before pressurizing the pipe among the Supported Test Pressure (STP) and the Maximum Design Pressure (MDP). Subsequently, the feed system (pump) must be disconnected, and in contrast to standard UNE-EN 805 [107], the pipe must remain a minimum of 12h in this state. Finally, the pressure drop and the water volume to be refilled are measured.

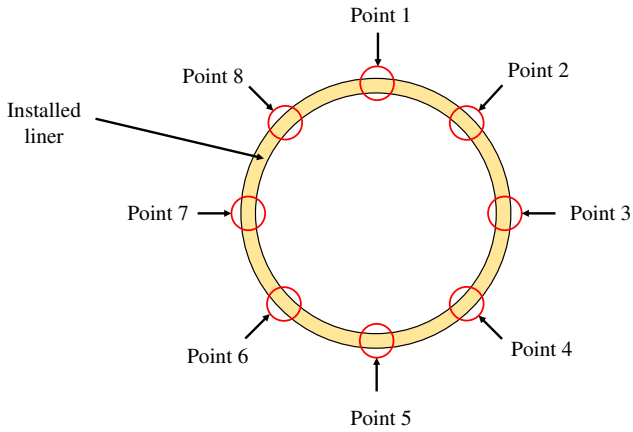

Figure 3.14: Equally spaced measurement points to evaluate the thickness of an installed liner.

- **Second visual inspection**: After the pressure and leaks test, a second TV robot inspection is required. Attention must be specially paid to identifying swollen areas or folds due to possible water drainage between the liner and the host pipe.

b) Laboratory tests

- **Initial ring deflection**: a ring sample is extracted from the cured liner to evaluate the strength of the liner to radial compressive forces. The test must be performed according to ISO 10466 [108], ASTM D2412 [109] or UNE-EN 1228 [110]. The stress-strain curves, the flexural modulus, and the ultimate stress and strain must be reported.
- **Differential Scanning Calorimetry (DSC)**: a DSC of the cured liner must be performed after the installation of the liner. It is important to perform this test to detect when an installed liner has not been completely cured. Hence, the liner performance might be negatively affected. The DSC test must be performed according to ISO 11357-1 [99].
- **Bending test**: the three-point bending test of curved samples specially designed for CIPP cured liners must be performed according to ISO 11296-4 [9] and ISO 178 [103]. An exhaustive analysis of this test is assessed in Chapter 4. In addition, in Chapter 4 a novel test, the Inner Balloon Pressure Test (IBPT) is proposed as a potential alternative to the three point bending test of curved CIPP samples of ISO 11296-4 [9].

3.4 Protocol implementation

Some sections of this protocol were implemented in real works and different liners. It is important to note that the timings in a CIPP rehabilitation are tight. Furthermore, the liner installation cannot begin until all the tests of the previous procedures and materials verification stages are successfully passed. Consequently, the laboratory tests from the materials verification stage should be performed

in a few days. Moreover, the simulation of the implementation of this quality control protocol was necessary to verify the feasibility of the laboratory tests proposed in the materials verification and post-installation verification stages.

3.4.1 Materials verification tests

The materials verification stage was evaluated with a semi-structural liner made of three main layers containing seams (see Figure 3.15). A resin certified to impregnate this liner was also assessed.

- **Layer 0**: this layer is made of a PP coating attached to a thin felt.
- **Layer 1**: this layer comprises a mesh of multidirectional glass fibers onto a polyester sheet. In addition, longitudinal bundles made of glass fiber are identified.
- **Layer 2**: this layer is identically distributed as layer 1.

Figure 3.15: Raw liner composition analyzed in the materials verification stage.

a) Raw liner inspection

- **Perimeter and diameter of the layers**
  The three layers were inspected according to the procedure described in Section 3.3.2.

  Layer 0: polymeric coating
  Three measures were taken, and a length of 1041 mm, 1045 mm, and 1049 mm were obtained, resulting in a mean value of 1045 mm with a standard deviation of 4 mm. Hence, it corresponds to a layer's diameter of 332.6 mm (see Figure 3.16a).

  Layer 1: Polyester sheet reinforced with glass fiber longitudinal bundles.
  A length of 1094 mm, 1097 mm, and 1100 mm were measured in layer 1. Thus, the mean value was 1097 mm with a standard deviation of 3 mm. Then, the raw layer's diameter was 349.2 mm (see Figure 3.16b).

  Layer 2: Second polyester sheet reinforced with glass fiber longitudinal bundles
  A length of 1063 mm, 1065 mm, and 1067 mm were measured in layer 2. Thus, the mean value

was 1065 mm with a standard deviation of 2 mm. Then, the raw layer's diameter was 339 mm (see Figure 3.16c).

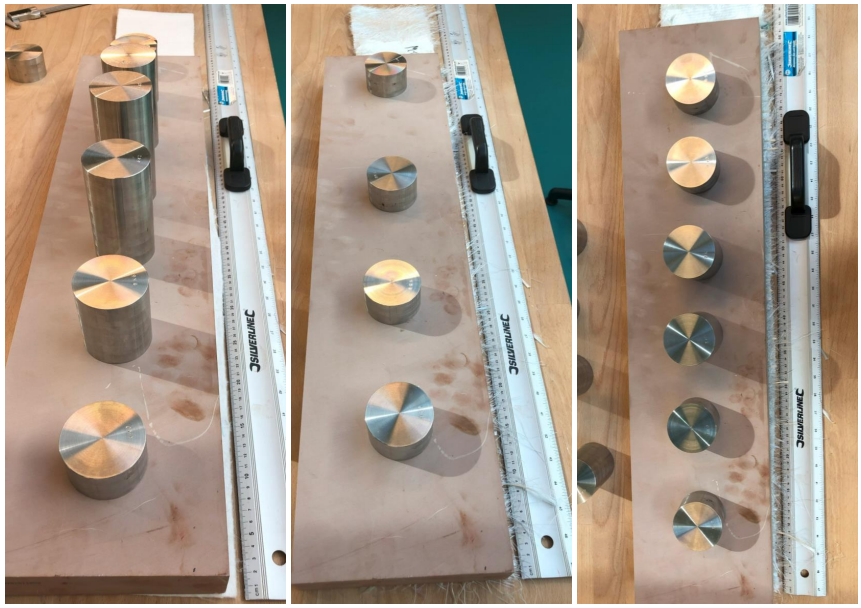

a) Layer 0 b) Layer 1 c) Layer 2

Figure 3.16: Perimeter measurement operation of the layers conforming the raw liner. Layer 0: polymeric coating (a). Layer 1: glass fiber (b). Layer 2: glass fiber (c).

- **Seams analysis**

  The same samples used for the perimeter and diameter inspection were used in the seams analysis.

  Layer 0: this layer presents a seam oriented in the longitudinal direction. Furthermore, in the inside face of the layer in contact with the drinking water, the seam is covered with a black polymeric sheet. In contrast, the felt presents a seam of 17 mm width in the outside face (see Figure 3.17).

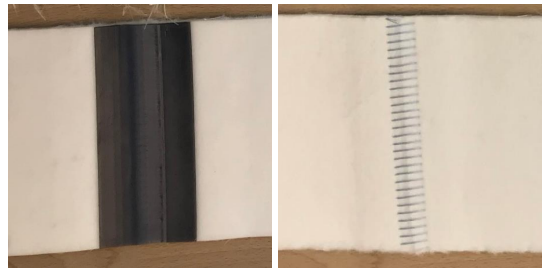

a) Outside view b) Inside view

Figure 3.17: Seam analysis of layer 0.

Layer 1: a longitudinal seam of 17 mm of width can be observed in Figure 3.18. The seam is covered with a 50 mm glass fiber sheet on the inside face.

a) Outside view b) Inside view

Figure 3.18: Seam analysis of layer 1.

Layer 2: the same seam system of layer one was identified in layer 2. However, the longitudinal seam of 17 mm of width was placed in a different location than layer 0 or layer 1. Again, the seam is covered with a 50 mm glass fiber sheet in the inside face (see Figure 3.19).

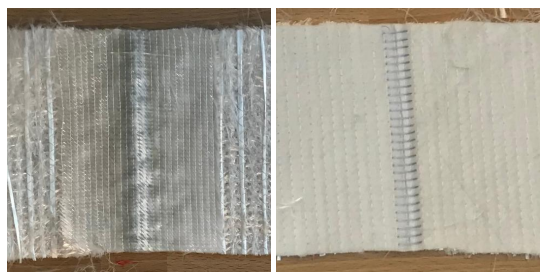

a) Outside view b) Inside view

Figure 3.19: Seam analysis of layer 2.

- **Liner's morphology**
  Two types of layers were identified in the analyzed liner. The structural layers are mainly made of fibers, while the non-structural layer is mainly made of a polymeric coating and a sheet of felt. The amount of fiber in both directions (hoop and longitudinal) that contains the structural layers was measured. According to the procedure described in Section 3.3.2, samples of 150×150 mm from layers 1 and 2 were cut. Seams, felts, or coatings were avoided.

  Both layers (1 and 2) had the same visual fiber distribution. Figure 3.20 depicts the inside view of layers 1 and 2. Longitudinal fiber bundles of 3 mm in width and separated by 11 mm can be appreciated onto the multidirectional sheet of fibers. It is important to note that the reinforcement bundles are distributed in the longitudinal direction and, therefore, do not contribute to withstand the efforts of internal pressure. Hence, multidirectional fiber is responsible for assuming the principal role of the structural reinforcement.

However, although both layers present the same fiber distribution, the amount of fiber that contains both layers is different. In layer 1, 84.9 g/m^2 of fiber was measured in the longitudinal direction, while 407.2 g/m^2 of multidirectional fiber was obtained. Then, in layer 2, 93.5 g/m^2 and 912.2 g/m^2 were obtained longitudinally and multidirectional respectively.

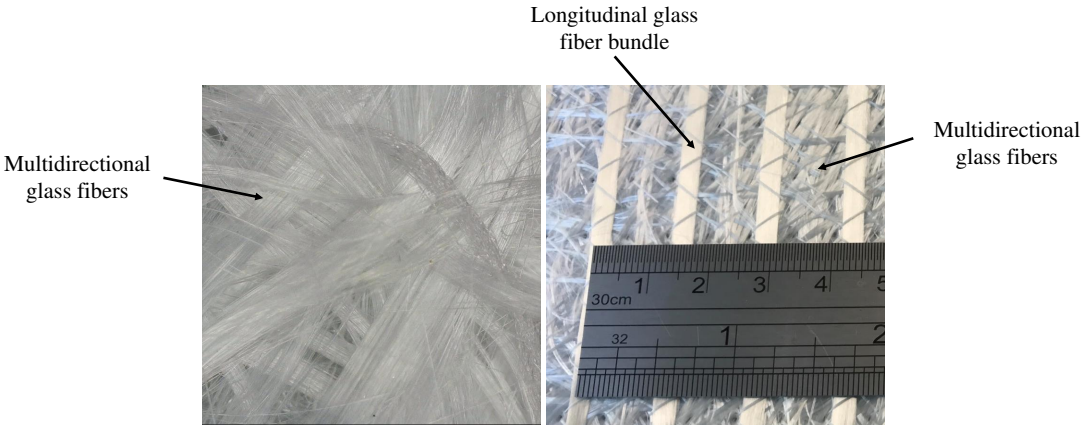

Figure 3.20: Inspection of layers 1 & 2 morphology. Detail of multidirectional glass fiber (a) and inside view with longitudinal bundles above the multidirectional glass fiber (b).

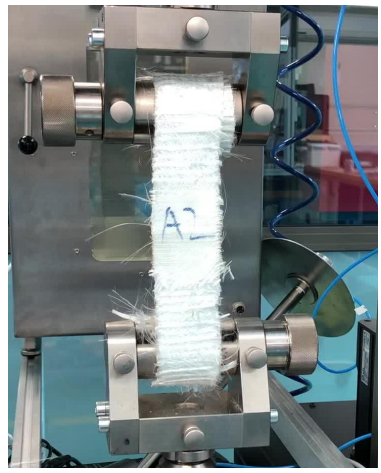

Figure 3.21: Raw liner layer subjected to the tensile test ASTM D6775 [96].

b) Raw liner tests

- **Longitudinal tensile-strength of each layer**
  Five samples of 60×1400 mm of each layer were cut in the longitudinal direction and tested according to ASTM D6775 [96] (see Figure 3.21). The tensile performance in the longitudinal direction of layer 2, layer 1, and layer 0 are represented in Figure 3.22. In addition, ultimate stress and strain, the Young modulus, and the ultimate force of each layer are presented in Table 3.1.

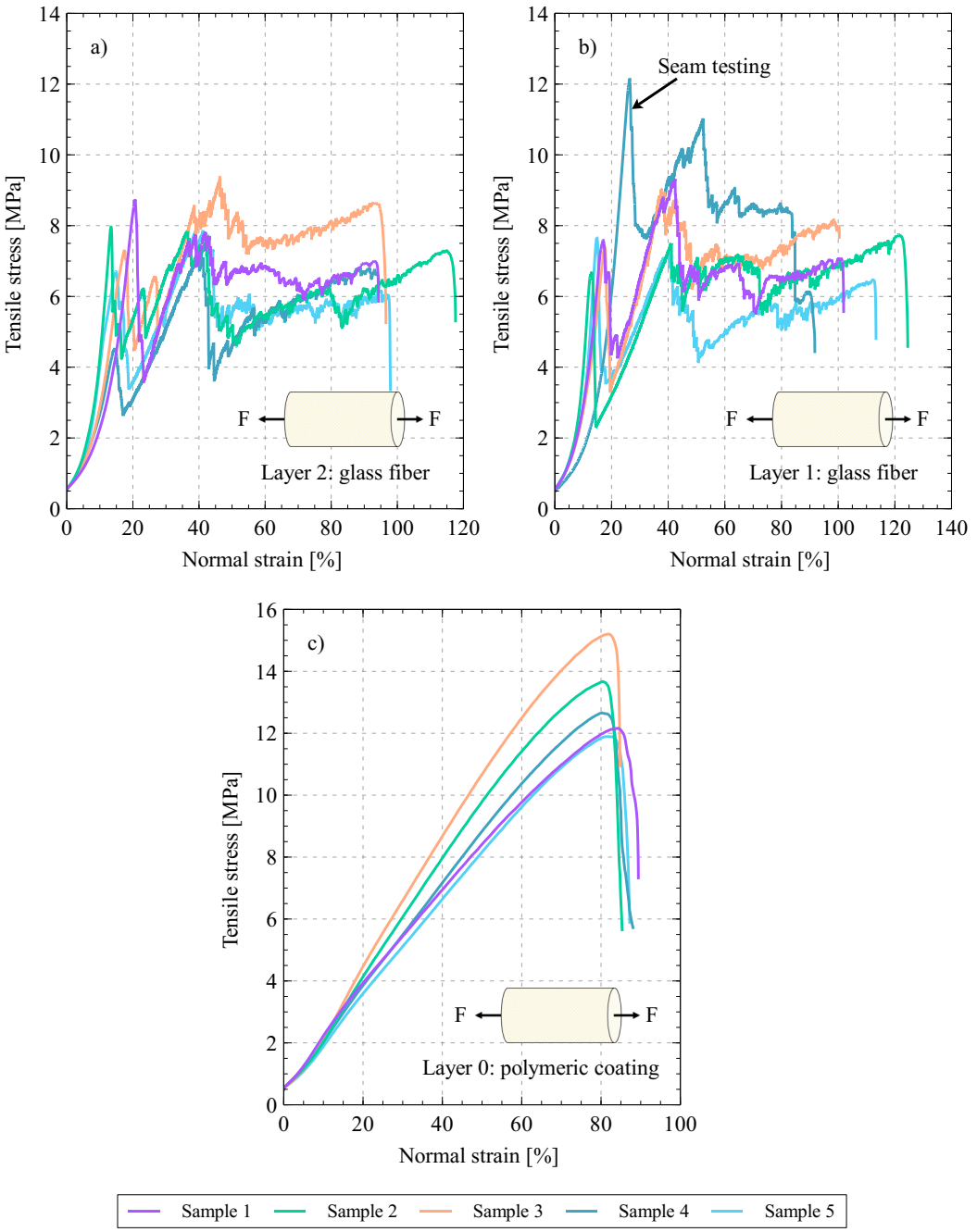

Figure 3.22: Longitudinal stress-strain performance of layer 2, layer 1 and layer 0 prior to the resin impregnation.

Layer 2: the first peak is considered the ultimate stress-strain point of layer 2 (see Figure 3.22a). After the first peak, the non-broken fibers' reorganization makes the load rise again. However, the wavy lines observed after the first peak (noise) are associated with the progressive breakage

of the fibers.

Layer 1: similar values of ultimate stress-strain strength are observed in layer 1 (see Figure 3.22b). Again, the first peak is considered the failure point. Then, the reorganization of the entire fibers makes the load rise again while wavy lines are created due to single fiber's failure. In this liner, the seam is not the limiting factor as sample 4 presents a tensile-strength performance higher than the seamless samples (see Table 3.1 and Figure 3.22b).

Table 3.1: Longitudinal tensile performance of layer 2, layer 1 and layer 0 prior to resin impregnation.

		E (MPa)	F_u (N)	ε_u (%)	σ_u (MPa)
Layer 2	Sample 1	4.13	1056	94.3	5.9
	Sample 2	3.06	955	117.6	5.3
	Sample 3	7.62	947	96.6	5.3
	Sample 4	2.30	1127	94.4	6.3
	Sample 5	2.41	606	97.9	3.4
	Mean	2.68	938	100.2	5.2
	Standard deviation	±3.86	±200	±9.9	±1.1
Layer 1	Sample 1	3.60	1003	101.9	5.6
	Sample 2	8.36	825	124.6	4.6
	Sample 3	6.79	1380	100.4	7.7
	Sample 4 (seam)	2.09	799	91.8	4.4
	Sample 5	1.24	866	113.4	4.8
	Mean	4.42	975	106.4	5.4
	Standard deviation	±3.06	±240	±12.7	±1.3
Layer 0	Sample 1	14.72	1319	89.4	7.3
	Sample 2	18.40	491	85.8	2.7
	Sample 3	20.19	1971	84.8	10.9
	Sample 4	16.50	455	96.2	2.5
	Sample 5	15.14	912	87.3	5.1
	Mean	16.99	1030	88.7	5.7
	Standard deviation	±2.30	±633	±4.5	±3.5

Layer 0: this layer corresponds to the polymeric coating. Hence, the strain obtained is higher than the layers exclusively made of fiber (see Table 3.1 and Figure 3.22c). However, the stress-strength performance is similar to the other layers because it has a very thin fiber layer between the felt and the polymeric coating.

- **Hoop tensile-strength of each layer**
  Five samples of 60×perimeter mm of each layer were cut in the hoop direction and tested according to ASTM D6775 [96]. It should be noted that the tested liner had a maximum perimeter of less than 1400 mm. Furthermore, all the samples contained a seam. It is important to note that the samples were placed in the tooling in such a way that the seam was placed in the middle of both the upper and lower grips.

  The tensile performance in the hoop direction of layer 2, layer 1, and layer 0 are represented in Figure 3.23. In addition, the ultimate stress and strain, the Young modulus, and the ultimate

force of each layer are presented in Table 3.2. It should be noted that a high hoop strain was obtained as it is a semi-structural liner. Thus, the expansion became crucial to perfectly fit the host pipe.

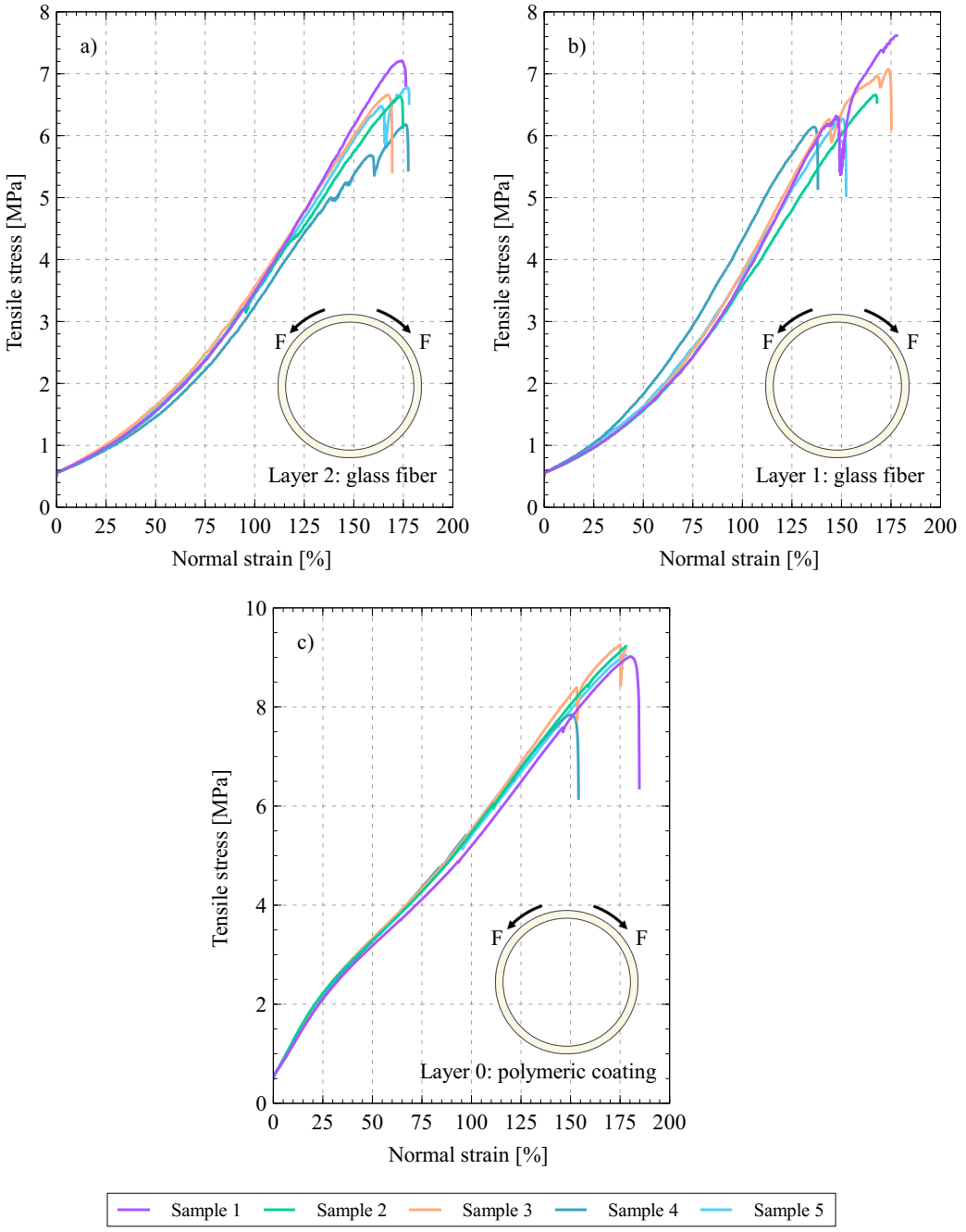

Figure 3.23: Hoop stress-strain performance of layer 2, layer 1 and layer 0 prior to the resin impregnation.

Table 3.2: Hoop tensile performance of layer 2, layer 1 and layer 0 prior to resin impregnation.

		E (MPa)	F_u (N)	ε_u (%)	σ_u (MPa)
Layer 2	Sample 1	2.44	1226	176.3	6.8
	Sample 2	2.46	1104	174.8	6.1
	Sample 3	2.58	975	169.4	5.4
	Sample 4	2.20	980	177.5	5.4
	Sample 5	2.53	1173	177.9	6.5
	Mean	2.44	1092	175.2	6.1
	Standard deviation	±0.15	±113	±3.4	±0.6
Layer 1	Sample 1	4.23	1145	184.7	6.4
	Sample 2	2.51	1177	167.9	6.5
	Sample 3	2.62	1100	175.2	6.1
	Sample 4	3.31	926	138.1	5.1
	Sample 5	2.62	906	152.4	5.0
	Mean	3.06	1051	163.7	5.8
	Standard deviation	±0.73	±126	±18.5	±0.7
Layer 0	Sample 1	2.55	1099	181.9	6.1
	Sample 2	4.19	1378	192.3	7.7
	Sample 3	4.37	1567	178.2	8.7
	Sample 4	4.53	1107	154.1	6.2
	Sample 5	4.39	1160	185.3	6.4
	Mean	4.00	1262	178.4	7.0
	Standard deviation	±0.82	±204	±14.6	±1.1

Layer 2: the sample's failure happened in a region without seams. Thus, as in the longitudinal direction, the seam seems to be stronger than the rest of the layer.

Layer 1: very similar hoop tensile-strength behavior is observed from layer 1 (see Table 3.2 and Figure 3.23b). Again, the sample's breakage was located out of the seam zone.

Layer 0: a higher strain than layers 1 and 2 was observed in the polymeric coating layer (see Figure 3.23c). However, similar ultimate stress was reported; again, the seam was not the limiting factor.

c) Resin tests

- **Resin's viscosity**
  The resin's viscosity as a function of the temperature was evaluated using a rheometer and according to the procedure described in Section 3.3.2. The test was performed with a shear stress of 250 Pa. Results depicted in Table 3.3 and Figure 3.24 indicate that the temperature factor highly influences the viscosity of the analyzed resin. The resin's viscosity was non-linear, ranging from 1.593 Pa·s to 0.051 Pa·s.

- **Thermogravimetric analysis (TGA)**
  The TGA analysis of the resin was performed with three different stages from 30°C to 900°C. First, the sample was subjected to N_2 atmosphere from 30°C to 600°C with a test speed of 10 K/min.

Table 3.3: Influence of the temperature on the resin's viscosity.

T (°C)	0	5	10	15	20	25	30	35	40	44.1
μ_d (Pa·s)	-	1.593	1.221	0.693	0.394	0.237	0.148	0.097	0.067	0.051

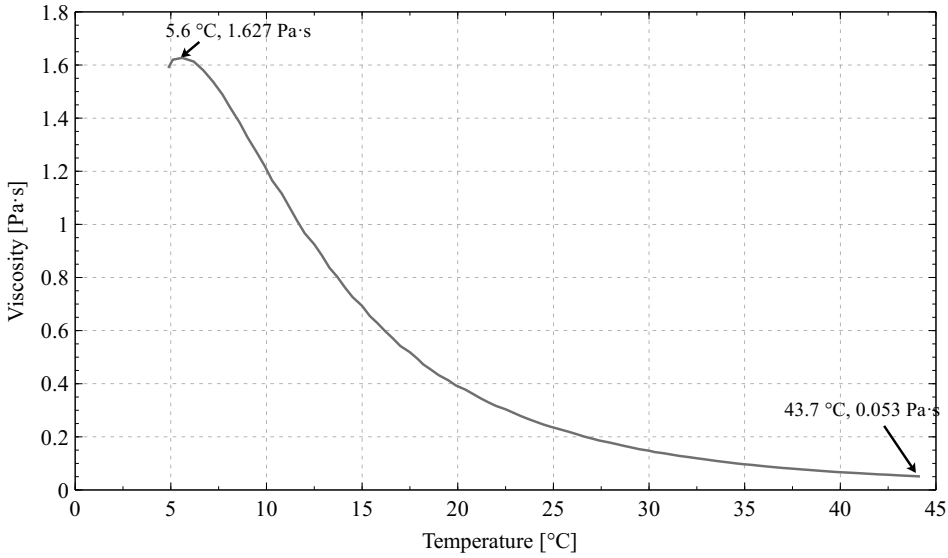

Figure 3.24: Influence of the temperature on the resin's viscosity.

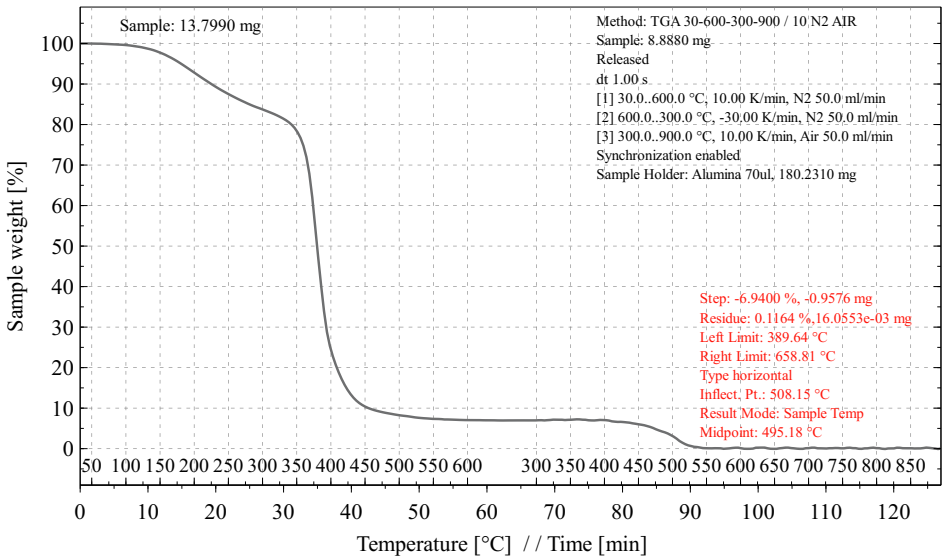

Figure 3.25: Thermogravimetric analysis of the resin.

Second, the sample was refrigerated in a N_2 atmosphere until 300°C was reached using a test speed of -30 K/min. Finally, the sample was exposed to an air atmosphere from 300°C to 900°C

with a test speed of 10 K/min. The results from Figure 3.25 reveal that the analyzed resin contains a 9% of fillers.

- **Differential Scanning Calorimetry (DSC)**
  A DSC analysis of the resin was performed for a range of temperatures from 30°C to 300°C in a N_2 atmosphere. The speed test was set to 10 K/min. Results from Figure 3.26 indicate that the analyzed resin starts to highly cure at a temperature around 40°C.

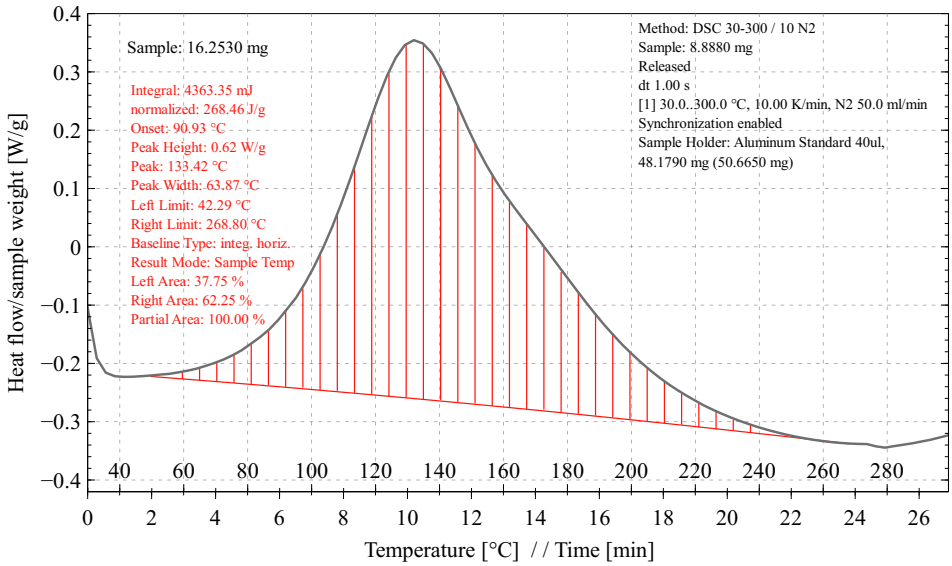

Figure 3.26: Differential Scanning Calorimetry analysis of the resin before being cured.

- **Tensile test**
  Five samples of dog-bone type I ASTM D638 [101] were cured in a mold according to the

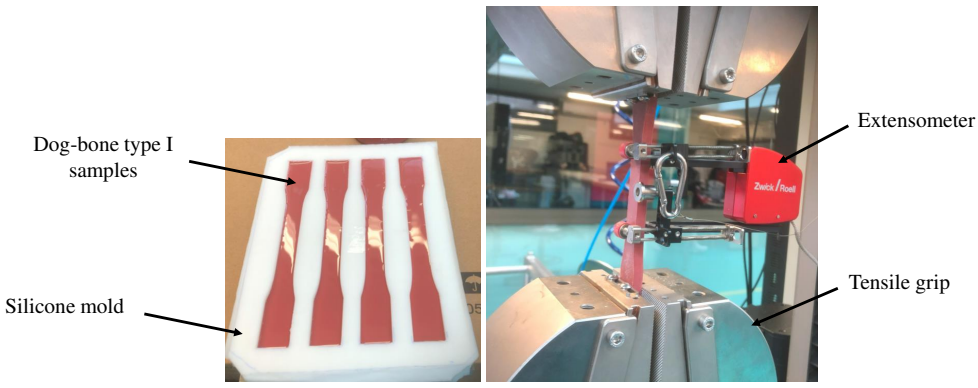

Figure 3.27: Assessment of the tensile performance of the resin. Laboratory sample manufacturing (a) and tensile test ASTM D638 [101] setup (b).

manufacturer's specifications (see Figure 3.27). In Table 3.4, the Young Modulus, the ultimate stress and strain were reported. In addition, the stress-strain curves were represented in Figure 3.28.

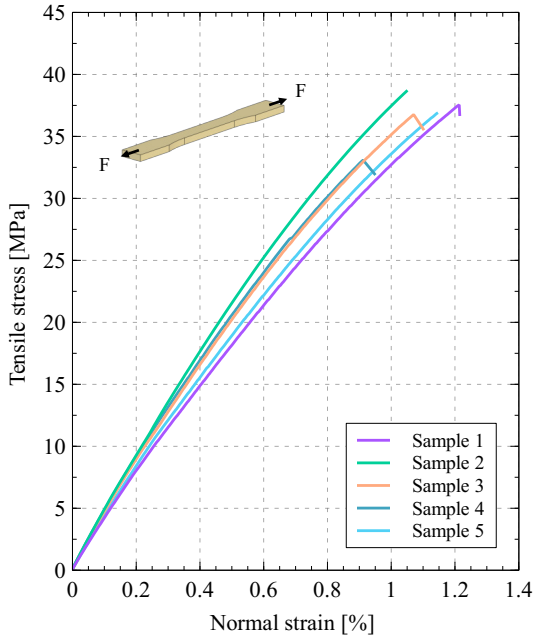

Figure 3.28: Resin's stress-strain curves resulted from the tensile test ASTM D638 [101] performed on laboratory-cured samples.

Table 3.4: Tensile performance of the analyzed resin.

	E (MPa)	σ_u (MPa)	ε_u (%)
Sample 1	3789	37.5	1.2
Sample 2	4359	38.6	1.0
Sample 3	4180	36.8	1.1
Sample 4	4304	33.1	0.9
Sample 5	4022	36.9	1.1
Mean	4131	36.6	1.1
Standard deviation	±231	±2.1	±0.1

3.4.2 Post-installation tests

Post-installation tests were performed with the liner used in the full-scale test described in Chapter 5.

a) Field tests

- **First visual inspection**
  A visual inspection was performed after the liner installation. As it can be appreciated in Figure 3.29a, the liner was perfectly installed and showed no apparent installation defects.

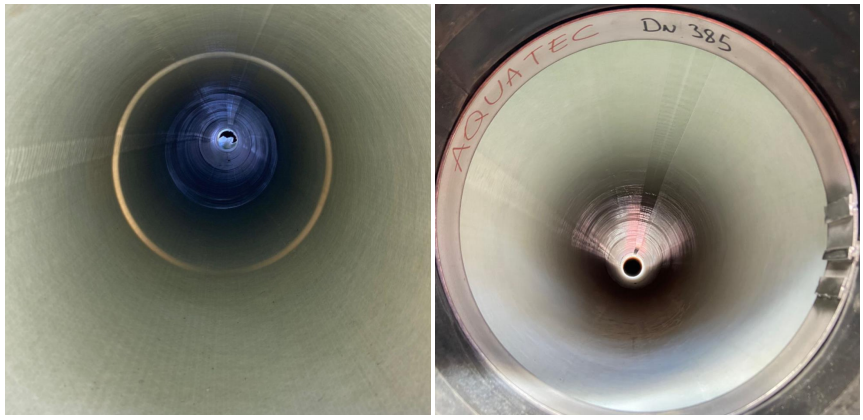

a) First visual inspection b) Second visual inspection

Figure 3.29: Visual inspection of the installed liner before (a) and after (b) the on-site tests.

- **Liner's thickness**
  Eight liner thickness measurements were performed according to the procedure described in Section 3.3.4. Figure 3.30 shows the exact location of the thickness measurements performed while results obtained are exposed in Table 3.5.

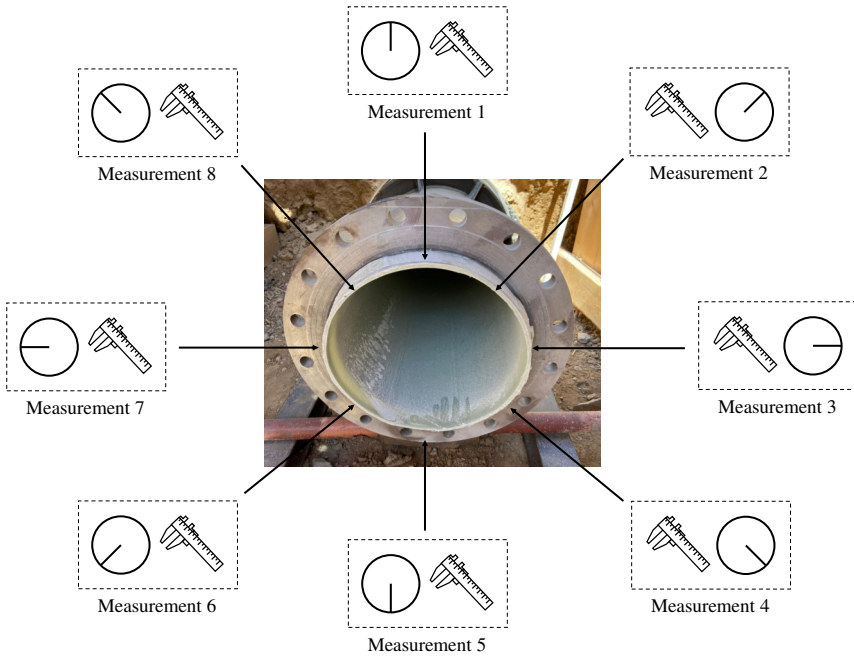

Figure 3.30: Schematic representation of the thickness measurements location of the installed liner.

- **Second visual inspection**
  After the pressure and tightness tests, a second visual inspection was performed (see Figure 3.29b).

The second visual inspection detected no signs of folds or swollen areas. Hence, the liner and the seals were perfectly installed.

Table 3.5: Thickness of the installed liner.

Measurement	0 h	1.5 h	3 h	4.5 h	6 h	7.5 h	9 h	10.5 h	Mean	Standard deviation
Thickness (mm)	5.48	6.05	5.31	5.13	7.25	5.39	5.93	5.85	5.80	±0.67

b) Laboratory tests

- **Differential Scanning Calorimetry (DSC)**
  A DSC analysis of the installed liner was performed to evaluate if it was completely cured after the curing process. The DSC was performed for a range of temperatures from 30 °C to 200 °C with a test speed of 10 K/min. In addition, an N_2 atmosphere was used. Figure 3.31 indicates that the analyzed liner was completely cured.

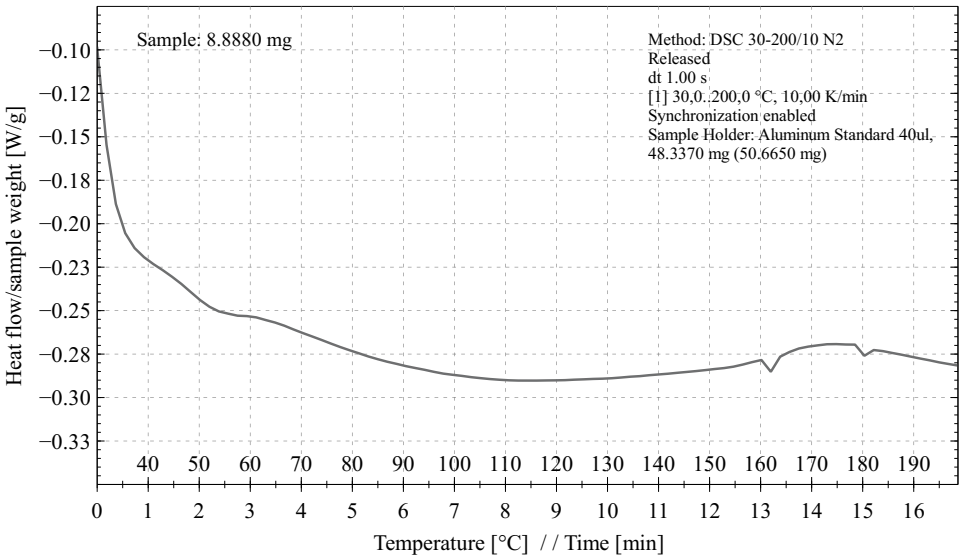

Figure 3.31: Differential Scanning Calorimetry of the installed liner.

- **Bending test**
  Curved samples were cut from ring samples from an installed liner according to ISO 11296-4 [9]. The tensile properties were evaluated by the three-point bending test of curved samples (see Figure 3.32). In Table 3.6, the geometrical features of the five samples are presented. Moreover, the Young Modulus, the ultimate stress, and the ultimate strain obtained are indicated in Table 3.7 before and after the curvature correction. The curvature correction coefficients are also indicated in Table 3.7. Finally, the stress-strain curves are represented in Figure 3.33.

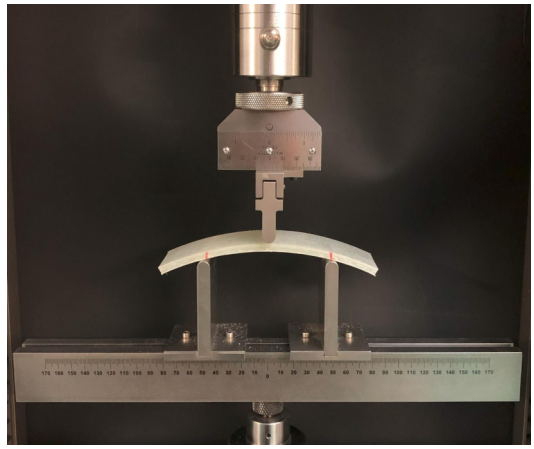

Figure 3.32: Sample subjected to the three-point bending test of curved samples ISO 11296-4 [9].

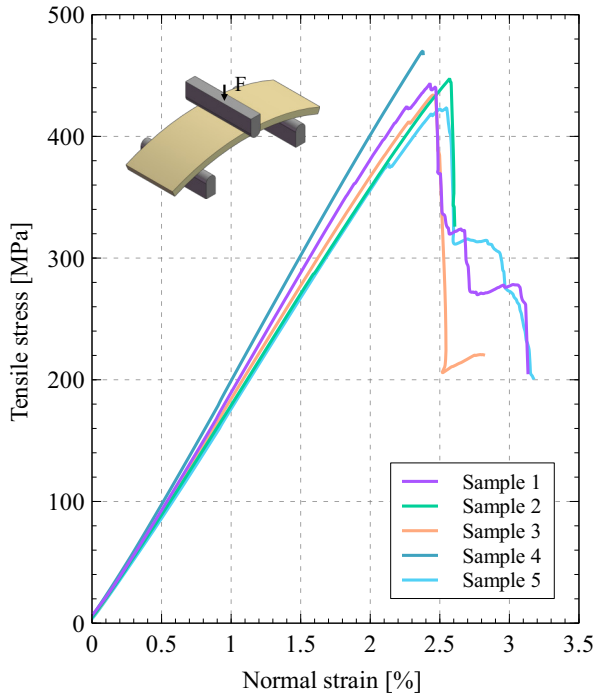

Figure 3.33: Stress-strain curves from the three-point bending test of curved samples ISO 11296-4 [9]. Results after the curvature correction.

Table 3.6: Geometrical features of samples performed by the three-point bending test of ISO 11296-4 [9].

	Thickness (mm)	Width (mm)	Area (mm^2)	L (mm)	L2 (mm)
Sample 1	5.37	49.93	268	96	99.94
Sample 2	5.42	50.00	271	96	99.95
Sample 3	6.21	49.84	310	96	100.15
Sample 4	5.59	50.08	280	96	99.99
Sample 5	5.45	49.77	271	96	99.96
Mean	5.61	49.92	280	96	100.00
Standard deviation	±0.35	±0.12	±17	±0	±0.09

Table 3.7: Stress-strain results from the three-point bending test ISO 11296-4 [9] before and after the curvature correction.

	Before curvature correction			Correction coefficients		After curvature correction		
	E_c (MPa)	σ_c (MPa)	ε_c (%)	C_E	C_σ	E_f (MPa)	σ_f (MPa)	ε_f (%)
Sample 1	19287	460.8	2.47	0.916	1.039	21056	443.5	2.43
Sample 2	18575	464.9	2.58	0.916	1.039	20278	447.4	2.57
Sample 3	18922	451.3	2.47	0.916	1.040	20657	433.9	2.45
Sample 4	20296	488.7	2.41	0.916	1.039	22157	470.4	2.38
Sample 5	17927	440.0	2.56	0.916	1.039	19571	423.5	2.55
Mean	19001	461.1	2.50	0.916	1.039	20744	443.8	2.47
Standard deviation	±880	±18.1	±0.07	±0.000	±0.000	±961	±17.5	±0.08

4

A novel test procedure to assess the performance of CIPP liners

This chapter analyzes the quality control tests to assess a liner's hoop tensile performance. In addition, the three-point bending test of curved samples ISO 11296-4 [9] considered by current CIPP standards is thoroughly examined, and the shortages detected in this test are exposed. Moreover, a novel test based on ring samples, the inner balloon pressure test, is presented as an alternative.

4.1 Test overview

The previous chapter highlighted the importance of establishing robust quality control procedures to ensure a liner is correctly installed and meets the minimum mechanical design properties after the installation process. As exposed, the QC protocol divides a CIPP project into four stages: the previous procedures, the materials verification, the installation process, and the post-installation verification.

In the post-installation verification, different tests were proposed to ensure the on-site installed liner preserves the initial mechanical properties according to the manufacturer. According to the worldwide procedures proposed in the previous section, most quality control procedures are based on laboratory tests. The aim of these tests is to obtain the tensile mechanical properties of the installed liner in the hoop direction. It is worth noting that the hoop direction is crucial in pressure pipes due to considerable internal loads.

Tensile laboratory tests are usually performed on flat dog-bone samples according to current standards (ASTM D638 [101], ISO 527-2 [111]). However, samples from installed liners are not flat at all. The ring shape of an on-site installed liner makes it impossible to obtain a perfectly flat sample in the hoop direction. Only huge host pipe diameters (DN > 1000) may allow machining dog-bone samples in the hoop direction because the curvature is less steep for the same dog-bone sample length than in smaller diameters. However, the curvature of the dog-bone sample may still be appreciated by visual inspection. Thus, the sample will be pre-stressed after the grips of the universal machine fix the dog-bone type sample (see Figure 4.1).

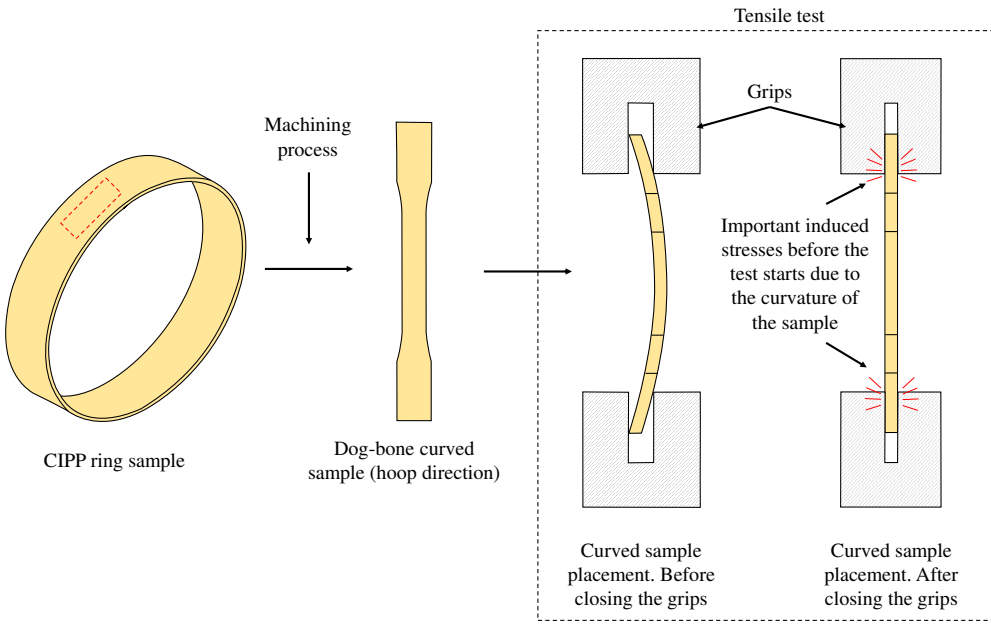

Figure 4.1: Operation scheme of the apparent hoop tensile strength test ASTM D2290 [53].

On the other hand, there are other procedures for evaluating the tensile properties of a curved sample that are mentioned in the literature [85, 86]. For instance, ASTM D2290 [53] offers the possibility of evaluating the tensile properties of ring samples with a couple of notches. The test consists of two split disks perfectly fitted inside the ring sample. Then, a vertical displacement is applied on the upper disk until the sample fails (see Figure 4.2). However, although this test is commonly used by some authors [84, 85] with glass fiber-reinforced pipes to evaluate the apparent hoop tensile properties, bending stresses are also induced as indicated in [86]. Therefore, this test may not be suitable for evaluating the pure tensile behavior of the liner in the hoop direction.

The three-point bending test is another procedure widely used to evaluate the tensile strength properties of composite materials [112–114] and brittle materials such as ceramics. Moreover, it is considered the main quality control test as indicated in most CIPP standards (ASTM F1216 [8], UNE 53929 [1], ISO 11296-4 [9] and ISO 11298-4 [10]) to asses the tensile strength properties of an installed liner. However, the current bending test of flat samples (ISO 178 [103] was adapted to compensate the curvature effect of curved samples. The bending test is a good option to perform due to its operational simplicity [112]. Nevertheless, in a bending test, the CIPP curved samples are subjected to a combination of stresses that may vary along the test. Thus, the sample is governed by tensile, compressive, and shear stresses. Consequently, failure modes are complex [90, 115, 116], and failure may occur due to a combination of stresses rather than pure tensile failure. The bending test could be questionable for assessing the tensile performance of an installed CIPP liner in the hoop direction, as indicated by the results exposed in this chapter.

Thereby, there is a need to create new procedures to assess the tensile performance of a CIPP liner in the hoop direction. A new test named the Inner Balloon Pressure Test (IBPT) was developed in the present thesis to address this challenge. The test pretends to reproduce the conditions of ring-in-tension that a CIPP liner is subjected to. A complete analysis of the IBPT and tests mentioned above is exposed in the following sections.

4.2 Mechanical performance

4.2.1 Apparent hoop tensile strength test

In CIPP liners, the apparent hoop tensile strength test (ASTM D2290 [53]) was used by some authors [52] to investigate the effect of installation defects. In this study, wrinkles were classified, and an estimation of the reduction of the mechanical properties of the liner in the hoop direction was provided. In these studies, the investigation aimed to establish a comparison between samples with different conditions. Thus, the apparent hoop tensile strength test was correctly chosen. However, as the name of the test indicates, the apparent hoop tensile strength test (ASTM D2290 [53]) provides an "apparent" hoop tensile strength rather than pure tensile strength as it is the case of ASTM D638 [101].

In Figure 4.2, the operation of the apparent hoop test is shown. The tooling consists of two split disks. Both are surrounded by a ring-shaped sample with two notches, as indicated in Figura 4.2. It should

be noted that at the beginning of the test, both split disks are very close, nearly in touch. Moreover, the liner should perfectly fit both split disks. Then, the upper split disk starts to move vertically until failure. However, although a perfect fit between the liner and the tooling is nearly achieved at the beginning of the test, the gap created between both split disks during the test induces a bending moment to the sample. Thus, failure is caused by a combination of tensile and bending stresses.

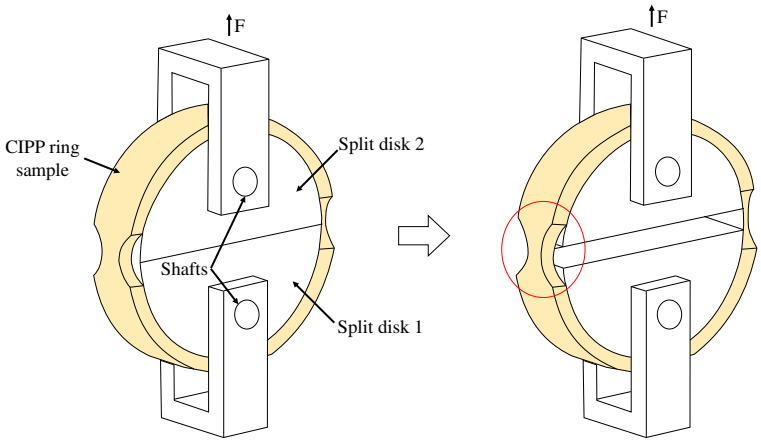

Figure 4.2: Operation scheme of the apparent hoop tensile strength test ASTM D2290 [53].

The apparent hoop tensile strength test is usually used in plastic or reinforced plastic pipes. The idea behind this test is to reproduce the effect of the inner pressure that a pipe is subjected to. Furthermore, it pretends that the sample behaves as a ring-in-tension. However, apart from the limitations commented above, there are also some other weaknesses to consider. First, the split disks may perfectly fit the sample. CIPP liners have custom inside diameters depending on the host pipe inside diameter and the thickness of the liner. Thus, custom split disks will be necessary to test samples from different pipes of the same apparent inside diameter. Moreover, the rehabilitated host pipes were usually built with the middle's twenty-century tolerances. Consequently, host pipes often have a notable percentage of ovality. A semi-structural liner must fit the host pipe, adopting its ovality during installation. It should be noted that according to UNE 53929 [1], the percentage of the host pipe ovality must be less than 10% in CIPP rehabilitation. Then, the oval samples may not perfectly fit the split disk or a custom split disk may be necessary for every project of CIPP.

Furthermore, although it may be the less important point, the operational mode for placing the sample surrounding both split disks is not as comfortable as other tensile or bending tests.

4.2.2 Three-point bending test

As introduced at the beginning of this chapter, the three-point bending test appears in most CIPP standards to evaluate the tensile hoop properties of installed liners. However, the current bending test of ISO 178 [103] was modified in ISO 11296-4 [9] to apply a correction due to the curvature of the samples.

4.2.2.1 Bending theory

As stated above, although the bending test is widely used due to its operational simplicity, the phenomena that occur during a bending test are complex. Simultaneous forces such as axial, shear, or torsional can appear in addition to the desired pure bending moment.

The bending equations based on pure bending were developed considering the assumptions below. Equations are also based on small deformations.

- The material of the sample is homogeneous and isotropic.
- Lineal elasticity: the Young's modulus is the same in tension and compression.
- The different transverse sections that were plane at the beginning of the test remain plane after bending (based on Navier-Bernoulli principle).
- The sample is initially straight, and longitudinal layers bend into circular arcs with a common center of curvature.
- The curvature radius is larger compared to the cross-section's dimensions.
- Independent of the layer above or below, each layer of the sample is free to expand or contract.

Navier-Bernoulli principal states:
"two initially flat and parallel cross sections remain flat but not parallel throughout the deformation process, even in the plastic region."
This principle was demonstrated by analytical calculations. Due to the symmetry of the sample, all of the elements of the sample must deform identically. Thereby, it is only possible to have identical deformations if the transverse cross sections remain flat during bending (see Figure 4.3). However, it should be noted that there will be deformations within the plane due to Poisson's effect.

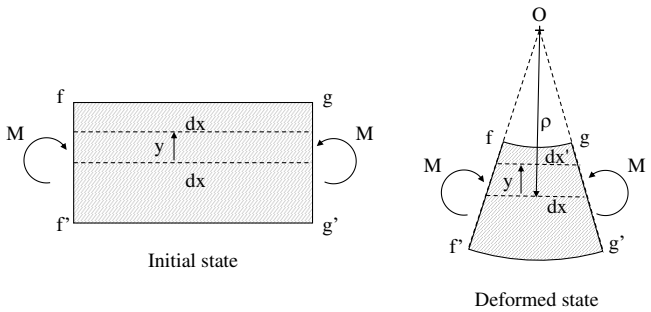

Figure 4.3: Straight beam of rectangular cross-section subjected to bending showing plane behavior assumption.

According to the assumption of linear elasticity, the lower layers of the sample are subjected to tensile stress while the upper layers are compressed. Hence, a layer located close to the middle, named the neutral layer, is not compressed or pulled. Thus, it does not experience a longitudinal variation during the test.

According to Hooke's law, the uniaxial stress along the cross-section of an elastic material subjected to bending can be deducted from Eq. 4.1.

$$\sigma_x = E\varepsilon_x = -\frac{Ey}{\rho} = -Eyk \tag{4.1}$$

Consequently, the longitudinal stress that every layer of the sample is subjected to can be calculated. It should be noted that according to Eq. 4.1, the longitudinal stress also depends on the distance between the layer and the neutral axis. However, although the resultant normal stress is the sum of axial forces and bending moment, there are no axial forces under the pure bending assumption. Thereby, the resultant moment is equal to the bending moment.

The Navier-Bernoulli equation (Eq. 4.2) can be deducted when a differential of area is studied (see Figure 4.4).

$$\sigma_x = -\frac{My}{I_z} \tag{4.2}$$

Where I_z is the second moment of area of the cross-section with respect to the neutral axis corresponding to the z and y is the distance to the neutral axis.

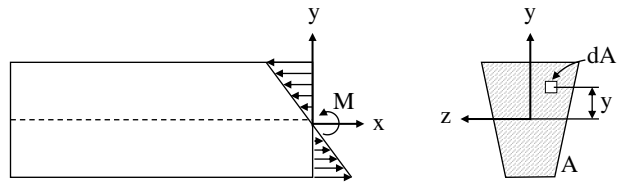

Figure 4.4: Stress distribution of a beam subjected to bending.

4.2.2.2 Curved beams

The beam's theory developed for straight beams is also applicable to deduct the curved beam's theory.

The linear elastic behavior of curved beams with a rectangular cross-section was addressed by Timoshenko and Goodier [15] using the theory of elasticity. Relations for radial stress σ_r, hoop stress σ_h, and shear stress σ_{rh} were obtained using polar coordinates. Then, the equations were generalized for any symmetrical cross-section. Furthermore, the curved beam equations are based on two assumptions:

- Plane sections at the beginning of the test remain plane after loading.
- The radial stress σ_r and the shear stress σ_{rh} are considered negligible as they should be small when cross sections do not have thin webs like I, T, or H cross sections.

In Figure 4.5, a curved beam subjected to a bending moment due to the applied load is considered. Firstly, it should be noted that in curved beams, the center of mass does not pass through the neutral axis.

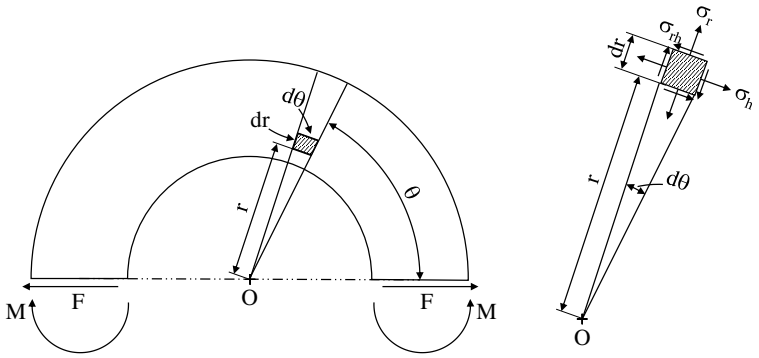

Figure 4.5: Loading state of a curved beam.

A differential of area dA subjected to axial force N_1, shear force V and bending moment M_x is considered. Then, these forces should be balanced by the resultants of the hoop stress σ_h and shear stress σ_{rh}. However, according to assumption 2, shear stress σ_{rh} can be neglected as it will be minimal compared to hoop stress. The equilibrium of forces in axis z and moment equilibrium respect to axis x is presented in Eq. 4.3 and Eq. 4.4.

$$\begin{aligned} \sum F_z &= \int \sigma_h dA - N_1 = 0 \\ \sum M_x &= \int \sigma_h (R_1 - r_1) dA - M_x = 0 \end{aligned} \tag{4.3}$$

Where R_1 is the distance from the center of curvature to the center of mass of the curved beam and r_1 is the distance of the differential of area to the center of curvature.

$$\begin{aligned} N_1 &= \int \sigma_h dA \\ M_x &= \int \sigma_h (R_1 - r_1) dA \end{aligned} \tag{4.4}$$

The strain in the hoop direction ε_h applied to the differential of area can be deducted from the deformed shape (Eq. 4.5). In Figure 4.6, the deformation state of a curved beam is represented. Planes F-G and T-U represent the initial shape of the element, while the deformed element is defined by f-g and t-u. Planes F-G and f-g intersect at the neutral axis of the cross-section (where hoop stress is null) and at a distance R_{1n} from the center of curvature O. Moreover, according to assumption 1 (plane sections remain plane), planes f-g and t-u remain plane after deformation occurs. However, an angle $\Delta d\theta$ is formed between planes F-G and f-g.

$$\varepsilon_h = \frac{\Delta_L}{L_0} = \frac{(R_{1n} - r_1)\Delta d\theta}{r_1 d\theta} = \left(\frac{R_{1n}}{r_1} - 1 \right) w \tag{4.5}$$

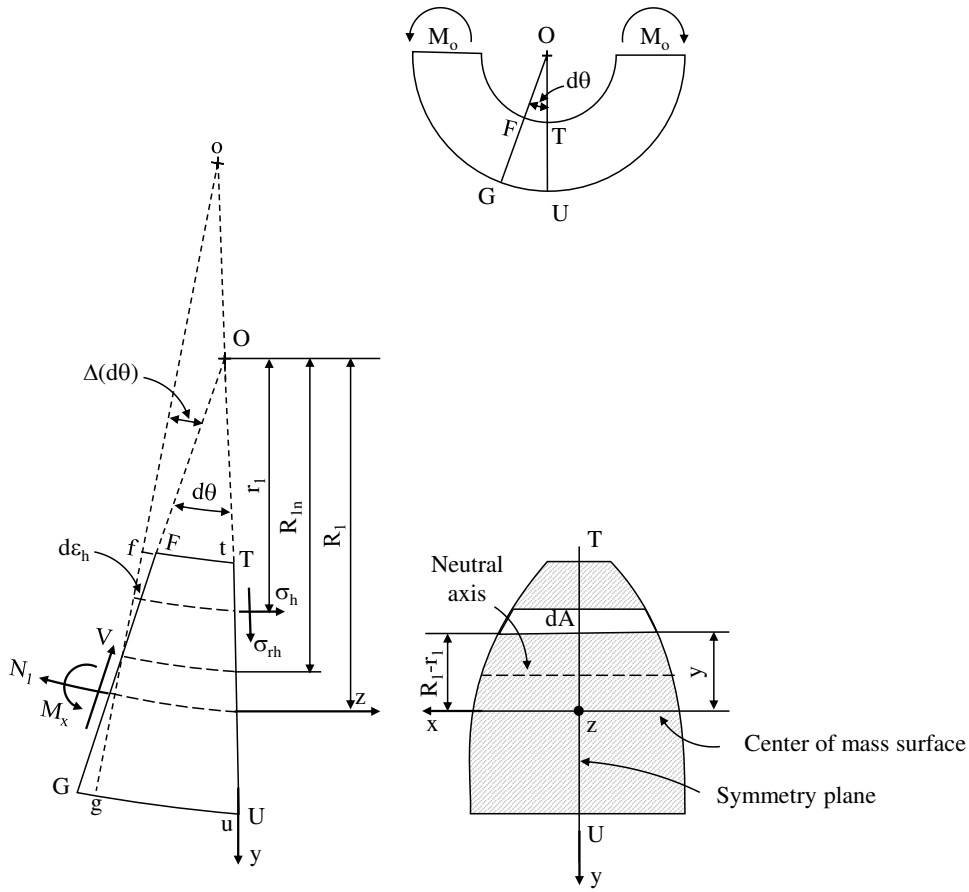

Figure 4.6: Deformed shape analysis of a curved beam. Infinitesimal approach.

where:

$$w = \frac{\Delta d\theta}{d\theta} \tag{4.6}$$

Then, according to Hooke's law:

$$\sigma_h = E\varepsilon_h = \left(\frac{R_{1n} - r_1}{r_1}\right) wE = \left(\frac{R_{1n} wE}{r_1}\right) - wE \tag{4.7}$$

Finally replacing Eq. 4.7 to Eq. 4.4:

$$\begin{aligned} N_1 &= R_{1n} wE \int \frac{dA}{r_1} - wE \int dA = R_{1n} wEA_m - wEA \\ M_x &= R_{1n} R_1 wE \int \frac{dA}{r_1} - (R_1 + R_{1n}) wE \int dA + wE \int r_1 dA \\ &= R_{1n} R_1 wEA_m - (R_1 + R_{1n}) wEA + wER_1 A = R_{1n} wE(R_1 A_m - A) \end{aligned} \tag{4.8}$$

where A is the cross sectional area of the curved beam and A_m is the length dimension defined by Eq. 4.9.

$$A_m = \int \frac{dA}{r_1} \tag{4.9}$$

The moment equation can be rewritten as:

$$R_{1n} w E = \frac{M_x}{R_1 A_m - A} \tag{4.10}$$

Then replacing to Eq. 4.8:

$$wE = \frac{A_m M_x}{A(R_1 A_m - A)} - \frac{N_1}{A} \tag{4.11}$$

Finally, replacing Eq. 4.10 and Eq. 4.11 to Eq. 4.7, the hoop stress distribution of a curved beam is obtained (see Eq. 4.12).

$$\sigma_h = \frac{N_1}{A} + \frac{M_x(A - r_1 A)}{A r_1 (R_1 A_m - A)} \tag{4.12}$$

Eq. 4.12 reveals that the hoop stress distribution of a curved beam has a hyperbolic shape rather than the lineal stress distribution of a straight beam (see Figure 4.7).

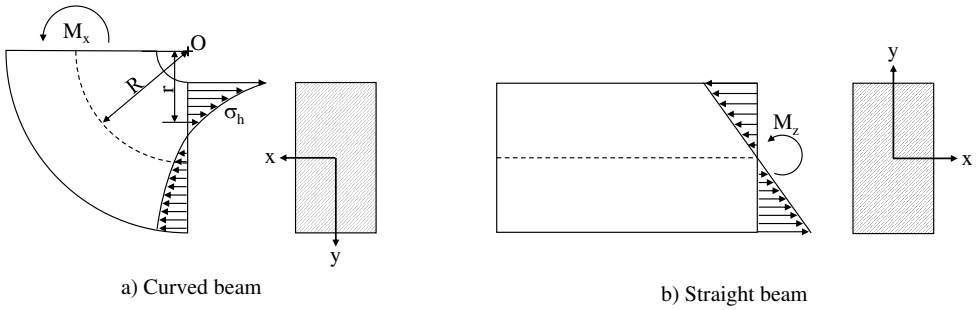

Figure 4.7: Stress distribution of a rectangular cross-section beam subjected to bending. Curved beam (a) vs straight beam (b).

Although in curved beams stress distribution is defined by Eq. 4.12 when the radius of curvature to the beam thickness ratio is more than five times, the Navier-Bernoulli equation (Eq. 4.2) of straight beams can be used on curved beams with an acceptable accuracy. For instance, considering a ratio of 8, the results using the straight beam equation differ by about 5% from the curved beam equations.

However, CIPP liners sample thicknesses range from 4 mm to 12 mm. Usually, the biggest thicknesses correspond to big pipes (DN 800 mm - DN 1200 mm) or seriously damaged pressure pipes. Hence, the radius of curvature to the beam thickness ratio is far over 8. For example, in this study, a DN 380 mm sample of 5-6 mm of thickness was tested, which corresponds to a ratio of 38-31.7. Moreover, the adapted three-point bending test for curved CIPP samples of ISO 11296-4 [9] considers the traditional beam theory rather than the curved beam theory when calculating stress and strain. In contrast, the

ISO 11296-4 [9] applies a correction on the final stress, strain, and Young Modulus due to the curvature of the sample. This correction is based on geometry to transform the curved sample into a flat sample.

4.2.2.3 Bending test of curved CIPP samples

Annex B of ISO 11296-4 [9] presents a procedure to calculate the tensile stresses that a CIPP curved sample is subjected to in the hoop direction in the three-point bending test. As stated in this chapter, tensile stresses due to bending in CIPP samples could perfectly be calculated according to the straight beam Navier-Bernoulli equation (Eq. 4.2) as the ratio radius of curvature to sample thickness is high. Thereby, implementing the curved beam equation Eq. 4.12 would increase the complexity of the hoop stress calculation rather than give a more accurate result. However, ISO 11296-4 [9] does not calculate stress as a curved beam. In contrast, the stress is calculated first by the straight beam equation, and then a correction based on geometry is applied directly to the stress obtained with the Navier-Bernoulli equation. Next, the procedure described in ISO 11296-4 [9] is addressed.

First, according to Eq. 4.2, the tensile stress of a straight beam of rectangular cross-section subjected to the three-point bending test (see Figure 4.13) can be obtained (Eq. 4.14). It should be noted that the distance between supports L must be replaced by the distance between sample contact points L_2 (see Figure 4.9). L_2 can be calculated by Tales transformations according to Eq. 4.13.

$$L_2 = \frac{L}{1 - \left(\frac{r_1 + \frac{h}{2}}{R_2}\right)} \tag{4.13}$$

Where r is the support's radius (r=5 mm), h is the liner's thickness (mm), and R_2 is the radius of curvature of the sample at half the thickness (mm).

$$\sigma_h = \frac{\frac{FL_2}{4}\frac{h}{2}}{\frac{bh^2}{12}} = \frac{3FL_2}{2bh^2} \tag{4.14}$$

The apparent hoop strain (ε_c) can also be calculated according to Eq. 4.15.

$$\varepsilon_c = \frac{6sh}{L_2^2} \tag{4.15}$$

Where s is the displacement of the sample's surface at the load point application from its initial position (mm).

Then, the apparent Young Modulus E_c can be calculated according Eq. 4.16.

$$E_c = \frac{\sigma_{c2} - \sigma_{c1}}{\varepsilon_{c2} - \varepsilon_{c1}} \tag{4.16}$$

Where σ_{c2} is the apparent stress at point 2 (MPa), σ_{c1} is the apparent stress at point 1 (MPa), ε_{c2} is the apparent strain at point 2 (mm/mm) and ε_{c1} is the apparent strain at point 1 (mm/mm). It should be noted that ε_{c2} must be calculated according to Eq. 4.17. In addition, ε_{c1} is defined between the range

[0.0005 - 0.004] mm/mm, and the value that maximizes the apparent Young Modulus must be chosen.

$$\varepsilon_{c2} = \varepsilon_{c1} + 0.002 \tag{4.17}$$

Furthermore, an initial correction due to the sample's accommodation must be applied to ε_c. Hence, ε_{c0} is obtained by the intersection of the straight defined by the apparent Young Modulus and the x axis (see Figure 4.8). Next, the strain is corrected by the following expression: $\varepsilon = \varepsilon_c - \varepsilon_{c0}$.

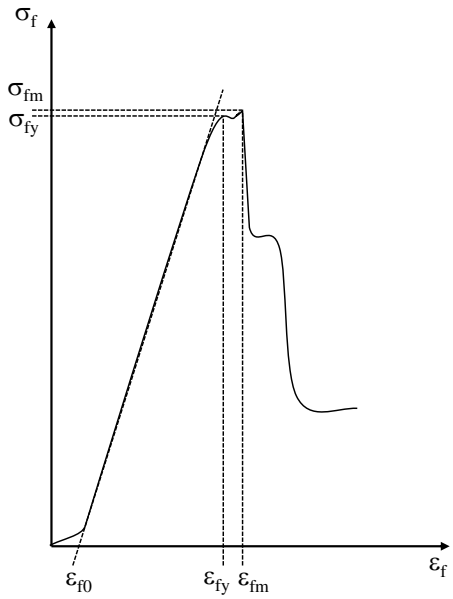

Figure 4.8: Representative scheme showing the strain correction ε_{f0} due to curvature of the sample according to ISO 11296-4 [9].

Then, a geometry correction due to curvature is applied on the apparent stress σ_c (Eq. 4.21) and the apparent Young Modulus E_c (Eq. 4.22). First, the respective correction coefficients C_σ and C_E are calculated according Eq. 4.18 and Eq. 4.20.

$$C_\sigma = \frac{1 + \frac{h}{6R_2}}{cos\,\phi} \tag{4.18}$$

Where C_σ is the curvature correction coefficient, R_2 is the radius of curvature of the sample at the average sample thickness, and ϕ is the half angle of an unloaded sample formed between the real contact points of the supports (see Fig. 4.9). It should be noted that ϕ cannot exceed the value of 45°. Therefore, the nominal distance between supports L to the outer diameter d_n of the sample ratio must be less than 0.7·ϕ can be calculated according Eq. 4.19.

$$\sin\phi = \frac{L_2}{2R_2} \tag{4.19}$$

$$C_E = \frac{\left(\frac{L_2}{2R_2}\right)^3 cos^2\phi}{1,5\left[\phi - \left(\frac{L_2}{2R_2}\right) cos\,\phi\right]} \tag{4.20}$$

$$\sigma_f = \frac{\sigma_c}{C_\sigma} \tag{4.21}$$

Where σ_f is the flexural stress of a flat sample subjected to bending loads (MPa).

$$E_f = \frac{E_c}{C_E} \tag{4.22}$$

E_f is the flexural modulus of a flat sample subjected to bending loads (MPa).

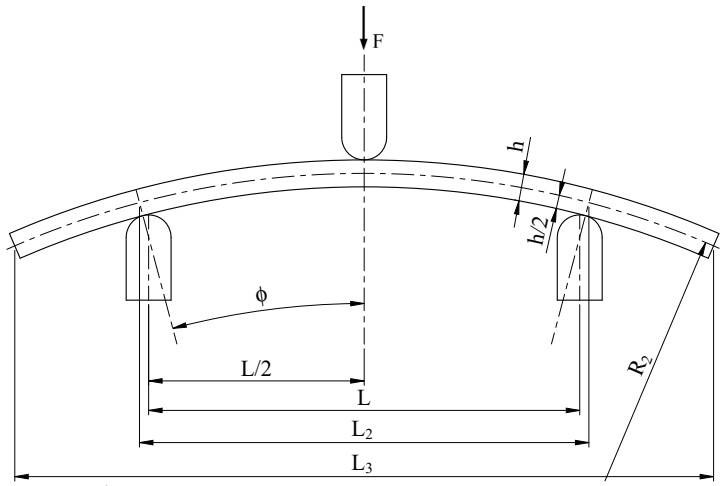

Legend
F: Applied force.
h: Total thickness of the sample.
L: Distance between supports.
L_2: Real distance between the supports of a curved sample.
L_3: Total length of the chord of a curved sample.
R_2: Radius of curvature of the sample at half the thickness
ϕ: Half-angle of an unloaded specimen formed between the actual contact points of the supports.

Figure 4.9: Operational scheme of the three-point bending test of curved samples according to ISO 11296-4 [9].

Test operational and failure modes observed

In the three-point bending test, the sample is placed onto two equally spaced supports, as seen in Figure 4.10. A third support, the loading nose, is positioned directly above the center of the specimen. Then, a vertical displacement of the loading nose applies a load on the specimen's center until failure. The flexural strain and stress are then calculated with the deflection of the center of the beam according to Eq. 4.23 and Eq. 4.24.

$$\sigma_c = \frac{3FL_2}{2bh^2} \tag{4.23}$$

where σ_c is the apparent stress of a curved sample subjected to bending before the curvature correction (MPa), F the applied force (N), L_2 the actual distance between the supports of a curved sample

subjected to bending (mm), b the width of the sample (mm) and h the thickness of the sample (mm).

$$\varepsilon_c = \frac{6\,s\,h}{{L_2}^2} \tag{4.24}$$

ε_c is the apparent strain of a curved sample subjected to bending before the curvature correction (mm/mm), s the displacement of the surface of the sample at the point of the load application from its initial position (mm).

In Figure 4.10, a sequence of three different states of a three-point bending test according to ISO 11296-4 [9] is shown. As can be observed, at the beginning of the test, the sample is curved as it was extracted from an installed liner. Then, the sample begins to rotate onto both supports. Hence, the ends of the sample start to elevate as the center lowers down. The rotation of the sample can be appreciated by the red marks evolution that the sample has above both supports (see Figure 4.10). Finally, the initially curved sample passes through a flat shape state and continues to deform until failure, adopting an inside curvature shape as it happens in current flexural tests described in ISO 178 [103].

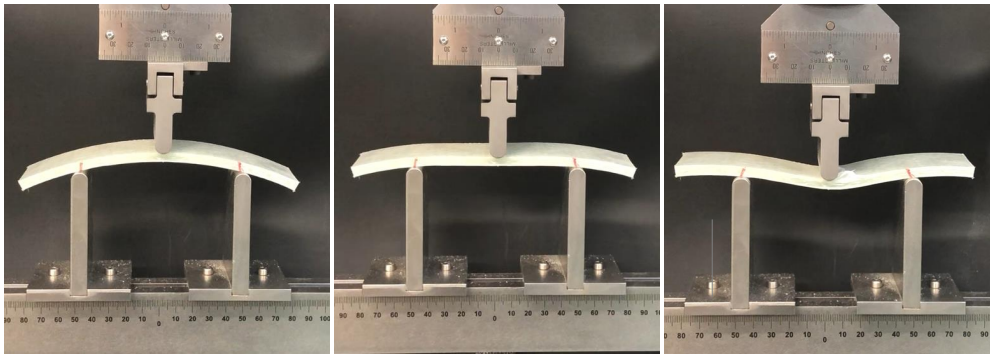

Figure 4.10: Experimental setup of a three-point bending test of a cured CIPP sample liner (DN 385 mm), according to the technical standard ISO 11296-4. [9].

During the test, a combination of tensile, compressive, and shear stresses are present. Failure may occur due to the sum of tensile/compressive stresses and shear stress. According to Eq. 4.23, the tensile/compressive stress distribution over the sample section is linear. As depicted in Figure 4.11, it varies from the maximum compressive stress at the top of the sample to the maximum tensile stress located at the bottom of the sample in agreement with Eq. 4.2. The zero-stress value is situated close to the middle plane, in the neutral axis. In contrast, shear stress acquires a parabolic shape through the sample's section with maximum shear stress located in the neutral axis (see Figure 4.11).

The shear stress is responsible for the delamination of the layers that compose the composite sample. Different failure modes were detected from the three-point bending test as represented in Figure 4.12.

- **Tensile fracture of fibers**: in this failure mode, rupture begins when single fibers of the outer layer of the sample begin to break due to tensile stress. Small breaks can be noticed during the test rather than big cracks, indicating that the fibers work separately rather than in a full composite

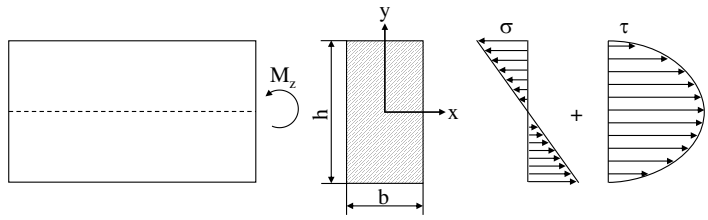

Figure 4.11: Combination of normal and shear stresses that a rectangular cross-section beam is subjected to under bending.

block. Moreover, wavy irregularities are detected in the stress-strain curve. Thus, it is not the desired failure mode.

- **Tensile fracture of the outer layer**: the ideal failure mode of the three-point bending test is to obtain a tensile fracture in the outer surface of the sample. According to Eq. 4.2, the maximum tensile stress is located in the outer layer of the sample. Moreover, the tensile strength of a sample should be lower than the compressive strength. Consequently, tensile failure may occur first. Furthermore, it should be noted that the fracture propagation is very fast, and a single big crack can be appreciated. The described breaking behavior is due to the reduction of the thickness of the section due to the outer layers' failure. When the most stressed layer, corresponding to the outer layer, begins to break, then the inertia of the section is reduced. Hence, according to the Navier-Bernoulli equation (Eq. 4.2), when the moment of inertia of the cross-section is reduced, the stress increases for the same bending moment applied.

- **Compressive fracture of the outer layer**: this failure mode can appear in composite materials made of fibers embedded into a resin matrix. Compressive failure can be related to two phenomena: punching and buckling. The punching of the upper layer of the sample is due to the loading nose effect onto the resin matrix. The fibers are no longer embedded when the resin matrix starts to crack. Thus, the strength of the composite decreases, and failure occurs. On the other hand, the buckling of the fibers is also a failure mode often observed. The resin matrix is responsible for avoiding buckling effects in the compressive layers. However, when all fibers are not perfectly surrounded by resin, the sample may be more sensitive to buckling effects. It should be noted that the resin impregnation process of samples with fibers sorted by bundles is complex. A thin layer of resin must surround every single fiber, conforming to the bundle.

- **Interlaminar shear**: composite materials, especially laminates, are susceptible to delamination. High-strength fibers are embedded into a weak resin matrix. When all the layers conforming the composite are stacked together, a composite material with both properties, high strength, and ductility is obtained. These awesome properties are achieved when only the composite remains as a single block. However, interlaminar shear stresses will try to separate the composite layers, resulting in premature failure. In the three-point bending test, shear stress is formed. The shear stress distribution along the sample section depicted in Figure 4.11 reveals that shear stress is maximum on the neutral axis and zero at the outer layers. However, in the neutral axis, no normal stresses

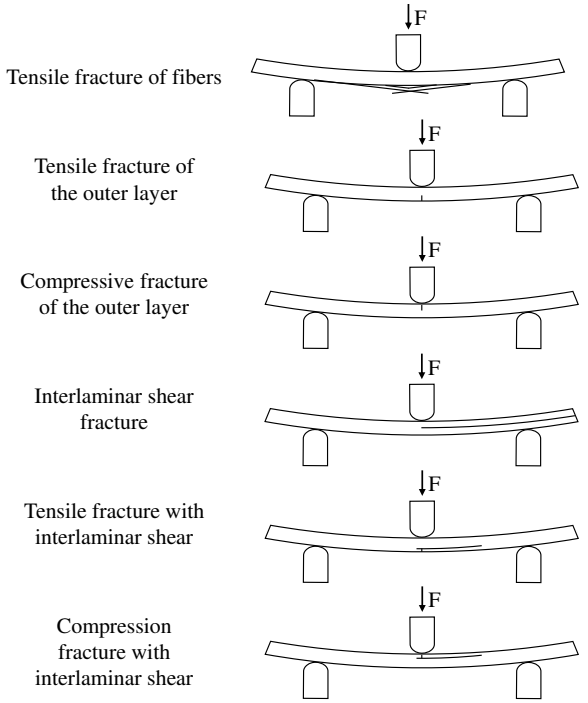

Figure 4.12: Possible failure modes in the three-point bending test.

are registered. Thus, interlaminar fractures may occur above or below the neutral axis before the surfaces of the sample. The interlaminar failure in the tensile zone can be appreciated as a longitudinal crack appears beneath the neutral axis and the outer layer of the sample subjected to tensile stresses. Moreover, it should be noted that shear stress cannot be avoided in the three-point bending test. However, bending failure is desired rather than interlaminar shear. The loading span to sample thickness ratio should be increased to solve the interlaminar failure problem because bending is susceptible to the distance between supports. In contrast, this ratio does not affect the interlaminar shear stress because it only depends on the applied load (see Figure 4.13). However, large span-to-thickness ratios may produce large deflections, and considerable horizontal forces may appear in the supports that should be considered when calculating the bending moment. Thereby, a compromise distance must be achieved to increase bending in front of shear stresses while at the same time avoiding large deflections.

- **Tensile fracture with interlaminar shear**: the combination of two failure modes can also appear. In these cases, it is often difficult to deduct which failure mode was first as they occur nearly simultaneously. However, the sample has reached its maximum tensile strength and shear strength.
- **Compression fracture with interlaminar shear**: again, two failure modes that may occur simultaneously are combined. Thus, it is difficult to determine which one happened first. The sample has reached its maximum compressive strength and maximum shear strength.

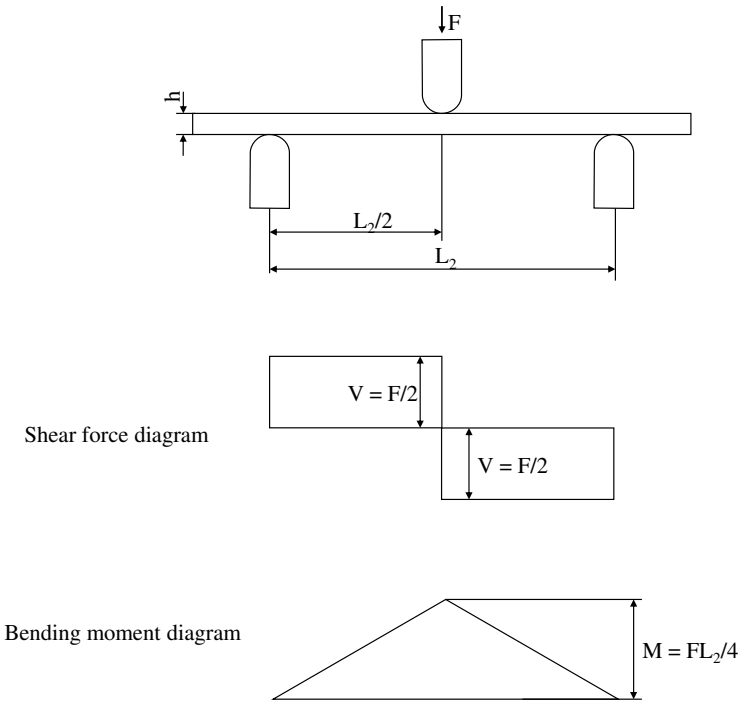

Figure 4.13: Shear and bending diagrams of a rectangular cross-section straight beam through the three-point bending test.

4.2.3 Proposed inner balloon pressure test

Although the three-point bending test and the correction presented in ISO 11296-4 [9] is widely used in the CIPP market, some authors [81] have reported the complexity of the phenomenons that takes place during a bending test of a composite. Moreover, a comparison between the pure tensile test and bending test of curved samples ISO 11296-4 [9] was addressed in this study, finding significant differences in results. Furthermore, the results stated in Section 4.4.1 indicate that higher performances of the liner are achieved in the three-point bending test of ISO 11296-4 [9]. Thus, this quality control test may induce wrong measurements of a liner's tensile hoop strength, indicating that it can withstand higher tensile loads than reality. Thereby, the result from the three-point bending test of ISO 11296-4 [9] can be questionable. In addition, new procedures to assess the tensile hoop strength of a liner are mandatory. Thus, some authors and enterprises have begun to develop their own tests. Most of them are inspired by burst pipe tests widely used in plastic pipe testing (see Figure 4.14). However, it is complex to perform burst pressure tests on a CIPP cured liner due to the considerable deformation that a liner can achieve, especially semi-structural liners. It should be noted that in these tests, the liner is held by a combination of grips at its ends. Thus, the ends of the liner cannot freely span, and consequently, the typical barrel shape is acquired before failure occurs. Hence, bending stresses can be induced and hidden between tensile stresses. Moreover, the likelihood of leaks increases as the pressure rises. It is considered the main cause reported by authors [50] to explain the pressure limitation of the

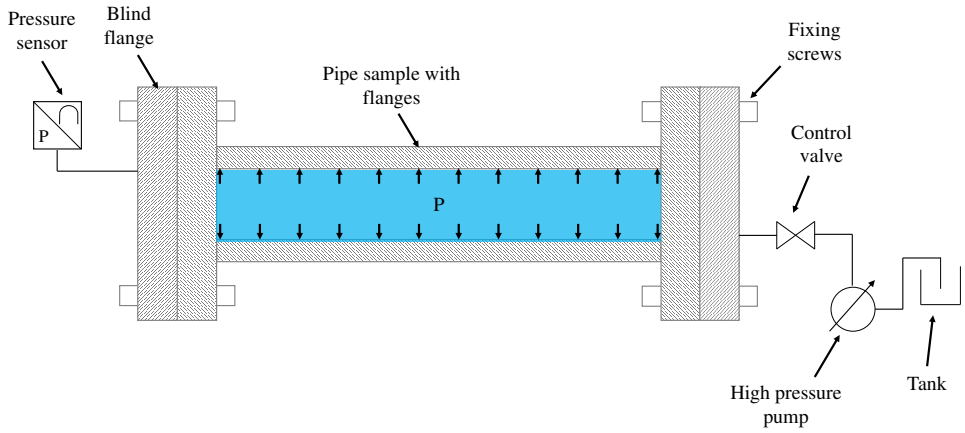

Figure 4.14: Scheme of a current burst pressure test widely used in the pipe market.

developed prototypes to assess the hoop tensile performance of a liner. Leaks were reported due to difficulties in sealing the ends at high pressures. In some cases, to increase the sealing, the ends of the samples were squared using a lathe and coated with liquid rubber. Moreover, enterprises have also tried to avoid leakage problems by curing the liner after being positioned in the tooling. However, this procedure complicates the testing process and does not address the initial goal of performing a quality control test for installed liners. Moreover, the problem of leaks at high pressures was not solved.

On the other hand, the tests commented above were in the line of obtaining the tensile hoop strength of a liner from a cylindrical sample, which consists of an extruded ring sample. The tensile strength of the liner can be deducted from Eq. 4.25 when the inner pressure P_I, the radius of the pipe R, and the thickness of the sample h are known.

$$\sigma = \frac{P_I R}{h} \tag{4.25}$$

Thereby, a ring sample test should be a good option rather than a bending test or the apparent hoop test if the tightness problems at high pressures (P>20 bar) are solved. It should be noted that pressure pipes can achieve nominal pressures higher than 10 bar. However, the design pressure is considered to be much higher than the nominal pressure. In addition, heavy safety factors are used in the market of CIPP due to uncertainty and the significant damages that can cause failures in big nominal diameters (DN 400 - DN 1200) pressure pipes. Consequently, most CIPP liners can withstand higher pressures than expected. Therefore, robust tooling free of leakages is mandatory to achieve the ultimate tensile strength of the liner applying inner pressure.

In the present doctoral thesis, the Inner Balloon Pressure Test (IBPT) was developed to assess the tensile hoop performance of a liner. The test is based on the ring sample idea exposed above. Although it was an idea previously checked by some authors (ring/cylindrical samples), the test procedure developed is completely different and novel in the field of CIPP. Hence, the tightness issues are solved, and high

pressures (P>25 bar) can be reached with considerable nominal diameters (DN>400).

The IBPT consists of a ring sample being pressurized between two rigid plates, as shown in Figure 4.15. It should be noted that the ring sample can freely expand in the hoop direction. Leaks between both plates and the sample are avoided by using an inside membrane responsible for guaranteeing tightness.

In Figure 4.15, the operational performance of the IBPT is represented. First, a ring sample is introduced between both plates. Then, the plates are adjusted to fit the ring sample smoothly and fixed with a threaded rod system. Subsequently, the membrane is fed with hydraulic pressure. At the beginning of the test, the membrane is not in contact with the sample. As the fluid continues to enter, the membrane expands freely until contact between the sample and the membrane is established. Thus, the accommodation state is complete. At that point, pressure can start to rise. Hence, the hydrostatic pressure applied inside the membrane is transferred to the inner ring sample face. Then, the sample radially expands until the burst pressure is reached. While a pressure sensor records the inner pressure, the hoop strain is obtained from previously installed strain gauges in the hoop direction. It should be noted that the IBPT is a destructive test. Hence, the ultimate tensile stress and strain of the liner are obtained.

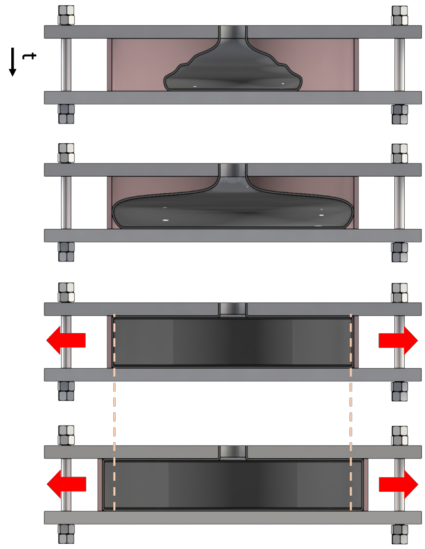

Figure 4.15: Operational scheme of the Inner Balloon Pressure Test.

4.3 Methodology

4.3.1 Materials

The research methodology employed in this chapter was first based on comparing the tensile strength properties of a cured CIPP liner obtained with the three-point bending test of ISO 11296-4 [9] and the tensile test of ASTM D638 [101]. The shortcomings of the current quality control test, the bending test,

are identified. Secondly, samples from the same liner are performed with the IBPT and compared to pure tensile strength test results.

Previously, the IBPT was numerically validated with the numerical results of the tensile test ASTM D638 [101]. Then, an experimental validation with Polyvinyl chloride (PVC) samples was also performed. PVC was chosen because of its well-known isotropic mechanical properties. Hence, flat dog-bone type samples were machined in the longitudinal direction, tested according to ASTM D638 [101], and compared with the experimental results from the IBPT.

The liner used in this study was specially designed for potable pressure water pipes. It was classified as structural class A according to ISO 11295 table 16 [12] and class IV according to AWWA CIPP classification [117]. As shown in Figure 4.16, the liner is composed of three layers of glass fiber (L_1, L_2 and L_3) and an additional layer (L_0) of Polyethylene (PE) that prevents fiber migration to the potable water.

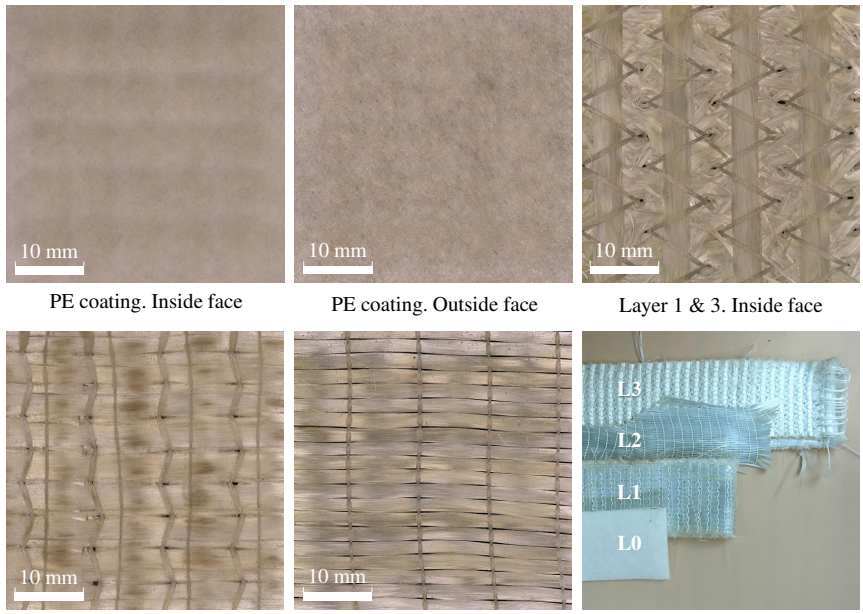

Figure 4.16: Raw liner morphology. Experimental thickness according to ISO 5084 [95]. Layer 0 (L0): 1.06 mm, Layer 1 and 3 (L1 and L3): 2.52 mm and Layer 2 (L2): 1.34 mm.

The thickness of each layer was measured according to ISO 5084 [95] procedure for non-woven materials. Figure 4.16 reveals each layer's raw liner's morphology. As it can be appreciated, layer 2 can be considered the liner's kernel as it is placed between layer 1 and layer 3. Moreover, it can be considered as the structural layer because only glass perfectly placed side-by-side fiber bundles in the hoop direction are observed. It should be noted that the hoop direction is considered the most requested direction due to the inner pressure. The glass fiber bundles are stacked together by a sewn thread that prevents the bundles from being one on top of the other and keeps them straight enough

to avoid reducing the mechanical performance of the liner. Layer two had a thickness of 1.34 mm, and it was initially longitudinally open (as a belt) with an overlap in the hoop direction to contribute to the expansion of the liner during its installation and before the curing process.

The structural layer is surrounded by two identical layers in composition (layers 1 & 3). These two layers have a thickness of about 2.52 mm, and their design indicates that these layers may hold the resin, assuring the structural layer is embedded in resin and preventing the resin from spreading out of the liner. The inside face of these layers may reinforce this idea as a mesh of non-directional glass fibers can be found to hold the resin. It should be noted that the mechanical properties of a liner are heavily reduced when impregnation problems appear. Furthermore, a few glass fiber bundles are observed in the longitudinal direction of layers 1 & 3. These longitudinal glass fiber bundles improve the bending strength of the liner and also in this case may be necessary as this UV liner is installed by the pulling process. Thus, the longitudinal direction is requested during the installation process. Moreover, the outside face of layers 1 & 3 present unconnected patches of glass fiber bundles in the hoop direction to improve the expansion capacity of the uncured soft liner in the installation process.

Finally, the PE coating of 1.06 mm is analyzed. A perfectly smooth inside surface is observed to help the water circulation, while a rough outside surface that may improve resin grip is noticed. On the other hand, the resin employed was styrene-free and ultra-low VOC (Volatile Organic Compounds) vinyl ester resin used for CIPP and specific for drinking water pressure pipes.

Two different processes were used to obtain CIPP cured samples. First, flat dog-bone samples in the hoop direction were obtained by a laboratory curing process (see Figure 4.17 and Figure 4.18). A laboratory curing process was chosen since obtaining flat samples in the hoop direction from a cylindrical pipe is not feasible. Hence, rectangular samples impregnated with resin from the manufacturer (see Figure 4.18a) were cut in the hoop direction. Then, the samples were cured by ultraviolet (UV) lamps type A, B, and C of 1 kW with an exposure time of two minutes. It should be noted that some pressure was applied to the rectangular sample during the curing process to ensure the liner's compression as much as possible. Thus, the inside air can be removed. Air bubbles inside the liner heavily reduce the mechanical properties of the liner. Moreover, the applied pressure prevented the sample from curving because it solidified so fast that a curvature of the cured sample was generated when no pressure was applied. Then, the rectangular samples were machined by a numerical control milling, and dog-bone type I samples were obtained according to ASTM D638 [101].

Second, ring and curved bending CIPP samples were obtained directly from a rehabilitated reinforced concrete pressure pipe of DN 400. The pipe was rehabilitated with the same liner that was cured in the laboratory to obtain the flat samples in the hoop direction. Moreover, the liner was installed in a real old pipe under field conditions by an installer enterprise and using the equipment usually employed. The liner was installed by the pulling method. Then, after pressurizing a bit (0.3 bar) the liner to keep it against the host pipe walls while the liner remained soft (uncured), the liner was cured by passing through a trolley of 9 UV lamps of 400 W each (see Figure 4.19). Subsequently, cured ring samples were obtained using a radial saw from the liner's ends. It should be noted that a minimum overhead of

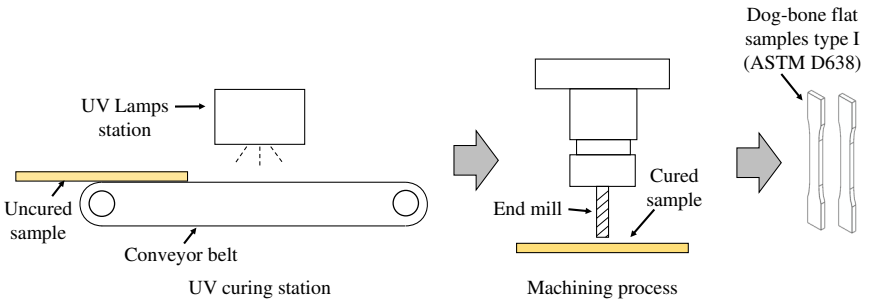

Figure 4.17: Scheme of the laboratory curing process procedure to obtain flat dog-bone samples in the hoop direction of a CIPP liner.

2 m set by the manufacturer must be respected on both ends to avoid generating wrinkles during the installation process. Consequently, the cured liner that sticks out of the host pipe must be removed. Moreover, a space inside the host pipe must be left to install the sealing pieces responsible for impeding water to drain between the host pipe and the liner. Thus, some ring samples can be obtained (see Figure 4.20). Then, curved samples can be cut from ring samples.

Figure 4.18: Manufacturing process of flat CIPP samples in the hoop direction: uncured rectangular flat sample (a), UV lamps station used to cure the samples (b) and the machining process of type I ASTM D638 [101] samples (c).

The composition of samples extracted from the field was analyzed using a high-resolution Olympus DSX1000 digital microscope (see Figure 4.21). The three layers and the polymeric coating identified in Figure 4.16 during the raw liner analysis can also be recognized in the cured sample. Moreover, hoop glass fiber bundles from the structural layer (layer 2) can be perfectly seen as an ellipse shape. Furthermore, longitudinal glass fiber bundles of layers 1 & 3 can be appreciated as straight-wavy lines. In the microscope view, glass fibers are associated with a spotted white color, while green corresponds to the resin. In addition to the PE coating, another thin plastic can also be identified in the liner's outer face, which is in contact with the host pipe's inner face. This thin plastic is supposed to be a mechanism that may help retain the resin during the impregnation process. Hence, it may be added during this process as it was not detected in the raw liner analysis. Moreover, it should be noted that the liner was perfectly installed as the resin embeds all the glass fibers without gaps or impregnation defects.

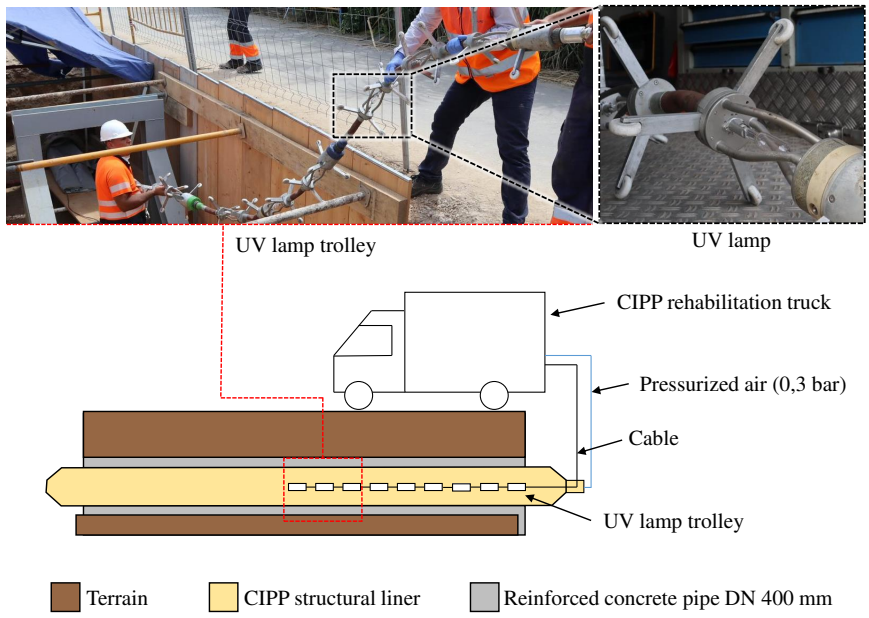

Figure 4.19: UV curing process of the samples extracted from the field.

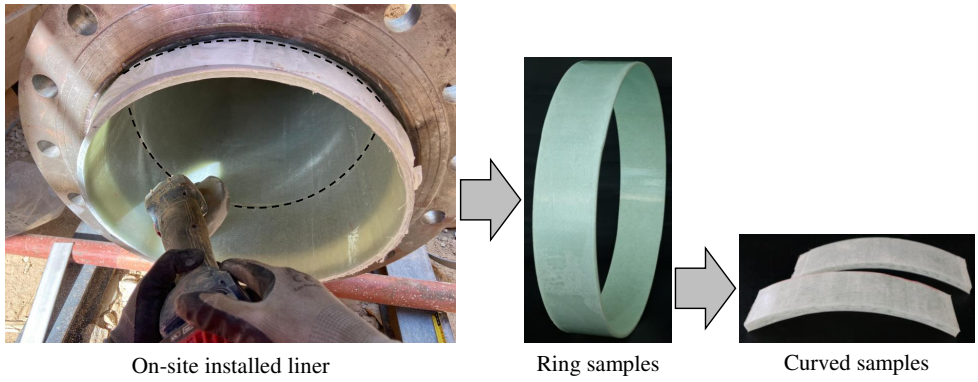

Figure 4.20: Extraction of ring and curved bending samples from a DN 400 rehabilitated pressure pipe.

On the other hand, the glass fiber hoop bundles from the raw liner were also examined in Figure 4.21. It should be noted that observing the single glass fibers of a bundle is a complex operation as the fibers conduct and reflect the light, generating severe brightness conditions. However, a diameter of 22 μm was measured in the single glass fibers composing the hoop bundles in agreement with the manufacturer's specifications.

4.3.2 Tensile testing

Tensile tests on PVC and CIPP flat dog-bone type I samples were performed according to ASTM D638 [101]. The PVC samples were obtained from a PVC pipe along the longitudinal direction, while CIPP liner samples were obtained from flat laboratory-cured samples. The universal machine

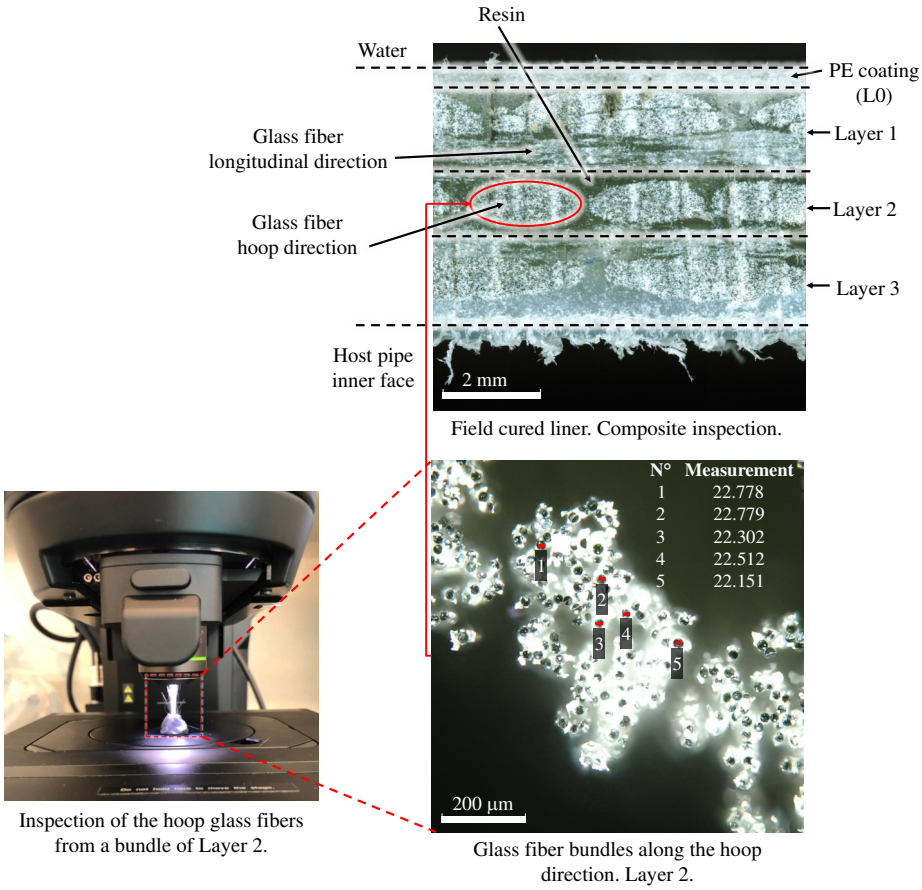

Figure 4.21: Microscope inspection of the cured liner used.

ZwickRoell Z30 with a 30 kN load cell was used to assess the tensile tests. Moreover, a 50 mm ZwickRoell extensometer was employed to measure the strain. In addition, a preload of 5 N and a test speed of 5 mm/min were used according to ASTM D638 [101]. The Young modulus was calculated using the regression method between the strain range of 0.05% and 0.25%. The test speed used to define the Young modulus was 1 %/min.

4.3.3 Three-point bending test

The three-point bending test defined in ISO 11296-4 [9] was performed using CIPP curved samples obtained from the rehabilitated DN 400 reinforced concrete pipe. The same universal machine, ZwickRoell Z30, was used. According to the sample parameters presented in ISO 11296-4 [9], the samples had an inner radius of 192.5 mm and a thickness of approximately 6 mm. Hence, a value of 195.5 mm was established for R_2. Moreover, the curved samples had 50 mm of width (b) according to ISO 11296-4 [9] specification. The distance between supports (L) was set to 96 mm. Hence, a value of 99.93 mm was established for L_2 according to Eq. 4.13. Then, a half angle ϕ of an unload sample formed between the real contact points of the supports of 0.258 rad (14.8°) was obtained (Eq. 4.19).

The curved samples were tested according ISO 11296-4 [9] and ISO 178 [103]. A preload of 2 MPa and a test speed of 10 mm/min were used. The Young Modulus was calculated according to Eq. 4.16 between the strain range of 0.05% and 0.25%. A strain rate of 1%/min was used to define the Young Modulus. Furthermore, the apparent stress (σ_c) and the apparent strain (ε_c) were obtained from Eq. 4.14 and Eq. 4.15. Then, the curvature correction coefficients for stress (C_σ) and Young Modulus (C_E) were calculated according Eq. 4.18 and Eq. 4.20. A value of 1.039 and 0.916 were respectively obtained. Finally, the curvature coefficient correction was applied to obtain the flexural stress (Eq. 4.21) and the flexural modulus (Eq. 4.22).

4.3.4 Digital image correlation setup

A 3D Digital Image Correlation (DIC) was used to assess the three-point bending test of curved CIPP samples. Hence, the strain distribution along the sample's thickness was analyzed. The samples were first airbrushed with different tip diameters to create the speckle pattern (see Figure 4.22). Two Allied Vision GigE MAKO G-507B GigE cameras with APO-Xenoplan 1.4/23-0903 objectives were used to record the surface displacement of the samples during the three-point bending test. Calibration was performed with a GOM CP20/MV55×44 panel with an offset of 0.021 pixels. The measurement volume resulting from the calibration was 150×130×110 mm. Finally, the image sequences were post-processed with GOM Correlate Professional software using a facet size of 12×12 pixels.

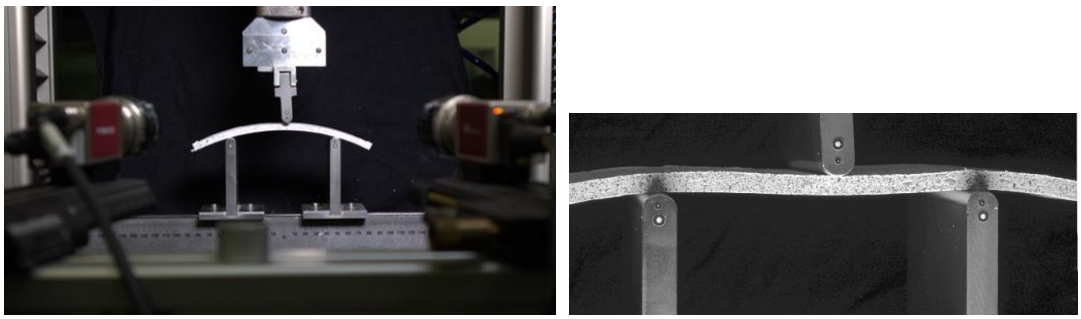

Figure 4.22: Digital Image Correlation of the three-point bending test. Setup and example of the speckle pattern created.

4.3.5 Inner balloon pressure test

A prototype of the IBPT was built to experimentally validate the proposed test to assess the hoop tensile behavior of a CIPP sample from an installed liner (see Figure 4.24). The prototype was designed to test cured ring liner samples up to DN 500, and it had a size of 600×600 mm. Two rigid wood plates formed the core of the tooling, each reinforced with six IPN 100 beams of steel type S275JR. Moreover, the center zone of the upper plate was reinforced with two 150×600 mm steel plates of 10 mm thickness. The extra reinforcement of the upper plate was necessary because a central hole of diameter 120 mm was drilled to install the entrance and exit system of the fluid used to apply hydrostatic pressure to the sample. This system consisted of a metallic cover ending with a thread of 1/2" to connect the hydraulic

connections. On the other side, the membrane is fixed between the cover and a steel disk fixed with screws (see Figure 4.23).

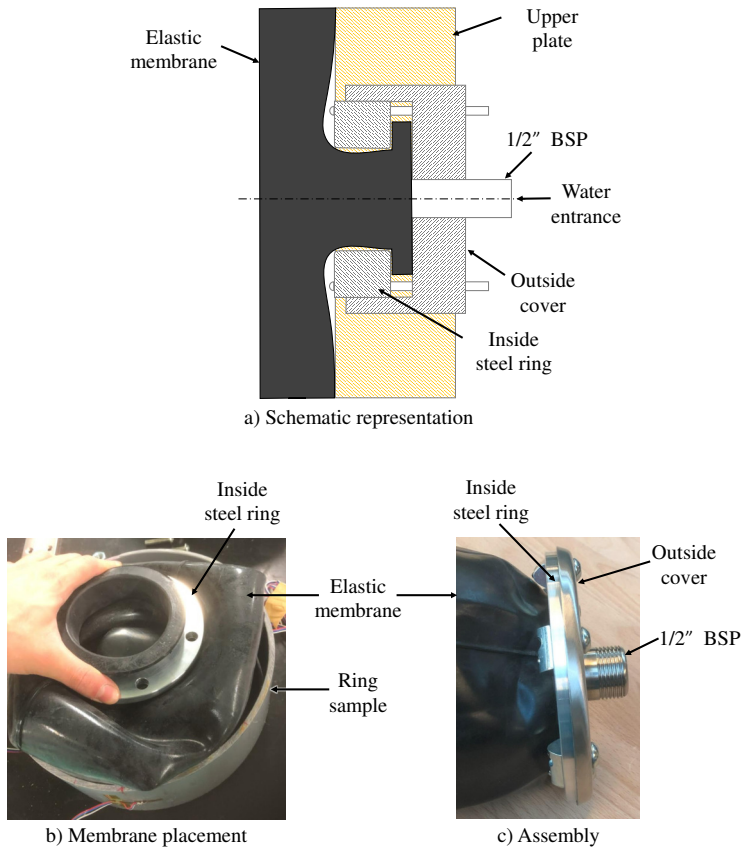

Figure 4.23: Detail of the fixing system employed to avoid leaks in the IBPT: schematic representation (a), placement of the membrane inside a ring sample (b) and assembly of the fixing mechanism before being placed in the IBPT tooling.

Furthermore, ten M16 threaded rods are responsible for fixing both rigid wood plates during the test. Moreover, the threaded rods are also used as sliding guides to lift the upper plate in an orderly mode to introduce the ring sample to be tested. The threaded rods are fixed with several nuts and double nuts. It should be noted that nuts were added in the region between both rigid wood plates to make the placement of the sample process easier. Thus, they are not tightened during the test (see Figure 4.24) as the inner pressure will try to separate both rigid wood plates, and thereby, the nuts located after the rigid plates will support the whole load. In addition, the IPN 100 beams are connected to the threaded rods by steel plates of 10 mm of thickness.

A pressure sensor Wika A-10 was used to monitor the pressure, and the hoop strain was collected through strain gauges type 1-LY41-6/350 that were installed in the hoop direction of the ring sample (see Figure 4.25). HBM's Quantum X MX840 B and Quantum X MX1615 B hardware and CatmanEasy AP software were employed for data acquisition. The prototype was first used to test a PVC sample, and

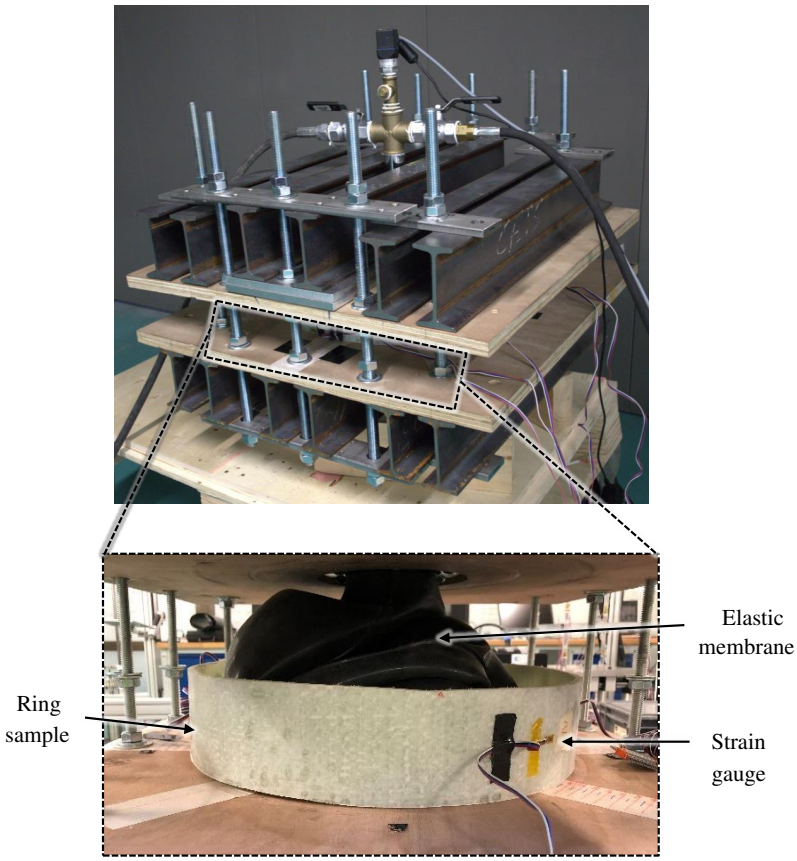

Figure 4.24: Prototype of the inner balloon pressure test used to evaluate the hoop tensile performance of a ring CIPP sample.

then rigid CIPP samples from a rehabilitated reinforced concrete pipe were tested. It should be noted that the ring samples must have parallel faces free of tips or protuberances that could easily provoke a puncture in the membrane of the tooling. Moreover, both rigid plates must fit the ring sample to test to avoid the membrane slipping through gaps between the plates and the sample, especially at high pressures. Furthermore, the PVC ring samples were obtained from a DN 240 mm pipe of 5 mm of thickness and 80 mm long, while the CIPP ring samples had a DN 385 mm, an average thickness of 6 mm and 80 mm of length.

4.3.6 Numerical model

A Numerical model of the tensile strength test ASTM D638 [101] and the IBPT were used to evaluate the tensile behavior of the IBPT. First, an implicit Ansys model of the tensile test was created and validated with experimental data. Due to the symmetry of the sample, the simulations were performed with half of the dog-bone type I sample described in ASTM D638 [101]. A higher-order 3D 10-node element, Solid 187, was used to create the mesh, and the element size was set to 3 mm. In addition,

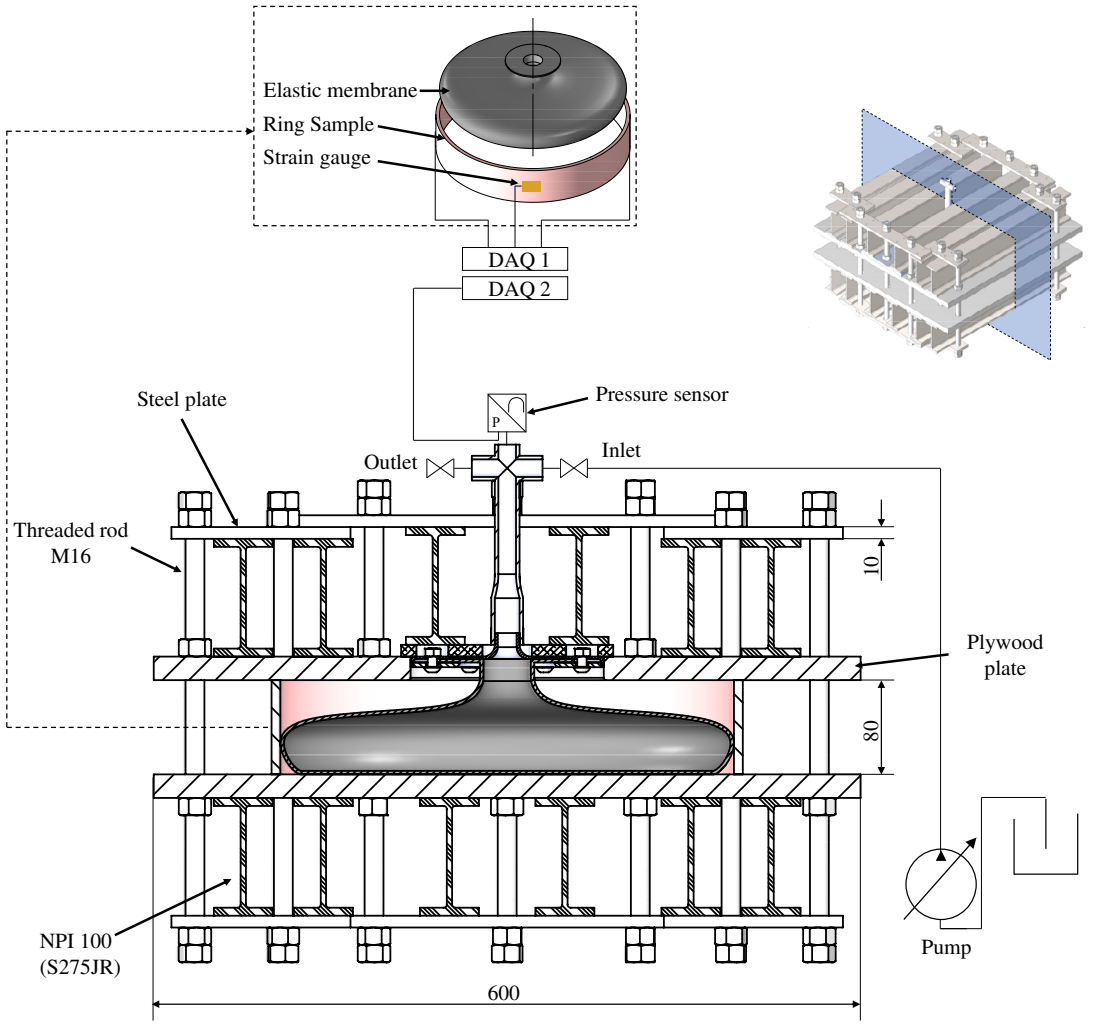

Figure 4.25: Assembly drawing of the inner balloon pressure test prototype built.

a type I refinement was applied in the stress concentration area (curved zone). Hence, the sample simulated had a total of 8,909 nodes. On the other hand, a fixed support was applied in the region where the grips in the experimental test fixed the sample. Moreover, a vertical displacement of 5 mm was applied on the upper face of the sample according to Figure 4.26. It should be noted that the mechanical properties of the materials used were obtained from the experimental tests. Previously, true stress compensation was applied to the experimental data as the plastic region was also studied. In the simulations, the multilinear plasticity option from the hardening isotropic material's behavior was activated.

Second, a static structural implicit Ansys model was also developed to assess the tensile properties of the inner balloon pressure test. Moreover, the simulations were also used to evaluate the effect of friction between the sample and the tooling. The IBPT simulations were carried out using two different

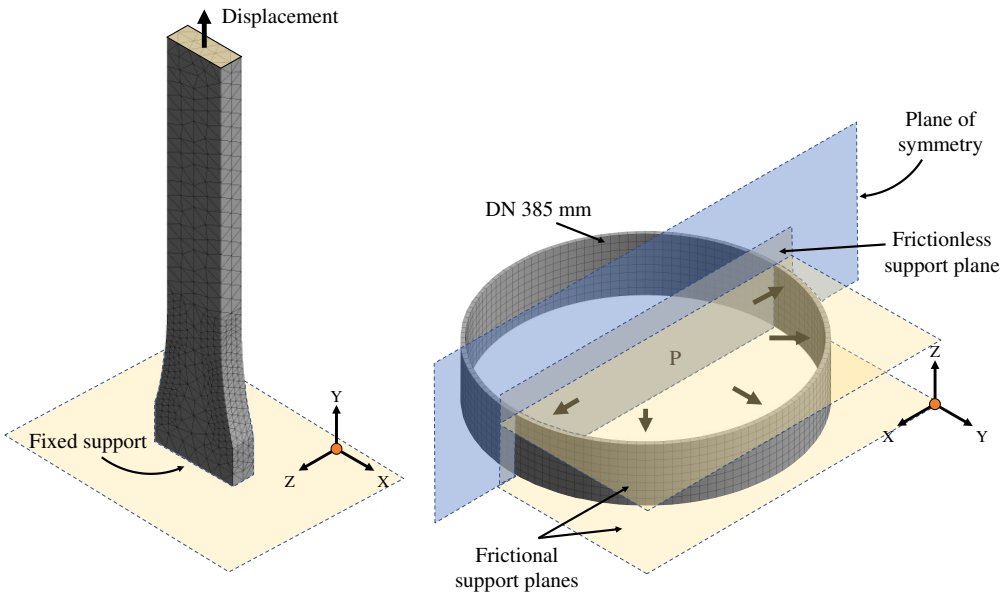

Figure 4.26: Schematic representation of the numerical models of the tensile strength test ASTM D638 [101] (left) and the inner balloon pressure test (right).

materials: PVC and the liner analyzed in Section 4.3.1. The represented PVC ring sample of DN 240 had a thickness of 5 mm and a length of 80 mm, while the DN 385 CIPP represented ring sample had a thickness of 6 mm and 80 mm of length. Both represented geometries are in agreement with the experimental ring sample dimensions tested with the prototype described in Section 4.3.5. Again, due to the symmetry of the samples, only half the ring sample was modeled. Both geometries were meshed with the higher-order 3D 20-node element Solid 186 with a maximum element size of 10 mm. The materials' properties were defined according to the Ansys materials database and complemented with experimental data from the tensile tests. The PVC samples were defined with a Young modulus of 3.4 GPa, a poison ratio of 0.4, a shear modulus of 1.2 GPa, and a density of 1392 kg/m^3. On the other hand, a Young modulus of 20.5 GPa, a poison ratio of 0.1543, a shear modulus of 8.9 GPa, and a density of 1857 kg/m^3 were defined for the CIPP sample. As represented in Figure 4.26 right, a frictional support plane of μ = 0.05 was applied in both faces of the ring, simulating the rigid plates of the IBPT prototype. Moreover, a frictionless support plane was defined in the XZ plane according to Figure 4.26 right, and two remote displacements were set. The first remote displacement was defined in the YZ plane at 3 and 9 o'clock to avoid x-displacement and z-rotation. Then, a second remote displacement was defined at 12 o'clock in the XZ plane to suppress the y-displacement and z-rotation (see Figure 4.26 right).

4.4 Results and discussion

4.4.1 Three-point bending test analysis

First, the failure modes obtained in the three-point bending test of curved samples were analyzed in Figure 4.27. Three failure modes were identified. A compression failure mode due to buckling of the fibers situated in the top layer can be appreciated in Figure 4.27a. Next, a delamination failure due to interlaminar shear was observed in Figure 4.27b. Finally, a tensile failure of the lower layer can be observed in Figure 4.27c. Thus, it is the only one that may occur in CIPP samples due to inner pressure. Nevertheless, the variety of failure modes exposed may reinforce the idea disclosed in Section 4.2.2, showing that the phenomena that occur in bending tests of CIPP composite liners are complex.

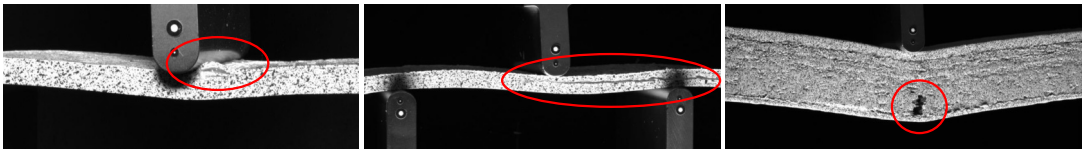

a) Compressive failure b) Delamination of layers c) Tensile failure

Figure 4.27: Failure modes identified in the three-point bending test of curved CIPP samples described in ISO 11296-4 [9]: compressive failure due to buckling of the upper fiber (a), delamination of layers (b), and failure of the external layer due to tensile stress (c).

In Figure 4.28, the tensile strength properties of a CIPP cured liner were obtained by two different tests. On the one hand, the three-point bending test of curved CIPP samples ISO 11296-4 [9] was performed. On the other hand, the tensile test of flat samples ASTM D638 [101] was executed. It should be noted that only a representative sample of the tensile test ASTM D638 [101] was depicted in Figure 4.28. In contrast, five samples from the bending test are represented because very close behavior was observed between samples in the tensile test, while some differences can be appreciated in the bending samples. As can be observed in Figure 4.28, the bending samples had a brittle behavior, and in most of them, a couple of cracks were appreciated after the first big crack. This behavior can be appreciated in Figure 4.28 by the stairs-shape that presents most of the bending curves over 2.3% of strain.

Both tests are able to assess the tensile strength behavior of a CIPP liner. However, although both types of samples came from the same liner, significant discrepancies can be found in the ultimate tensile strength of the tested samples. Shockingly, the ultimate hoop tensile stress obtained in the three-point bending test of ISO 11296-4 [9] was up to three times higher than the value derived from the tensile test ASTM D638 [101]. Therefore, experimental data shows that the bending test results may not accurately reflect the ultimate stress of a CIPP liner. This finding can have a negative impact on the structural safety of an installed liner since the tensile strength of a liner is a crucial parameter considered in the design process. On the other hand, Figure 4.28 reveals that the bending test is suitable to evaluate the Young Modulus of the liner as similar values were obtained in both tests.

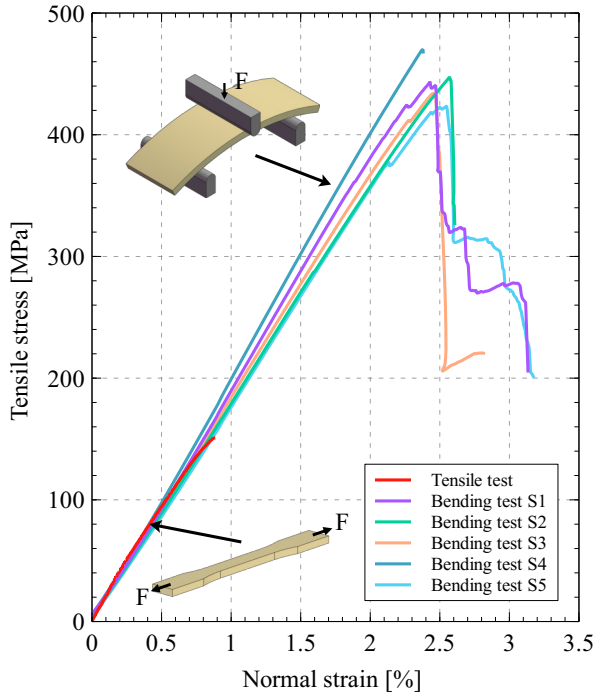

Figure 4.28: Tensile strength properties of the same liner assessed by the three-point bending test of curved samples (ISO 11296-4 [9]) and the tensile strength test of flat samples ASTM D638 [101].

Results from the three-point bending test of Figure 4.28 suggested an analysis of the strain distribution along the sample's thickness. Although in Section 4.2.2, it was assumed that CIPP samples had a radius of curvature to thickness ratio far over five and thereby flat bending theory could be applied to curved CIPP samples, a non-linear strain distribution described in bending of curved beams theory could explain the behavior observed in Figure 4.28. Consequently, a lower ultimate stress should be obtained.

To validate this hypothesis, the strain distribution along the sample thickness in the three-point bending test was measured by digital image correlation. Figure 4.29 shows the strain distribution presented by the curved CIPP sample at two different instants. First, the strain distribution in a middle state was represented in violet, while in red, the instant before failure occurred was depicted.

Figure 4.29 reveals that a bilinear behavior rather than the hyperbolic behavior expected from a curved beam subjected to bending was obtained. Hence, the linear strain distribution can be calculated with equations derived from the theory of straight beams subjected to bending. However, it should be noted that the intersection point of the straight forming the bilinear behavior in Figure 4.29 corresponds with the thickness of the polymeric coating (layer zero). Moreover, the bilinear behavior is more accentuated instants before failure occurred (red), suggesting that the polymeric coating was deformed in the plastic zone before the brittle failure of the fiber-resin region occurred.

To have a better understanding of the failure mechanism, the middle state strain distribution represented

in violet in Figure 4.29 was carefully selected to obtain the strain distribution at the moment when the outer layer, corresponding to the coating, reached the maximum strain of the composite measured in the tensile test of flat samples. In that initial state, a nearly completed linear behavior can be observed. Then, the polymeric coating starts to yield, but there is no crack propagation along the sample as the fiber-resin region has not reached the ultimate tensile stress of the liner. At this stage, the inertia of the sample is not reduced because the thickness of the sample is conserved, as the coating can still be deformed in the plastic region. Consequently, the sample failure occurs when the fiber resin region, after the polymeric coating, achieves the ultimate tensile stress of the liner.

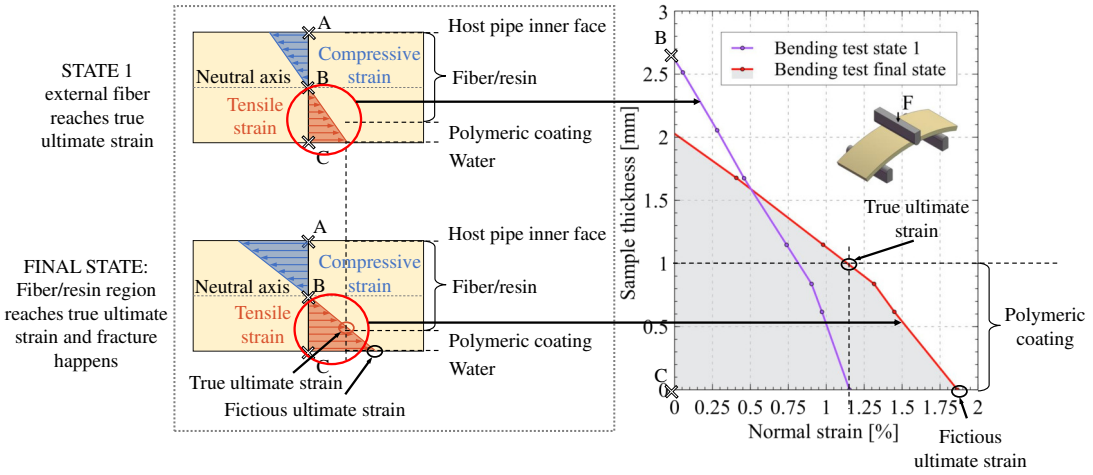

Figure 4.29: Strain distribution of a sample tested by the three-point bending test of curved samples captured an instant before failure occurred. Measurements made with experimental digital image correlation.

The fracture propagation system of curved CIPP samples subjected to bending was examined through the digital image correlation frames in Figure 4.30. A tensile failure is observed in Figure 4.30 (left). Furthermore, the fracture starts in the outer layer and propagates inwards, as expected in a bending test. For clarity, a second liner of 30 mm of thickness was used to visually magnify the crack propagation (see Figure 4.30b). Moreover, the same behavior was observed.

In both cases, two different behavior of the crack can be noticed. First, the outer layer corresponding to the polymeric coating was not entirely broken, as yielding can be appreciated. Second, a completely open fracture starting at the beginning of the fiber-resin region is identified. This phenomenon can be explained as both materials, the composite formed by the fiber-resin region and the polymeric coating, have different structural behaviors. It should be noted that the coating is responsible for avoiding fiber migration to the drinking water rather than contributing to the structural capacity of the liner. However, in the three-point bending test, the tensile properties of the outermost layer are evaluated. This layer corresponds to the polymeric coating in CIPP samples with a highly ductile behavior with high strain values compared to the fiber-resin region. Therefore, even if the ultimate tensile strain of the composite is reached (state 1 Figure 4.29), the polymer layer continues to deform. Thus, failure

(final state, Figure 4.29) occurs in the inner zone adjacent to the polymer layer when the composite reaches its tensile limit.

It should be noted that in the final state of Figure 4.29, the change in slope can be located around 1 mm from the bottom face in agreement with the polymeric coating dimensions. Moreover, the ultimate strain registered in the fiber-resin region is similar to the ultimate strain of the composite obtained in the tensile test of flat samples (1.15% and 0.89% respectively).

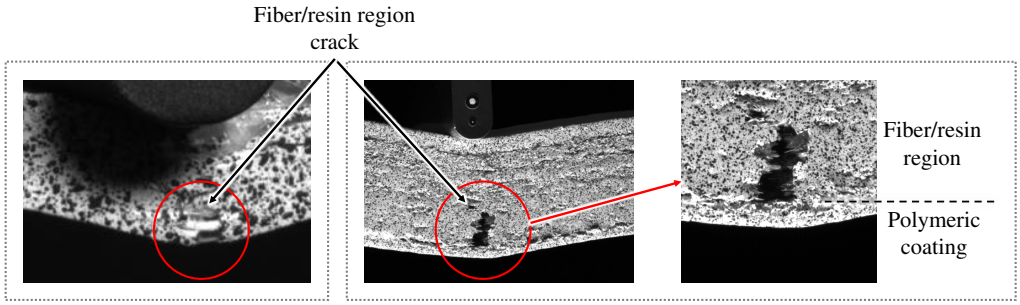

a) Fracture propagation of the studied liner

b) Example of fracture propagation using a 2nd liner with a thickness of 30 mm.

Figure 4.30: Analysis of the crack propagation observed in the performed three-point bending tests of curved samples assessed with the digital image correlation system.

4.4.2 Inner balloon pressure test validation

4.4.2.1 Numerical analysis: friction effect and tensile performance

The tensile behavior of the inner balloon pressure test was analyzed numerically prior to experimental tests. The simulations were performed with PVC samples as its well-known properties allowed the numerical model to be calibrated. Moreover, an experimental validation was also possible to be performed afterwards taking advantage of the isotropic properties of PVC to assess the hoop stress from flat samples cut in the longitudinal direction. In Figure 4.31, the tensile behavior of the IBPT was numerically compared with the pure tensile behavior of the tensile test ASTM D638 [101]. The stress-strain curves of both simulations were represented and nearly superposed. A minimum error under the curve of 0.25% was obtained. Consequently, the results demonstrate that the IBPT can reproduce the tensile behavior of the tensile test of flat samples ASTM D638 [101] in ring samples.

On the other hand, the friction effect was also analyzed in the simulations performed. It should be noted that at the beginning of the test, the ring sample is in contact with both upper and lower plates. Consequently, friction is generated. A high coefficient of friction will negatively affect the tensile performance of the sample as bending forces will appear. Thereby, the results from the IBPT should differ from the tensile test of flat samples.

In Figure 4.32, the numerical results show that the ring sample acquired a barrel shape when a considerable coefficient of friction (μ = 1) was applied. This barrel shape could also cause problems

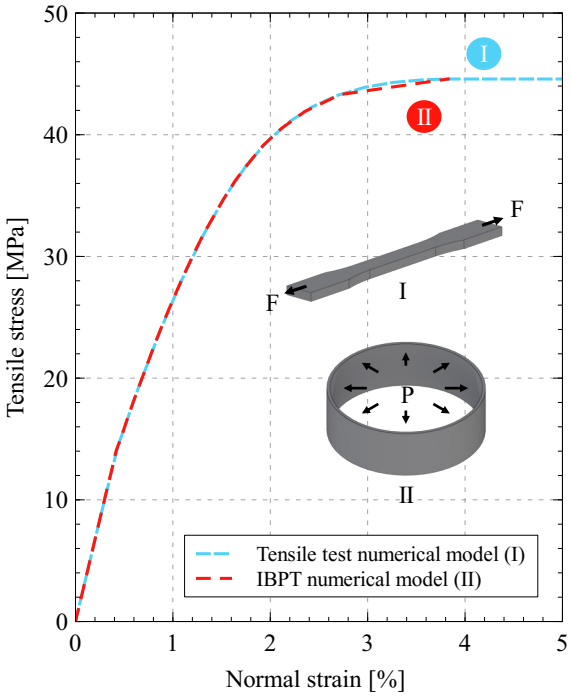

Figure 4.31: Tensile properties of the PVC assessed with the tensile test ASTM D638 [101] and the inner balloon pressure test.

in the operation of the test. The inner membrane could slip through the gap between the tooling and the samples generated by the barrel shape. However, the use of lubricant and the nature of the IBPT prevent having a considerable frictional coefficient. Two phenomena contribute to reducing friction during the test. First, the membrane also exerts pressure on the upper and lower plates of the tooling. Hence, a minimum gap between the ring sample and the plates is intended to be created. In addition, the shrinkage of the sample due to the Poisson effect also increases this gap. Consequently, the sample is subjected to a minimum frictional coefficient, and the behavior of the sample is closer to the frictionless model presented in Figure 4.32.

4.4.2.2 Experimental validation on PVC samples

The hypothesis regarding friction was validated through experimental results. Three strain gauges separated by 120° were installed in the hoop direction of the PVC ring sample. In Figure 4.33, the experimental stress-strain curves obtained with the IBPT (I, II, III) were compared with the numerical IBPT (IV) results and a representative curve of the experimental tensile test of flat samples ASTM D638 [101] (V). The results from the three strain gauges showed a similar trend. For example, 1.29% (channel 1), 1.51% (channel 2), and 1.16% (channel 3) of strain were obtained at 15 bar. The channel differences can be attributed to small misalignments of the strain gauges during installation. Thereby, the three strain gauges were not perfectly aligned due to the nature of the installation process.

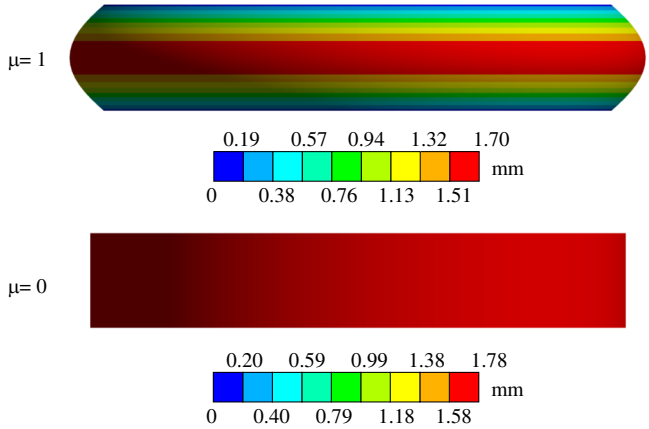

Figure 4.32: Analysis of the friction effect due to the boundary conditions that the inner balloon pressure test is subjected to.

However, the results are consistent, while a slight standard deviation of 0.18% at 15 bar was obtained.

On the other hand, the experimental tensile test results ASTM D638 [101] (V) are in good agreement with the IBPT numerical model (IV). It should be noted that a frictional coefficient of μ = 0.05 was implemented in the numerical model to reproduce the experimental behavior of the IBPT. Hence, the low coefficient of friction allows the tensile behavior of the tensile test of flat samples to be reproduced in the IBPT. In addition, a good agreement was also observed between the experimental results of the tensile test of flat samples and the numerical results of the IBPT.

However, some differences can be observed between the experimental IBPT (I, II, and III) and the experimental tensile test. A maximum deformation of 8% was reached in the tensile test, while the average maximum deformation of the three channels in the IBPT was 3.06%. The significant decrease in strain (161%) and the slight increase in stress (6.39%) can be attributed to the difference in load rate between both tests. As commented by some authors [118], the test speed has a severe impact on the mechanical properties measured. Consequently, the traditional laboratory tests are guided by international standards where test conditions are described. However, the IBPT is a novel test, and there are no international standards yet. Furthermore, in the tensile test ASTM D638 [101], the test speed was accurately controlled by the hardware of the universal mechanical machine, while in the IBPT, the test speed was manually controlled by the pressure valve of the pump. Nevertheless, the control of the pressure speed rate was not sufficiently gradual. Therefore, in the plastic region of the stress-strain curve, the material experienced a tearing process rather than smoothly yielding. This phenomenon can be noticed in Figure 4.33 by the wavy lines that appear at the end of all three curves in the experimental IBPT test (I, II, and III). Besides this difference, the tensile behavior observed on the tensile test of flat samples is reproduced in the ring samples. Thus, the IBPT is presented as a potential test to asses the hoop tensile performance of a cylindrical sample as an alternative to the traditional bending test of curved samples.

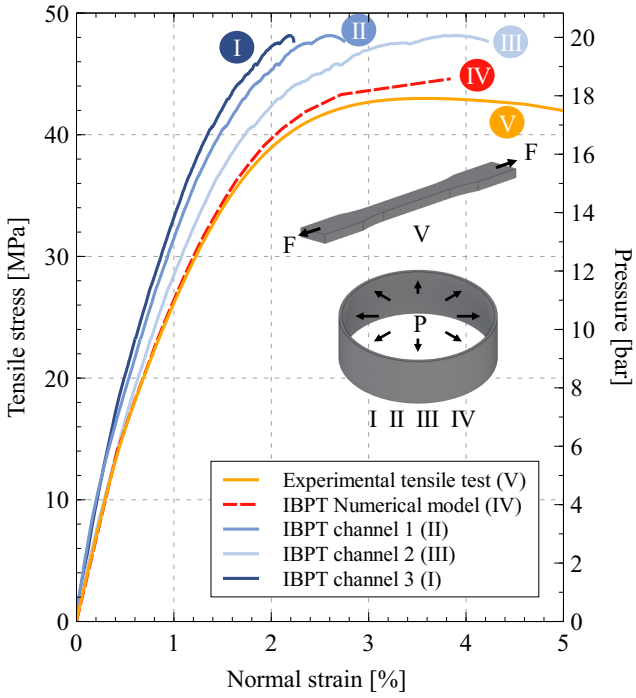

Figure 4.33: Experimental validation of the IBPT with PVC samples.

4.4.2.3 Experimental validation on CIPP composite samples

The IBPT was also experimentally validated with CIPP samples. A CIPP liner is more complex than the perfectly homogeneous PVC samples. Moreover, this test was designed to evaluate the tensile properties of installed liners without the shortages detected in the three-point bending test of curved samples.

In Figure 4.34, the tensile performance of the liner described in Section 4.3.1 was evaluated with the IBPT (curves I and II) and compared to the tensile test of flat samples ASTM D638 [101] (curve III). As in the previous section, slight differences can be found between strain channel readings that are attributed to the small misalignments on strain gauge installation. Moreover, the sample was capable of freely expanding as with the PVC samples. However, although similar ultimate strains were identified in both tests (tensile test 0.89%, IBPT ch1 0.77%, IBPT ch2 1.03%), important differences can be found in terms of stress. The ultimate hoop stress obtained in the IBPT was 201.4 MPa, while an ultimate stress of 150.9 MPa was reached in the tensile test, indicating that the ultimate stress obtained with the IBPT was 1.34 times higher.

Nevertheless, the curing process can explain the differences in stress observed in Figure 4.34. It should be noted that although the samples were impregnated by the manufacturer and came from the same liner, the curing process of ring and flat samples was different. The ring samples were extracted from an installed liner cured under field conditions by a certified installer. Moreover, an internal pressure was

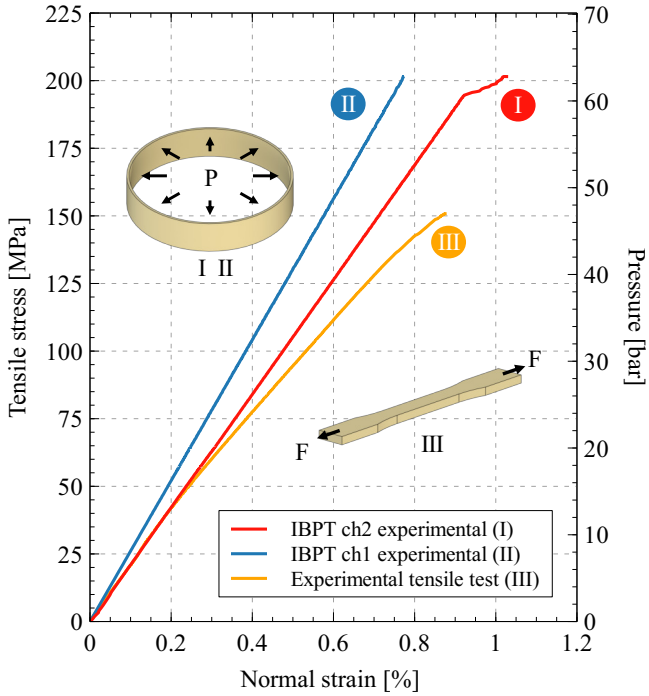

Figure 4.34: Experimental validation of the IBPT with CIPP composite samples.

applied during the curing process. In contrast, the flat samples were cured in the laboratory, attempting to reproduce the conditions of the certified equipment but without the possibility of applying a uniform pressure equivalent to on-site installation. The SEM microscope images from Figure 4.35 revealed that the samples from the liner installed on-site (d-f) were perfectly cured and presented no apparent installation defects. Furthermore, the glass fibers were well impregnated and surrounded by resin, as can be appreciated in Figure 4.35f. However, the laboratory-cured samples (a-c) presented a lack of resin in some regions. The resin's absence was noticed between the glass fiber bundles rather than inside the bundles. Hence, these defects were attributed to the absence of compaction pressure during the laboratory curing process, and it was considered responsible for the decrease in tensile strength of the flat samples.

Finally, in Figure 4.36, the tensile performance of the same liner was evaluated by three different tests. Representative stress-strain curves of the IBPT, the three-point bending test of curved samples, and the tensile test of flat samples were depicted in Figure 4.36. For clarity, the graph on the right displays the magnified data for the first third of the curve. As it can be appreciated, the Young Modulus obtained in the three tests was in good agreement. A flexural Young Modulus of 21.1 GPa was obtained in the bending test after the curvature correction, 20.5 GPa was deducted from the tensile test, and finally 21.2 GPa of Young Modulus was obtained from the IBPT. In the three cases, the Young Modulus was calculated on the strain range 0.05% to 0.25% according to their respective standards.

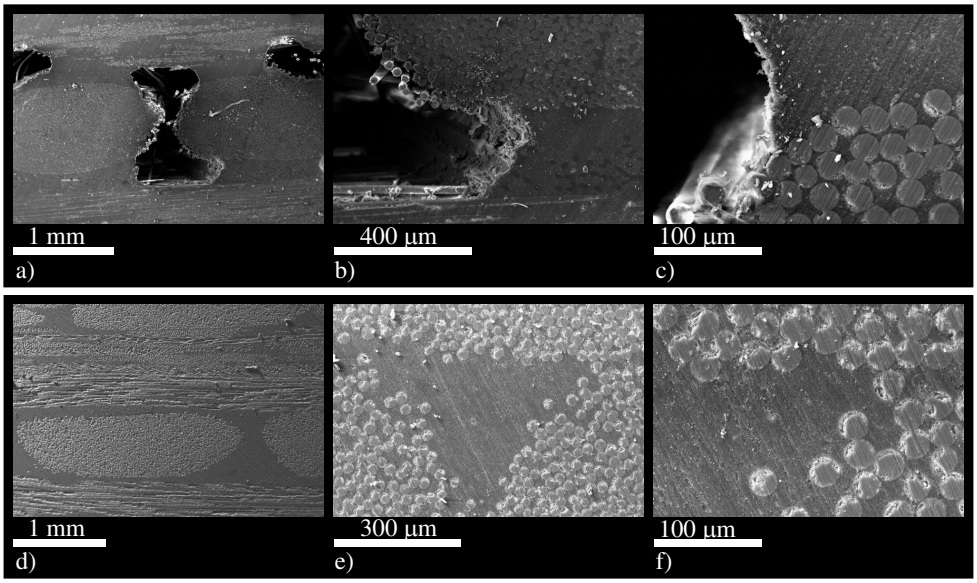

Figure 4.35: SEM images of the cross-section of a sample cured in laboratory conditions without compression pressure (a, b, and c) and cured by a certified installer with internal pressure (d, e, and f).

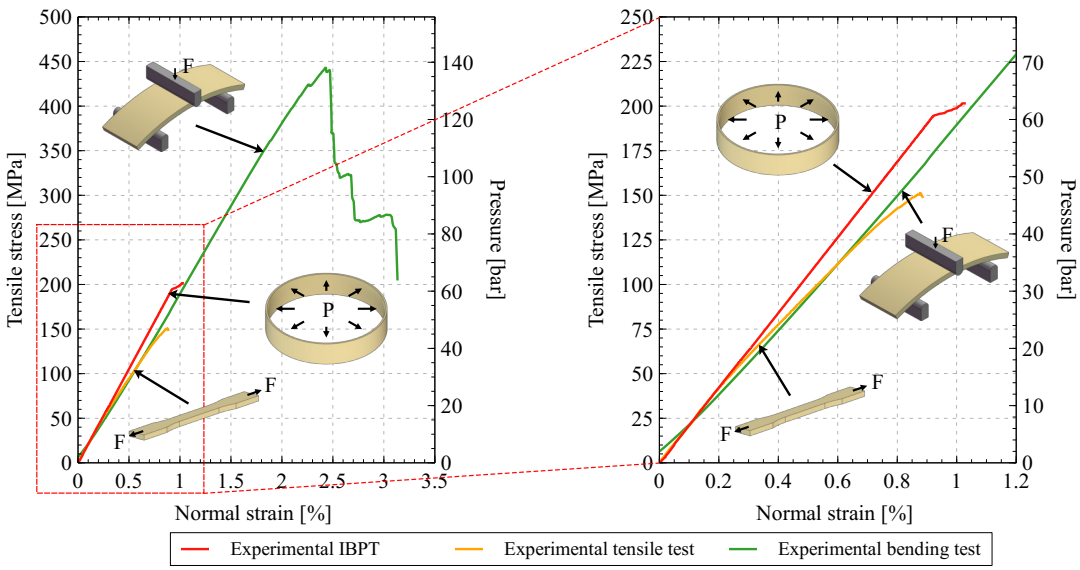

Figure 4.36: Tensile strength performance of a CIPP liner assessed with the three-point bending test, the IBPT, and the tensile test of flat samples.

However, as anticipated, significant differences were found in the ultimate stress of the liner. The IBPT and the tensile test showed a closer value, although the tensile test samples presented impregnation defects discussed in the previous paragraphs. Nevertheless, the samples tested by the IBPT and the three-point bending test were extracted from the same installed liner that presented no impregnation defects appreciated in Figure 4.35c, d, and f. However, the ultimate tensile stress obtained with the

bending test of curved samples was 443.4 MPa, corresponding to a burst pressure of 138.2 bar, while a value of 201.4 MPa (65.4 bar) was derived from the IBPT. It should be noted that the IBPT tries to reproduce the working conditions of inner pressure that an installed liner is subjected to, and it was previously demonstrated that it reproduces the tensile behavior of the tensile test. Thus, the more than two times burst pressure obtained in the three-point bending test can be considered wrong and negatively contribute to the structural safety of the installed liner. It is important to note that determining higher burst pressure values in a quality control test can lead to future failures, as the real burst pressure will be much lower than expected. Hence, the experimental evidence highlighted the unsuitability of the three-point bending test to assess the hoop tensile performance of a CIPP liner.

5

New design approach for semi-structural CIPP liners

This chapter focuses on optimizing the design of semi-structural liners in pressure pipes. First, the design procedures described in current standards are analyzed. Then, a mathematical model approach is proposed. Moreover, full-scale test results used to develop both, the numerical and the mathematical model are presented.

5.1 Design practices

The design of a liner has an important role in the mechanical properties of a rehabilitated pipe. According to the existing standards (ASTM F1216 [8], UNE 53929 [1],...) and AWA [117], CIPP liners are classified into gravity, semi-structural and structural. The state of the host pipe will define the type of liner to use. Gravity liners are used to stop the host pipe's small inner corrosion or deterioration. They are mainly used in gravity pipes where the host pipe is structurally sound and can withstand inner and outer loads. The liner does not have a structural capacity. Then, semi-structural liners are installed in damaged host pipes that preserve enough structural capacity to withstand external loads. However, the liner must perfectly fit the host pipe, and it will be subjected to inner loads, especially in the host pipe's cracks or voids. Finally, structural liners have a higher percentage of fiber and can withstand internal and external loads. Thus, the host pipe is considered to be heavily damaged and has no contribution.

Determining the state of a buried pipe can be challenging. Inner cracks, inner corrosion, or voids can be detected through TV camera robot examination. Nevertheless, outer corrosion and outer defects are difficult to detect. Pressure pipes are subjected to heavy inner loads due to pressure. Thus, choosing the incorrect liner can end in disaster. Due to this scenario of uncertainty, structural liners have been chosen to be installed in pressure pipes with small damage where a semi-structural liner could work perfectly. Structural liners are the strongest in terms of mechanical properties and, at first glance, should be the best option regarding safety. However, structural liners are thick, heavy, and have a small maneuverability compared to semi-structural liners. Hence, the installation process is complex, and defects exposed in Chapter 3 can arise. In pressure pipes, a small defect can heavily reduce the mechanical properties of an installed liner. Consequently, liner failures have been reported in some projects [43, 44]. Therefore, liner oversizing can negatively affect the safety of the rehabilitated pipe. Thus, the optimization of liners became crucial to improve the installation efficiency.

To address the challenge exposed in this chapter, first, the design equations for semi-structural liners were analyzed. Oversizing of the liner has been detected when analytical equations of the hole criterion defined by ASTM F1216 [8] and UNE 53929 [1] are used. Especially when host pipe holes are not circular. Then, a mathematical model has been developed to optimize the thickness of a semi-structural liner by the hole's criterion. A numerical model validated with a full-scale test was used to build the mathematical model.

5.2 Semi-structural design equations

According to ASTM F1216 [8] and UNE 53929 [1], the liner thickness of a semi-structural liner is subjected to four calculation criteria, and the greatest thickness obtained is used.

a) Hydraulic loads: the CIPP liner is designed to withstand hydraulic loads due to groundwater. According to UNE 53929 [1], the minimum groundwater loads (P) to consider is 0.015 MPa. The

liner must be thick enough to avoid buckling and is calculated according to Eq. 5.1.

$$t = \frac{IDx}{1 + \sqrt[3]{\frac{2KE_LC}{P(1-\nu^2)N}}} \tag{5.1}$$

Where t is the liner thickness (mm), IDx the mean inside diameter of the host pipe (mm), K the recommended enhancement factor of the soil and existing pipe adjacent to the new pipe according to ASTM F1216 [8] and experimentally developed by Aggarwal and Cooper (1984) [17], E_L the long-term tensile modulus (MPa), C the ovality reduction factor, P the groundwater load (for UV-cured fiberglass liners (MPa), ν the Poisson's ratio (0.3 is recommended) and N is the safety factor (N_{min}=2).

b) Host pipe ovality: first, the ovality reduction factor must be calculated to calculate the thickness due to the ovalization of the host pipe (Eq. 5.2). Second, a quadratic equation (Eq. 5.3) must be solved. Finally, Eq. 5.4 is used.

$$\begin{aligned} C &= \left(\frac{[1 - \frac{\Delta}{100}]}{[1 - \frac{\Delta}{100}]^2} \right)^3 \\ \Delta &= 100 \left(\frac{IDM - IDx}{IDx} \right) \end{aligned} \tag{5.2}$$

Where Δ is the ovality of the host pipe (%) and IDM is the maximum inside diameter of the host pipe (mm).

$$1.5 \frac{\Delta}{100} \left(1 + \frac{\Delta}{100} \right) SDR^2 - 0.5 \left(1 + \frac{\Delta}{100} \right) SDR - \frac{\sigma_L}{PN} = 0 \tag{5.3}$$

$$SDR = \frac{IDx}{t} \tag{5.4}$$

Where SDR is the dimension ratio of the liner, and σ_L is the long-term bending stress (MPa).

c) Holes: CIPP liners must withstand inner pressure loads across any hole of the host pipe. According to ASTM F1216 [8] and UNE 53929 [1], the liner can behave as a circular flat plate (Eq. 5.6) fixed at the edge and subjected only to transverse pressure when Eq. 5.5 is satisfied. Otherwise, the liner is calculated as a ring-in-tension (Eq. 5.7) as there was no host pipe. It should be noted that all holes are treated as circular.

$$\frac{d}{IDx} \leq 1.83 \left(\frac{t}{IDx} \right)^{0.5} \tag{5.5}$$

Where d is the hole diameter (mm).

$$t = \frac{IDx}{1 + \sqrt{5.33 \left(\frac{IDx}{d} \right)^2 \frac{\sigma_L}{NP_I}}} \tag{5.6}$$

Where P_I is the inner pressure (MPa).

$$t = \frac{IDx}{2\left(1 + \frac{\sigma_{TL}}{NP_I}\right)} \tag{5.7}$$

Where σ_{TL} is the tensile hoop stress of the liner (MPa).

d) Negative pressure: the rehabilitated pipe can be subjected to a vacuum in some specific cases. In this case, the liner must be designed as a gravity pipe with the external hydraulic pressure increased by the negative pressure.

5.2.1 Non-circular holes approach

ASTM F1216 [8] and UNE 53929 [1] consider holes as perfectly circular. However, Figure 2.19 reveals that real holes are not perfectly circular and, in some cases, are far from being circular (Figure 2.19f, g, and i). Consequently, the liner thickness calculated with the above analytical equations should be oversized. Some authors [54, 58] have realized the importance of considering the shape of the hole to optimize the liner thickness and mentioned ASTM F2207[62]. It is a standard limited to steel gas pipes that presents a mathematical model for sizing semi-structural liners subjected to non-circular hole shapes. The model is also limited to orthotropic elastomer-fabric type liners where the shear stiffness is non-existent or very small compared to the hoop and longitudinal stiffness of the liner. For pressure pipes (between 6.9 and 20.7 bar), the model requires that the steel pipe retain its structural capacity, and therefore, the liner is designed considering the inner pressure.

ASTM F2207[62] model is based on analytical equations. It considers the deformed shape of the liner spanning through a hole as a circular arc.

The model uses two failure criteria. The worst must be used to define the thickness of the liner.

a) The maximum stress criterion: failure occurs when the liner reaches its maximum admissible stress in the longitudinal or hoop direction (see Eq. 5.8).

$$\begin{aligned} \frac{\sigma_h}{\sigma_{uh}} &= 1 \\ \frac{\sigma_l}{\sigma_{ul}} &= 1 \end{aligned} \tag{5.8}$$

Where σ_h is the hoop stress (MPa), σ_{uh} the ultimate hoop stress of the liner (MPa), σ_l the longitudinal stress (MPa), and σ_{ul} the ultimate longitudinal stress of the liner (MPa),

b) The interactive stress criterion: in the ASTM F2207[62] model, failure can occur before the hoop or longitudinal ultimate stresses are reached. Thus, the liner fails due to the interaction between longitudinal and hoop stresses (see Eq. 5.9).

$$\left(\frac{\sigma_h}{\sigma_{uh}}\right)^2 - \frac{\sigma_h \sigma_l}{\sigma_{uh}^2} + \frac{\sigma_l}{\sigma_{ul}} = 1 \tag{5.9}$$

Moreover, holes are defined by two dimensions: hoop length and longitudinal length of the hole. Therefore, the hole is treated as a rectangular shape that could better fit ellipse or groove holes than the circular approach used in ASTM F1216 [8] and UNE 53929 [1]. However, further investigation may be required to have an even more realistic approach to the hole's shape, as shown in Figure 5.13.

Although the mathematical model presented has been validated by at least two commercial tests, ASTM F2207 [62] is conservative and also requires experimental tests.

5.2.2 Proposed model approach

A novel approach through a mathematical model was developed to calculate the thickness of a liner when circular or not circular holes are detected in the host pipe. The model implements the Gradient Boosting Regression method from the Scikit-learn library.

The Gradient Boosting Regressor

The Gradient Boosting algorithm is used to build a forward stage-wise fashion model by optimizing a loss function. It is known for excellent results in prediction speed and accuracy. Moreover, it is widely used by many authors [90, 119–122] by producing the best results from Kaggle competitions to scientific research.

This estimator combines the predictions from multiple decision trees to generate the final predictions. In each stage, a regression tree is fit on the negative gradient of the given loss function. It is important to note that the nodes in every decision tree take a different subset of data for selecting the best split. Thus, every decision tree is different. Thereby, the whole data behavior is considered in the final predictions. The new tree considers the error accumulated from previous trees to improve the prediction. Thus, every successive decision tree is built on the errors of the previous trees (see Figure 5.1).

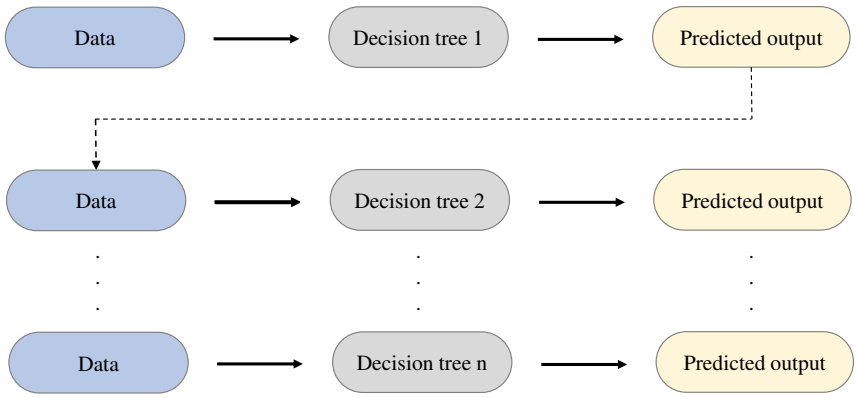

Figure 5.1: General idea of the working process of the Gradient Boosting Regressor.

In the mathematical model used for semi-structural liners thickness prediction, a first base model was built with the training data. Moreover, initial equal weights were assigned to all data variables, and an initial decision stump was built. It should be noted that weights can take values from 0 to 1.

After the first prediction, an error was calculated, representing how far from the optimal solution the predicted value was. Then, according to the error obtained, the weights were modified. The weight was increased for values with big errors, while the weight was reduced for correct predicted values. Consequently, the next model (model 1) was built considering a larger number of weak values. Thus, successive models were built and combined to generate a final strong model (see Figure 5.2).

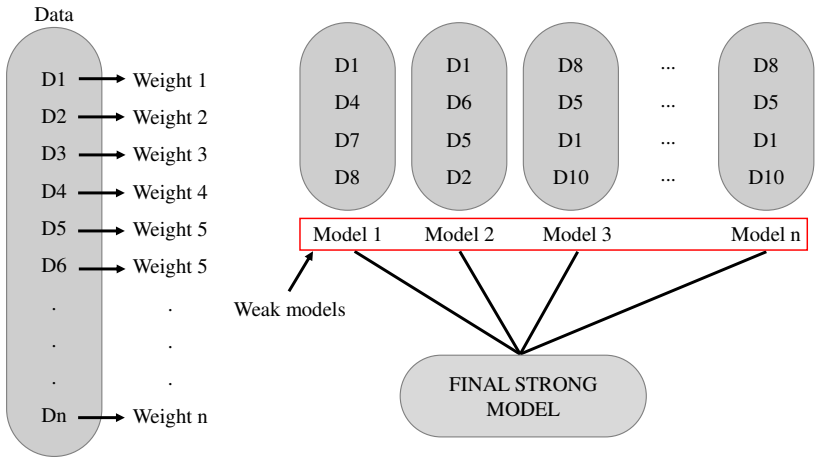

Figure 5.2: Scheme representing the architecture of the mathematical model.

The base model was created according to Eq. 5.10.

$$F_0(x) = \underset{\gamma}{argmin} \sum_{i=1}^{n} L_s(y_i, \gamma) \tag{5.10}$$

Where F_0 is the base model, L_s is the loss function, y_i is the real value, γ is the predicted value, and the operator $argmin$ is used to find a minimum in the Loss function. The minimum is found by differentiating the loss function with respect to γ and then solving the equation equal to 0.

Then, the pseudo residuals errors are calculated according to Eq. 5.11.

$$r_{im} = -\left[\frac{\partial L_s(y_i, F(x_i))}{\partial F(x_i)}\right]_{F(x)=F_{m-1}(x)} \quad for\ i = 1, ..., n. \tag{5.11}$$

Where r_{im} is the pseudo residual errors (intermediate error), $F(x_i)$ is the previous model and m the number of distribution trees.

Afterwards, the output values of each leaf of the decision tree were calculated according to Eq. 5.12. However, there is the possibility that one leave gets more than one residual. In those cases, the average of all residuals of the same leave was performed to obtain a final output.

$$\gamma_m = \underset{\gamma}{argmin} \sum_{i=1}^{n} L_s(y_i, F_{m-1}(x_i) + \gamma h_m(x_i)) \tag{5.12}$$

Where $h_m(x_i)$ is the decision tree made on residual and γ_m is the output value of a particular leave.

Finally, the predictions of the previous model were updated according to Eq. 5.13.

$$F_m(x) = F_{m-1}(x) + \nu_m h_m(x) \tag{5.13}$$

Where $F_m(x)$ is the new prediction, $F_{m-1}(x)$ is the previous prediction, ν_m is the learning rate and $h_m(x)$ is the decision tree made on residuals.

The learning rate is the parameter that determines the contribution of each individual tree in the ensemble. It controls how much information from each tree is incorporated into the final prediction. Thereby, it acts as a scaling factor for the predictions made by each individual tree. A lower learning rate means that each tree's contribution is reduced, while a higher learning rate allows each tree to have a stronger impact on the final model.

The learning rate can have values from 0 to 1. A low learning rate can help to prevent the algorithm from missing a local minimum. However, more steps should be taken to achieve a good solution. On the other hand, a high learning rate can lead to fast convergence and require fewer trees, but there is the risk of missing a local minimum.

Huber Loss function

There are two basic functions that are usually used in predictive models: the mean squared error and the mean absolute error.

According to Eq. 5.14, the mean squared error consists of calculating the square of the difference between the predictive and the real value across the whole data set. It is a good option when the outliers are desired to be considered in the model. The square of the function gives huge errors when an outlier appears. Thus, the MSE puts a larger weight on these errors. However, a single big outlier can be responsible for having a weak model.

$$MSE = \frac{1}{n}\sum_{i=1}^{n}(y_i - \gamma)^2 \tag{5.14}$$

According to Eq. 5.15, the mean absolute error consists of calculating the absolute value of the difference between the predicted and the real value across the whole data. Therefore, all errors will be weighted on the same linear scale. Thus, the outliers will not have an extra effect on the model; consequently, a weak model can be obtained.

$$MAE = \frac{1}{n}\sum_{i=1}^{n}|y_i - \gamma| \tag{5.15}$$

Hence, the MSE is a good option for learning from outliers, while the MAE is good for ignoring them. However, considering only one of them can lead to a weak model. The Huber Loss function (Eq. 5.16) combines both, the MSE and the MAE to take the best part of each one. Thus, it offers a compromise

solution and gives the outliers some weight but not too much, leading to a strong model.

$$L_\omega(y,\gamma) = \begin{cases} \frac{1}{2}(y-\gamma)^2 & for\ |y-\gamma| \leq \omega \\ \omega|y-\gamma| - \frac{1}{2}\gamma^2 & \text{otherwise} \end{cases} \tag{5.16}$$

Where ω defines the switch from a quadratic to a linear error function.

5.3 Methodology

5.3.1 Materials

The liner described in the previous chapter was used in the experimental and numerical tests presented in this chapter.

The mechanical properties of the liner used and obtained from experimental tests described in the previous chapters are presented in Table 5.1:

Table 5.1: Mechanical properties of the liner.

Property	Value	Property	Value
Short-term Young's modulus (E)	20600 MPa	Short-term flexural stress (σ_f)	440 MPa
Long-term Young's modulus (E_L)	10300 MPa	Long-term flexural stress (σ_{fL})	220 MPa
Short-term tensile hoop stress (σ_T)	204 MPa	Poisson's ratio (ν)	0.3
Long-term tensile hoop stress (σ_{TL})	102 MPa		

5.3.2 Full-scale test

A full-scale test was conducted using a reinforced concrete pipe located at the outliers of Barcelona, Spain. The pipe was disconnected from the pipeline a few weeks before this study began.

Liner one described in section 5.3.1 was used to rehabilitate 6 m of the buried reinforced concrete pressure pipe of DN 400 mm. In addition, one extra meter of cast iron pipe was added at both ends to fit both blind flanges with the ends of the reinforced concrete pipe. Therefore, eight meters of liner were installed. The setup test was divided into three monitoring sections: downstream, middle section, and upstream (see Figure 5.3 and Figure 5.4)

The reinforced concrete pipe had a thickness of 70 mm and two layers of reinforcement that can be appreciated in Figure 5.6b. The upper half of the middle section was unburied for monitoring tasks. Prior to installation, the host pipe inspection revealed it was in good condition, and no sign of severe damage was observed (see Figure 5.5). Therefore, before the installation of the liner, three holes of ø150 mm separated by 0.5 m were drilled to impair the performance of the original pipe and to install strain gauges onto the liner (see Figure 5.6). It should be noted that after the installation of the liner, the outer protector UV plastic shown in Figure 5.6c was removed to install strain gauges directly onto the liner (see Figure 5.6d).

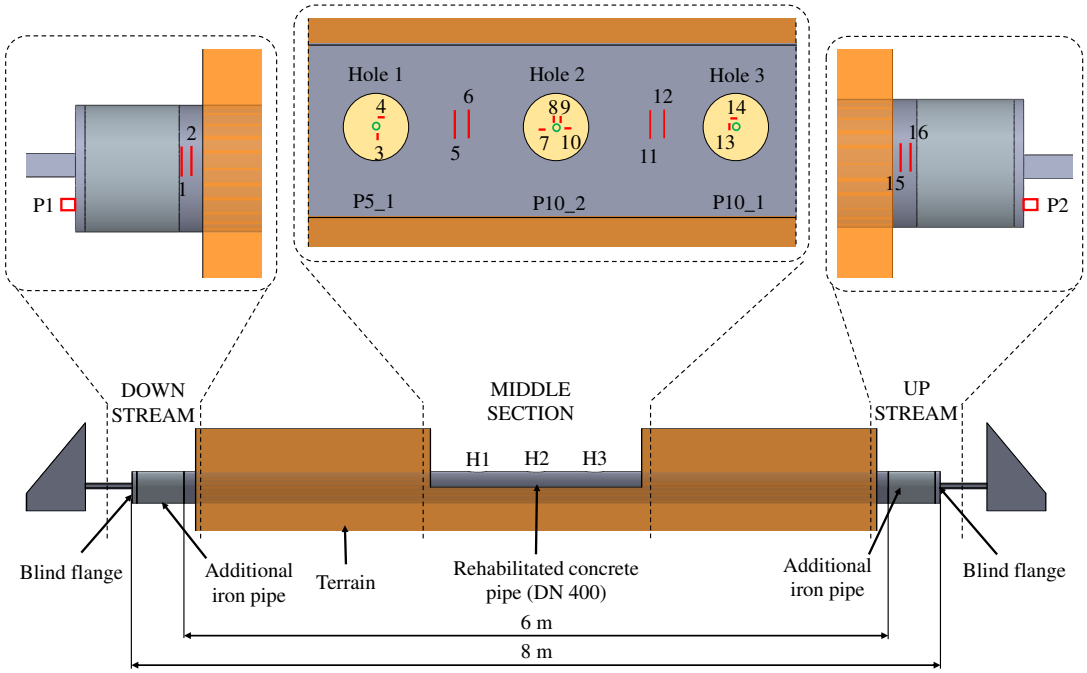

Figure 5.3: Schematic representation of the full-scale test setup showing the location of sensors and components employed in the test.

a) Downstream view b) Middle section c) Upstream view

Figure 5.4: Field view of the experimental setup and testing environment during the full-scale on-site test: downstream view (a), middle section of the tested pipe showing severe damage (b) and upstream view (c).

On the other hand, a setup of HEA beams and railway ends was built up to fix the host pipe endings (see Figure 5.7). The setup was designed to withstand more than 25 bar in a DN 400 with a robust safety factor. The HEA beams were welded to the railway ends. Then, each railway end was fixed to its respective reinforced concrete foundation (see Figure 5.7a) of the upstream and downstream sections. A close look at the setup is shown in Figures 5.7d-e. Then, the liner was installed (see Figure 5.8a). A close look at the inside of the rehabilitated host pipe before and after the installation of the liner is shown in Figure 5.8b-c. Finally, current commercial seals were installed.

a) Inside view b) Entrance view c) General view

Figure 5.5: Host pipe used in the full-scale test: inside view (a), entrance view and general view.

a) Circular holes drilled in the middle section

b) Detail view of hole 3

c) Before UV protective plastic removal

d) After UV protective plastic removal

Figure 5.6: Damage inferred to the host pipe prior to the rehabilitation: middle section view showing three circular holes of ø150 mm (a), detailed view where the host pipe thickness can be appreciated (b), detailed view of hole 3 after the rehabilitation process, with the CIPP liner preserving the UV protective plastic (c), and detailed view of hole 3 after the rehabilitation process, with the UV protective plastic removed for monitoring tasks (d).

The rehabilitated host pipe was monitored with 16 strain gauges, three displacement transducers, and two pressure sensors (see Figure 5.9b). Eight strain gauges were installed directly onto the liner through the pipe holes. Strain gauges 3, 8, 9, and 13 were installed in the hoop direction, and strain gauges 4, 7, 10, and 14 were installed in the longitudinal direction. In addition, strain gauges 1, 2, 5, 6, 11, 12, 15, and 16 were installed on the reinforced concrete pipe in the hoop direction to monitor the host pipe according to the installation procedure shown in Figure 5.10. Three displacement transducers were held in the center of each hole. Two temperature sensors were also set to calibrate the strain gauges.

Finally, two pressure sensors, Wika A-10, were installed at the lowest part of the ends of the pipe (see Figure 5.9a). HBM Quantum X MX840 B, Quantum X MX1615 B, and CatmanEasy AP software collected data from the full-scale test (Figure 5.11). Finally, a 40 bar Rothenberger RP Pro III pump was used to feed the test with hydraulic pressure until 25 bar. A scheme of the setup of the test is shown in Figure 5.3.

a) Foundation-reinforced concreting

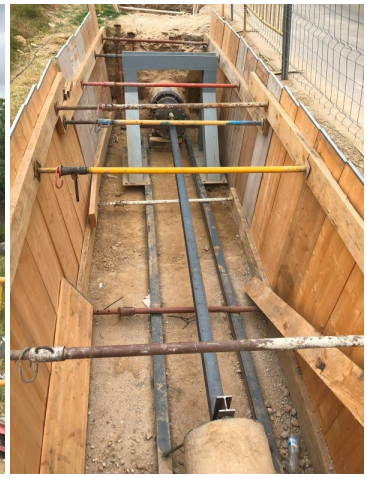

b) Downstream view

c) Overall work

d) Upstream view

e) Welded HEA beams

Figure 5.7: Detailed setup for fixing the blind flanges to withstand 25 bar in a DN 400 mm pipe: foundation-reinforced concreting (a), detail of the downstream view (b), general view of the work (c), detail of the upstream view (d), and detail view of the welded HEA beams (e).

a) Liner introduction

b) Inside view before the rehabilitation

c) Inside view after the rehabilitation

Figure 5.8: Installation of the CIPP UV liner: introduction of 8 m of liner (a), inside view of the reinforced concrete host pipe with the additional iron pipe before the installation of the liner (b) and inside view after the rehabilitation (c).

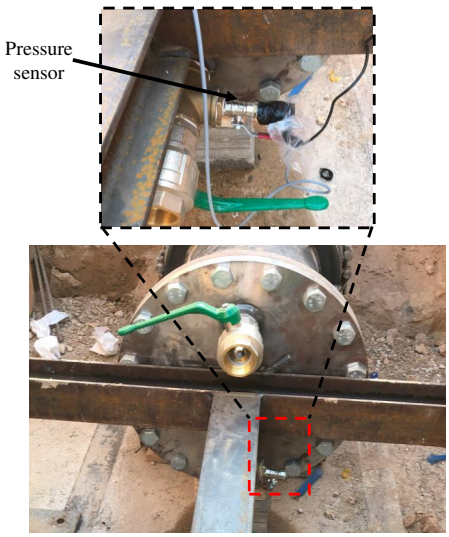

a) Upstream pressure sensor location

b) Deployment of all sensors used

Figure 5.9: Sensors installed to monitor the host pipe and the installed CIPP liner. Detailed view of the upstream pressure sensor location (a) and deployment of all sensors used: strain gauges, displacement, and pressure sensors (b).

a) Surface cleaning b) Surface preparation c) Strain gauges installed

Figure 5.10: Concrete's hoop strain gauges installation procedure: surface cleaning (a), surface preparation (b) and strain gauges installed (channels 15 and 16) (c).

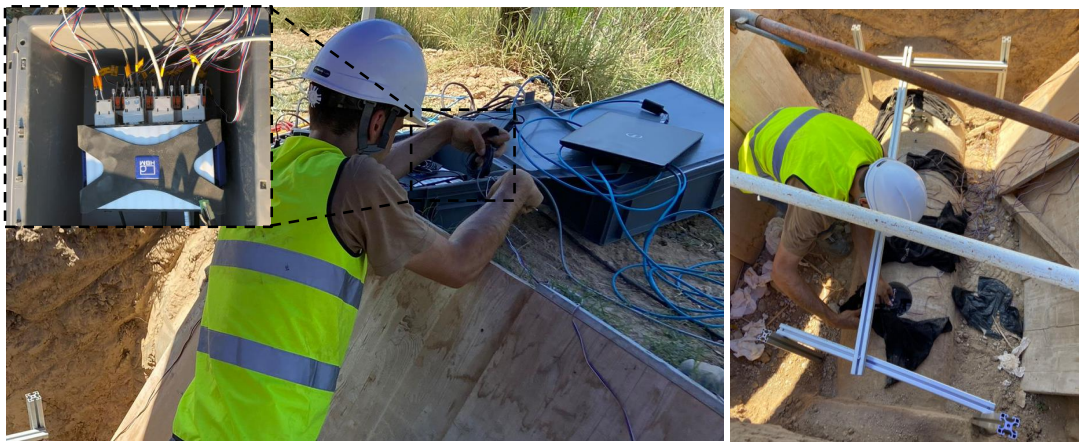

Figure 5.11: Installation of the middle section liner's strain gauges under challenging field conditions (July, Barcelona).

5.3.3 Numerical model

The full-scale test was used to validate a static structural implicit Ansys model. The central hole (Hole 2) was represented. Prior numerical models indicated that the liner behavior was identically reproduced in the three holes. Only the upper longitudinal section was modeled (see Figure 5.12). The host pipe had an inner diameter of 400 mm and an ovalization of 1.28%. The liner used had a thickness of 6 mm.

A cylindrical coordinate system was set. The y-axis was defined in the hoop direction, the z-axis in the longitudinal direction, and the x-axis in the radial direction (see Figure 5.12). The model was meshed using a 20-node higher-order Solid 186 element. An element size of 0.5 mm was used to mesh the liner.

The liner used in the full-scale test was defined as an orthotropic material with the mechanical properties presented in Table 5.2.

Table 5.2: Mechanical properties of the liner used in the numerical model.

Young's modulus (GPa)			Shear modulus (GPa)			Poisson's ratio		
E_x	E_y	E_z	τ_{xy}	τ_{xz}	τ_{yz}	ν_{xy}	ν_{xz}	ν_{yz}
11	20.6	20.6	7	7	9	0.3	0.3	0.3

The mechanical properties of the host pipe were defined according to the Ansys database. The reinforced concrete had a Young's modulus (E) of 30 GPa, a Poisson ratio (ν) of 0.18, and a shear modulus (τ) of 12.71 GPa.

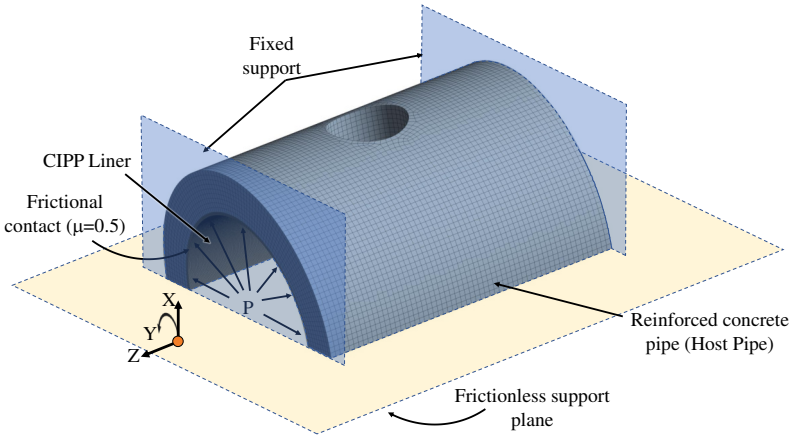

Figure 5.12: Schematic representation of the geometry and boundary conditions implemented in the numerical model.

A frictional contact (μ) of 0.5 was defined between the outer face of the liner and the inner face of the host pipe in agreement with the simulations performed by [58]. A fixed support plane was set on the end faces of the rehabilitated pipe. As shown in Figure 5.12, a frictionless support was also set. Then, an inner pressure of 25 bar was applied. Finally, the vertical displacement of the liner at the center of the hole, the longitudinal and hoop strains of the liner, and the host pipe's hoop strain were obtained.

5.3.4 Mathematical model

The parameters presented in Table 5.3 were used in the mathematical model according to the Scikit-learn library.

The mathematical model developed must be previously fed with multiple representative points to consider the maximum number of cases. The numerical model adjusted with the full-scale test results was used to generate different scenarios of holes in the host pipe. First, the circular holes described in the UNE 53929 [1] and ASTM F1216 [62] standards were simulated.

Then, the perfect circumference was degenerated, passing through ellipse-shaped holes and reaching linear grooves. Finally, the linear grooves were stretched to obtain more complex shapes such as

Table 5.3: Parameters used to adjust the mathematical model.

Parameter	Value	Parameter	Value
Learning rate	0.05	Min samples leaf[3]	15
Number of estimators[1]	3000	Loss[4]	Huber
Max depth	4	Max features[5]	sqrt
Random state[2]	5		

[1] Number of decision trees corresponding to the number of boosting stages to perform
[2] It controls the random seed given to each tree estimator at each boosting iteration.
[3] The minimum number of samples required to be at a leaf node.
[4] Loss function.
[5] The number of features to consider when looking for the best split..

angular grooves (see Figure 5.14). It should be noted that the four classes of simulated holes were inspired by holes detected in real pipes (see Figure 2.19).

In the mathematical model, a hole is defined by four parameters (see Figure 5.13):

- Hole dimension in the longitudinal direction (a_1)
- Hole dimension in the hoop direction (b_1)
- Hole area
- Hole perimeter

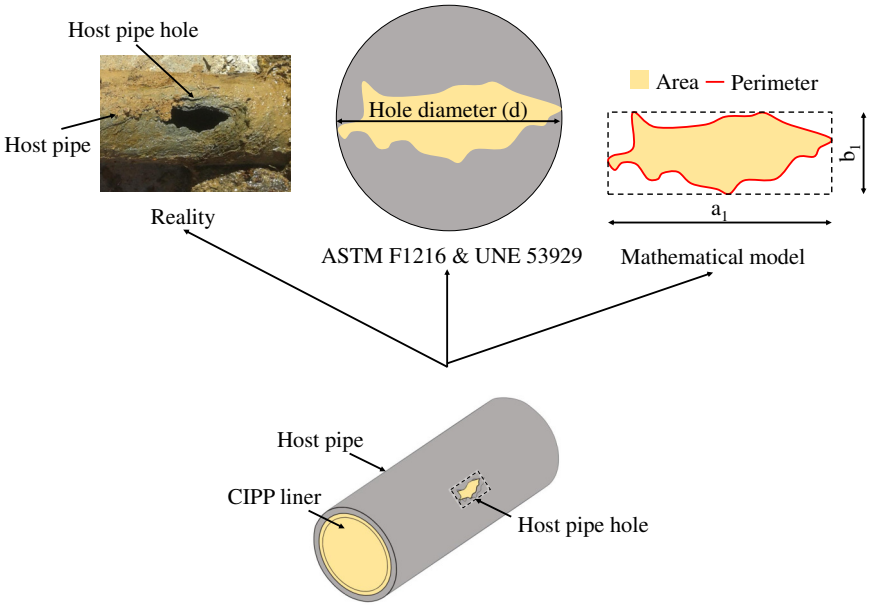

Figure 5.13: Comparison of the hole definition in the mathematical model with the definitions outlined in UNE 53929 [1] and ASTM F1216 [8].

Figure 5.14 shows the combinations of holes simulated with the numerical model. A total of 14,646 scenarios were simulated: 23% circular holes, 20% ellipses, 25% linear grooves, and 33% of angular

grooves. 80% of the simulations were used to build the model, while 20% were kept unseen by the model for its validation.

In the validation process, first, each class of hole (circular, ellipse, linear, and angular grooves) was studied separately. Finally, a global validation was performed using data from the four mixed classes.

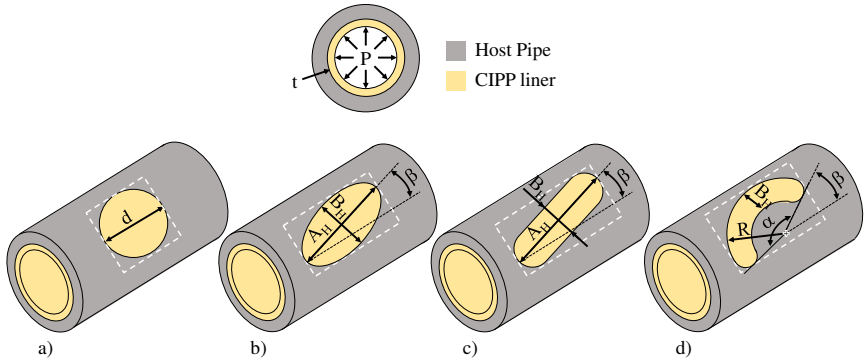

	Circular (a)		Ellipse (b)		Linear groove (c)		Angular groove (d)	
Parameter	Levels	Range	Levels	Range	Levels	Range	Levels	Range
d (mm)	37	40-400	-	-	-	-	-	-
A_H (mm)	-	-	9	80-360	6	50-300	-	-
B_H (mm)	-	-	6	(0.15-0.9)·A_H	4	10-40	4	90-180
β (°)	-	-	3	0-90	5	0-90	2	30-40
α (°)	-	-	-	-	-	-	5	0-90
R (mm)	-	-	-	-	-	-	4	150-350
P (bar)	10	5-25	3	5-25	5	5-25	5	5-25
t (mm)	9	2-10	6	2-7	6	2-7	6	2-7
Total	3330		2916		3600		4800	

Figure 5.14: Types of simulated holes in the study.

There are two options when using the mathematical model. (see Figure 5.15)

- **Option one:** the liner thickness, the four hole parameters (a_1, b_1, area and perimeter), and the inner pressure of the pipe are defined as input values. Then, the maximum stress of the liner is obtained.
- **Option two:** the ultimate stress of the liner, the four hole parameters (a_1, b_1, area and perimeter), and the inner pressure of the pipe are defined as input values. Then, the thickness of the liner is obtained. This option can be used when designing a semi-structural liner.

The mathematical model is limited to pipes with an inside diameter of 400 mm and liners with the mechanical properties of the liner described in Section 5.3.3 in the elastic region.

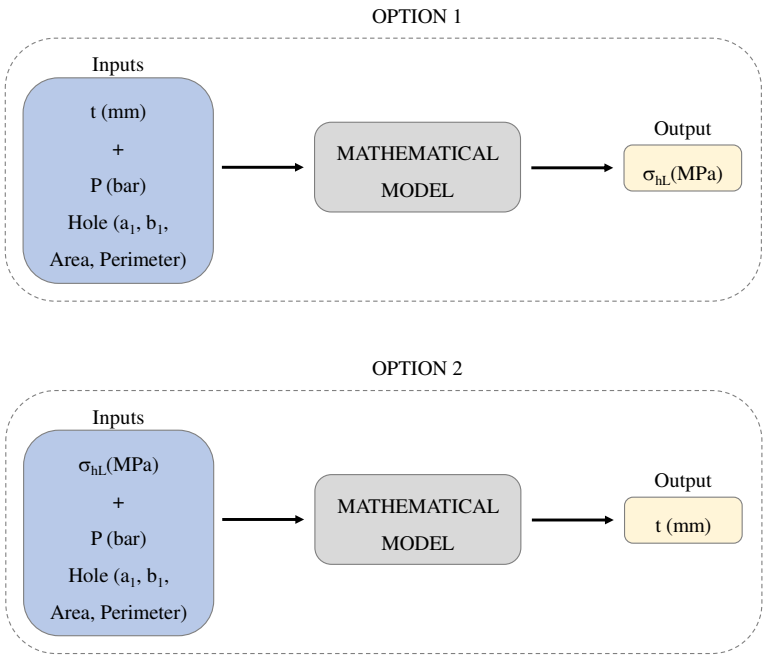

Figure 5.15: Schematic representation of the usage of the mathematical model proposed.

5.4 Results and discussion

5.4.1 Semi-structural liner design

This section focuses on identifying the dominating calculus criterion in the design of a semi-structural liner in accordance with UNE 53929 [1] and ASTM F1216 [8]. The effect of the hydraulic groundwater loads, ovality, and host pipe holes on the final thickness of the liner is analyzed in Figures 5.16-5.18. Identifying the dominant criterion is the first step for optimizing the thickness of the liner. Then, the liner will be lighter, nimble, and consequently easier to install.

Different scenarios of the host pipe were contemplated to demonstrate the importance of optimizing the hole criterion equations from UNE 53929 [1] and ASTM F1216 [8] to reduce the final thickness of a liner. Host pipes with an ovality of 0% to 10% were used in the analytical calculations. Higher percentages of ovality were not considered. According to UNE 53929 [1] and ASTM F1216 [8], CIPP rehabilitation is only allowed when the ovality of the host pipe is equal or less than 10%. The analysis was conducted for a range of inner pressures (P_I) between 5 and 20 bars. No external loads were considered as the study was focused on semi-structural liners.

Circular holes were also considered. A relationship between the hole's diameter and the inside diameter of the host pipe (d/D) between 0 and 1 was contemplated. According to ASTM F1216 [8] and UNE 53929 [1], the following factors were used in the hydraulic loads criterion. A recommended

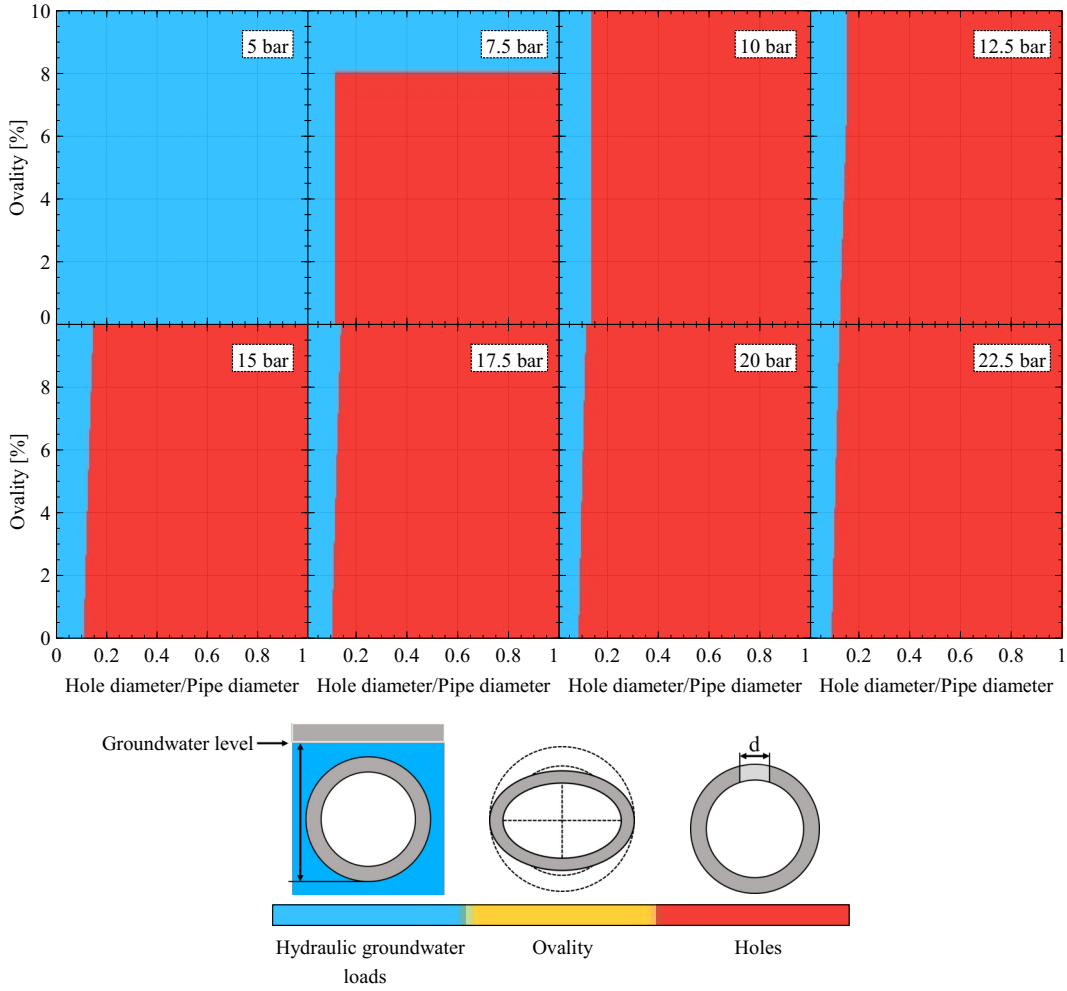

Figure 5.16: Dominant design criterion analyses for semi-structural liners. Liner 1 used in the full-scale test.

enhancement factor of the soil and the existing pipe adjacent to the new pipe (K) of 7, a minimum groundwater load (P_{min}) of 0.015 MPa, and a minimum safety factor (N) of 2 were used.

Three liners of different mechanical properties were used to extract solid conclusions. First, the liner's mechanical properties described in section 5.3.1 were used. Then, the mechanical properties of a second liner were set according to the minimum specifications dictated by UNE 53929 [1] (table 13) for fiber liners cured by UV and installed in pressure pipes. This second liner exhibited a long-term Young's modulus (E_L) of 2500 MPa, a long-term flexural stress (σ_{fL}) of 51.5 MPa, and a long-term tensile stress (σ_{TL}) of 10.5 MPa. Lastly, the mechanical properties of a third liner in service were used. The third liner had a long-term Young's modulus (E_L) of 3000 MPa, a long-term flexural stress (σ_{fL}) of 40 MPa, and a short-term tensile stress (σ_{TL}) of 17.5 MPa. Liner 1 was used in the full-scale test. Liner 2 corresponds to the weakest liner that can be installed according to UNE 53929 [1]. Finally, liner 3 was installed seven

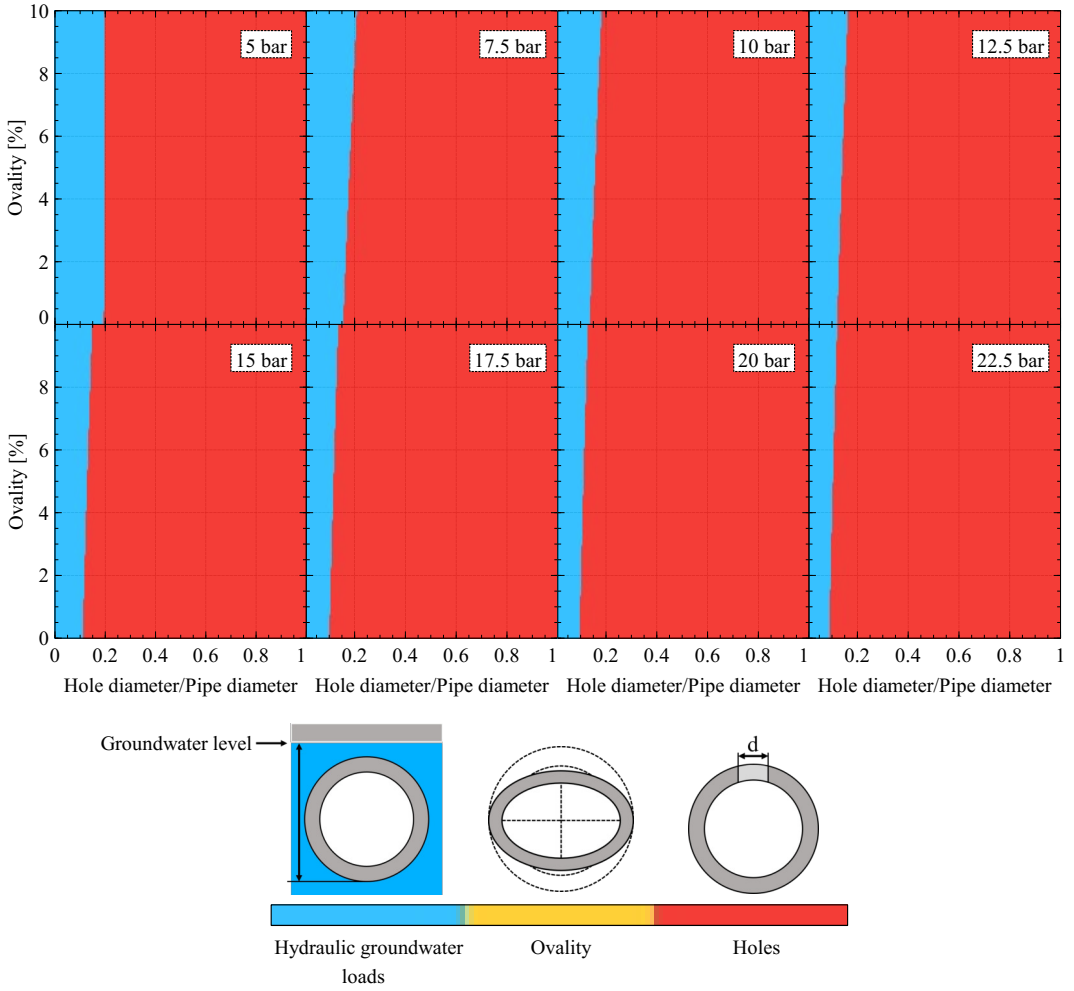

Figure 5.17: Dominant design criterion analyses for semi-structural liners. Liner 2. Minimum mechanical properties required by UNE 53929 [1].

years ago and is still in service. According to Figures 5.16-5.18, the hole's criterion in red is leading the final thickness of the liner in most of the studied cases. However, the groundwater loads criterion is dominant in liner one when a pressure of 5 bar was applied (see Figure 5.16). This phenomenon observed only in liner one is attributed to the high performance of this liner. It should be noted that a long-term ultimate hoop stress (σ_{hL}) of 110 MPa and an ultimate flexural stress (σ_{fL}) of 220 MPa were registered for liner one while the minimum mechanical properties required by UNE 53929 [1] are 10.5 MPa and 51.5 MPa respectively. Thereby, liner one is over those values by 10.5 and 4.3 times. While both mechanical properties, σ_{hL} and σ_{fL} have an impact on the ovality and the hole's criterion, according to Eq. 5.1, they have no impact on the groundwater loads criterion.

Moreover, the three studied liners present the same behavior as the pressure rises. As deducted from Figures 5.16-5.18, the blue-shaded area representing the groundwater loads criterion diminishes as

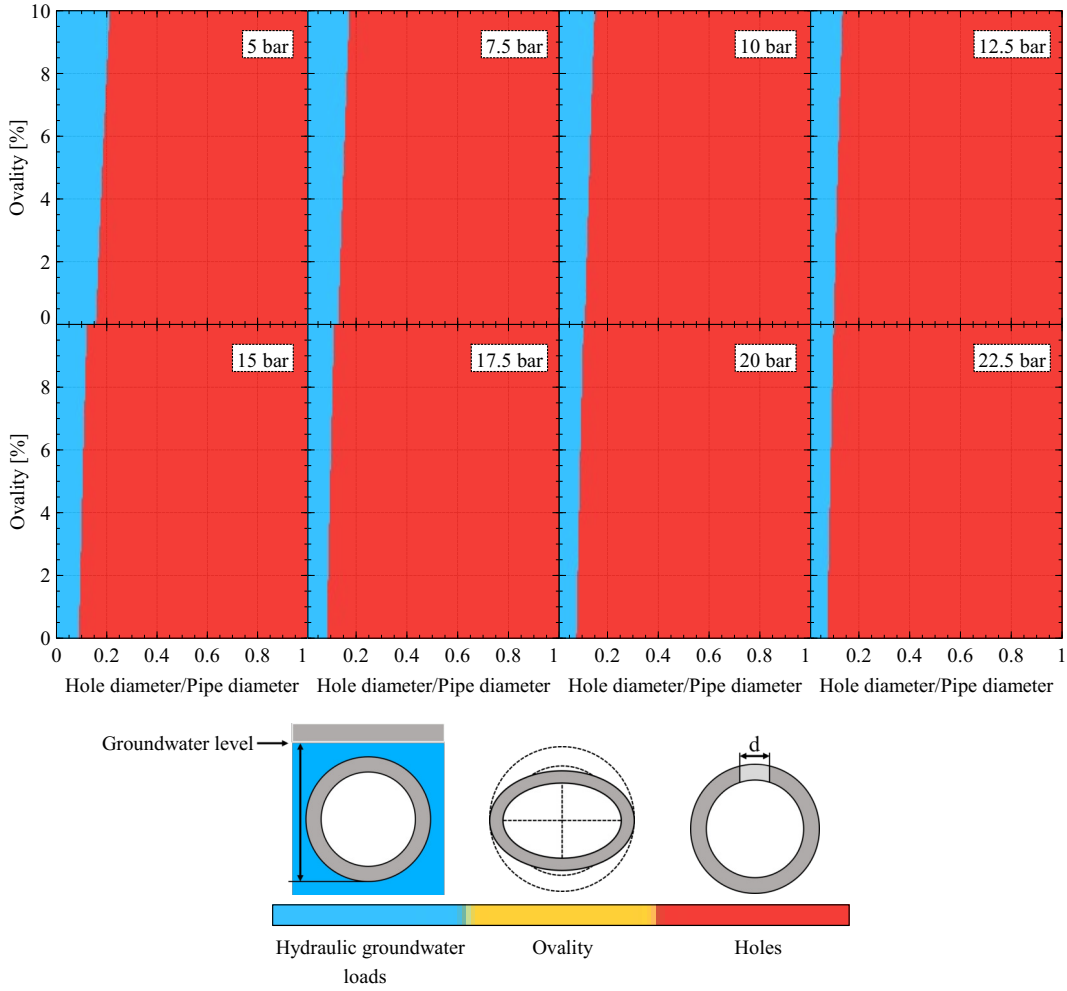

Figure 5.18: Dominant design criterion analyses for semi-structural liners. Liner 3. In service liner.

pressure increases, giving precedence to the hole's criterion. Thereby, it can be concluded that the hole's criterion will govern most pressure pipes with host pipe holes. Nevertheless, in the presence of small host pipe holes (d/D<0.15), the final thickness of the liner is governed by the groundwater loads criterion. In these circumstances, the flexural stresses generated by the hole's cantilever are less relevant than the hydraulic groundwater loads.

On the other hand, the absence of the ovality criterion is noticed in all of the studied cases. Analyzing the ovality criterion Eq. 5.2, Eq. 5.3 and Eq. 5.4, it can be deduced that the ultimate flexural stress of the three studied liners is high enough to avoid mechanical problems from ovality. Even when the host pipe presents a 10% of ovality, which is the maximum value allowed by UNE 53929 [1], the ovality criterion does not define the final thickness of the liner.

Therefore, results from Figures 5.16-5.18 indicate that improving the hole's criterion is crucial to reduce

the thickness of semi-structural liners. Consequently, a comprehensive investigation of the calculation in the hole's criterion is needed to enhance the CIPP semi-structural liner technology and boost the overall efficiency of liners.

Analysis of the hole design criterion

In this study, the author has identified three procedures that could be used to calculate the thickness of a liner subjected to host pipe holes: the ASTM F1216 [8] and UNE 53929 [1], the ASTM F2207 [62] and finite elements simulations procedures.

ASTM F1216 [8], UNE 53929 [1], and ASTM F2207 [62] rely on analytical equations to model the behavior of liners spanning through host pipe holes. However, these equations are still approximations, while covering the widespread types of holes is a complex task. Both ASTM F1216 [8] and UNE 53929 [1] only address circular holes. According to the numerical model depicted in Figure 5.19, circular holes are the worst case, indicating that liners calculated by ASTM F1216 [8] and UNE 53929 [1] could be optimized when the host pipe holes are not circular.

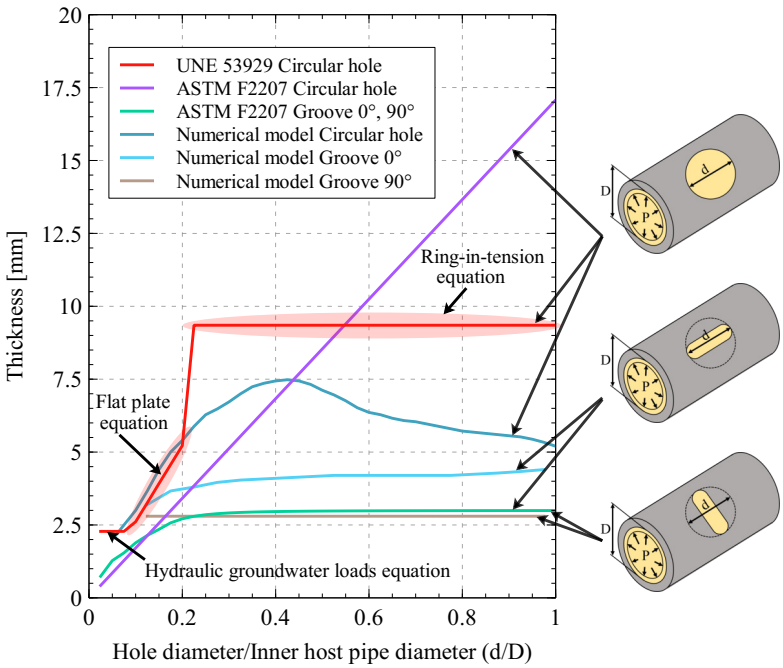

Figure 5.19: Impact of host pipe holes on CIPP liners design.

In Figure 5.19, the three existing procedures for calculating the thickness of a liner with host pipe holes are compared. Circular and groove holes were represented. The change of equation (Eq. 5.6 to Eq. 5.7) in the ASTM F1216 [8] and UNE 53929 [1] procedure can be perfectly appreciated in Figure 5.19. On the one hand, the numerical model reveals that the flat plate model of Eq. 5.6 perfectly defines the behavior of the liner when holes in the host pipe are small (d/D<0.2). However, the liner is not governed by ring tension after the relation of Eq. 5.5 is achieved. The ring-in-tension equation (Eq. 5.7) does not

consider the host pipe's residual structural capacity. Nevertheless, the numerical model indicates a reduction of the liner's thickness between 19% and 44% for d/D>0.2 when the residual structural capacity of the host pipe is not neglected. Therefore, the liner does not behave as a ring-in-tension as already advanced (He et al. 2019 [63]).

Non-circular holes were also analyzed. It should be noted that the ASTM F1216 [8] and UNE 53929 [1] standards calculate the non-circular holes as if they were inscribed into a circumference (see Figure 5.13). Thus, the non-circular host pipe hole is considered as a bigger circular hole, adopting a conservative attitude. For instance, Figure 5.19 shows that in linear groove holes, a thickness of 9.35 mm was obtained when the ring-in-tension equation was used. However, maximum thicknesses of 2.99 mm for hoop grooves and 4.4 mm for longitudinal grooves were obtained when the numerical model was used. Thus, a more significant reduction in the thickness of the liner can be achieved when the hole is not circular. It should be noted that the direction in which the linear groove is defined is important. The longitudinal hole length is the most critical parameter as there is a more extensive area of the hole subjected to hoop stress, according to Allouche et al. (2008) [54] findings with rectangular and elliptical shaped holes.

The thickness obtained with the mathematical model of ASTM F2207 [62] was also represented in Figure 5.19. Circular holes, longitudinal linear grooves (0°), and hoop linear grooves (90°) were calculated. Results were compared against the numerical simulations. Results reveal that the ASTM F2207 [62] model was in good agreement with the numerical model when linear longitudinal grooves were calculated. However, an error of 47% was detected when linear grooves were rotated 90°, indicating some weaknesses in the mathematical model of ASTM F2207 [62]. Furthermore, in circular host pipe holes, the thickness of the liner obtained severely differs from the numerical model analysis. The parabolic curve shape obtained in the numerical model is not reproduced. The differences observed could be attributed to the assumptions made by the ASTM F2207 [62] model. The liner used presented a non-zero shear modulus of 7-9 GPa. Additionally, the deformed shape of the liner spanning through host pipe holes of different shapes did not behave as a circular arc. It should be noted that the model presented in ASTM F2207 [62] is based on the analytical equations of a circular arc for the deformed shape.

The deformation shapes of a linear groove, a circular, and an angular groove hole are represented in Figure 5.20. As can be observed, the resultant deformations do not have an exact circular arc shape. The deformation in circular holes has the shape of a dome with a non-constant radius. Non-circular holes, such as linear and angular grooves, exhibit even more deviation from a completely circular arc, resulting in a virtually flat area at the center.

5.4.2 Developed model

5.4.2.1 Validation of the numerical model through a full-scale test

Figure 5.22 presents a representative result from the full-scale test. Safety and mechanical limitations were considered, and the tests were conducted until a maximum pressure of 25 bar. To accurately

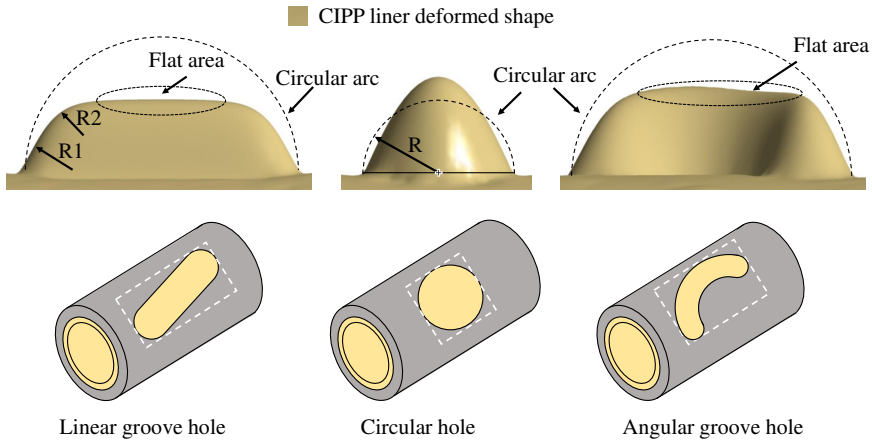

Figure 5.20: Comparison of deformed shapes: numerical model vs. circular arc assumption by ASTM F2207 [62] for CIPP liner installed in a host pipe with holes.

measure strains, strain gauges were strategically positioned in the most critical direction, the hoop direction. The strain gauge distribution can be observed in Figure 5.3. Surprisingly, the concrete strain gauges (see Figure 5.22a) recorded no strain readings, despite the reinforced concrete pipe exhibiting significant damage with three ø150mm holes (see Figure 5.6). This phenomenon suggests that the mechanical behavior of the full-scale test was predominantly influenced by the excellent performance of the liner, which contained a substantial amount of glass fiber in the hoop direction. Consequently, this discovery reinforces the idea that the fiber content in the liner can be reduced, making installation easier while still leveraging the residual structural capacity of the host pipe.

As shown in Figure 5.22c, the analysis of the experimental data demonstrates a linear connection between strain and pressure in the hoop direction. However, an accommodation phase was seen in the longitudinal direction (see Figure 5.22b), showing that the liner was not completely in touch with the host pipe during the full-scale test. This phenomenon can be attributed to the slight shrinkage reported by some authors [44, 45] due to the UV curing process. Consequently, at the beginning of the test, the liner was not in contact with the top of the host pipe (see Figure 5.21).

The analysis of the experimental data reveals a clear linear relationship between strain and pressure in the hoop direction, as depicted in Figure 5.22c. However, in the longitudinal direction (see Figure 5.22b), an initial accommodation phase was observed, indicating the liner was not perfectly in contact with the host pipe in the full-scale test. Some authors [44, 45] reported a slight resin shrinkage during the UV curing process that could explain the lack of contact between the liner and the host pipe at the top. Hence, the behavior of the liner can be characterized as a ring-in-tension until the liner makes complete contact with the host pipe. Consequently, while the hoop strain increases, the longitudinal strain remains near zero until the liner establishes contact and spreads over the host pipe hole. The accommodation process observed in Figure 5.22b concludes at approximately 5 bar of pressure, which corresponds to a vertical displacement of the liner of 0.25 mm, as shown in Figure 5.22d. The initial gap of 0.25 mm was intentionally incorporated into the numerical model. The results shown in Figure 5.22b

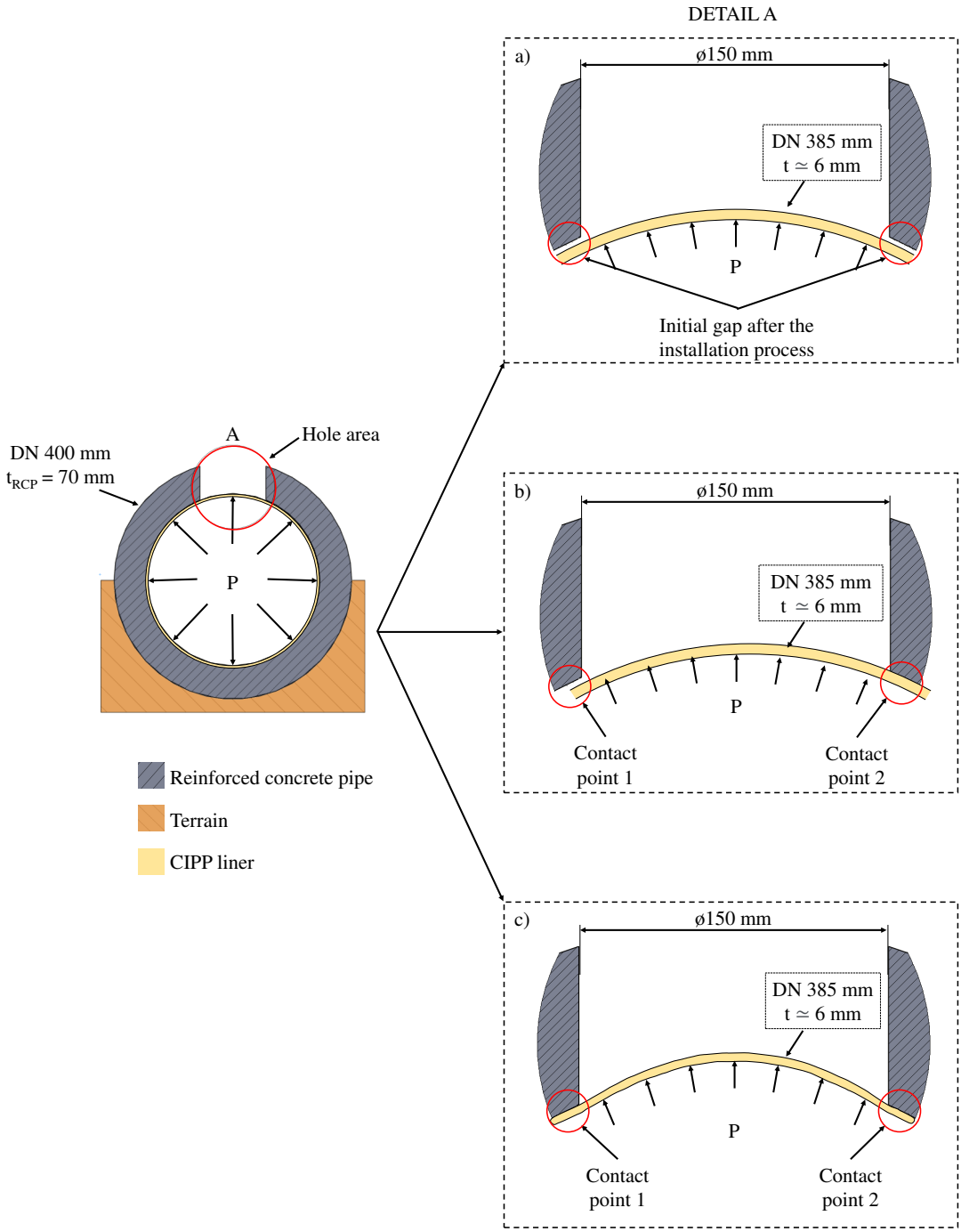

Figure 5.21: Schematic representation of the behavior observed in the full-scale tests. a) Initial gap of 0.25 mm detected after the installation process. b) Fully contact between the liner and the host pipe established at 5 bar of pressure. c) Liner spanning through the host pipe hole at P>5 bar.

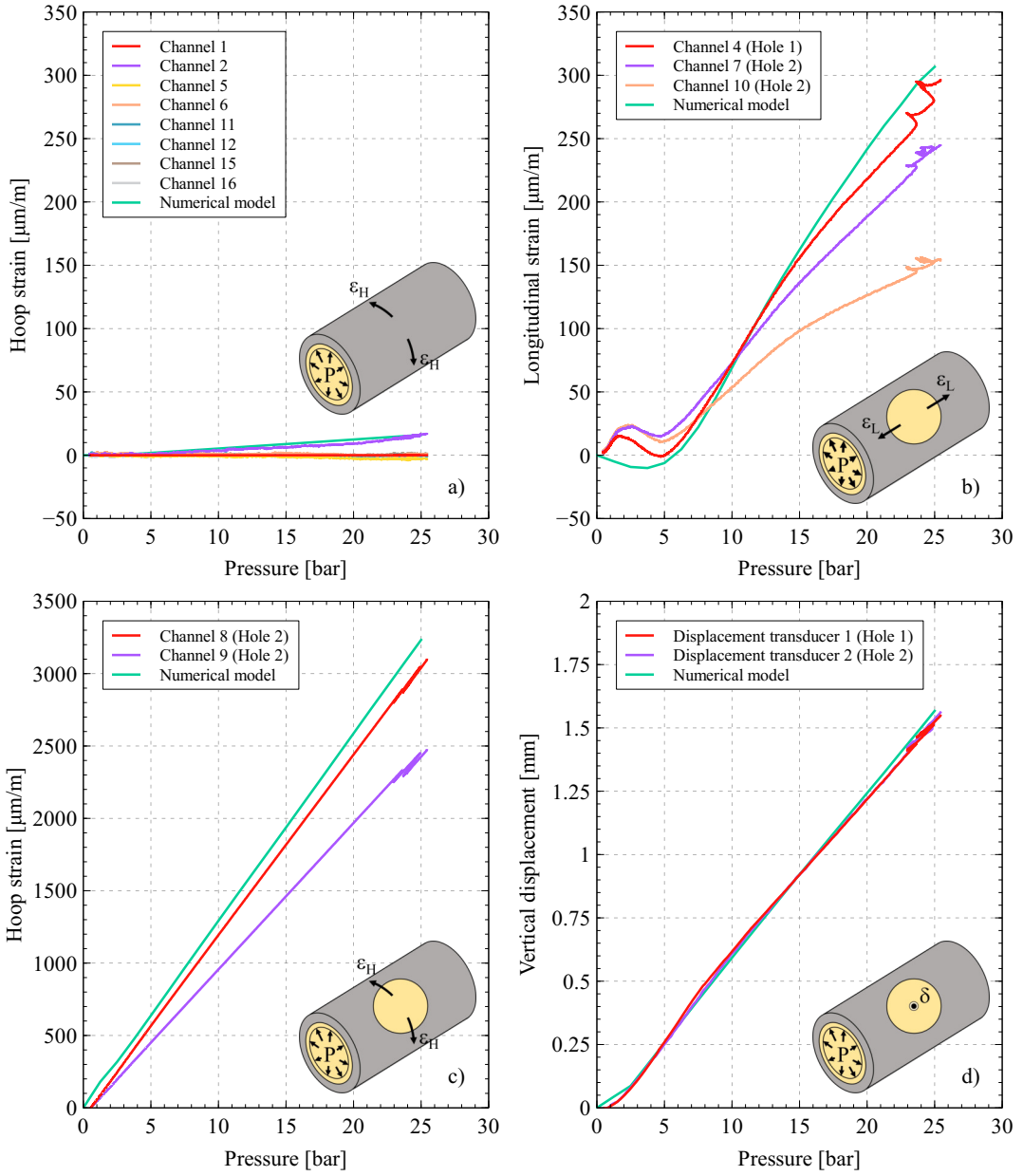

Figure 5.22: Results of the full-scale test: a) Concrete's hoop strain. b) CIPP liner's longitudinal strain. c) CIPP liner's hoop strain. d) Vertical displacement of the liner at the center of the hole.

demonstrate a strong agreement between the numerical model and the full-scale test, with the initial accommodation in the numerical model being faithfully replicated in the longitudinal strain.

In addition, Figure 5.22d illustrates the behavior of the vertical displacement sensors $P5\_1$ and $P10\_2$, positioned at the centers of holes one and two, respectively. These sensors exhibited identical behavior

throughout the test, with registered vertical displacements of $\delta = 1.55$ mm and $\delta = 1.56$ mm, respectively. The numerical model also demonstrated good agreement with the experimental results, yielding a vertical displacement of 1.57 mm at the center of the hole.

Figure 5.22b and Figure 5.22c show discrepancies in the strain readings obtained from various strain gauges. As can be observed in Figure 5.23, the numerical model revealed that strain can vary a lot along the hole. For example, the hoop strain can vary 1127 μm/m from two points separated by 15 mm. Strain gauge installation in field conditions and onto curved surfaces and narrowed spaces is always a challenge. Consequently, strain gauges were installed separately by a minimum of 20 mm. Moreover, installing strain gauges in different holes at the same exact location is difficult. Hence, the experimental strain differences reported were obtained. For example, channel 9 reported a maximum hoop strain (ε_h) in hole 2 of 2471 μm/m, whereas channel 8 reported a value of 3096 μm/m, which is a 25% increase. The distance between these two strain gauges was 20 mm.

A similar pattern was observed in the longitudinal direction, where strain gauges installed in the same hole (channel 7 and channel 10) exhibited a noticeable strain difference, with channel 7 recording a strain that was 94 μm/m higher than channel 10. In contrast, the longitudinal strains (ε_L) measured in different holes, Hole 1 (channel 4, ε_L = 295 μm/m) and Hole 2 (channel 7, ε_L = 243 μm/m), displayed similar behavior because a closer strain location reading was achieved.

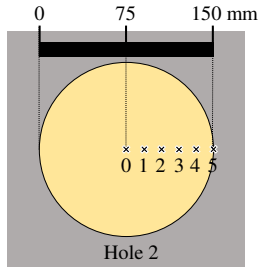

Point	ε_h (μm/m)	Level (mm)
0	5648	75
1	4521	90
2	2906	105
3	1214	120
4	617	135
5	38	150

Figure 5.23: Hoop strain variation analysis along hole 2 at P=25 bar using the adjusted numerical model.

5.4.2.2 Validation of the mathematical model

In Figure 5.24, the ultimate hoop stress predicted by the mathematical model was compared to those obtained from the numerical model, considering the same hole, pressure, and CIPP liner conditions. The model was used in option one mode for the validation process. As depicted in Figure 5.24, the circular hole type exhibited the best fit. It is worth noting that the circular hole is the only type considered by current standards (UNE 53929 [1] and ASTM F1216 [8]). The coefficient of determination, with a value of 0.994, demonstrates the model's robustness for circular holes. Moreover, the model also exhibits a strong behavior with other types of non-circular holes. Although there is a slight decrease of 0.03 in the coefficient of determination as the hole shape deviates from a perfect circle, the model still demonstrates a good fit with coefficients of determination close to 1. For ellipses, the coefficient of determination R^2=0.986, for grooves R^2=0.962, and for angular grooves R^2=0.967. This

finding highlights the model's capability to accurately predict results for circular holes while providing acceptable predictions for non-circular holes commonly encountered in current pipelines, such as grooves (see Figure 2.19).

Finally, a coefficient of determination of 0.980 was obtained in the overall validation of the model, where 20% of the simulations from each hole class were combined, which is consistent with the individual findings obtained for each hole class.

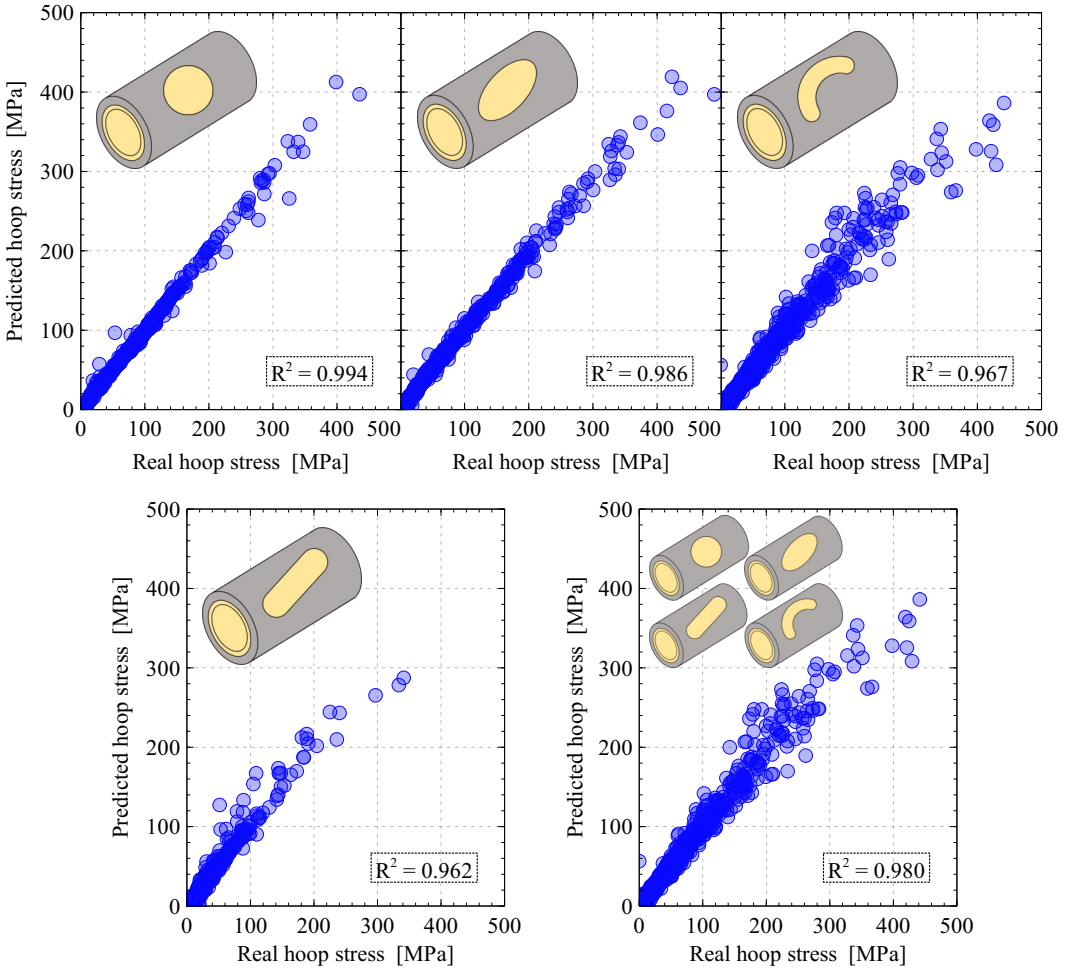

Figure 5.24: Comparison of the ultimate hoop stress calculated according to the mathematical model with the ultimate hoop stress obtained using the numerical model under the same conditions.

5.4.2.3 Thickness reduction reached with the mathematical model

Figure 5.25 and Figure 5.26 present the thickness reduction achieved using the mathematical model compared to the thickness calculated using the analytical equations provided by UNE 53929 [1] and ASTM F1216 [8] standards. The analysis considered various hole shapes, including circular and

non-circular holes such as ellipses, linear grooves, and angular grooves at 0° and 90° orientation. A hole diameter (d) to host pipe inner diameter (D) relation from 0 to 1 was considered. Moreover, the calculations were conducted for different pressures, ranging from 5 to 25 bar, and a range of liner's ultimate hoop stress values from 10.5 to 300 MPa. 10.5 MPa was chosen as it is considered the minimum hoop stress required by UNE 53929 [1] for pressure pipes.

Only liners with thicknesses over 3 mm were represented because the installation of a thinner liner became complex and more susceptible to buckling, as indicated in UNE 53929 [1]. Furthermore, when the thickness obtained with the hole's criterion is low, the groundwater loads criterion becomes the limiting design criterion. For example, in Figure 5.19, when the host pipe holes are small (d/D<0.1), the thickness obtained with the hole's criterion is below 3 mm, and then the final thickness of the liner is governed by the groundwater loads criterion. On the other hand, when pressure is increased, the liner becomes thicker, and for that reason, in Figures 5.25-5.26, more points are represented.

In Figure 5.25, the circular holes study reveals that liner's thickness reduction from 20% to 40% is possible for most of the studied cases. These significant reductions were achieved when the ring-in-tension equation of UNE 53929 [1] and ASTM F1216 [8] was used. In contrast, as can be noticed in the scenario of 25 bar (see Figure 5.25), for small holes with hole diameter to inside pipe diameter ratio (d/D) less than 0.23, the flat plate subjected to bending equation was employed. No reduction of the liner's thickness was detected in agreement with results from Figure 5.19.

In the case of non-circular shapes, when the hole deviates from the perfectly circular shape, the model achieves a bigger optimization. Various non-circular hole shapes oriented in the longitudinal direction (0°, see Figure 5.25) were considered: ellipses with a B_H/A_H ratio of 0.3, linear grooves with a width (B_H) of 30 mm, and angular grooves with an angle (α) of 180° and width (B_H) of 30 mm (see Figure 5.14 for design parameters). When considering ellipse holes, areas with a thickness reduction ranging from 40-60% (green) and 60-80% (ocher) are more pronounced compared to circular holes. However, regions with a reduction below 40% still maintain a significant impact. In the case of complete deformation of the circumference, as observed in linear grooves, the achieved thickness reduction ranges from 40-60% for high hoop stresses and 60-80% for low hoop stresses. Finally, reductions between 40% and 80% were reached in the majority of the cases studied for angular grooves.

In contrast, the thickness reduction is considerably more pronounced when non-circular holes are positioned at 90° (see Figure 5.26). In this configuration, the longitudinal dimension (a_1) is smaller than the hoop dimension (b_1). As a result, a smaller longitudinal area of the hole is subjected to significant hoop stress, as suggested by Allouche [54]. In particular, an extra reduction in thickness of 20% for ellipses, 40% for linear grooves, and 20% for angular grooves was obtained when holes were rotated 90°. It should be noted that reductions of 80% to 90% of the thickness of the liner were reached with linear grooves oriented at 90°. Therefore, linear hoop grooves are found to be the most unfavorable shape among those studied due to their lower A_H/B_H ratio. It is important to note that the standards provided by UNE 53929 [1] and ASTM F1216 [8] do not differentiate between more or less unfavorable orientations for non-circular holes, as they consider all holes to be circular. As a result, the oversizing of

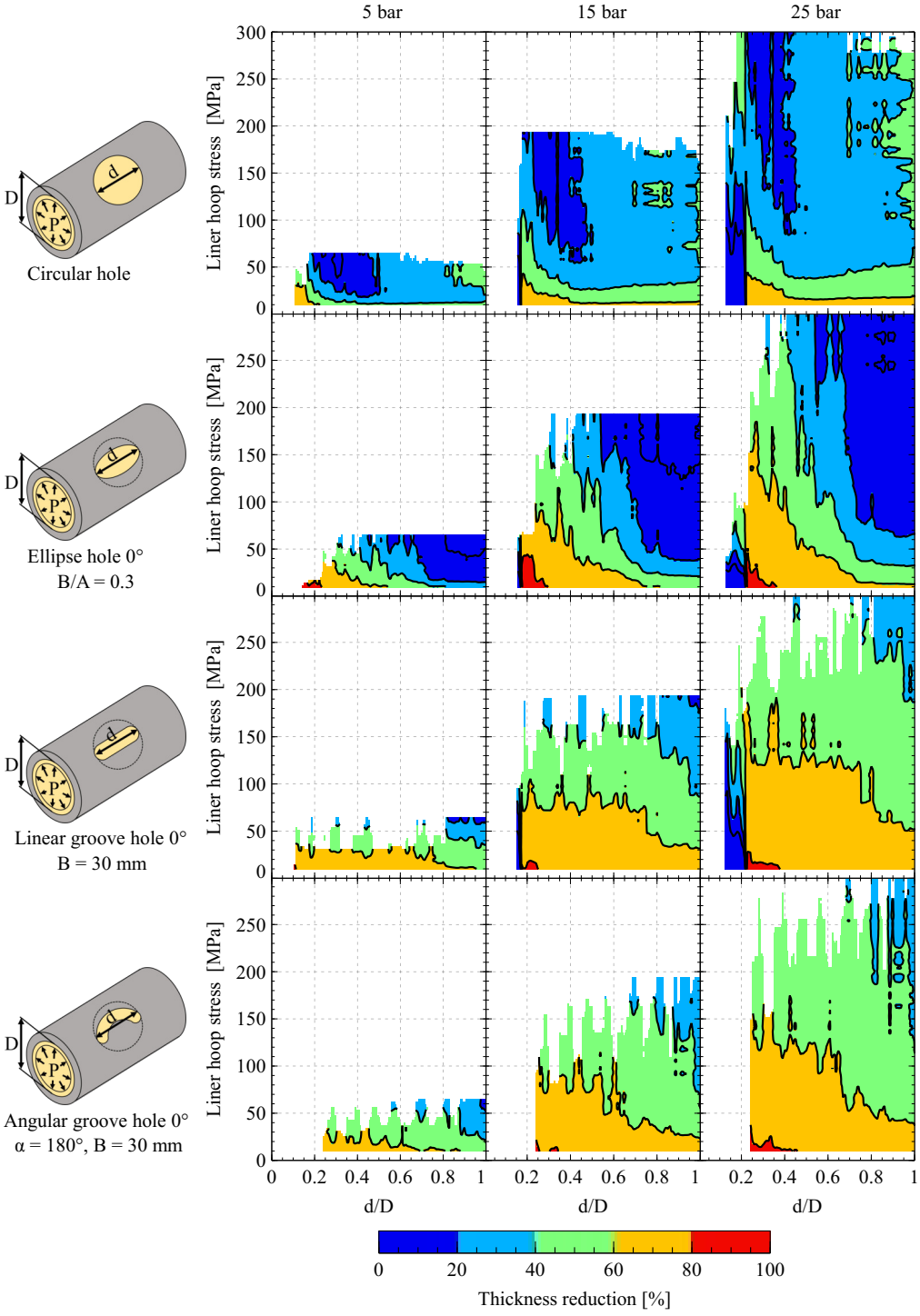

Figure 5.25: Thickness reduction achieved through the mathematical model compared to that proposed by UNE 53929 [1] and ASTM F1216 [8]. Circular and non-circular holes: ellipses, linear grooves, and angular grooves at 0°.

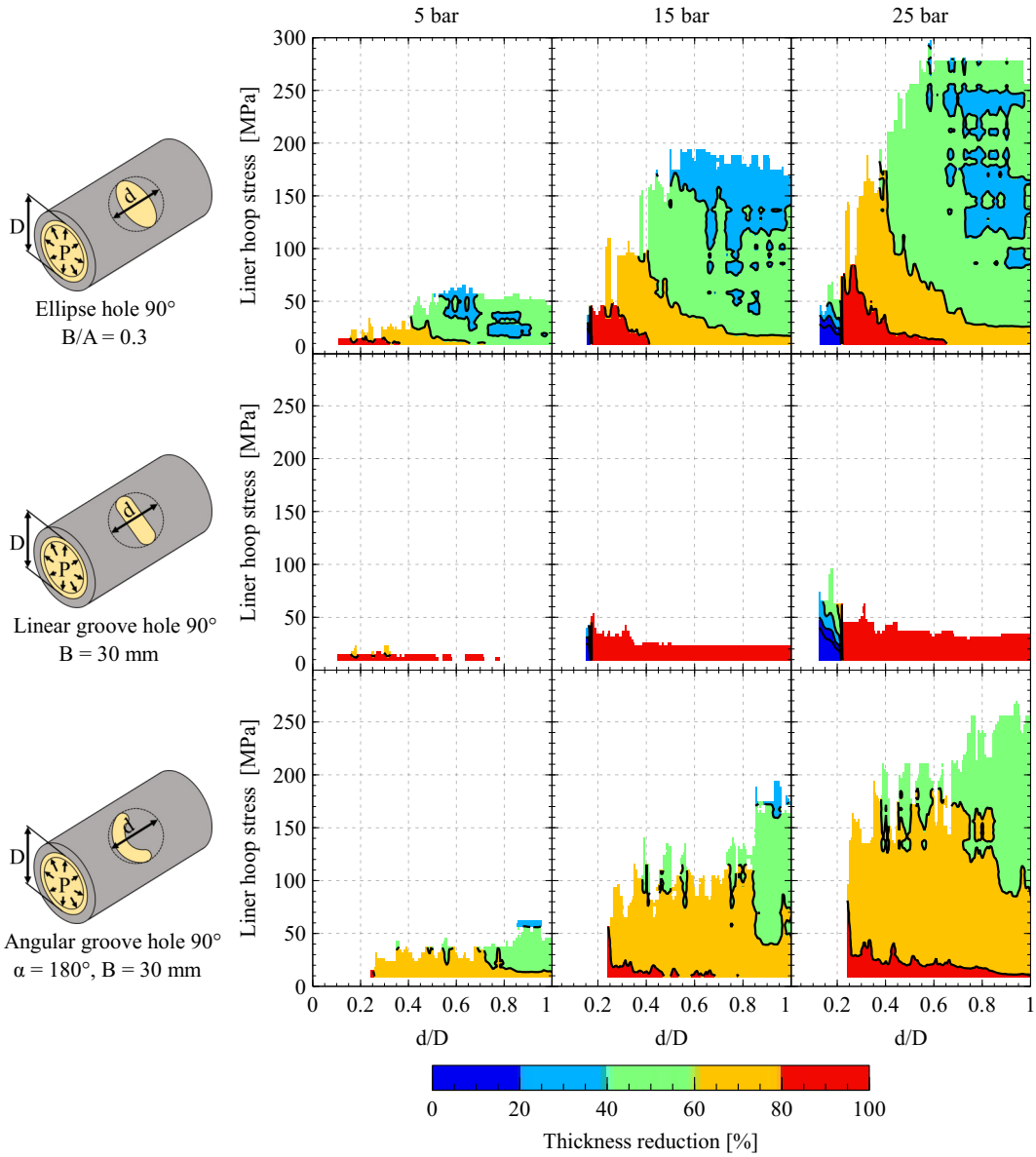

Figure 5.26: Thickness reduction achieved through the mathematical model compared to that proposed by UNE 53929 [1] and ASTM F1216 [8]. Non-circular holes: ellipses, linear grooves, and angular grooves at 90°.

the liner is significantly greater when the non-circular hole is oriented in the circumferential direction (90°).

The optimization of the CIPP liner's thickness is crucial. For pipe sizes ranging from DN 300-1000, the liner cost generally represents 40–70% of the project cost. Moreover, it is not only about lowering costs; a lighter liner is easier to install due to the increase in its maneuverability, and thereby, the likelihood of installation defect is reduced to the minimum. In pressure pipes, these defects can cause significant damage to third parties due to initial small leaks that, together with high pressures, become huge.

5.4.2.4 Application of the mathematical model in real scenarios

The mathematical model was finally tested with real host pipe holes shown in Figure 2.19. In Figure 5.27, the thickness of a liner subjected to real host pipe holes was calculated through the analytical equations of ASTM F1216 [62] and UNE 53929 [1], the mathematical model developed and finally, the numerical finite element model was also used. A comparison against the numerical model results is also set in Figure 5.27.

The results from the mathematical model are in good agreement with the numerical model results for all the holes studied. It should be noted that the six holes studied are not perfectly geometrical shapes. Thus, the results from Figure 5.27 demonstrate the robustness acquired by the mathematical model. On the other hand, results from the UNE 53929 [1] standard indicate an oversizing of the liner of 2.7 to 9.7 times (see Table 5.4) the optimal thickness defined by the numerical model. However, the UNE 53929 [1] predictions are not so far from optimal thickness when real host pipe holes are similar to circular shapes. For example, in holes five and six, the relative errors with UNE 53929 [1] calculations are respectively 18.8% and 36.6%. However, an error of 871.5% was obtained in hole 4. That was an overestimation of 26.1 mm, while the oversizing obtained with the mathematical model was 0.5 mm. The same trend is repeated in the rest of the holes that are far from perfectly circular shape. Consequently, the accuracy of the mathematical model is better in all of the studied real holes. In nearly circular holes, such as holes five and six, the relative error obtained with the mathematical model was -1.3% and 7.3%. Moreover, in the worst case predicted by the mathematical model (hole four), a relative error of 18.2% was obtained. However, this relative error corresponds to a deviation of 0.5 mm in the liner's thickness. Thus, it is an acceptable deviation in the design of a liner.

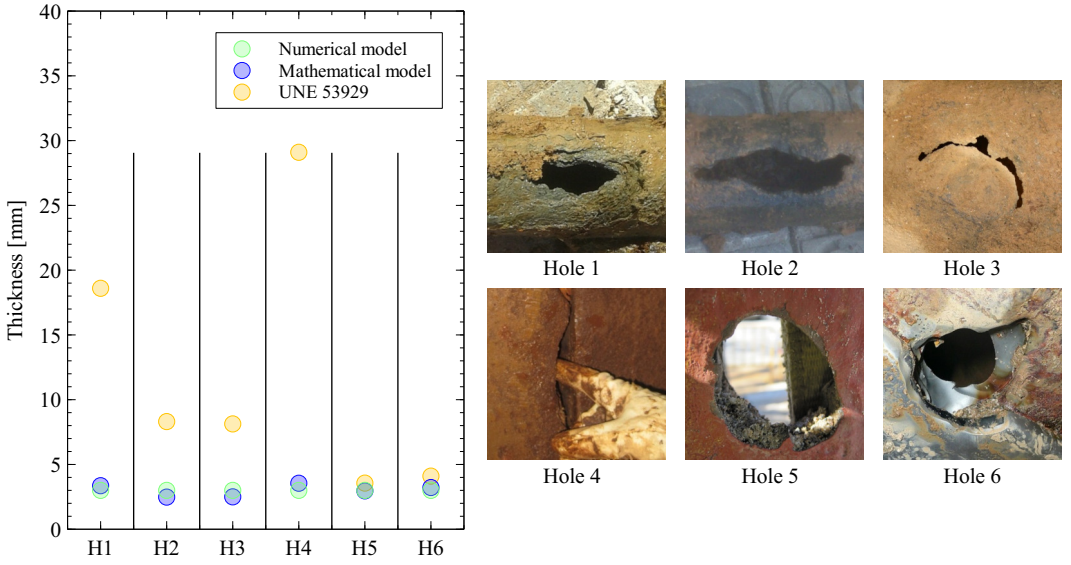

Figure 5.27: Comparison of different methodologies to define the thickness of a CIPP liner subjected to a pressure of 25 bar facing host pipe holes observed in real projects.

Table 5.4: Comparison of different methodologies to define the thickness of a CIPP liner subjected to a pressure of 25 bar facing host pipe holes observed in real projects.

	Numerical model		Mathematical model		UNE 53929	
Hole	σ_h (MPa)	t (mm)	t (mm)	RE[1](%)	t (mm)	RE[1](%)
1	29.2	3	3.4	12.0	18.6	520.9
2	69.2	3	2.5	-17.2	8.3	177.1
3	70.8	3	2.5	-16.7	8.1	170.9
4	17.6	3	3.5	18.2	29.1	871.5
5	165.3	3	3.0	-1.3	3.6	18.8
6	143.4	3	3.2	7.3	4.1	36.6

[1] Relative error

6

Conclusions and future works

In this chapter, the main contributions and implications of the doctoral thesis are exposed presenting the most relevant insights. Moreover, potential research lines for further investigations deducted from the results obtained are provided.

6.1 General conclusions

This doctoral thesis contributes to developing the Cured-In-Place Pipe (CIPP) technique applied to pressure pipelines. The results have focused on three fundamental areas: optimizing liner designs, developing new testing methods to evaluate the mechanical performance of installed liners, and proposing a rigorous quality control specific to CIPP. This research significantly aids in reducing uncertainties associated with the rehabilitation of pressurized water pipelines using CIPP. The main conclusions derived from the results are presented below.

- Sizing errors, installation defects, and complex procedures during installation have been identified as significant factors leading to failures in rehabilitated pressure pipelines. Accordingly, the proposed protocol has been designed for implementation in CIPP rehabilitation projects, providing detailed information about the entire process, from analyzing constituent materials to on-site installation and post-installation testing.

- The standardized tensile test, commonly used to assess raw liner mechanical properties, has been adapted from the textile industry. However, this method has shown limitations in assessing the mechanical performance of multi-layer CIPP liners due to severe sample slippage. To address this issue, the "hoop test" was implemented. Experimental results revealed annular deformations ranging from 140% to 170% using the adapted textile test, while the hoop test successfully reduced circumferential deformations to approximately 70%, demonstrating an effective solution to the slippage problem.

- The recommended bending test for curved CIPP samples according to standards has demonstrated that the conditions to which the installed liner is subjected are not accurately reproduced. Compared to the tensile test on flat samples, the maximum circumferential stress at failure is three times higher, potentially leading to a false sense of security in the design. The polymeric coating on the outermost layer of the CIPP liner is believed to play a significant role during the bending test. In the tensile test, the entire load-bearing section of the liner is subjected to tension. However, in the bending test, the outermost layer of the sample, namely the polymeric coating, experiences higher stress than the rest of the section due to the stress distribution in the sample. Therefore, the polymeric coating significantly influences the bending test, resulting in experimental results that diverge from reality, as in actual operating conditions, the liner section is primarily subjected to membrane stresses.

- The hoop stress in a cured liner can be accurately assessed using the proposed Inner Balloon Pressure Test (IBPT). The test has been validated, and experimental results demonstrate that it overcomes the deficiencies and limitations identified in curved and flat sample tensile testing. Consequently, the IBPT significantly contributes to quality control in the CIPP industry.

- Due to the uncertainties identified in using a CIPP in pressure pipelines, liners are often oversized, directly affecting the installation process. An oversized liner adds weight, compromising its maneuverability and increasing the complexity of installation. Hence, adjusting sizing procedures to achieve more optimized and lightweight designs has been deemed necessary.

- Analysis of the sizing equations has shown that the hole criteria prevail over others. Therefore, it is demonstrated that this factor is essential in semi-structural liner designs, making it the most relevant parameter to address in the optimization strategy.
- In the sizing of semi-structural liners, the flat plate bending model, as considered by current CIPP standards for liner design against small host pipe openings, has proven accurate. However, the ring-in-tension model, employed for larger openings, does not account for the residual structural contribution of the host pipe. Therefore, it is a conservative approach that results in oversized liners. For instance, a host pipe with significant damage and a hole ratio d/D=0.38 has been shown to provide a substantial structural contribution. Hence, an optimized liner design considering the ring-in-tension model has successfully reduced thickness by 20% to 40% for circular holes.
- Current standards only consider circular holes. Non-circular holes, such as real-world openings, are simplified as inscribed within a circle. While circular holes are the most critical, treating all holes as circular leads to oversized liners. The developed mathematical model demonstrates that, for non-circular voids, orientation is crucial, resulting in thickness reductions ranging from 20-80%. Holes oriented in the longitudinal direction are the most critical.

6.2 Research contributions

The results presented in the present doctoral thesis have yielded valuable insights, innovative approaches, and the contributions listed below:

- A robust quality control protocol for CIPP liners installed on pressure pipes has been proposed. The procedure is currently in use by companies, and the main guidelines of the protocol have been added to the UNE 53929 [1] CIPP standard to contribute to its dissemination.
- A novel test, named the IBPT, has been proposed, aimed to overcome the shortcomings identified in the current procedures to assess the hoop tensile performance of an installed liner.
- Experimental evidence from a full-scale test performed on a reinforced concrete pressure pipe of DN 400 mm has been provided. The results served to validate the numerical model, which is useful to further contribute to the development and optimization of the CIPP liners' design.
- A mathematical model based on machine learning approach has been proposed and validated to optimize the semi-structural liner's design used in pressure pipes damaged with holes. The model considers circular holes as well as irregular shapes. Thus, it is considered a relevant contribution to the CIPP semi-structural liner's design.

6.3 Future research

Guidelines for future research that arise from the findings and insights presented in the preceding chapters are listed below.

- Conduct an experimental analysis of the long-term deterioration in host pipes rehabilitated with CIPP liners. Specific projects have suggested that the structural integrity of host pipes significantly improves after rehabilitation. Nevertheless, a precise assessment of the extent of host pipe deterioration, based on its specific characteristics, would enhance our understanding of this field. Consequently, the development and application of optimized semi-structural liners could be explored to simplify the installation process.
- The innovative test designed to assess the hoop performance of cured liners, known as IBPT, was effectively evaluated using a laboratory-scale prototype with a limited number of representative liners. Nevertheless, to fully integrate this test into the CIPP quality control industry, a robust tooling system with increased strength and capacity for testing larger liner diameters is necessary. Additionally, a comprehensive range of liners made from diverse materials and configurations should undergo testing through the IBPT to validate and refine the proposed new testing method.
- Experimental validation of the mathematical model was provided through full-scale tests. Moreover, the model could be enhanced by incorporating additional parameters related to the main pipeline and the liner to account for additional variables accurately.
- Investigation of the impact of external loads as a function of ground depth in buried damaged host pipes with irregular holes. At certain depths, external loads are distributed through the terrain; therefore, the pipe is subjected to lower forces. Hence, in this case, using semi-structural rather than structural liners should be considered and carefully analyzed through comprehensive studies.

7

Appended publications

Publication I:

A novel test procedure for evaluating the performance of composite cured-in-place-pipe liners in water pressure pipe rehabilitation

10.1016/j.cscm.2023.e02381

Case Studies in Construction Materials 19 (2023) e02381

Contents lists available at ScienceDirect

Case Studies in Construction Materials

journal homepage: www.elsevier.com/locate/cscm

A novel test procedure for evaluating the performance of composite cured-in-place-pipe liners in water pressure pipe rehabilitation

Ferran Gras-Travesset [a,b], Antoni Andreu-Torras [b], Marco A. Pérez [a,*]

[a] IQS School of Engineering, Universitat Ramon Llull, Via Augusta 390, 08017 Barcelona, Spain
[b] Aigües de Barcelona, General Batet, 1-7, Barcelona 08028, Spain

ARTICLE INFO

Keywords:
Trenchless technology
Cured-in-place pipe CIPP
Water pipe rehabilitation
Sewer rehabilitation
Pipe lining
Experimental testing
Inner Balloon Pressure Test IBPT

ABSTRACT

The cured-in-place pipe (CIPP) is a pipe rehabilitation technique that is becoming increasingly popular due to its cost advantages, reduced environmental impact, and decreased time requirements compared to traditional pipe replacement. However, some CIPP rehabilitation projects have revealed deficiencies in predicted liner performance. This paper proposes and validates the Inner Balloon Pressure Test, a new test procedure for the quality control of CIPP rehabilitation liners. The test is intended to replicate the working stress conditions of an installed CIPP liner, and is proposed as an alternative to the curved specimen bending test recommended by the current CIPP standard and which has been shown to overestimate the ultimate stresses of cured CIPP liner specimens by more than 200%. Consequently, in a liner of DN 385 and 6 mm of thickness, a burst pressure of 138.2 bar was predicted through the bending test, whereas 62.8 bar was deducted from tensile tests. The experimental evidence provided in this study can significantly impact the design of CIPP pressure pipe liners. Inadequate sizing of the structural reinforcement can compromise the liner functionality and the rehabilitation of the pipeline. Therefore, this study provides a novel test that reduces uncertainties related to the strength analysis of CIPP liners. Furthermore, it contributes to optimizing and advancing existing design and quality control techniques.

1. Introduction

The quality of the water supply network is essential to ensure a continuous water supply and prevent the loss of potable water during transport from the treatment plant to the consumer. However, the water supply and sewage networks have aged and deteriorated over the years, causing a significant increase in faults as reported in [1]. This is demonstrated in a recent study [2] conducted by the American Society of Civil Engineers (ASCE), which estimated that a water leak occurs every 2 min in the US and that 22.7 hm^3 of potable water is lost daily. The greatest challenge in addressing this problem is the extensive mileage. In 2020, supply lines extended 248,245 km [3] in Spain, 875,000 km [4] in France, and $3.54 \cdot 10^6$ km [2] in the United States.

Rehabilitation techniques have proven to be an alternative to traditional and costly pipe replacement. Rehabilitation rather than replacement is a faster solution, is more cost-effective and environmentally friendly, and significantly reduces the disruption to city

* Corresponding author.
E-mail address: marcoantonio.perez@iqs.url.edu (M.A. Pérez).

https://doi.org/10.1016/j.cscm.2023.e02381
Received 4 March 2023; Received in revised form 26 July 2023; Accepted 5 August 2023
Available online 26 August 2023

activity caused by pipe replacement. The most widely used techniques are spraying, pipe bursting, slip-lining, thermoformed pipe lining (Fold-and-Form), and Cured-In-Place-Pipe (CIPP). Among them, CIPP has expanded considerably in recent years. CIPP is a rehabilitation technique that involves the insertion of an initially soft liner impregnated with resin into a host pipe, as detailed in Section 2. In Germany, rehabilitation with CIPP represented 17.9% of the repair and renovation market in 2020 [5]. It is predicted that in 2023, the global investment in CIPP will be approximately 2615.4 million dollars [6].

Though CIPP is widely used in the wastewater sector, the pressure reached in supply pipes (which can exceed 10 bars) make the rehabilitation process more challenging. As recognized by experts, slight imperfections during installation limit the performance of the rehabilitated pipe. In some cases, even resulting in a pipe going out of service.

Several problems may also arise after installation (see Fig. 1), as stated in [7] where field experiences from four CIPP projects were exposed. The most common installation defects are cracks, longitudinal wrinkles, lack of contact between the host pipe and the liner in semi-structural or non-structural liners, impregnation imperfections, swollen areas due to water drainage between the liner and the host pipe, and wall buckling [8]. For these reasons, rigorous quality control is required during and after installation. According to current standards such as ASTM F1216 [9], EN ISO 11296–4 [10], and ISO 11298–4 [11], quality control tests are based mainly on bending tests of cured samples of the installed liner. However, deficiencies detected in several CIPP rehabilitation projects suggest that the predicted performance estimated by standard tests may not approximate the actual pipe performance. Due to this uncertainty [12], several CIPP market companies are developing specific quality control procedures. However, there is yet to be a consensus on it. Recently, various organizations have started to centralize, unify and standardize these quality control procedures. For example, a standard on CIPP technology (EN ISO 11298–4 [13] and UNE 53929 [14]) was recently developed in Spain.

Researchers have contributed to the current design standards by investigating the CIPP rehabilitation process through experimental testing on the pipes themselves [15–18]. In a pioneering study [16], the six limit states of CIPP were presented, and it was concluded that longitudinal wrinkles significantly affect the mechanical properties of the liner. Allouche et al. [15] addressed the numerical and analytical verification of the burst pressure of a pipe with circular holes between 38.1 and 203.2 mm (1.5–8 in.) presented in the ASTM F2207 standard [19]. The study tested a PVC (Polyvinyl Chloride) pipe reinforced with steel rings to determine the effect of the holes and better understand the long-term behavior of CIPP. The authors concluded that the deformation of the liner during primary fluence was directly related to the size of the circular hole. Other researchers numerically and experimentally investigated the effect of longitudinal wrinkles on the liner and the appearance of holes in the host pipe using laboratory-scale prototypes [17,20]. The authors established that the passage of a wrinkle through a circular hole in the host pipe further decreased the mechanical performance of the installed liner.

The wrinkles in CIPP are classified according to their geometry into SW (i.e. only the inner layer is lifted), IW (i.e. symmetric wrinkle), and LW (i.e. asymmetric wrinkle) [21]. Further research has focused on investigating the reduction of the mechanical properties of sewer CIPP liners in service between 5 and 25 years with a nominal diameter (DN) of 203.2–1219.2 mm (8–48 in.) [22]. In these studies, it has been concluded that reduction in the liner properties was not detected. The authors also highlighted that just four of the tested liners reached half of their life expectancy. In addition, only the first liner installed worldwide has reached 50 years of it's expected life [22]. Moreover, full-scale tests have been consistently investigated [23,24] providing useful data to validate the multiple numerical models found in the literature [18,25,26].

Scientific findings have undoubtedly contributed to the design and improvement of lining pipes and CIPP technology. However, due to the high number of incidents and unsatisfactory rehabilitations, in recent years, there has been a need to establish strict quality controls to ensure that the liner has been correctly installed and meets the specified requirements. Currently, due to its operational simplicity [27], the three-point bending test of cured samples presented in EN ISO 11296–4 [10] is the main quality control test used to assess the tensile performance of CIPP liners.

The flexural test is widely used in the characterization of composite specimens [28–30]. Accordingly, the standard practice for the rehabilitation of existing pipelines (i.e., EN ISO 11296–4 [10] and ISO 11298–4 [13]) has adopted this procedure for the mechanical characterization of CIPP specimens. Nonetheless, the CIPP liners are mainly subjected to tensile loads due to the inner pressure of the pipe. However, the impracticality of extracting flat samples in the hoop direction makes the conventional tensile test unfeasible. Furthermore, the stress state (tensile, compressive, and shear stresses) and failure modes (see Fig. 13) that occur in a sample subjected

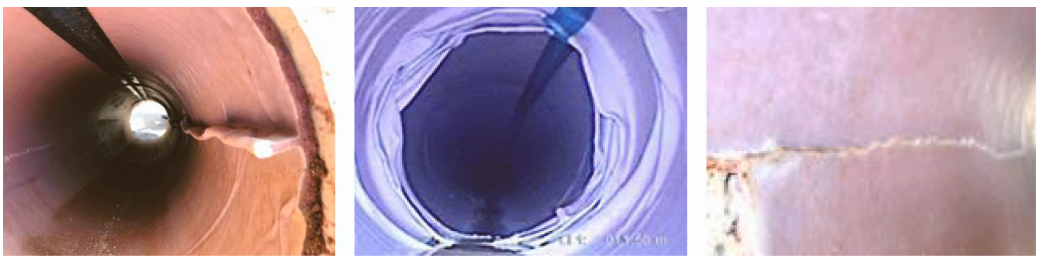

a) b) c)

Fig. 1. Example of defects resulting from improper CIPP installation. a) Longitudinal wrinkle. b) Hoop wrinkles. c) Longitudinal crack.

to flexure are complex [31–33] and different from tensile. Consequently, the bending test could be questionable for assessing the performance of an installed CIPP liner.

Accordingly, this paper proposes and validates a new test procedure for testing ring samples. The Inner Balloon Pressure Test (IBPT), aimed to reproduce the working conditions of a CIPP-installed liner and is proposed as an alternative to the three-point bending test of curved samples recommended by the current CIPP regulations.

2. CIPP design considerations

The advantage of trenchless rehabilitation technologies is that they use the existing pipes as a host taking advantage of their residual mechanical performance. Thus a new pipe is created within the damaged one, with minimal reduction in nominal diameter. There are different rehabilitation techniques, and each has its application and market. Particularly, CIPP is a technique that involves inserting an initially soft and resin-impregnated liner into a host pipe. The liner is a layered composite formed by fibers embedded in a resin matrix that acts as a binding component. An external polymer coating prevents resin migration and fibers from contacting the potable water. Once inserted into the damaged pipe, the liner is expanded by pressure to fit the host pipe and after the resin curing process (by steam or ultraviolet light), the soft lining solidifies, creating a new solid pipe within the host pipe (see Fig. 2).

According to the American Water Works Association (AWWA) [34], CIPP liners are classified as non-structural, semi-structural, or structural. Non-structural liners do not improve the host pipe's structural performance. Hence, they are mainly used to prevent clean water from coming into contact with corrosion from the host pipe. Semi-structural liners can partially withstand internal and external loads, such as small voids, corrosion pits, or joint gaps, but require residual structural contribution from the host pipe. Finally, structural liners are designed to withstand all internal and external loads. Thus, structural liners are used when the host pipe is severely damaged and has lost its structural capacity.

CIPP liners are designed considering the host pipe's residual load-bearing capacity. The technical standard ASTM F1216 [9] provides a detailed dimensioning procedure, defining the minimum performance the liner must achieve once cured to verify that the installation has been completed correctly. The expansion coefficient and burst pressure are critical mechanical properties in CIPP liners. Especially in semi-structural liners, the maximum coefficient of expansion of the uncured liner is crucial because the liner should completely fit the host pipe. The burst pressure is directly proportional (Eq. (1)) to the ultimate stress of the liner in the hoop direction (see Fig. 2):

$$\sigma = \frac{P\,r}{h} \tag{1}$$

where σ is the hoop stress (MPa), P is the internal pressure (MPa), r is the inner radius (mm), and h is the thickness (mm). As stated before, obtaining the tensile standard dog-bone type sample along the hoop direction is unfeasible due to the curved geometry of the cured samples. For this reason, the current technical standard (EN ISO 11296–4 [10]) uses curved shape samples to perform a three-point bending test, as shown in Fig. 3. The tensile stress-strain results can be analytically extrapolated from the bending test, assuming a linear distribution of stresses and strains along the thickness according to Eq. (2), and after applying the curvature correction (Eqs. (5) and (6)) proposed in EN ISO 11296–4 [10].

However, as proven below, the experimental evidence shows that the ultimate stress obtained in the bending test is significantly higher than in the tensile strength test of flat CIPP samples. Therefore, in the authors' opinion, the test can be questioned. Consequently, it is considered necessary to develop, compare and validate a test for curved samples capable of better reproducing the working conditions to which an installed CIPP liner is subjected.

3. Inner Balloon Pressure Test

The new test procedure, called Inner Balloon Pressure Test (IBPT), is proposed as an alternative to the three-point bending test of curved samples recommended by the current standard and aims to reproduce the working stress conditions of a CIPP-installed liner. The IBPT obtains the hoop stress and burst pressure of a ring sample extracted from an installed CIPP liner. The test involves applying

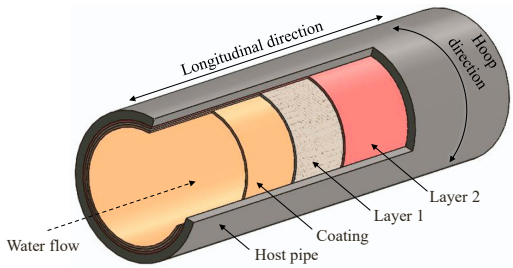

Fig. 2. Representation of a pipeline rehabilitated using CIPP.

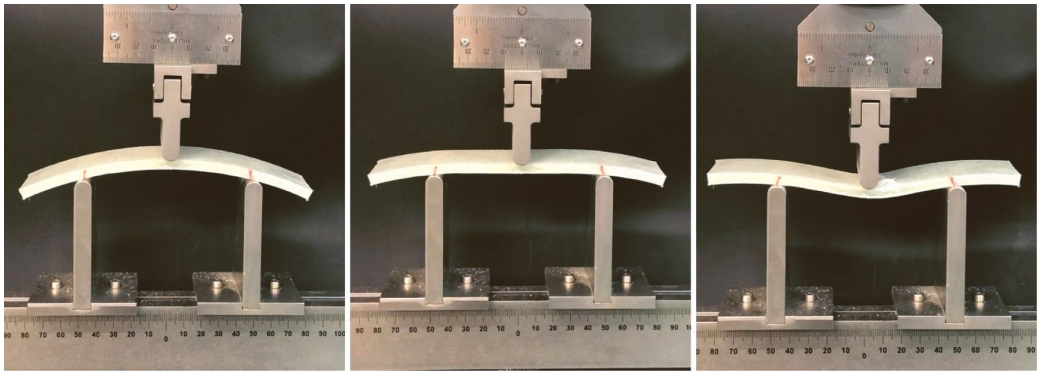

Fig. 3. Experimental setup of a three-point bending test of a cured CIPP sample liner (DN385 mm), according to the technical standard EN ISO 11296–4. [10].

hydrostatic pressure to the ring sample's inner face to obtain the sample's tensile properties in the hoop direction (see Figs. 4 and 5).

The schematic drawing of the test set-up is shown in Figs. 4 and 5. The samples are located between two rigid plates joined by threaded rods to support the internal pressure. The upper plate has a central hole that allows the pressurized fluid to enter and exit. The fluid is introduced into the membrane inside the sample to avoid leakage. Thus, the membrane transfers the hydrostatic pressure to the inner face of the tested ring sample. The test system allows the sample to expand radially by sliding between the two tooling plates. Using lubricant minimized the friction between the sample and the tooling plates.

4. Materials and methods

Firstly, the research methodology was designed to compare the tensile test of CIPP flat samples with the three-point bending test of curved CIPP composite samples to identify the shortcomings of the bending test as a CIPP quality control test. Secondly, the proposed IBPT was validated by comparing the test results with PVC and CIPP composite ring samples, with experimental tensile tests and results from a developed numerical model. Details of materials, samples, test setups and numerical models are given below.

4.1. CIPP liner test samples

The CIPP liner used in this study was of type structural class A according to ISO 11295: 2019 table 16 [35] and class IV according to AWWA CIPP classification [34]. The liner is composed of three layers of fiberglass and a polyethene (PE) coating that prevents fiber migration to the drinking water (see Fig. 2). The resin used was a styrene-free vinyl ester resin with very low VOC (Volatile Organic

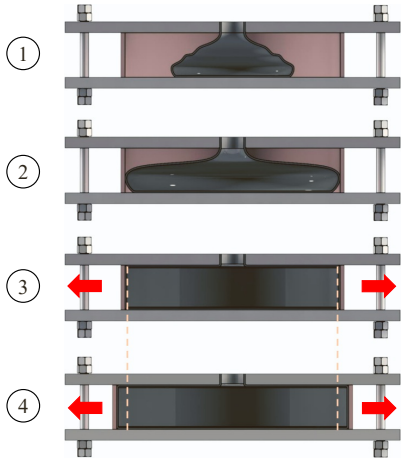

Fig. 4. Schematic drawing of the Inner Balloon Pressure Test (IBPT) setup.

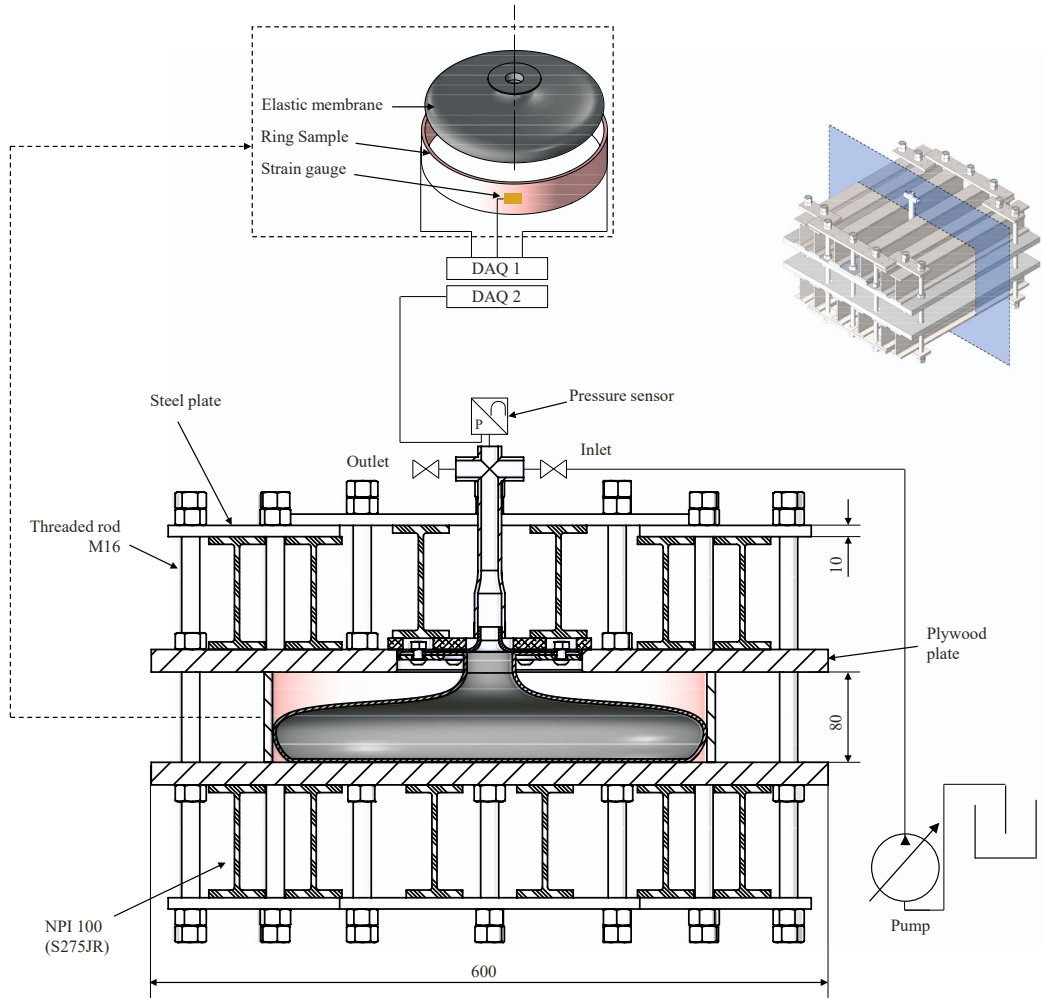

Fig. 5. Assembly drawing of the Inner Balloon Pressure Test (IBPT) setup.

Compound) content, used for CIPP and specific for potable water pipes. A UV curing process solidifies the resin. The liner was first analyzed with a high-resolution Olympus DSX1000 digital microscope (see Fig. 6).

Two different curing processes obtained samples of the cured liner. First, flat samples were cured under controlled laboratory conditions because obtaining flat samples from an installed liner in a cylindrical pipe was unfeasible. These flat laboratory samples were cured by UV lamps type A, B, and C with an exposure time of 2 min. Afterwards, a numerically controlled machining process was used to obtain the type I dog-bone samples according to ASTM D638 [36]. Second, CIPP ring samples were obtained from a rehabilitated DN400 reinforced concrete pipe (Fig. 8) with the same liner. The curing process was performed under real installation conditions using a trolley of 9 UV lamps of 400 W each (see Fig. 7)

4.2. Tensile test

Tensile testing of PVC flat samples and CIPP liner samples was carried out according to ASTM D638 [36] using a type I geometry. Due to the isotropy of PVC material, the PVC tensile samples were obtained by machining a PVC pipe along the longitudinal direction. As stated before, the CIPP liner tensile samples were cured in the laboratory on a flat surface and then machined to obtain flat samples in the hoop direction. Tests were conducted on a ZwickRoell Z30 universal mechanical testing equipment with a 30 kN load cell and a

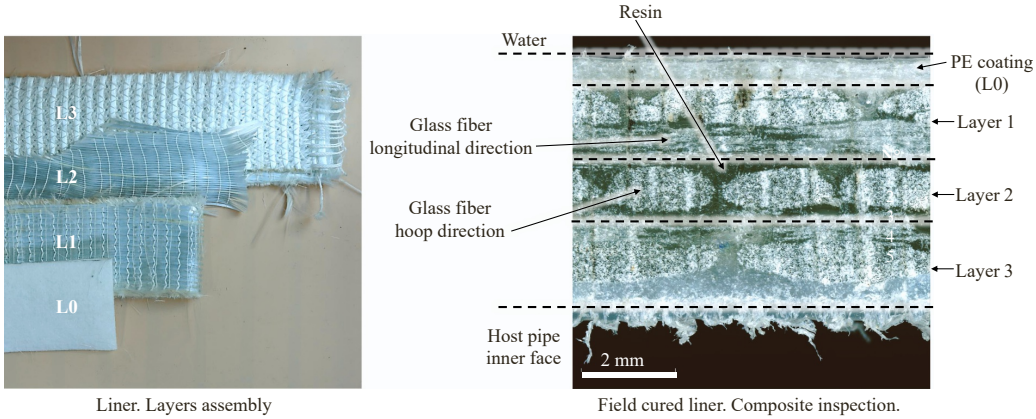

Fig. 6. Arrangement of the CIPP composite liner used.

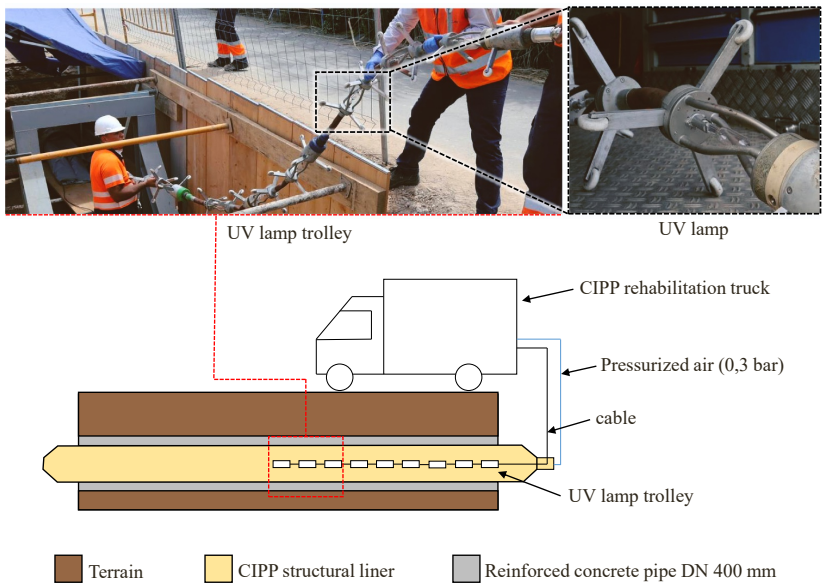

Fig. 7. Field UV and pressure curing process of the installed liner.

50 mm ZwickRoell extensometer. Samples were tested with a preload of 5 N and a test speed of 5 mm/min. Young's modulus was calculated by the regression method between the strain range [0.05–0.25%]. The test speed for calculating the elastic modulus was 1%/min.

4.3. Three-point bending test

Three-point bending tests were performed following EN ISO 11296–4 [10] and ISO 178 [37] on curved samples using the same ZwickRoell Z30 universal mechanical testing equipment. The samples tested had an inner radius of 192.5 mm, a width (b) of 50 mm, and a thickness (h) of approximately 6 mm. The distance between supports (L) was set at 96 mm, so the actual support distance L_2 of the sample was 99.93 mm. The samples were tested according to the standard using a preload of 2 MPa and a test speed of 10 mm/min. The strain rate to calculate the modulus of elasticity was set to 1%/min. Young's modulus was calculated according to Eq. (4) between the strain range [0.05–0.25%], where $\varepsilon_2 = \varepsilon_1 + 2000.10^{-6}$ mm/mm and ε_1 takes the value that maximizes Young's modulus. The

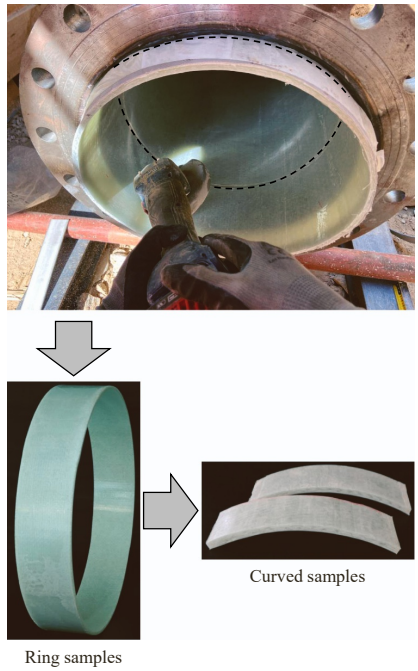

Fig. 8. Extraction of the ring samples of an installed CIPP liner of DN 385 mm.

apparent stress and strain were respectively calculated according to Eqs. (2) and (3):

$$\sigma_c = \frac{3FL_2}{2bh^2} \tag{2}$$

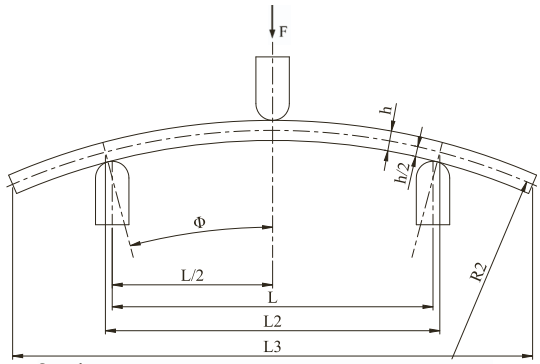

Legend
F: Applied force.
h: Total thickness of the sample.
L: Distance between supports.
L2: Real distance between the supports of a curved sample.
L3: Total length of the chord of a curved sample.
R2: Radius of curvature of the sample at half the thickness
Φ: Half-angle of an unloaded specimen formed between the actual contact points of the supports.

Fig. 9. Three-point bending test scheme of a curved sample according to EN ISO 11296–4 [10].

where σ_c is the apparent stress of a curved sample subjected to bending before the curvature correction (MPa), F is the applied force (N), L_2 is the actual distance between the supports of a curved sample subjected to bending (mm), b is the width of the sample (mm) and h is the thickness of the sample (mm).

$$\varepsilon_c = \frac{6\, s\, h}{{L_2}^2} \tag{3}$$

ε_c is the apparent strain of a curved sample subjected to bending before the curvature correction (mm/mm), s is the displacement of the surface of the sample at the point of the load application from its initial position (mm):

$$E_c = \frac{\sigma_{c2} - \sigma_{c1}}{\varepsilon_{c2} - \varepsilon_{c1}} \tag{4}$$

where E_c is the apparent bending modulus of a curved sample subjected to bending before the curvature correction (MPa), σ_{c2} is the apparent stress at point 2 (MPa), σ_{c1} is the apparent stress at point 1 (MPa), ε_{c2} is the apparent strain at point 2 (mm/mm), and ε_{c1} is the apparent strain at point 1 (mm/mm).

Finally, the curvature correction coefficients C_σ Eq. (5) and C_E Eq. (7) were calculated. Then, Eq. (6) and Eq. (8) were applied according to EN ISO 11296–4 [10], to calculate the flexural modulus (E_f) and the flexural stress (σ_f):

$$C_\sigma = \frac{1 + \frac{h}{6R_2}}{cos\ \phi} \tag{5}$$

where C_σ is the curvature correction coefficient, R_2 is the radius of curvature of the sample at the average sample thickness, and ϕ is the half angle of an unloaded sample formed between the real contact points of the supports (see Fig. 9). In the tests performed, a value of $\phi = 0.258$ rad ($\phi = 14,8^{\circ}$) was used, obtaining $C_\sigma = 1.039$.

$$\sigma_f = \frac{\sigma_c}{C_\sigma} \tag{6}$$

σ_f is the flexural stress of a flat sample subjected to bending loads (MPa).

$$C_E = \frac{\left(\frac{L_2}{2R_2}\right)^3 cos^2\phi}{1,5\left[\phi - \left(\frac{L_2}{2R_2}\right) cos\ \phi\right]} \tag{7}$$

C_E is the curvature correction coefficient for the flexural modulus.

$$E_f = \frac{E_c}{C_E} \tag{8}$$

E_f is the flexural modulus of a flat sample subjected to bending loads (MPa).

4.4. Digital Image Correlation setup

A 3D Digital Image Correlation (DIC) system was used during the three-point bending tests to analyze the strain distribution along the thickness of the CIPP samples. To create the speckle pattern, the samples were airbrushed with different tip diameters (see Fig. 10). Two Allied Vision GigE MAKO G-507B GigE cameras with APO-Xenoplan 1.4/23–0903 objectives were used to record the surface displacement of the samples. Calibration was performed with a GOM CP20/MV55×44 panel with an offset of 0.021 pixels. The measurement volume resulting from the calibration was 150 × 130 × 110 mm. Finally, the image sequences were post-processed with GOM Correlate Professional software using a facet size of 12 × 12 pixels.

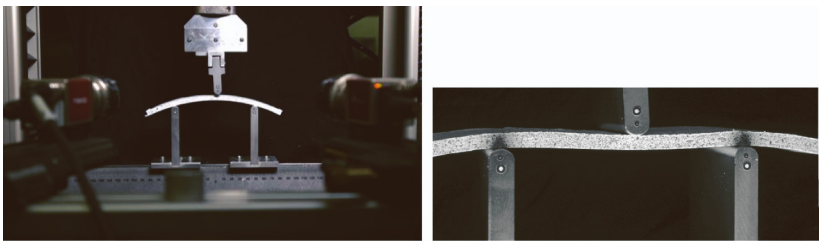

Fig. 10. Digital Image Correlation setup used during the three-point bending test of curved samples.

4.5. Inner Balloon Pressure Test

To experimentally validate the proposed test, a 600 × 600 mm prototype (Fig. 5) was designed and built (Fig. 11) to test samples up to DN500 mm. The prototype consisted of two rigid plates reinforced with 6 IPN 100 (S275JR) steel beams joined with M16 threaded rods. A Wika pressure sensor type A-10 was used to monitor the pressure. HBM strain gauges type 1-LY41–6 / 350 were used in the hoop direction to measure the hoop strain during the test. HBM's Quantum X MX840 B and Quantum X MX1615 B hardware and CatmanEasy AP software were employed for data acquisition. The prototype was used to test both PVC and cured CIPP liner samples from an installed liner. The PVC sample had a nominal diameter of 240 mm, a thickness of 5 mm, and a length of 80 mm. The CIPP liner ring sample had a nominal diameter of 385 mm, a length of 80 mm, and an average thickness of 6 mm (Fig. 11).

4.6. Numerical models

A static structural implicit Ansys model was created to model the tensile performance of flat and ring samples. Due to the symmetry of both sample geometries, simulations were performed using half of the sample (Fig. 12). For the tensile sample, the ASTM D638 [36] type I standard test geometry was meshed using higher-order 3-D 10-node (Solid 187) 3 mm elements size. A type 1 refinement was applied to the area where the stress concentration was located. The mesh had 8909 nodes. Fixed support was set on the sample's lower face (xz plane) to simulate the effect of the grips in the experimental test. A displacement of 5 mm on the y-axis was defined on the upper face of the sample. The material's mechanical properties were obtained by applying true stress compensation to the data acquired from the experimental tensile-strength test. Finally, the plastic region was defined by the hardening isotropic multilinear plasticity option.

The IBPT numerical models' geometry was different for each material. Ring PVC model had a DN of 240 mm, a thickness of 5 mm, and a length of 80 mm. Ring CIPP model had a DN of 385 mm, a thickness of 6 mm, and a length of 80 mm. Ring geometries were meshed using higher-order 3-D 20-node (Solid 186) 10 mm elements size. The properties of the materials were defined according to the Ansys data base and completed with the results of the experimental tensile tests for each material. The CIPP liner used had a Young modulus of 20.5 GPa, a Poisson's ratio of 0.1543 a shear modulus of 8.9 GPa and a density of 1857 kg/m^3. On the other hand, the PVC used had a Young modulus of 3.4 GPa, a Poisson's ratio of 0.4 a shear modulus of 1.2 GPa and a density of 1392 kg/m^3. For both models, a frictionless support was defined on the semicircular section (YZ plane) and two frictional supports of $\mu = 0.05$ on the top and bottom face of the ring (XY plane). Next, two remote displacements were set. The first remote displacement was defined at 3 and 9 o′clock in the YZ plane to avoid x-displacement and z-rotation. The second remote displacement was defined at 12 o′clock in the XZ plane to suppress the y-displacement and z-rotation (Fig. 12). Finally, the total stress and strain curves in the hoop direction were obtained.

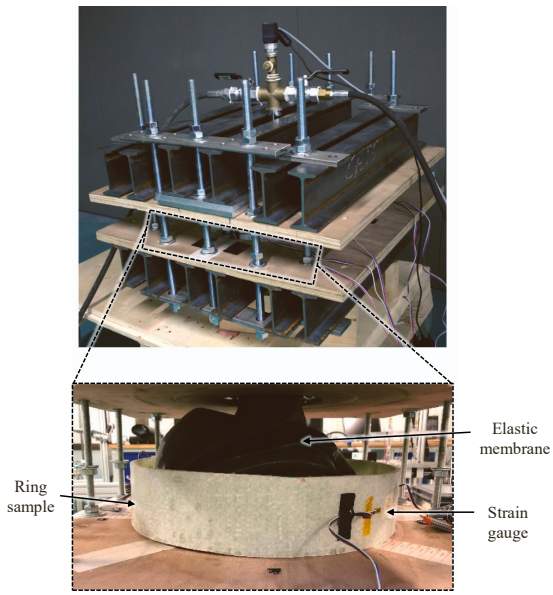

Fig. 11. Inner Balloon Pressure Test setup.

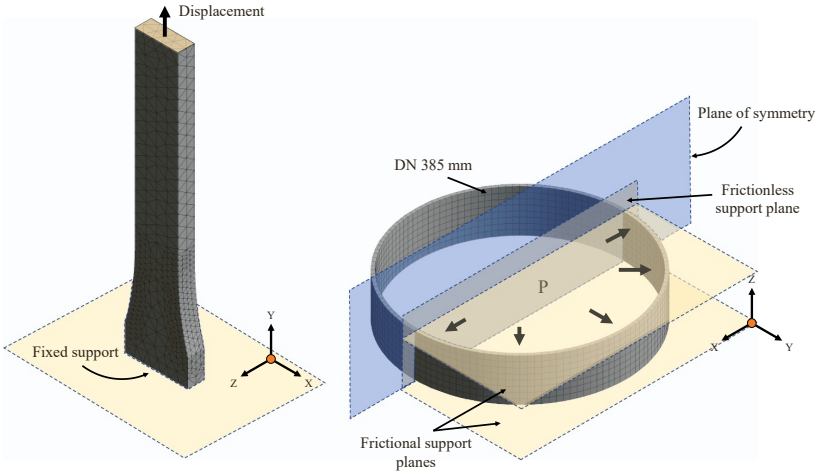

Fig. 12. Numerical model geometry of the tensile strength test ASTM D638 (left) and the Inner Balloon Pressure Test (right).

5. Results and discussion

5.1. Comparison between the bending and tensile test performance

During the three-point bending test, three failure modes were identified, as shown in Fig. 13. Among them, compressive failure due to buckling of the top layer fibers (Fig. 13a), and delamination failure (Fig. 13b) due to shear stresses are undesirable phenomena when trying to determine the tensile strength of the composite material. Only the failure of the outer layer due to tensile stress (Fig. 13c) is expected to occur under the operational conditions of the CIPP liner. The variety of failure modes demonstrates that the mechanical phenomena along the sample thickness are complex because a combination of tensile, compressive and shear stresses are given simultaneously.

Fig. 14 compares the results of the tensile strength test of flat CIPP samples to the three-point bending test of CIPP curved samples. As shown, the stress-strain curves differ markedly between the two tests, despite the samples being manufactured using the same material. Stress and strain at break obtained in the bending test according to standard EN ISO 11296–4 [10] are up to three times higher than those obtained on the tensile ASTM D638 test [36]. Hence, experimental evidence suggests that the obtained values from the bending test may not represent the ultimate stress of the CIPP liner. Since strength is a parameter used in the design of the liner, this finding could negatively affect the structural safety of the installed liner.

An incorrect assumption of a linear strain distribution inside the liner could explain the aforementioned result. To validate this hypothesis, Fig. 15 depicts the strain distribution along the sample thickness in the bending test obtained by the DIC results. The strain distribution is represented at two instances during the test. The first state corresponds to the external layer of the sample reaching the composite's ultimate strain measured in the tensile test. The second is the state just before failure when the fiber-resin region reaches the maximum strain of the composite measured in the tensile test.

As shown in Fig. 15, the DIC system shows at both states a linear strain distribution along the thickness of the sample, demonstrating the validity of the linear strain distribution model described by the equations in EN ISO 11296–4 [10].

Fracture propagation was also examined (see Fig. 16). In the three-point bending test, the outermost layer of the specimen is subjected to the highest tensile stress, meaning the fracture starts in the outer layer and propagates inwards. Fig. 16(a) shows the phenomenon. For clarity, Fig. 16b) shows the same failure mechanism using a 30 mm thick liner. In both cases, the fracture originated just after the polymer coating at the beginning of the resin-fiber region and propagated inwards. This phenomenon occurs because the

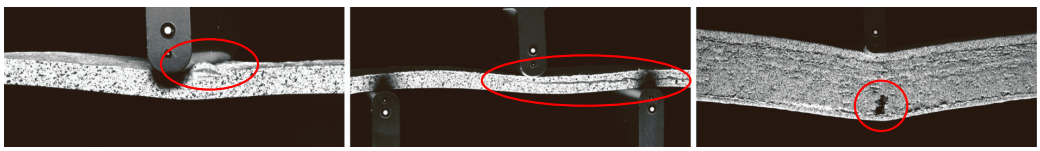

Fig. 13. Types of failure modes identified in the three-point bending test of CIPP composite liner: a) Compressive failure due to buckling of the upper fiber. b) Delamination of layers. c) Failure of the external layer due to tensile stress.

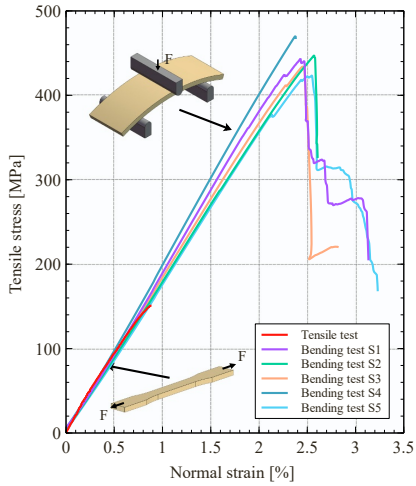

Fig. 14. Comparison between results of tensile strength of flat CIPP samples and three-point bending CIPP curved samples. The ultimate stress obtained with the bending test is up to three times higher than in the tensile test.

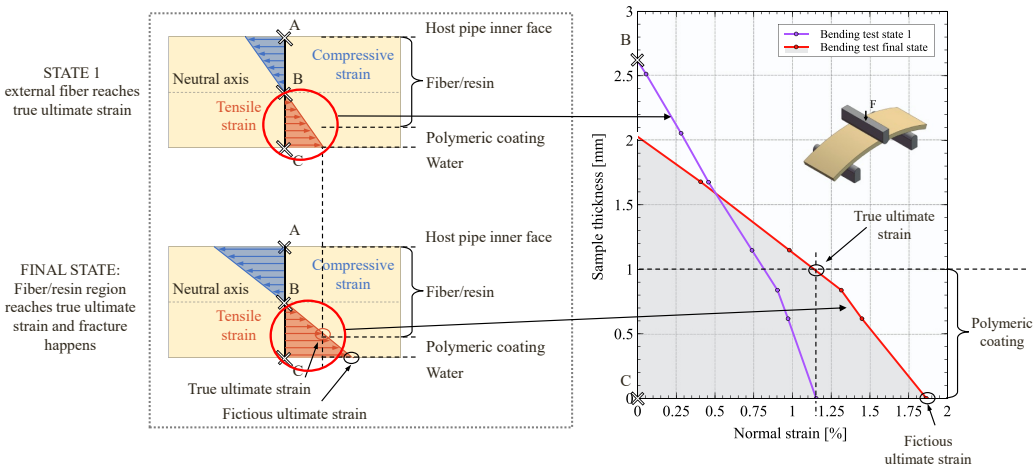

Fig. 15. Through-thickness strain distribution of a three-point bending test at two instants measured by experimental Digital Image Correlation.

outermost layer of the sample consists of a polymer coating with a ductile behavior. Therefore, even if the strain-to-rupture limit of the composite is reached (state 1, Fig. 15), the polymer layer continues to deform. Thus, failure (final state, Fig. 15) occurs in the inner zone adjacent to the polymer layer when the composite reaches its tensile limit. The thickness of the polymer coating was approximately 1 mm.

Fig. 15 (right) shows that, in the final state, the slope change in the strain distribution occurs around 1 mm from the bottom face, corresponding to the crack location. Moreover, the strain determined is similar to the ultimate strain of the composite obtained in the tensile test of the flat specimens (1.15% and 0.89%, respectively).

5.2. Inner Balloon Pressure Test validation

5.2.1. Numerical analysis: friction effect and tensile performance

As a preliminary step to the validation of the test, a numerical analysis was performed to analyze the boundary conditions of the IBPT and verify its performance as a tensile test of ring samples. The analysis is carried out on PVC samples as their well-determined

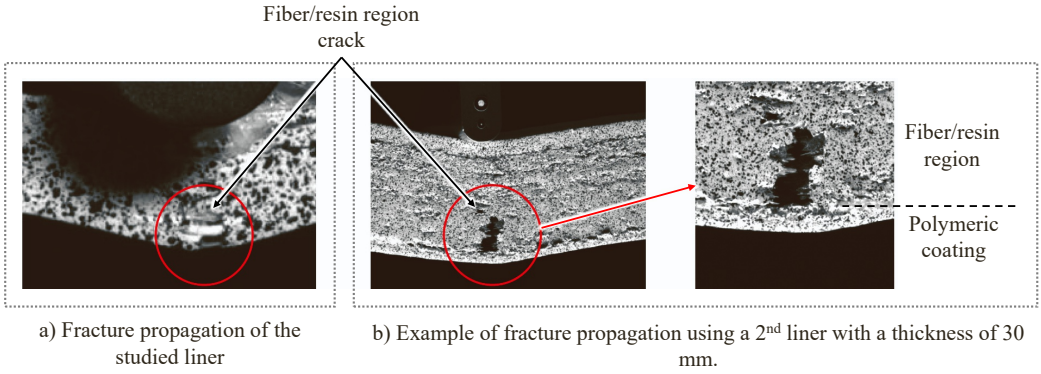

Fig. 16. Crack propagation analysis of the three-point bending test of CIPP liners experimentally observed by Digital Image Correlation.

properties allow the numerical model to be calibrated.

Initially, the ring sample is in contact with the upper and lower plates of the tooling (Fig. 5). Therefore, a frictional contact appears that could negatively affect the results and the performance of the test. Considerable friction ($\mu = 1$) would bend the sample into a barrel shape, as shown in Fig. 17, generating longitudinal stresses and causing problems with the inner membrane of the tooling (Fig. 11). However, the use of lubricant and the nature of the IBPT prevent the appearance of friction effect. During the test, the inner membrane also exerts pressure on the tooling's lower and upper plates, generating a gap between both plates and the test sample. In addition, the longitudinal shrinkage caused by the Poisson effect increases the gap between the tooling covers and the sample. Thus, the ring sample can expand with a minimum friction coefficient, and the barrel shape of the sample represented in Fig. 17 is discarded.

The stress-strain curves of PVC samples obtained using the IBPT model (II) and the ASTM D638 [36] tensile test numerical model (I) are represented in Fig. 18. IBPT results have been obtained assuming a friction coefficient of $\mu = 0.05$. As shown, the IBPT model presents a tensile behavior in agreement with the flat sample tensile test, identifying an error under the curve of 0.25%. Hence, the results demonstrate that the IBPT can reproduce the tensile stress performance with ring samples analogous to the tensile test.

5.2.2. Validation results on PVC samples

Fig. 19 shows the results obtained from PVC samples for the experimental validation of the IBPT. The graph compares a representative stress-strain curve of the tensile test (V) (ASTM D638 [36]) with the numerical (IV) and experimental (I, II and III) IBPT results. In the experimental IBPT, the results of the three strain channels corresponding to the three strain gauges installed on the outer surface of the specimen are plotted. As shown, these strain results display a similar trend. For example, the strain at 15 bar was 1.29% (channel 1), 1.51% (channel 2) and 1.16% (channel 3). The differences (0.18% standard deviation) between the channels are attributed to small misalignments in the placement and alignment of the strain gauges during installation. Consistent results are also concluded from the experimental tensile test (V) and the numerical simulation (IV).

In contrast, more variation is observed between the IBPT experimental curves (I, II and III) and the tensile test (V). The maximum deformation average reported by the three channels of the IBPT was 3.06%, while a maximum deformation of 8% was reached in the standard tensile test of flat specimens. This significant decrease in strain (161%) and increase in stress (6.39%) is attributed to the difference in load rate during the test [38]. In the IBPT, the pressure rate was controlled manually to increase the balloon's internal pressure. However, the control of the inlet pressure was not sufficiently gradual, which occasionally caused the material in the plastic zone to tear instead of yield. This tearing phenomenon can be seen in Fig. 19 by observing the wavy lines at the end of the curves in the experimental IBPT (I, II and III). In contrast, the tensile test was performed according to ASTM D638 [36], with a constant loading rate controlled by the hardware of the test equipment. Aside from this difference, the IBPT allows for a reliable reproduction of the working conditions of the ring specimens, permitting the assessment of the mechanical performance as an alternative to the tensile and flexural classical tests.

5.2.3. Validation results on CIPP composite samples

Fig. 20 shows the IBPT experimental stress-strain results (curves I and II), and a representative tensile test curve (III) of a flat specimen. Both tests used CIPP composite specimens. As in the previous section, the IBPT results reveal that the specimen could expand freely in the hoop direction. However, the results show differences in ultimate stresses. In both tests, the ultimate strain was consistent (tensile test 0.89%, IBPT ch1 0.77%, IBPT ch2 1.03%). However, the IBPT shows a higher ultimate stress ($\sigma_u = 201.4$ MPa, 1.34 times) compared to the ultimate stress of the tensile test ($\sigma_u = 150.9$ MPa). The type of curing process of the specimens could explain this phenomenon of non-correlation of ultimate strength.

In the IBPT, the specimens were taken from an installed liner and cured with internal pressure by a certified installer. In contrast, the flat specimens were cured in the laboratory, in an attempt to reproduce the conditions of the certified equipment but without pressure. The SEM microscopy images in Fig. 21 show that the cross-section of a sample of the installed liner (d, e and f) does not show

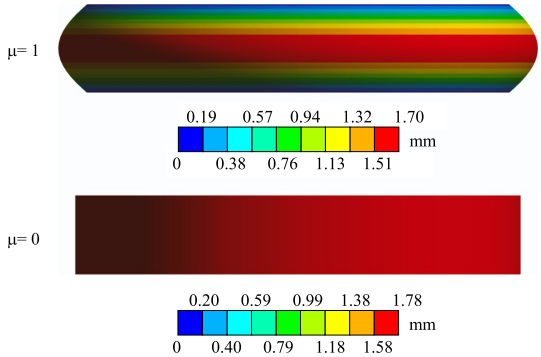

Fig. 17. Adjustment of the friction boundary conditions of the IBPT numerical model.

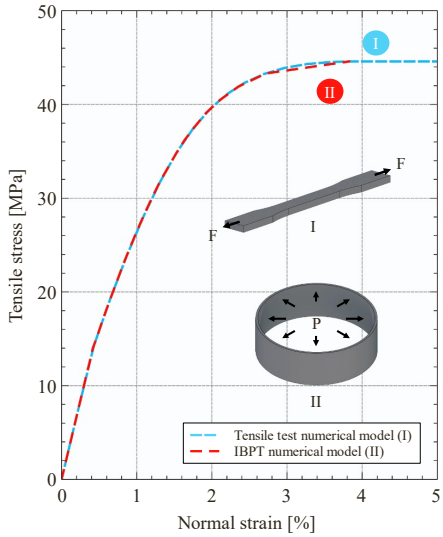

Fig. 18. Comparison between the stress-strain numerical results of the tensile and IBP PVC sample tests.

any defects, which guarantees good compaction of the laminate. In contrast, the samples cured in the laboratory (a, b and c) show defects indicating an apparent absence of resin. This defect during curing is attributed to the absence of compaction pressure and is considered responsible for the decrease in the mechanical properties of the flat samples.

Finally, Fig. 22 compares representative stress-strain curves obtained from the three-point bending test of curved specimens, the experimental IBPT of ring specimens and the tensile test of flat specimens. The graph on the right shows the magnified data of the first third of the curve. Overall, a good correlation is found in the stiffness of the specimens: $E_{flexural} = 21.1$ GPa ($E_c = 19.3$ GPa before curvature correction, see Eqs. (7) and (8), $E_{tensile} = 20.5$ MPa and $E_{IBPT} = 21.2$ GPa. According to the standard test, stiffnesses have been calculated on the strain range [0.05–0.25%].

However, as anticipated, a significant difference is recognized in the ultimate stress. The burst pressure obtained from the tensile test should not be considered as it was influenced by the aforementioned impregnation defects. As shown, the burst pressure obtained from the bending test of curved specimens is 138.2 bar (443.4 MPa), which is greater than twice the 62.8 bar (201.4 MPa) obtained in the IBPT. It should be noted that both samples were taken from the same installed liner. Hence, this experimental evidence highlights once again the possible unsuitability of the bending test to characterize the behavior of CIPP composite liners.

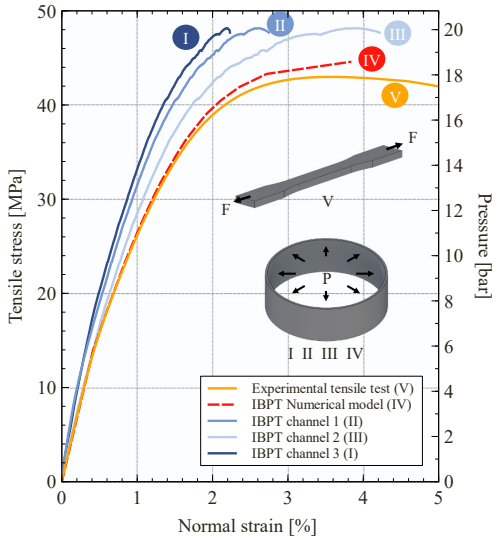

Fig. 19. Validation of the IBP test with PVC samples.

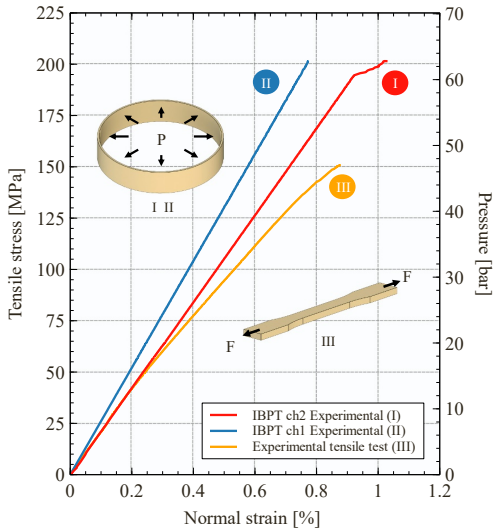

Fig. 20. Validation of the IBP test with CIPP composite samples.

6. Conclusions

This paper proposes and validates the Inner Balloon Pressure Test, a new test procedure for the quality control of CIPP rehabilitation liners. The test aims to reproduce the working stress conditions of an installed CIPP liner to evaluate its hoop tensile strength. Although the traditional tensile test should be the most suitable test to assess the tensile properties of an installed liner due to its operational simplicity, the impracticality of extracting flat specimens in the hoop direction from an installed cylindrical liner makes the tensile test unfeasible. Consequently, current CIPP standards EN ISO 11296–4 [10] and ASTM F1216 [9] suggest using the three-point bending test to assess the hoop tensile performance of an installed liner. However, experimental evidence indicates that the bending test of curved samples overestimates the ultimate stresses of a cured CIPP liner by more than two times. Hence, the IBPT on ring

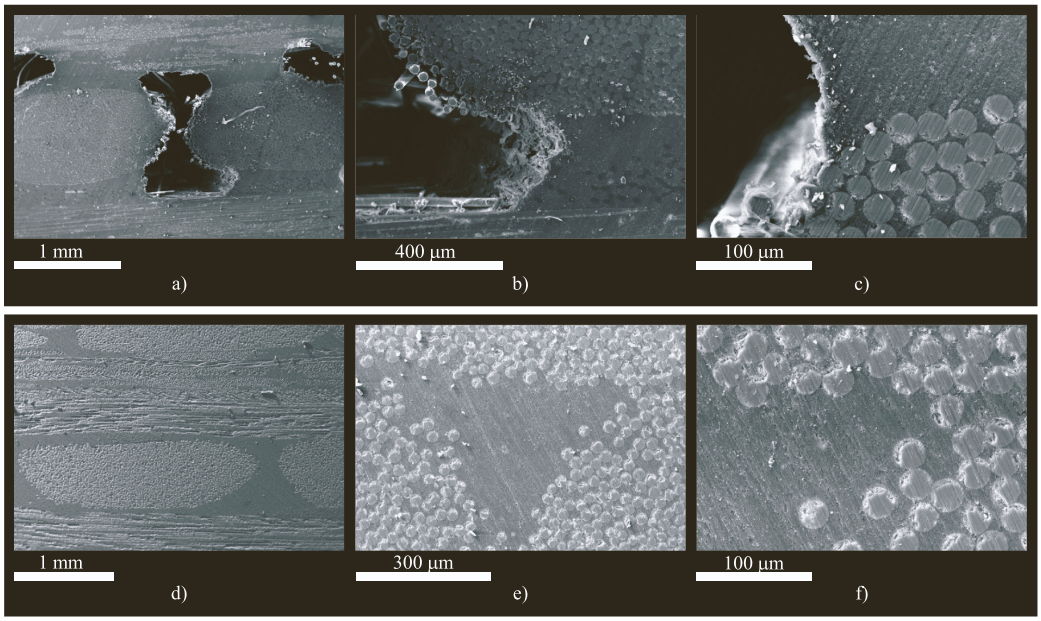

Fig. 21. Comparison of SEM microscopy images of the cross-section of a sample cured in laboratory conditions without compression pressure (a, b, and c), and cured by a certified installer with internal pressure (d, e, and f).

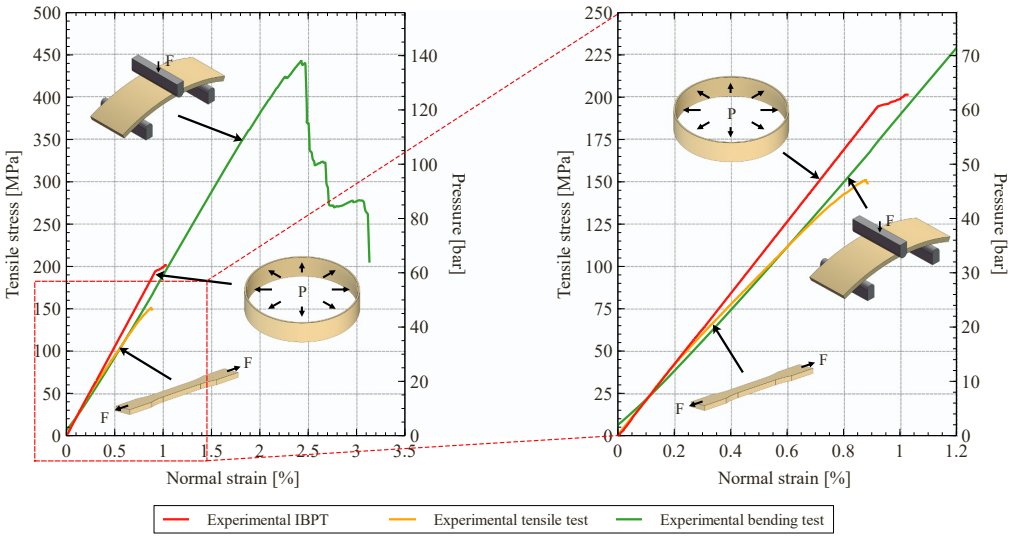

Fig. 22. Comparison between tensile, bending and IBPT of CIPP composite tests results.

samples is proposed as an alternative to the curved specimen bending test recommended by current CIPP standards. The proposed IBPT effectively addresses the limitations detected in the three-point bending test conducted on curved specimens. Furthermore, it provides a solution to the challenge of extracting flat samples in the hoop direction for the tensile test, as the IBPT is performed on ring samples, which can be easily cut on-site after the liner has been installed. Furthermore, the experimental results obtained with the IBPT show a high correlation with the flat specimen tests.

The experimental evidence provided in this study have a significant impact on the design of CIPP pressure pipe liners. Inadequate sizing of the structural reinforcement can compromise the functionality of the liner and the rehabilitation of the pipeline. Assuming a strength value higher than the actual strength of the liner means reducing the thickness required for rehabilitation. It is important to note that the relationship between the obtained burst pressure overestimates is close to the sizing safety coefficients. On the other hand, an oversizing of the liner increases the complexity of the installation, reduces its maneuverability, and requires a higher installation pressure. It also increases the likelihood of installation defects. Therefore, the repair or replacement of the rehabilitated pipe with installation defects may involve a higher cost than the initial replacement.

For all these reasons, correct sizing and quality control through representative tests increase the reliability of the rehabilitation system, reducing the uncertainties that limit the applicability of this technology. Consequently, the IBPT is a relevant contribution to the quality control of the CIPP industry. Therefore, this study provides a novel test that reduces the uncertainties related to the strength analysis of CIPP liners. Furthermore, it contributes to the optimization and advancement of existing design and quality control tests.

Declaration of Competing Interest

The authors declare that they have no known competing financial interests or personal relationships that could have appeared to influence the work reported in this paper.

Data availability

Data will be made available on request.

Acknowledgments

The authors would like to gratefully acknowledge the financial support provided by Agència de Gestió d'Ajuts Universitaris i de Recerca and the Pla de Doctorats Industrials del Department de Recerca i Universitats de la Generalitat de Catalunya with reference project 2019 DI45. The authors also appreciate the collaboration of companies SAERTEX multiCom Group and Aquatec S.A. for contributing materials, data, and services. Finally, a special mention to Ludwing Felipe Libreros from Aquatec S.A. and Timo Münstermann from SAERTEX multiCom Group.

References

[1] M.V. Seica, J.A. Packer, M.W. Grabinsky, B.J. Adams, Evaluation of the properties of Toronto iron water mains and surrounding soil, Can. J. Civ. Eng. 29 (2) (2002) 222–237, https://doi.org/10.1139/l01-090.
[2] ASCE (American Society of Civil Engineers), A Comprehensive Assessment of America's Infrastructure, Tech. rep., 2021.
[3] AEAS, AGA, XVI Estudio nacional de suministro de agua potable y saneamiento en España 2020, Tech. rep., Spain, 2020.
[4] E. Renaud, A. Husson, A. Vacelet, Y. LeGat, A.E. Stricker, Statistical modelling of French drinking water pipe inventory at national level using demographic and geographical information, H2Open J. 3 (1) (2020) 89–101, https://doi.org/10.2166/h2oj.2020.028.
[5] C. Berger, C. Falk, F. Hetzel, J. Pinnekamp, J. Ruppelt, P. Schleiffer, J. Schmitt, Zustand der Kanalisation in Deutschland: Ergebnisse der DWA-Umfrage 2020, KA Korresp. Abwasser Abfall 67 (12) (2020) 939–953, https://doi.org/10.3242/kae2020.12.001.
[6] Stratview Research Cured-In-Place Pipe (CIPP) Market by Pipe Diameter Type, by Resin Type, by Fabric Type, by Cure Type, by Weaving Type, by Coating Type, and by Region, Trend, Forecast, Competitive Analysis, and Growth Opportunity: 2018–2023, Tech. rep., 2018.
[7] S. Khan, C. Dobson, Trouble shooting for trenchless liner installation during sewer line rehabilitation, In: Proceedings of the Water Environment Federation, Vol. 1, Sacramento, California, 2006, pp. 5420–5435. ⟨10.2175/193864706783763192⟩.
[8] S. Das, A. Bayat, L. Gay, M. Salimi, J. Matthews, A comprehensive review on the challenges of cured-in-place pipe (CIPP) installations, J. Water Supply. Res. Technol. AQUA 65 (8) (2016) 583–596, https://doi.org/10.2166/aqua.2016.119.
[9] ASTM F1216, Standard Practice for Rehabilitation of Existing Pipelines and Conduits by the Inversion and Curing of a Resin-Impregnated Tube, ASTM International, West Conshohocken, PA, 2022. ⟨www.ASTM.org⟩.
[10] EN ISO 11296–4, Plastics Piping Systems for Renovation of Underground Non-pressure Drainage and Sewerage Networks - Part 4: Lining with Cured-in-place Pipes, 2018. ⟨www.iso.org⟩.
[11] ISO 11298–4, Plastics Piping Systems for Renovation of Underground Water Supply Networks – Part 4: Lining with Cured-in-place Pipes, 2021. ⟨www.iso.org⟩.
[12] H. Zhu, T. Wang, Y. Wang, V.C. Li, Trenchless rehabilitation for concrete pipelines of water infrastructure: a review from the structural perspective, Cem. Concr. Compos. 123 (2021), 104193, https://doi.org/10.1016/j.cemconcomp.2021.104193.
[13] UNE-EN ISO 11298–4, Sistemas de canalización en materiales plásticos para la renovación de redes de conducción de agua enterradas. Parte 4: Entubado continuo con tubo curado en obra, 2022. ⟨www.iso.org⟩.
[14] UNE 53929, Plásticos. Rehabilitación de conducciones de abastecimiento y alcantarillado con tubos continuos curados in situ (CIPP).Diseño, cálculo e instalación, 2022. ⟨www.une.org⟩.
[15] E.N. Allouche, G. Shanghai, M. Baumert, A. Amobi, K. Bainbridge, The design and performance of pressure pipe liners under static and cyclic loading, In: Proceedings of the Pipelines Congress 2008 – Pipeline Asset Management: Maximizing Performance of Our Pipeline Infrastructure, 321, 2008, pp. 1–10. ⟨10.1061/40994(321)38⟩.
[16] E.N. Allouche, K. Bainbridge, I.D. Moore, H.C. Council, Laboratory Examination of a Cured In Place Pressure Pipe Liner for Potable Water Distribution System, In: NASTT, No-Dig 2005, Vol. 13689, Orlando, Florida, 2005, pp. 1–10.
[17] A. Jaganathan, E. Allouche, M. Baumert, Experimental and numerical evaluation of the impact of folds on the pressure rating of CIPP liners, Tunn. Undergr. Space Technol. 22 (5–6) (2007) 666–678, https://doi.org/10.1016/j.tust.2006.11.007.
[18] Z. Yahong, H. Sheng, M. Baosong, Z. Cong, Y. Xuefeng, T. Zhongsen, L. Han, D. Caiying, Experiment and evaluation model of liner design for renewal of deteriorated reinforced concrete pipes utilizing cured-in-place-pipe technology, Tunn. Undergr. Space Technol. 132 (2023), https://doi.org/10.1016/j.tust.2022.104866.
[19] ASTM F2207, Standard Specification for Cured-in-Place Pipe Lining System for Rehabilitation of Metallic Gas Pipe, ASTM International, West Conshohocken, PA, 2019. ⟨www.astm.org⟩.
[20] N. Ampiah, A. Fam, I.D. Moore, Effect of wrinkles on the circumferential strength of a cast-in-place composite polymer liner used in retrofitting pressure pipes, J. Mater. Civ. Eng. 22 (12) (2010) 1304–1314, https://doi.org/10.1061/(ASCE)MT.1943-5533.0000160.

[21] N. Ampiah, A. Fam, I.D. Moore, Wavy imperfections and the strength of cast-in-place pressure pipe liners, In: Proceedings of the Pipelines Congress 2008 – Pipeline Asset Management: Maximizing Performance of Our Pipeline Infrastructure, 321, 2008. ⟨10.1061/40994(321)54⟩.
[22] E. Allouche, S. Alam, J. Simicevic, R. Sterling, W. Condit, J. Matthews, A. Selvakumar, A pilot study for retrospective evaluation of cured-in-place pipe (CIPP) rehabilitation of municipal gravity sewers, Tunn. Undergr. Space Technol. 39 (2014) 82–93, https://doi.org/10.1016/j.tust.2012.02.002.
[23] K. Yang, H. Fang, J. Bu, X. Zhang, B. Li, X. Du, Z. Zhang, Full-scale experimental investigation of the mechanical characteristics of corroded buried concrete pipes after cured-in-place-pipe rehabilitation, Tunn. Undergr. Space Technol. 117 (2021), 104153, https://doi.org/10.1016/j.tust.2021.104153.
[24] K. Yang, H. Fang, X. Zhang, B. Li, Q. Hu, Investigation of mechanical properties of corroded concrete pipes after cured-in-place-pipe (CIPP) rehabilitation under multi-field coupling, Tunn. Undergr. Space Technol. 128 (2022), https://doi.org/10.1016/j.tust.2022.104656.
[25] J.M. Hsu, K.J. Shou, Experimental study of the separated joint of an underground pipeline rehabilitated by cured-in-place pipe, Undergr. Space 7 (4) (2022) 543–563, https://doi.org/10.1016/j.undsp.2021.11.005.
[26] J.A. Hudson, H. Cardenas, J. Matthews, S. Alam, Performance evaluation of deteriorated and rehabilitated corrugated metal pipe culverts using multiphysics simulation, Tunn. Undergr. Space Technol. 131 (2022) (2023), 104827, https://doi.org/10.1016/j.tust.2022.104827.
[27] T. Abel, Laboratory tests and analysis of CIPP epoxy resin internal liners used in pipelines-part II: comparative analysis with the use of the FEM and engineering algorithms, Stud. Geotech. Mech. 43 (3) (2021) 307–322, https://doi.org/10.2478/sgem-2021-0007.
[28] X. Sun, M. He, Z. Li, Novel engineered wood and bamboo composites for structural applications: State-of-art of manufacturing technology and mechanical performance evaluation, Constr. Build. Mater. 249 (1239) (2020), 118751, https://doi.org/10.1016/j.conbuildmat.2020.118751.
[29] N.M. Nurazzi, M.R. Asyraf, S. FatimahAthiyah, S.S. Shazleen, S.A. Rafiqah, M.M. Harussani, S.H. Kamarudin, M.R. Razman, M. Rahmah, E.S. Zainudin, R. A. Ilyas, H.A. Aisyah, M.N. Norrrahim, N. Abdullah, S.M. Sapuan, A. Khalina, A review on mechanical performance of hybrid natural fiber polymer composites for structural applications, Polymers 13 (13) (2021) 1–47, https://doi.org/10.3390/polym13132170.
[30] Z. Kamble, B.K. Behera, Sustainable hybrid composites reinforced with textile waste for construction and building applications, Constr. Build. Mater. 284 (2021), 122800, https://doi.org/10.1016/j.conbuildmat.2021.122800.
[31] W. Fan, W. Dang, T. Liu, J. Li, L. Xue, L. Yuan, J. Dong, Fatigue behavior of the 3D orthogonal carbon/glass fibers hybrid composite under three-point bending load, Mater. Des. 183 (2019), 108112, https://doi.org/10.1016/j.matdes.2019.108112.
[32] X. Guijun, G. Rui, L. Chenggao, Combined effects of sustained bending loading, water immersion and fiber hybrid mode on the mechanical properties of carbon/glass fiber reinforced polymer composite, Compos. Struct. 281 (2022), 115060, https://doi.org/10.1016/j.compstruct.2021.115060.
[33] Y. Xia, M. Shi, C. Zhang, C. Wang, X. Sang, R. Liu, P. Zhao, G. An, H. Fang, Analysis of flexural failure mechanism of ultraviolet cured-in-place-pipe materials for buried pipelines rehabilitation based on curing temperature monitoring, Eng. Fail. Anal. 142 (2022), 106763, https://doi.org/10.1016/j.engfailanal.2022.106763.
[34] AWW Committee Report, Structural Classifications of Pressure Pipe Linings, Suggested Protocol for Product Classification, Tech. rep., 2019.
[35] ISO 11295, Classification and Information on Design and Applications of Plastics Piping Systems Used for Renovation and Replacement, 2018. ⟨www.iso.org⟩.
[36] ASTM D638, Standard Test Method for Tensile Properties of Plastics, ASTM International, West Conshohocken, PA, 2022. ⟨www.ASTM.org⟩.
[37] ISO 178, Determination of Flexural Properties Plastics – Determination of Flexural Properties, 2019. ⟨www.iso.org⟩.
[38] E.A. Campo. Selection of Polymeric Materials: How to Select Design Properties from Different Standards, first ed., William Andrew, 2008.

Publication II:

Optimizing thickness for semi-structural CIPP liners in pressure pipes: A mathematical modeling approach

Preprint submitted to Tunnelling and Underground Space Technology incorporating Trenchless Technology Research (June 2023)

Optimizing thickness for semi-structural CIPP liners in pressure pipes: A mathematical modeling approach

Ferran Gras-Travesset[a,b], Marco A. Pérez[a,*], Antoni Andreu Torras[b]

[a] *IQS School of Engineering, Universitat Ramon Llull, Via Augusta 390, 08017 Barcelona, Spain*
[b] *Aigües de Barcelona – General Batet, 1-7, Barcelona 08028 , Spain*

Abstract

This paper introduces a novel mathematical model to optimize the thickness of semi-structural liners in Cured-In-Place-Pipe (CIPP) rehabilitation based on the host pipe holes criterion defined in current standards. The model considers the residual structural mechanical properties of the damaged host pipe, and holes are defined considering the direction, the area, and the perimeter of the host pipe hole, providing a more accurate estimation of the liner behavior. Results indicate potential thickness reductions of 20-40% for circular holes, while non-circular holes offer even greater optimization possibilities ranging from 40 to 80%. Moreover, a full-scale test was conducted on a reinforced concrete host pipe of DN 400, damaged with three holes 150 mm in diameter. The full-scale test results were used to refine the numerical model employed in developing the mathematical model, ensuring its accuracy and reliability.

Keywords: CIPP, Semi-structural liner, Pressure pipes, Mathematical model, Holes criterion, Full-scale test

1. Introduction

Across the world, a vast network of pipelines provides drinking water to populations. However, these infrastructures are deteriorating in many countries due to their aging. For instance, according to AEAS and AGA (2020), approximately 26% of the distribution network is over 40 years old in Spain. The renewal rate needs to be increased. Only a 0.43% renewal is reached compared to the recommended 2% set by experts. Similarly, 44% of sewerage pipes have surpassed their life expectancy. Consequently, it is crucial to address the issue of infrastructure renewal in the following years. Nevertheless, replacing these pipes with conventional methods requires high costs and long execution times. Several countries have adopted trenchless technologies for pipe rehabilitation to overcome these challenges (Berger et al. (2020)). Among these technologies, Cured-In-Place Pipe (CIPP) has gained significant popularity in recent decades (Stratview Research (2018)). CIPP consists of inserting an initially flexible liner composed of fiber and resin, into the damaged pipe. Subsequently, the liner hardens to create a new pipe within the existing one.

*Corresponding author.
Email address: marcoantonio.perez@iqs.url.edu (Marco A. Pérez)

According to ASTM F1216 (2022) classification, CIPP liners are categorized into non-structural, semi-structural, and structural. Structural liners contain an important amount of reinforcement fibers. Thus, the liner can withstand both internal and external loads. In contrast, semi-structural liners rely on the residual strength of the original pipe and are only required to support internal loads in areas with cracks or holes. However, there is significant uncertainty in the field of CIPP (Das et al. (2016); Khan and Dobson (2006)), especially in pressure pipes. This uncertainty has led to a conservative trend favoring structural liners in projects where a semi-structural liner with reduced thickness and mechanical properties should be sufficient (Yahong et al. (2023))

However, several projects have demonstrated that oversizing a Cured-In-Place Pipe (CIPP) liner does not necessarily increase rehabilitation safety. An oversized liner contains a higher amount of fiber, increasing its cost and weight and making it more challenging to handle, as stated in section 7.5.2.3 of UNE 53929 (2022). As a result, the installation becomes more complex and increases the likelihood of installation defects that can negatively affect the mechanical properties of the liner. Furthermore, in most cases, when installation defects cannot be rectified, the rehabilitated pipe must be replaced. Therefore, in addition to the costs of rehabilitation, there is an additional cost of replacing the pipe that was initially intended to be avoided using CIPP. For these reasons, it is highly relevant to delve into the sizing of semi-structural liners. The advantage does not only rely on saving reinforcement material or reducing costs (Ji et al. (2020)) but also on the fact that semi-structural liners offer a simpler installation process.

Currently, liner sizing is primarily based on the use of analytical expressions with experimentally adjusted factors, as proposed in UNE 53929 (2022) and ASTM F1216 (2022). In some cases, finite element methods are employed for liner sizing (Shou and Chen (2018)). However, the high computational and time costs make their application impractical. On the other hand, in recent years, technological advancements have enabled the development of complex mathematical models, including machine learning. After a training process, these models can instantly provide results for complex calculations, overcoming the computational cost issue associated with finite element methods. Recently, several authors have successfully developed complex mathematical models with good performance in their respective fields (Genger and Hammad (2023); Lado-Roigé et al. (2023); Lado-Roigé and Pérez (2023); Xia et al. (2022)).

Therefore, this article proposes a new calculation methodology for sizing semi-structural liners using a mathematical model to optimize the sizing of CIPP liners. This approach significantly reduces the thickness of installed liners, reducing product costs and facilitating the installation process. Moreover, the probability of installation defects is reduced without compromising safety. The model was experimentally validated through a full-scale test.

2. Background

Several authors have investigated the impact of installation defects in Cured-In-Place Pipe (CIPP) liners (Gras-Travesset et al. (2023)). Allouche et al. (2005) identified the six limit states of CIPP that can cause instabilities due to internal pressure and uneven ground movements. Limit state LS5 considers the local bending of the liner through a hole in the host pipe. The same study numerically analyzed the presence of longitudinal wrinkles through a hole. It was concluded that this type of defect significantly and negatively affects the mechanical properties of the liner. Then, wrinkles were classified by Ampiah et al. (2008, 2010) based on their geometry as SW (only the inner layer lifts), IW (symmetric wrinkles), and LW (asymmetric wrinkles). Each type of wrinkle has its failure mechanism and decreases the mechanical properties of the liner to a greater or lesser extent.

In recent years, the liner's thickness calculation by the host pipe holes criterion has caught the attention of several authors (Allouche et al. (2008); Brown et al. (2020); He and Shawn (2019)). The behavior of the liner around holes (LS5) was studied numerically and experimentally by Allouche et al. (2008). The same study emphasizes the importance of investigating non-circular hole typologies and numerically analyzes elliptical and rectangular holes with equivalent areas to circular holes. It is worth noting that the hole calculation included in the ASTM F1216 (2022) and UNE 53929 (2022) standards only considers perfectly circular voids. However, it is difficult to find perfectly circular holes in deteriorated pipes. Figure 1 shows real cases of pressure pipe deterioration with different diameters and materials. As observed, the encountered holes can take shapes that deviate significantly from a perfect circle. Regarding the shape typologies, circular-like holes (f, g, i), longitudinal grooves (a, b), hoop grooves (c), angular grooves (d), and completely irregular shapes that do not resemble any specific geometric form (e, h) were identified. In these cases, hole calculations are performed in such a way that the non-circular hole is circumscribed within a circle (see Figure 6) using its diameter (d) in the hole calculation.

On the other hand, some numerical studies (Brown et al. (2020); He and Shawn (2019)) indicated that the behavior of a liner through a circular hole was not exactly governed by the analytical equation of a ring-in-tension described in ASTM F1216 (2022). He and Shawn (2019) concluded that for a ratio of hole diameter (d) to the inside diameter of the host pipe (D) greater than 0.4, the hoop stress decreases. In contrast to the ring-in-tension concept, the liner extends freely in the radial direction. The same study emphasizes the importance of correctly defining the friction coefficient between the host pipe and the liner in the simulations. The effect of friction between the liner and the host pipe was studied by Brown et al. (2020) using an orthotropic numerical model. The study concluded that friction reduces the liner stress in the host pipe hole area. Also, the usage of minimum friction conditions was recommended in numerical models (in the absence of experimental data) to obtain a conservative model.

Some authors (Allouche et al. (2008); Brown et al. (2020)) suggested adapting the mathematical model of ASTM

F2207-06 (2019) for non-circular holes in gas-rehabilitated pipes. The model is based on two liner failure criteria: the maximum stress criterion and the interactive stress criterion. In the maximum stress criterion, failure occurs when the liner reaches the maximum allowable stresses in either the hoop or longitudinal directions separately. On the other hand, the interactive criterion considers the interaction of stresses in both directions, causing the liner to fail before the ultimate hoop or ultimate longitudinal stresses of the liner are reached. Brown et al. (2020) concluded that for small holes governed by the equation of a flat plate subjected to bending (ASTM F1216 (2022)), the interactive stress criterion governed the model. However, the limiting factor for larger holes was primarily the maximum stress criterion, especially the hoop stress. It is important to note that the model is limited to the elastomer-fabric type orthotropic liners, where shear stiffness is either negligible or significantly smaller compared to the stiffness in the hoop and longitudinal directions. Nevertheless, ASTM F2207-06 (2019) is conservative and requires experimental testing of the detected holes, and then the worst-case scenario must define the liner thickness design.

Few authors have studied the behavior of an installed liner on a full-scale test subjected to both internal and external loads. However, in the available studies in the literature (Argyrou et al. (2019); Yang et al. (2021, 2022)), the host pipe used did not present holes. Therefore, comprehensive field testing is necessary to support the numerically developed theories by Allouche et al. (2008); Brown et al. (2020); He and Shawn (2019) for a specific type of liner and host pipe.

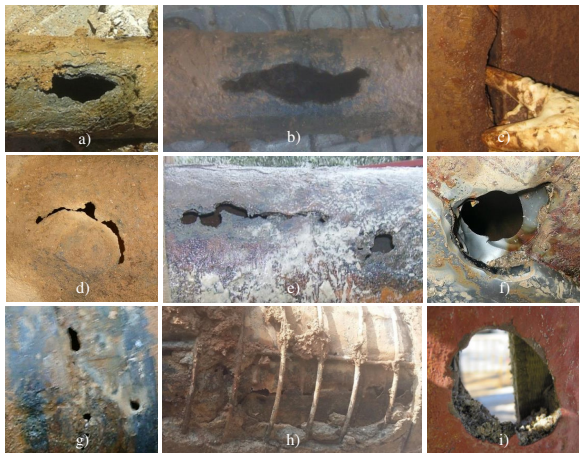

Figure 1: Examples of holes detected in damaged pipes.

3. Materials and methods

First, the design procedure for semi-structural liners of UNE 53929 (2022) and ASTM F1216 (2022) was analyzed to identify the predominant calculation criteria that, in most cases, define the final thickness of the liner. Next, the study focused on the calculation criterion for perfectly circular host pipe holes. Then, the analytical model proposed in ASTM F2207-06 (2019) for non-circular holes was analyzed. Finally, a numerical model was developed to establish a mathematical model for determining the thickness of a semi-structural liner when non-circular holes are detected in the host pipe. Prior, a full-scale test was conducted to validate the numerical model through a DN 400 host pipe damaged with three holes of diameter 150 mm.

3.1. CIPP liner used in simulations and experimental testing

The liner was composed of three layers of fiberglass and a polyethylene (PE) coating that prevents fiber migration into the drinking water. A styrene-free vinyl ester resin with minimal Volatile Organic Compound (VOC) content, specifically designed for Cured-In-Place Pipe applications and specific for drinking water pipes, was used. The resin was cured and therefore solidified through a UV curing process. To analyze the liner, a high-resolution Olympus DSX1000 digital microscope was employed (see Figure 2). The curing process took place under real installation conditions using a trolley equipped with nine 400 W UV lamps.

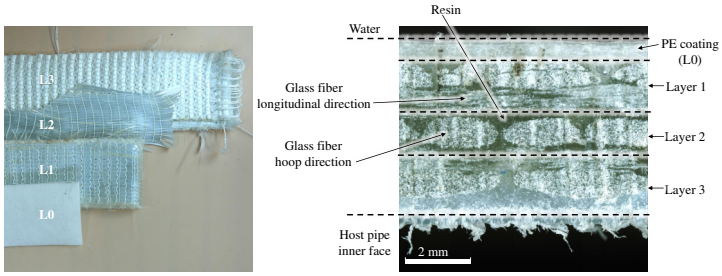

Liner. Layers assembly

Field cured liner. Composite inspection.

Figure 2: Morphology of the CIPP liner used for numerical and experimental tests.

3.2. Design of semi-structural liners

The design criteria of semi-structural CIPP liners defined in UNE 53929 (2022) and ASTM F1216 (2022) were thoroughly examined to determine the predominant criterion. The four analyzed calculation criteria are defined as hydraulic groundwater loads, ovality, holes, and negative pressure. In the negative pressure criterion, the liner must be designed as a gravity pipe with the external hydrostatic pressure increased by the negative pressure.

The analytical calculations used a hydraulic load enhancement factor K=7 (Aggarwal and Cooper (1984)). A percentage of ovality for the host pipe ranging from 0% to 10% was considered, as it represents the maximum allowable ovality according to UNE 53929 (2022) for CIPP rehabilitation. Circular holes in the host pipe were assumed for the calculations. The hole diameter to host pipe internal diameter ratio (d/D) ranging from 0 to 1 was studied. Additionally, a minimum groundwater pressure (P) of 0.015 MPa and a safety factor (N) of 2, according to UNE 53929 (2022), were considered. The study was conducted for a range of inner pressures P_I between 5 to 20 bar, and external loads were discarded as this study focuses on developing semi-structural liners.

The same liner described in the previous section was initially used. The liner had the following mechanical properties obtained from tensile tests: a short-term Young's modulus (E) of 20,600 MPa, corresponding to a long-term Young's modulus (E_L) (according to UNE 53929 (2022)) of 10,300 MPa, a Poisson's ratio (ν) of 0.3, and a short-term tensile strength (σ_T) of 204 MPa, corresponding to a long-term tensile stress (σ_{TL}) of 102 MPa. From EN ISO 11296-4 (2018) and ISO 178 (2019), a short-term flexural stress (σ_f) of 440 MPa and a long-term flexural stress (σ_{fL}) of 220 MPa were obtained.

Then, a second liner was used. Liner 2 met the minimum required properties for UV-cured fiber liners for pressure pipes according to UNE 53929 (2022), as specified in Table 13. The liner had a long-term Young's modulus (E_L) of 2,500 MPa, long-term flexural stress (σ_{fL}) of 51.5 MPa, and long-term tensile strength (σ_{TL}) of 10.5 MPa.

3.3. Full-scale test

The CIPP liner described in section 3.1 was used to rehabilitate a 6-meter out-of-service buried reinforced concrete pressure pipe of DN 400 mm. An extra meter of cast iron pipe was added to both ends to accommodate blind flanges and connect them to the ends of the reinforced concrete pipe. Thus, 8 meters of the liner were installed (fig. 3). The reinforced concrete pipe had a thickness of 70 mm, with only 2 meters in the middle section being semi-unburied. The top of the pipe in the middle section was left unburied for monitoring tasks. Before installing the liner, three holes of diameter ø150 mm were drilled at intervals of 0.5 meters (see Figure. 4). These holes were created to compromise the performance of the original pipe and to facilitate the installation of strain gauges onto the liner (fig. 3). Eight strain gauges were directly installed onto the liner through the pipe holes. Strain gauges 3, 8, 9, and 13 were installed in the hoop direction, while strain gauges 4, 7, 10, and 14 were installed in the longitudinal direction.

Additionally, strain gauges 1, 2, 5, 6, 11, 12, 15, and 16 were installed on the reinforced concrete pipe in the hoop direction to monitor the host pipe. Three displacement transducers were placed at the center of each hole, and two temperature sensors were used to calibrate the strain gauges. Furthermore, two pressure sensors, Wika A-10, were installed at the lowest points of the pipe ends. Data from the full-scale test were collected using HBM Quantum X MX840 B, Quantum X MX1615 B, and CatmanEasy AP software. Hydraulic pressure was applied to the test using

a 40-bar Rothenberger RP Pro III pump, reaching a maximum pressure of 25 bar. The test setup is illustrated in Figure. 3.

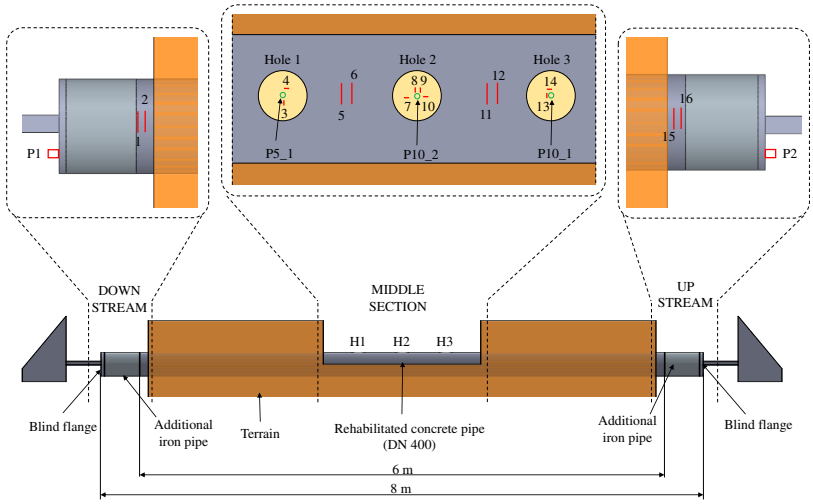

Figure 3: Schematic representation of the full-scale test setup showing the location of sensors and components employed in the test.

a) b) c)

Figure 4: Field view of the experimental setup and testing environment during the full-scale on-site test.

3.4. Numerical model

An implicit static structural Ansys model was created, adjusted, and validated using the results from the full-scale test. The model was focused on the central section, specifically the area around hole two. Only half pipe was represented (see Figure 5). The modeled host pipe had an inner diameter of 400 mm and an ovality of 1.28%. Additionally, a 6 mm thick orthotropic CIPP liner was represented in the model. A cylindrical coordinate system

was established, where the y-axis represented the circumferential direction, the z-axis represented the longitudinal direction, and the x-axis represented the radial direction (see Figure 5). The model was meshed using a 20-node higher-order Solid 186 element with a CIPP liner mesh size of 0.5 mm. The CIPP liner had the following mechanical properties: Young's modulus in the x-direction (E_x) of 11,000 MPa, Young's modulus in the y-direction (E_y) of 20,600 MPa, Young's modulus in the z-direction (E_z) of 11,000 MPa, Poisson's ratio (ν_{xy}, ν_{yz}, ν_{xz}) of 0.3, shear modulus in the xy-plane (τ_{xy}) of 7,000 MPa, shear modulus in the yz-plane (τ_{yz}) of 9,000 MPa, and shear modulus in the xz-plane (τ_{xz}) of 7,000 MPa. The mechanical properties of the host pipe were defined according to the Ansys database. The simulated reinforced concrete had a Young's modulus (E) of 30 GPa, Poisson's ratio (ν) of 0.18, and shear modulus (τ) of 12,712 MPa.

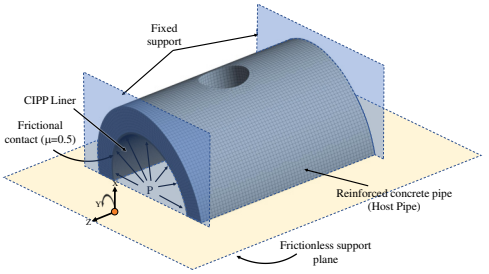

Figure 5: Schematic representation of the geometry and boundary conditions implemented in the numerical model.

A frictional contact with a coefficient of friction (μ) of 0.5 was defined between the outer surface of the CIPP liner and the inner surface of the host pipe in agreement with Brown et al. (2020). Fixed supports were defined at the end faces of the model, while a frictionless support plane was applied to the flat faces of the longitudinal section of the rehabilitated pipe. An inner pressure of 25 bar was also applied. Finally, the vertical displacement at the center of the hole, the hoop and longitudinal strains of the liner, and the hoop strain of the reinforced concrete pipe were read.

3.5. Mathematical model

A mathematical model based on the Gradient Boosting Regressor method was developed to optimize the thickness of a CIPP liner used to rehabilitate a host pipe with both circular and non-circular holes. The Huber Loss function was used as the loss function, as it minimizes the impact of outliers without completely disregarding them. This loss function combines squared and absolute errors in regression to optimize the solution, relying on previously known data points.

The numerical model, adjusted using the full-scale test results, was used to generate different scenarios of holes in the host pipe that a CIPP liner could be subjected to. Initially, simulations were conducted with circular holes, ac-

cording to UNE 53929 (2022) and ASTM F1216 (2022) guidelines. Then, the circular shape was gradually distorted, progressing to elliptical holes and eventually linear grooves. Finally, the linear grooves were deformed to obtain more complex shapes, such as angular grooves (fig. 7). It is worth noting that these four simulated hole types were inspired by real pipe holes (fig. 1).

Unlike UNE 53929 (2022) and ASTM F1216 (2022), in the model, a hole is defined by its maximum length in the longitudinal direction (a), the maximum length in the hoop direction (b), area, and perimeter (see Figure 6). It should be noted that all of the hole parameters definition are projected dimensions. The combinations of parameters used in the simulations are shown in Figure 7. A total of 14,646 simulations were performed, consisting of 23% circular holes, 20% ellipses, 25% linear grooves, and 33% angular grooves. 80% of the simulations were utilized for model construction, the remaining 20% were used for validation. First, the validation process was performed within the same hole class. Thus, a validation process was done for each hole class (circular, elliptical, linear grooves, and angular grooves). Finally, the overall model fit was assessed using mixed data from all four-hole classes.

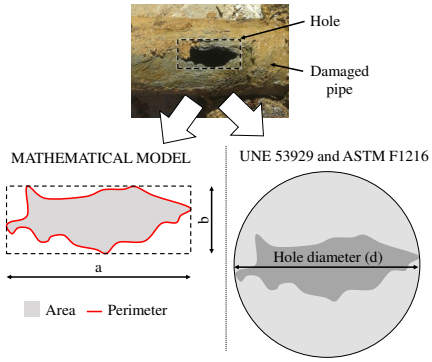

Figure 6: Comparison of hole definition in the mathematical model with the definitions outlined in UNE 53929 (2022) and ASTM F1216 (2022).

Model usage

There are two options to use the model. In option one, the liner thickness, the four-hole parameters (a, b, area, and perimeter), and the inner pressure of the pipe are defined as input values. Then, the maximum stress of the liner is obtained. In contrast, in option two the ultimate stress of the liner, the four (a,b, area, and perimeter) hole parameters, and the inner pressure of the pipe are defined as input values. Then, the thickness of the liner is obtained. This option should be used when designing a semi-structural liner. However, this study is limited to pipes of DN400 mm and CIPP liners that exhibit the mechanical properties described in section 3.4 within the elastic zone.

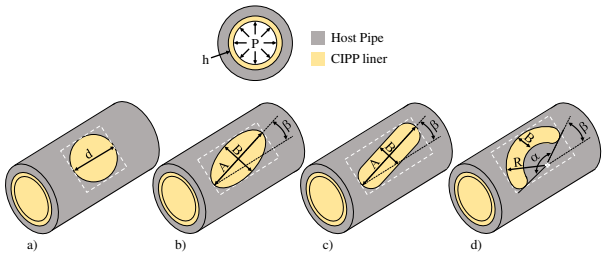

	Circular (a)		Ellipse (b)		Linear groove (c)		Angular groove (d)	
Parameter	Levels	Range	Levels	Range	Levels	Range	Levels	Range
d (mm)	37	40-400	-	-	-	-	-	-
A (mm)	-	-	9	80-360	6	50-300	-	-
B (mm)	-	-	6	(0.15-0.9)·A	4	10-40	4	90-180
β (°)	-	-	3	0-90	5	0-90	2	30-40
α (°)	-	-	-	-	-	-	5	0-90
R (mm)	-	-	-	-	-	-	4	150-350
P (bar)	10	5-25	3	5-25	5	5-25	5	5-25
h (mm)	9	2-10	6	2-7	6	2-7	6	2-7
Total	3330		2916		3600		4800	

Figure 7: Types of simulated holes in the study.

4. Results and discussion

4.1. Semi-structural liners design

In Figure 8, the influence of the three design criteria on the final thickness of the liner was examined. The negative pressure criterion was discarded as the studied cases did not involve vacuum conditions in the host pipe. The analysis was performed using the mechanical properties of liner one, also employed in the full-scale test of this study. Then, a second liner that presented the minimum mechanical properties set by UNE 53929 (2022) for UV-cured fiberglass pressure pipes was examined.

As observed, the hole calculation criterion (in red) in both cases defines the final liner thickness in most of the studied cases. Consequently, it is crucial to thoroughly analyze the hole calculation criterion to reduce the liner thickness to facilitate the installation process. Only with liner 1, at pressures of 5 bar, the calculation criterion for hydraulic groundwater loads prevails. This is due to the liner exhibiting significantly higher long-term hoop stress and long-term bending stress (10.5 and 4.3 times, respectively) compared to the minimum values recommended by UNE 53929 (2022) (liner 1: σ_{TL} = 110 MPa, σ_{fL} = 220 MPa, liner 2: σ_{TL} = 10.5 MPa, σ_{fL} = 51.5 MPa). These properties positively affect the ovality and hole criteria but do not have an impact on the hydraulic groundwater load criterion. However, the inner pressures in pressure pipes are usually higher than 5 bar. The inner pressure the liner must withstand in the areas where it is not confined by the host pipe due to the presence of holes generates significant

stresses in the liner, leading to the predominance of the hole criterion. Only when the hole diameter ratio to the host pipe's inner diameter is small (d/D ≤ 0.15) the hydraulic groundwater loads criterion dominates. This is because the cantilever generated by the hole is small, reducing bending stresses.

Furthermore, it is worth noting the absence of the ovality criterion. Even when the host pipe exhibits the maximum allowed ovality for CIPP rehabilitation (10%), the ovality criterion does not prevail in any of the studied cases. Thus, the flexural strength of the liner is sufficiently high to prevent the ovality criterion from having a significant impact. Notably, even in the case of liner 2, which possessed the minimum mechanical properties required by UNE 53929 (2022), the ovality criterion does not significantly impact the liner's final thickness.

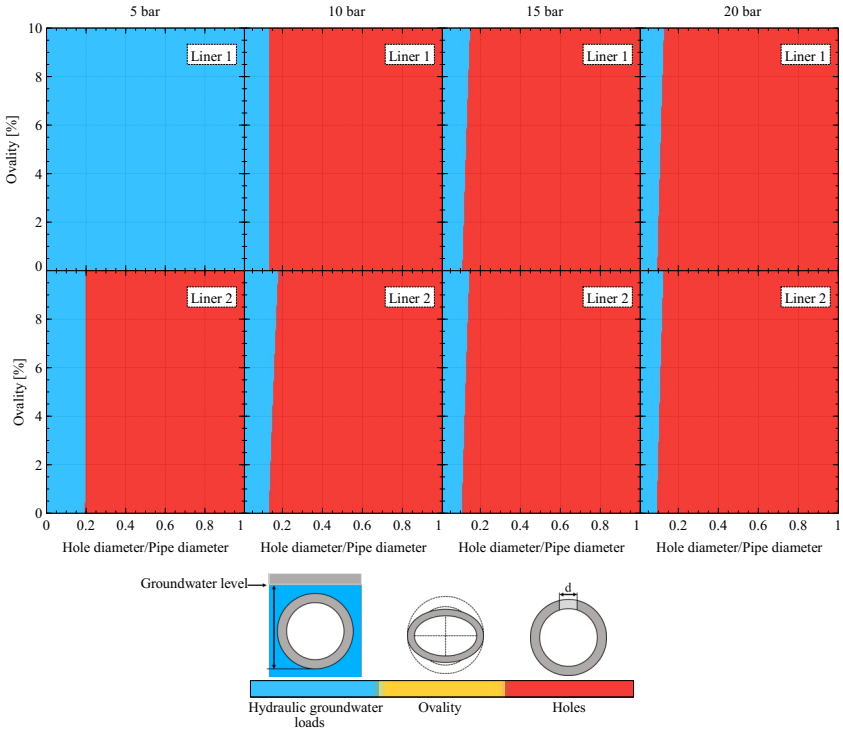

Figure 8: Analysis of the dominant thickness calculation criterion in the design of semi-structural liners. Liner 1: liner used in the full-scale test. Liner 2: liner that meets the minimum mechanical requirements established in UNE 53929 (2022).

Figure 9 displays the liner thickness obtained using the circular hole calculation criterion from UNE 53929 (2022), the numerical model, and the calculations from ASTM F2207-06 (2019). Circular holes and linear grooves were considered at 0° and 90° orientations. Among the studied shapes, the numerical model reveals that the largest liner

thicknesses are obtained in circular holes. Therefore, the analytical calculation based on UNE 53929 (2022) is conservative and encompasses the worst-case scenario, resulting in slight to significant oversizing of the liner depending on the hole geometry.

Regarding the analytical formulas for circular hole calculation according to UNE 53929 (2022) (Eq. 1 and Eq. 2), the numerical model indicates that Eq. 1, which considers a flat plate subjected to bending, correctly describes the behavior of the liner. However, the same level of accuracy is not observed when using the ring-in-tension model (Eq. 2). In this equation, the residual load-bearing capacity of the host pipe is completely disregarded. Nevertheless, the numerical model indicates that considering the host pipe's residual structural capacity, the liner thickness can be reduced by 19% to 44% for $d/D > 0.2$. Therefore, as it was suggested by He and Shawn (2019), the liner does not behave as a ring-in-tension.

$$t = \frac{IDx}{1 + \sqrt{5.33\left(\frac{IDx}{d}\right)^2 \frac{\sigma_{fL}}{NP_I}}} \tag{1}$$

Where t is the liner thickness (mm), IDx is the average inner diameter of the host pipe (mm), d is the hole diameter (mm), σ_{fL} is the long-term bending stress of the liner (MPa), P_I is the inner pressure (MPa), and N is the safety factor.

$$t = \frac{IDx}{2\left(1 + \frac{\sigma_{TL}}{NP_I}\right)} \tag{2}$$

Where σ_{TL} is the long-term tensile stress of the liner in the hoop direction (MPa).

When the hole is non-circular, such as a linear groove, UNE 53929 (2022) calculates it as if the groove was inscribed in a circumference (fig. 6). Then, when the ring-in-tension equation is used, thicknesses of 9.35 mm are obtained, while the numerical model indicates maximum thicknesses of 2.99 mm and 4.40 mm for hoop (90°) and longitudinal (0°) grooves, respectively. Therefore, a more significant reduction in the thickness of the liner can be achieved when the hole is non-circular. It is worth noting that the direction in which the groove is defined is crucial, being the hoop direction the most critical in line with conclusions from Allouche et al. (2008) when rectangular and elliptical-shaped holes were studied.

Finally, the results obtained from the mathematical model of ASTM F2207-06 (2019) for calculating non-circular holes were analyzed. As shown in Figure 9, the results obtained using the ASTM F2207-06 (2019) mathematical model in longitudinal grooves are in good agreement with the numerical model results. However, when the groove is rotated 90°, the results differ by 47% compared to the numerical model. On the other hand, when the holes are circular, the ASTM F2207-06 (2019) mathematical model shows significant discrepancies compared to the numerical model and UNE 53929 (2022). The mismatches detected in the ASTM F2207-06 (2019) mathematical model could be

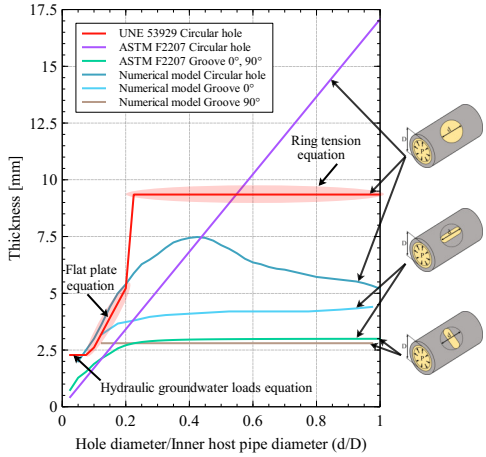

Figure 9: Effect of hole typology in the host pipe on the thickness of a semi-structural CIPP liner under pressure.

because the used liner had a non-zero shear modulus (7-9 GPa). Additionally, the ASTM F2207-06 (2019) mathematical model assumes that the deformation of the liner through the host pipe hole is defined as a circular arc. However, depending on the orifice geometry, the obtained deformation patterns often deviate significantly from a circular arc shape.

Figure 10 shows the deformations obtained using the numerical model for different types of holes in the host pipe. As can be observed, the deformations obtained do not exhibit a perfectly circular arc shape. In circular holes, the deformation acquires the shape of a dome with a non-constant radius. For non-circular holes, such as linear and angled grooves, the deformation deviates even further from a perfectly circular arc, resulting in a nearly flat zone in the central region.

Furthermore, the model presented in ASTM F2207-06 (2019) for calculating non-circular holes was analyzed. As shown in Figure 9, in the case of longitudinal grooves, the results obtained using the ASTM F2207-06 (2019) model are in good agreement with the numerical model results. However, when the linear groove is rotated 90°, the results differ by 47% compared to the numerical model. Regarding circular holes, the model presented by ASTM F2207-06 (2019) does not capture the parabolic behavior observed in the numerical model.

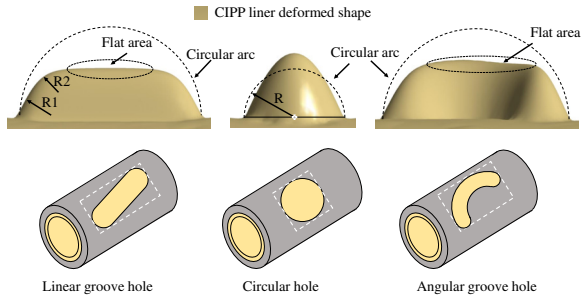

Figure 10: Comparison of deformed shapes: numerical model vs. circular arc assumption by ASTM F2207-06 (2019) for CIPP liner installed in a host pipe with holes.

4.2. Mathematical model proposed

4.2.1. Validation of the numerical model through the full-scale test

A representative result obtained from the on-site tests is presented in Figure 12. The tests were conducted up to a maximum pressure of 25 bar, considering safety and mechanical limitations. Strain gauges were strategically placed in the most critical direction, namely the hoop direction, as indicated by the strain gauge distribution in Figure 3. In agreement with the numerical model, no strain readings were observed on the concrete strain gauges (fig. 12 a)), despite the reinforced concrete pipe exhibiting significant damage with three ø150 mm holes (fig. 4 b)). This phenomenon suggests that the mechanical behavior of the full-scale test was primarily governed by the exceptional performance of the liner, owing to its substantial glass fiber content in the hoop direction. This finding reinforces the notion that the fiber content of the liner can be reduced, thereby facilitating its installation while still leveraging the residual structural capacity of the host pipe.

The analysis of the experimental data reveals a clear linear relationship between strain and pressure in the hoop direction, as depicted in Figure 12 c). However, in the longitudinal direction (fig. 12 b)), an initial accommodation phase was observed, indicating the liner was not perfectly in contact with the host pipe in the full-scale test. Some authors (Das et al. (2016); Ji et al. (2018)) reported a slight shrinkage of the resin during the UV curing process that could explain the lack of contact between the liner and the host pipe at the top. Consequently, the liner behavior can be considered as a ring-in-tension until full contact with the host pipe is reached. Thus, the hoop strain starts raising while the longitudinal strain remains nearly zero until contact is achieved and the liner starts to spread over the host pipe hole. The accommodation process observed in Figure 12 b) finishes at almost 5 bar of pressure corresponding to a vertical displacement of the liner of 0.25 mm according to fig. 12 d). The initial gap of 0.25 mm was introduced in the numerical model. Then, the results of fig. 12 b) indicate that the numerical model is in good agreement with the

full-scale test, and the initial accommodation in the numerical model is reproduced in the longitudinal strain while the hoop strain remains linear according to the full-scale test strain readings.

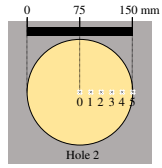

Point	ε_h (μm/m)	Level (mm)
0	5648	75
1	4521	90
2	2906	105
3	1214	120
4	617	135
5	38	150

Figure 11: Hoop strain variation analysis along hole 2 at P=25 bar using the adjusted numerical model

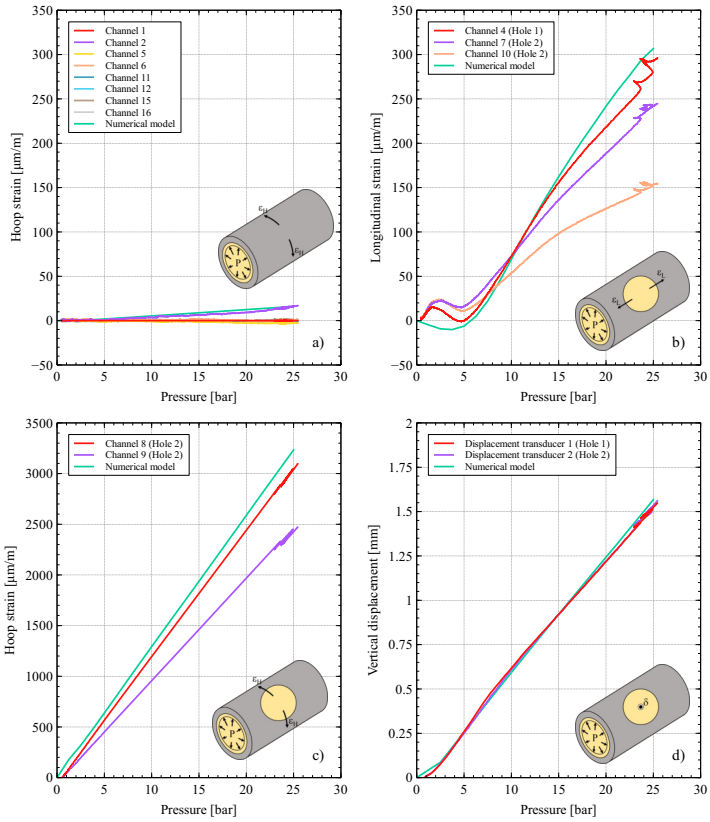

Figure 12: Results of the full-scale test: a) Concrete's hoop strain. b) CIPP liner's longitudinal strain. c) CIPP liner's hoop strain. d) Vertical displacement of the liner at the center of the hole.

Furthermore, in Figure 12 d), the vertical displacement sensors $P5\_1$ and $P10\_2$ placed at the center of holes one and two exhibited identical behavior throughout the test, reaching δ=1.55 mm and δ=1.56 mm. The numerical model was also in good agreement with the experimental vertical displacements reaching 1.57 mm at the center of the hole.

However, differences between strain readings from different strain gauges can be observed in Figures 12 b) and c). Results from the numerical model in Figure 11 revealed that the measurement location of the strain within the hole has a significant effect. The observed experimental strain reading differences between channels are attributed to this phenomenon. For example, in Hole 2, a maximum hoop strain (ε_h) of 2471 μm/m was obtained in channel 9, while 3096 μm/m was reported in channel 8, resulting in a 25% increase. Both strain gauges were separated by 20 mm. Similarly, in the longitudinal direction, the same phenomenon was observed. The strain gauges installed in the same hole (channel 7 and channel 10) exhibit a notable strain difference, with channel 7 recording 94 μm/m higher than channel 10. Installing both strain gauges at the same point, or even a few millimeters apart, was impossible due to operational difficulties and challenging field conditions. In contrast, the longitudinal strains (ε_L) measured in different holes, Hole 1 (ch4 ε_L=295 μm/m) and Hole 2 (ch7 ε_L=243 μm/m), demonstrated similar behavior.

4.2.2. Validation of the Mathematical Model

In Figure 13, the ultimate hoop stress predicted by the mathematical model was compared with those obtained from the numerical model under the same hole, pressure, and CIPP liner conditions. As shown in Figure 13, the best fit was achieved with the circular hole type. The coefficient of determination of 0.994 validates the robustness of the model for the only type of hole considered by the current regulations (UNE 53929 (2022) and ASTM F1216 (2022)).

Regarding other types of holes, although there is a slight decrease of 0.03 in the coefficient of determination, as the hole shape deviates from a perfect circle, the model continues to exhibit a good fit with coefficients of determination close to 1 (ellipses R^2=0.986, grooves R^2=0.962, and angular grooves R^2=0.967). This finding demonstrates that the model can accurately predict results for circular holes and provides acceptable predictions for non-circular holes commonly found in current pipelines, such as grooves (fig 1). Finally, in the overall validation of the model, when 20% of the simulations from each hole class mixed were used, a coefficient of determination of 0.980 was obtained, in agreement with the individual results from each hole class.

4.2.3. Thickness reduction

Figures 14 and 15 illustrate the thickness reduction achieved using the mathematical model compared to the thickness obtained through the analytical equations of hole calculation provided by UNE 53929 (2022) and ASTM F1216 (2022) standards. The calculation was performed for three different pressures (5, 15, and 25 bar), for a ratio of host pipe hole diameter to pipe diameter (d/D) ranging from 0 to 1, and a range of liner's ultimate hoop stress from

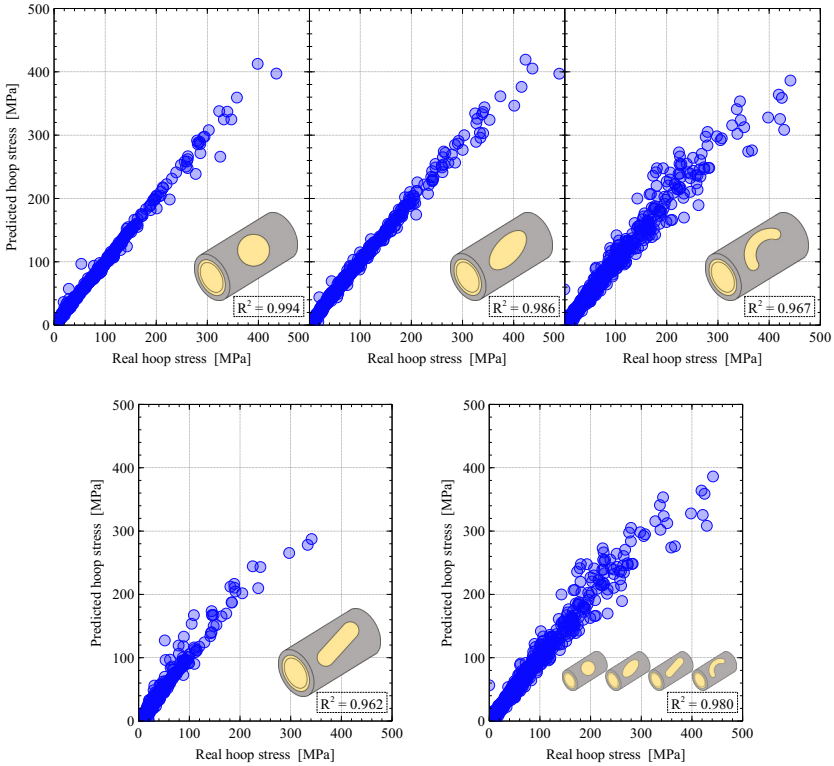

Figure 13: Comparison of the ultimate hoop stress calculated according to the mathematical model with the ultimate hoop stress obtained using the numerical model under the same conditions.

10.5 to 300 MPa. The minimum hoop stress required by UNE 53929 (2022) for pressure liners is 10.5 MPa.

It is worth noting that only calculated liners with a minimum thickness of 3 mm are represented. Liners with thickness below this threshold are difficult to install and are susceptible to collapse, as indicated by UNE 53929 (2022). Moreover, when the thickness defined by the hole criterion is low, the hydraulic groundwater loads criterion is usually the limiting factor, as can be seen in Figure. 8. For instance, in Figure. 9, a liner thickness slightly below 3 mm was observed using the UNE 53929 (2022) hydraulic groundwater loads criterion when the host pipe presented small holes (d/D < 0.1). As the pressure increases, more data points are represented in Figures 14 and 15 due to larger liner thicknesses obtained as expected.

Regarding perfectly circular holes, in most cases, the mathematical model demonstrates a 20-40% reduction in

liner thickness compared to the analytical equations provided by UNE 53929 (2022) and ASTM F1216 (2022) standards. However, this reduction was achieved for holes of a specific size calculated using the ring-in-tension equation. In contrast, for small holes, the standard calculations of the thickness of the liner are based on the flat plate bending equation. In these cases, as seen in the 25 bar scenario (d/D < 0.23), the mathematical model shows no thickness reduction, demonstrating the analytical equation's validity, as previously observed in Figure 9 with the comparison against the numerical model.

However, the thickness reduction achieved by the mathematical model increases as the shape of the hole deviates from a perfect circle. Figure 14 shows holes at 0° of the following shape classes: ellipses with a B/A ratio of 0.3, linear grooves with a width (B) of 30 mm, and angular grooves with an angle (α) of 180° and width (B) of 30 mm (see Figure 7). In ellipses holes, the areas with a thickness reduction between 40-60% (green) and 60-80% (ocher) have increased compared to circular holes results, although areas with a reduction below 40% still have an important role. When the deformation of the circumference is complete, for example, linear grooves, the achieved thickness reduction ranges from 40-60% for high hoop stresses and 60-80% for low hoop stresses. Finally, for more complex hole shapes, such as angular grooves, the reduction stabilizes between 40-80% for most of the studied cases.

On the other hand, the thickness reduction is even more significant when non-circular holes were oriented at 90° (fig. 15). In this position, the longitudinal dimension (a) is smaller than the hoop dimension (b) (see fig. 6). Consequently, a smaller longitudinal area of the hole is subjected to significant hoop stress as previously suggested Allouche et al. (2008). Specifically, compared to the same holes at 0°, an increase in thickness reduction of 20% for ellipses, 40% for linear grooves, and 20% for angular grooves was obtained. In the case of linear grooves, reductions up to 80-90% compared to the thickness defined by UNE 53929 (2022) and ASTM F1216 (2022) were achieved. Thus, it can be concluded that linear hoop grooves are the most unfavorable shape studied as they have a lower a/b ratio. It is worth noting that UNE 53929 (2022) and ASTM F1216 (2022) standards do not differentiate if the non-circular hole is oriented in a more or less unfavorable direction since all holes are considered circular. Therefore, the oversizing of the liner is considerably greater when the non-circular hole is oriented in the circumferential direction (90°).

The reduction of the CIPP liner's thickness is crucial. The economic weight of a liner oscillates between 40-70% of the total cost of the work for DN300-DN1000. In addition to the economic benefits, reducing the liner thickness also improves its maneuverability. Consequently, the installation process becomes easier, reducing the likelihood of installation defects that could leave the rehabilitated pipe out of service and cause severe damage to third parties.

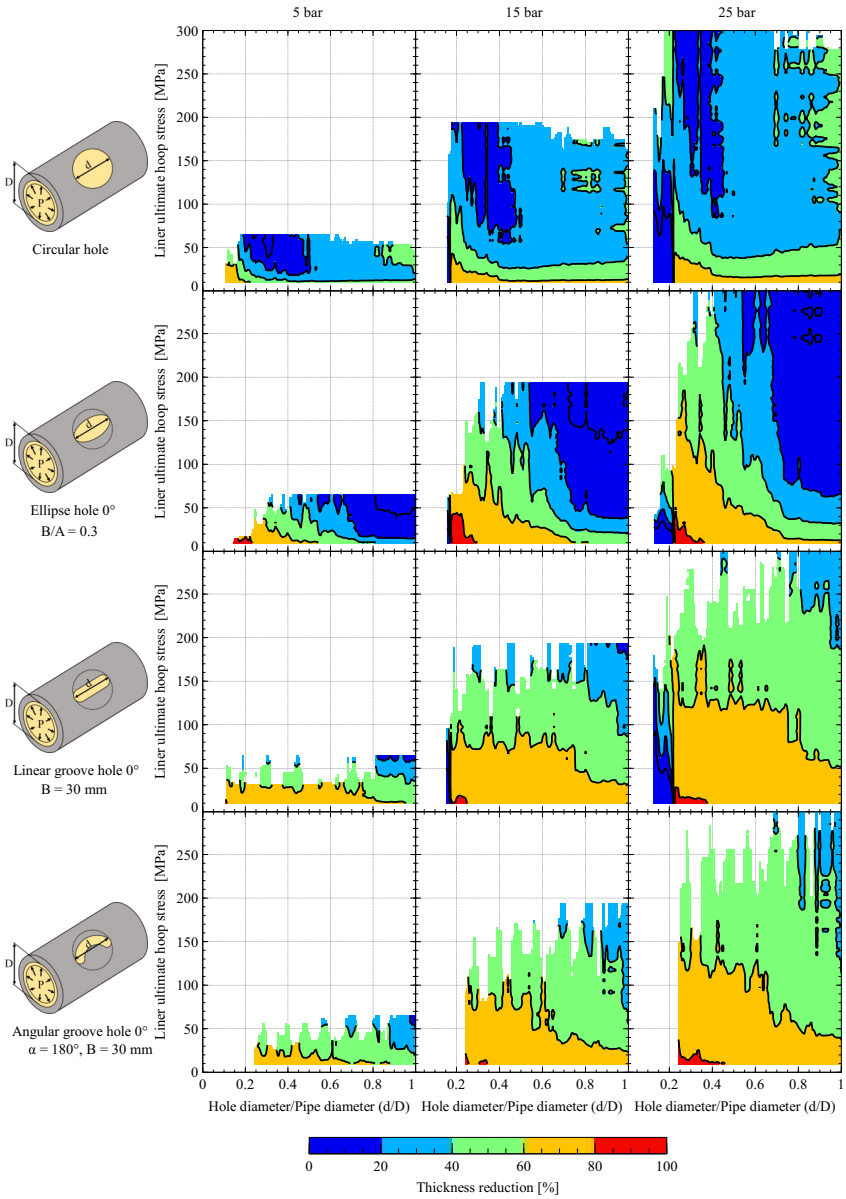

Figure 14: Thickness reduction achieved through the mathematical model compared to that proposed by UNE 53929 (2022) and ASTM F1216 (2022). Circular and non-circular holes: ellipses, linear grooves, and angular grooves at 0°.

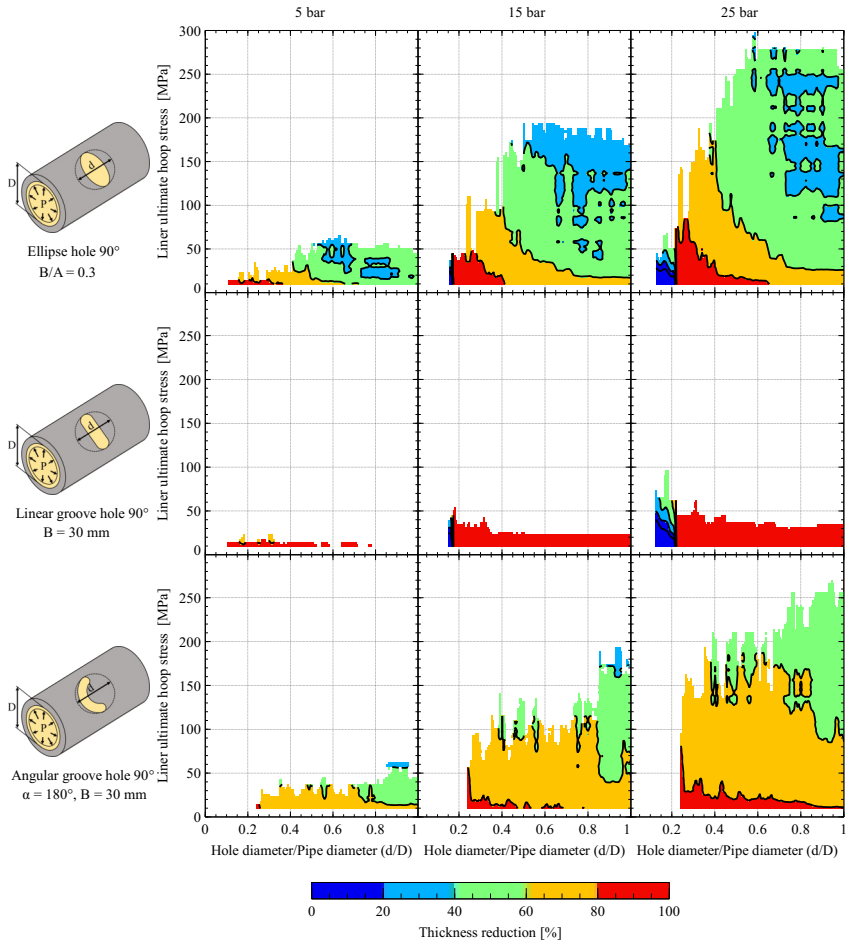

Figure 15: Thickness reduction achieved through the mathematical model compared to that proposed by UNE 53929 (2022) and ASTM F1216 (2022). Ellipses, linear grooves, and angular grooves at 90°.

4.2.4. Application of the mathematical model in real scenarios

Finally, in Figure 16, the mathematical model was tested under real host pipe holes subjected to 15 bars. The mechanical properties of liner 1 described in Section 3.1 was used, except for the ultimate hoop stress of the liner, which is shown in Figure 16. The results have been compared to the numerical finite element model. As seen in Figure 16, the UNE 53929 (2022) standard exhibits an overestimation ranging from 2.7 to 9.7 times the optimal thickness obtained by the finite element analysis.

However, when the hole shape is similar to a perfect circle, such as in holes 5 and 6, the relative error obtained using the UNE 53929 (2022) standard was around 20-40%, consistent with the reduction observed for circular holes in Figure 14. On the other hand, the mathematical model achieves better accuracy in all cases studied, differing by only -1.3% for the nearly circular hole (hole 5) and 18.2% in the worst case, which still represents an acceptable deviation of 0.5 mm in the final thickness of the CIPP liner.

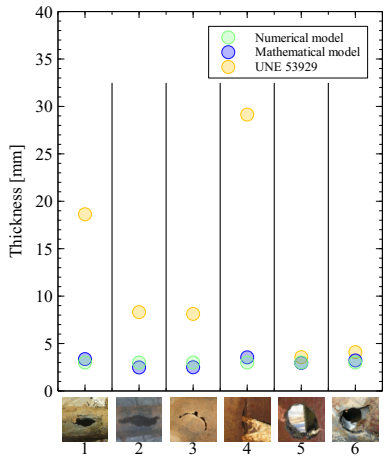

Hole	Numerical model		Mathematical model		UNE 53929	
	σ_h (MPa)	t (mm)	t (mm)	RE[1] (%)	t (mm)	RE[1] (%)
1	29.2	3	3.4	12.0	18.6	520.9
2	69.2	3	2.5	-17.2	8.3	177.1
3	70.8	3	2.5	-16.7	8.1	170.9
4	17.6	3	3.5	18.2	29.1	871.5
5	165.3	3	3.0	-1.3	3.6	18.8
6	143.4	3	3.2	7.3	4.1	36.6

[1]Relative error

Figure 16: Thickness determination of a CIPP liner subjected to a pressure of 25 bar and host pipe holes observed in real projects.

5. Conclusions

According to ASTM F1216 (2022) and UNE 53929 (2022), the hole calculation criterion prevails in semi-structural liners design. The flat plate bending model used for small holes performs accurately according to the simulations. However, for larger holes, the ring-in-tension model should be used to calculate the liner thickness, which completely disregards the residual structural contribution of the host pipe. Nevertheless, the numerical model adjusted through a full-scale test, where the host pipe had significant damage (holes of d/D=0.38), demonstrates that a severely damaged host pipe still provides a noticeable structural contribution, allowing for optimization of current liners by 20-40% in the case of perfectly circular holes calculated as a ring-in-tension.

The circular hole represents the worst-case scenario and is the only one considered by ASTM F1216 (2022) and UNE 53929 (2022). Consequently, thickness reductions are more significant when considering the hole shape. The mathematical model reveals that it is possible to optimize the liner thickness by 40% in ellipses, 40-80% in linear grooves, and 40-80% in angular grooves positioned in the longitudinal direction (0°). These thickness reductions

increase by 20%, 40%, and 20%, respectively, when positioned in the hoop direction (90°). Therefore, the hole orientation is crucial, with the hoop direction being the most critical.

A closer approach to the real liner behavior through a host pipe hole was achieved as the developed mathematical model considers the hole direction, the area, and the perimeter of the hole. Results from the global validation process (R^2 of 0.980) and the real host pipe holes studied demonstrate the validity of the mathematical model. In real host pipe holes, a maximum deviation in the thickness of the liner of less than 0.5 mm (18.2% error) was achieved. In contrast, 26.1 mm (871.5% error) was obtained through the analytical calculation of UNE 53929 (2022) and ASTM F1216 (2022).

The significant reduction in thickness achieved by the developed mathematical model for semi-structural liners not only reduces the economic costs of CIPP rehabilitation but also enhances the maneuverability and light weight of the liner, thereby facilitating the installation process. Thus, the risk of having installation defects is minimized and prevents potential problems that may arise shortly after a bad installation. Consequently, severe damage caused by the failure of a pressure pipe is avoided. Thus, the model's capability to reduce thickness contributes to cost savings, enhances installation efficiency, and reduces the likelihood of future complications, ensuring the longevity and reliability of the rehabilitated pipelines.

Acknowledgements

The authors would like to gratefully acknowledge the financial support provided by Agència de Gestió d'Ajuts Universitaris i de Recerca and the Pla de Doctorats Industrials del Department de Recerca i Universitats de la Generalitat de Catalunya with reference project 2019 DI45. The authors also appreciate the collaboration of companies SAERTEX multiCom Group and Aquatec S.A. for contributing materials, data, and services. Finally, a special mention to Ludwing Felipe Libreros from Aquatec S.A. and Timo Münstermann from SAERTEX multiCom Group.

Declaration of Competing Interest

The authors declare that they have no known competing financial interests or personal relationships that could appear to influence the work reported in this paper.

References

AEAS, AGA, 2020. XVI Estudio nacional de suministro de agua potable y saneamiento en España 2020. Technical Report. Spain.

Aggarwal, S., Cooper, M., 1984. External pressure testing of 'Insituform' linings, Internal Report, Coventry (Lanchester), Polytechnic, UK .

Allouche, E.N., Bainbridge, K., Moore, I.D., Council, H.C., 2005. Laboratory Examination of a Cured In Place Pressure Pipe Liner for Potable Water Distribution System. North American Society for Trenchless Technology (NASTT) 13689, 1–10.

Allouche, E.N., Shanghai, G., Baumert, M., Amobi, A., Bainbridge, K., 2008. The design and performance of pressure pipe liners under static and cyclic loading, in: Proceedings of Pipelines Congress 2008 - Pipeline Asset Management: Maximizing Performance of Our Pipeline Infrastructure, pp. 1–10. doi:10.1061/40994(321)38.

Ampiah, N., Fam, A., Moore, I.D., 2008. Wavy imperfections and the strength of cast-in-place pressure pipe liners, in: Proceedings of Pipelines Congress 2008 - Pipeline Asset Management: Maximizing Performance of Our Pipeline Infrastructure. doi:10.1061/40994(321)54.

Ampiah, N., Fam, A., Moore, I.D., 2010. Effect of Wrinkles on the Circumferential Strength of a Cast-in-Place Composite Polymer Liner Used in Retrofitting Pressure Pipes. J. Mater. Civ. Eng. , 1304–1314.

Argyrou, C., O'Rourke, T.D., Stewart, H.E., Wham, B.P., 2019. Large-Scale Fault Rupture Tests on Pipelines Reinforced with Cured-in-Place Linings. J geotech geoenviron. 145, 1–11. doi:10.1061/(ASCE)GT.1943-5606.0002018.

ASTM F1216, 2022. Standard Practice for Rehabilitation of Existing Pipelines and Conduits by the Inversion and Curing of a Resin-Impregnated Tube, ASTM International, West Conshohocken, PA, URL www.astm.org.

ASTM F2207-06, 2019. Standard Specification for Cured-in-Place Pipe Lining System for Rehabilitation of Metallic Gas Pipe, ASTM International, West Conshohocken, PA, URL www.astm.org.

Berger, C., Falk, C., Hetzel, F., Pinnekamp, J., Ruppelt, J., Schleiffer, P., Schmitt, J., 2020. Zustand der Kanalisation in Deutschland : Ergebnisse der DWA-Umfrage 2020. KA : Korrespondenz Abwasser, Abfall 67, 939–953. doi:10.3242/kae2020.12.001.

Brown, M.J., Moore, I.D., Fam, A., 2020. Analysis of a cured-in-place pressure pipe liner spanning circular voids. Tunnelling and Underground Space Technology 101, 103424. URL: https://doi.org/10.1016/j.tust.2020.103424, doi:10.1016/j.tust.2020.103424.

Das, S., Bayat, A., Gay, L., Salimi, M., Matthews, J., 2016. A comprehensive review on the challenges of cured-in-place pipe (CIPP) installations. J. Water Supply: Res. Technol. - AQUA 65, 583–596. doi:10.2166/aqua.2016.119.

EN ISO 11296-4, 2018. Plastics piping systems for renovation of underground non-pressure drainage and sewerage networks - Part 4: Lining with cured-in-place pipes, URL www.iso.org.

Genger, K.T., Hammad, A., 2023. Street closure prediction based on the combined conditions of spatially collocated municipal infrastructure assets at the segment level. Expert Systems with Applications doi:https://doi.org/10.1016/j.eswa.2023.119671.

Gras-Travesset, F., Pérez, M.A., Andreu Torras, A., 2023. A novel test procedure to assess the performance of composite cured-in-place-pipe liners for rehabilitation of water pressure pipes. [Submitted for publication] .

He, X., Shawn, K., 2019. Mechanical performance of a pressure pipe CIPP liner with stress concentration effects associated with local defects, in: Conference on Pipeline Engineering - Concepts in Harmony, pp. 515–527.

ISO 178, 2019. Plastics, Determination of flexural properties Plastics - Determination of flexural properties, URL www.iso.org.

Ji, H.W., Koo, D.D., Kang, J.H., 2020. Short-and long-term structural characterization of cured-in-place pipe liner with reinforced glass fiber material. International Journal of Environmental Research and Public Health 17, 1–15. doi:10.3390/ijerph17062073.

Ji, H.W., Yoo, S.S., Kim, J., Koo, D.D., 2018. The mechanical properties of high strength reinforced Cured-in-Place Pipe (CIPP) liner composites for urbanwater infrastructure rehabilitation. Water (Switzerland) 10, 1–12. doi:10.3390/w10080983.

Khan, S., Dobson, C., 2006. Trouble Shooting for Trenchless Liner Installation During Sewer Line Rehabilitation, in: Proceedings of the Water Environment Federation, Sacramento, California. pp. 5420–5435. doi:10.2175/193864706783763192.

Lado-Roigé, R., Font-Moré, J., Pérez, M.A., 2023. Learning-based video motion magnification approach for vibration-based damage detection. Measurement: Journal of the International Measurement Confederation 206, 112218. URL: https://doi.org/10.1016/j.measurement.2022.112218.

Lado-Roigé, R., Pérez, M.A., 2023. STB-VMM: Swin Transformer Based Video Motion Magnification. Knowledge-Based Systems 269, 110493. doi:10.1016/j.knosys.2023.110493, arXiv:2302.10001.

Shou, K.J., Chen, B.C., 2018. Numerical analysis of the mechanical behaviors of pressurized underground pipelines rehabilitated by cured-in-place-pipe method. Tunnelling and Underground Space Technology 71, 544–554. URL: http://dx.doi.org/10.1016/j.tust.2017.11.005.

Stratview Research, 2018. Cured-In-Place Pipe (CIPP) Market by Pipe Diameter Type, by Resin Type, by Fabric Type, by Cure Type, by Weaving Type, by Coating Type, and by Region, Trend, Forecast, Competitive Analysis, and Growth Opportunity: 2018-2023. Technical Report.

UNE 53929, 2022. Plásticos. Rehabilitación de conducciones de abastecimiento y alcantarillado con tubos continuos curados in situ (CIPP). Diseño, cálculo e instalación, URL www.une.org .

Xia, Y., Shi, M., Zhang, C., Wang, C., Sang, X., Liu, R., Zhao, P., An, G., Fang, H., 2022. Analysis of flexural failure mechanism of ultraviolet cured-in-place-pipe materials for buried pipelines rehabilitation based on curing temperature monitoring. Engineering Failure Analysis 142. doi:https://doi.org/10.1016/j.engfailanal.2022.106763.

Yahong, Z., Sheng, H., Baosong, M., Cong, Z., Xuefeng, Y., Zhongsen, T., Han, L., Caiying, D., 2023. Experiment and evaluation model of liner design for renewal of deteriorated reinforced concrete pipes utilizing cured-in-place-pipe technology. Tunnelling and Underground Space Technology 132. doi:https://doi.org/10.1016/j.tust.2022.104866.

Yang, K., Fang, H., Bu, J., Zhang, X., Li, B., Du, X., Zhang, Z., 2021. Full-scale experimental investigation of the mechanical characteristics of corroded buried concrete pipes after cured-in-place-pipe rehabilitation. Tunnelling and Underground Space Technology 117, 104153. URL: https://doi.org/10.1016/j.tust.2021.104153.

Yang, K., Fang, H., Zhang, X., Li, B., Hu, Q., 2022. Investigation of mechanical properties of corroded concrete pipes after cured-in-place-pipe (CIPP) rehabilitation under multi-field coupling. Tunnelling and Underground Space Technology 128. doi:10.1016/j.tust.2022.104656.

References

1. UNE 53929. Plásticos. Rehabilitación de conducciones de abastecimiento y alcantarillado con tubos continuos curados in situ (CIPP). Diseño, cálculo e instalación, URL www.une.org (2022).
2. ASCE (American Society of Civil Engineers). *A comprehensive assessment of america's infrastructure* tech. rep. (2021), 168.
3. AEAS & AGA. *XVI Estudio nacional de suministro de agua potable y saneamiento en España 2020* tech. rep. (Spain, 2020).
4. Renaud, E., Husson, A., Vacelet, A., Le Gat, Y. & Stricker, A. E. Statistical modelling of French drinking water pipe inventory at national level using demographic and geographical information. *H2Open J.* **3,** 89–101. doi:10.2166/h2oj.2020.028 (2020).
5. Berger, C. *et al.* Zustand der Kanalisation in Deutschland : Ergebnisse der DWA-Umfrage 2020. *KA : Korrespondenz Abwasser, Abfall* **67,** 939–953. doi:10.3242/kae2020.12.001 (2020).
6. Stratview Research. *Cured-In-Place Pipe (CIPP) Market by Pipe Diameter Type, by Resin Type, by Fabric Type, by Cure Type, by Weaving Type, by Coating Type, and by Region, Trend, Forecast, Competitive Analysis, and Growth Opportunity: 2018-2023* tech. rep. (2018), 336.
7. Stratview Research. *Cured-in-Place Pipe Market Size, Share, Trend, Forecast, Competitive Analysis, and Growth opportunity: 2023-2028* tech. rep. (2023), 140.
8. ASTM F1216. *Standard Practice for Rehabilitation of Existing Pipelines and Conduits by the Inversion and Curing of a Resin-Impregnated Tube, ASTM International, West Conshohocken, PA, URL www.astm.org* 2022.
9. EN ISO 11296-4. *Plastics piping systems for renovation of underground non-pressure drainage and sewerage networks - Part 4: Lining with cured-in-place pipes, URL www.iso.org* 2018.
10. ISO 11298-4. *Plastics piping systems for renovation of underground water supply networks — Part 4: Lining with cured-in-place pipes, 2021, URL www.iso.org*
11. American Water Works Association. *Rehabilitation of Water Mains Contents AWWA Manual M28* 3rd (2014).
12. ISO 11295. *Classification and information on design and applications of plastics piping systems used for renovation and replacement, 2018, URL www.iso.org* Madrid.
13. ASTM F1743. Standard Practice for Rehabilitation of Existing Pipelines and Conduits by Pulled-in-Place Installation of Cured-in-Place Thermosetting Resin Pipe (CIPP), ASTM International, West Conshohocken, PA, 2022, URL www.astm.org.
14. Levy, M. Mémoire sur un nouveau cas intégrable du problème de l'élastique et l'une de ses applications. *Journal de mathématiques pures et appliquées* **10,** 5–42 (1884).

15. Timoshenko, S. P. & Goodier, J. N. *Theory of elasticity* 506. doi:10.1201/b16095-7 (McGraw Hill, 1970).
16. Glock, D. Post-critical behavior of a rigidly encased circular pipe subject to external water pressure and temperature rise. *Der Stahlbau* **46** (1977).
17. Aggarwal, S. & Cooper, M. External pressure testing of 'Insituform' linings, Internal Report, Coventry (Lanchester), Polytechnic, UK (1984).
18. Zhu, M. & Hall, D. E. Creep induced contact and stress evolution in thin-walled pipe liners. *Thin-Walled Structures* **39,** 939–959. doi:10.1016/S0263-8231(01)00019-2 (2001).
19. Zhao, W., Nassar, R. & Hall, D. Design and reliability of pipeline rehabilitation liners. *Tunnelling and Underground Space Technology* **20,** 203–212. doi:10.1016/j.tust.2004.07.002 (2005).
20. Boot, J. C. Elastic buckling of cylindrical pipe linings with small imperfections subject to external pressure. *Tunnelling and Underground Space Technology* **12,** 3–15. doi:10.1016/s0886-7798(98)00018-2 (1997).
21. ATV-DVWK M-127 E. Part 2. *Static Calculation for the Rehabilitation of Drains and Sewers Using Lining and Assembly Procedures* German, 2000.
22. El-Sawy, K. & Moore, I. D. Stability of Loosely Fitted Liners Used to Rehabilitate Rigid Pipes. *Journal of Structural Engineering* **124,** 1350–1357. doi:10.1061/(asce)0733-9445(1998)124:11(1350) (1998).
23. RERAU. *Restructuration des collecteurs visitables. Guide technique, tome 1. RERAU, projet national Réhabilitation des Réseaux d'Assainissement Urbains* 154 (2002).
24. Thépot, O. International Comparison of Methods for the Design of Sewer Linings International Comparison of Methods for the Design of Sewer Linings Ein internationaler Vergleich der Konstruktionsmethoden für.
25. Thépot, O. A new design method for non-circular sewer linings. *Tunnelling and Underground Space Technology* **15,** 25–41. doi:10.1016/S0886-7798(00)00064-X (2000).
26. Thépot, O. Structural design of oval-shaped sewer linings. *Thin-Walled Structures* **39,** 499–518. doi:10.1016/S0263-8231(01)00013-1 (2001).
27. Boot, J. C., Naqvi, M. M. & Gumbel, J. E. A new method for the structural design of flexible liners for gravity pipes of egg-shaped cross section: Theoretical considerations and formulation of the problem. *Thin-Walled Structures* **85,** 411–418. doi:10.1016/j.tws.2014.09.001. http://dx.doi.org/10.1016/j.tws.2014.09.001 (2014).
28. Li, Z., Zheng, J. & Wang, R. Effects of grouting voids on the elastic buckling of confined pipe liners subjected to uniform pressure. *Thin-Walled Structures* **137,** 502–514. doi:10.1016/j.tws.2018.12.045. https://doi.org/10.1016/j.tws.2018.12.045 (2019).
29. Omara, B. A.-a. M., Guice, L. K., Straughan, W. T. & Akl, F. Instability of Thin Pipes Encased in Oval Rigid Cavity, 381–388 (2000).
30. Wang, J. H. & Koizumi, A. Experimental investigation of buckling collapse of encased liners subjected to external water pressure. *Engineering Structures* **151,** 44–56. doi:10.1016/j.engstruct.2017.08.008. http://dx.doi.org/10.1016/j.engstruct.2017.08.008 (2017).

31. Wang, X., Zhao, Y., Ariaratnam, S. T. & Yan, X. Study on the impact of ovality defect on structural stability of CIPP liner of drainage pipeline. *Tunnelling and Underground Space Technology* **140,** 105338. doi:10.1016/j.tust.2023.105338. https://doi.org/10.1016/j.tust.2023.105338 (2023).
32. El-Sawy, K. M. Inelastic stability of tightly fitted cylindrical liners subjected to external uniform pressure. *Thin-Walled Structures* **39,** 731–744. doi:10.1016/S0263-8231(01)00026-X (2001).
33. El-Sawy, K. M. Inelastic Stability of Loosely Fitted Cylindrical Liners. *Journal of Structural Engineering* **128,** 934–941. doi:10.1061/(asce)0733-9445(2002)128:7(934) (2002).
34. El-Sawy, K. M. Inelastic stability of liners of cylindrical conduits with local imperfection under external pressure. *Tunnelling and Underground Space Technology* **33,** 98–110. doi:10.1016/j.tust.2012.09.004. http://dx.doi.org/10.1016/j.tust.2012.09.004 (2013).
35. Li, Z. & Huang, H. Structural failure performance of the confined liner with a non-uniformly annular gap subjected to a point load under a thermal rise field. *Engineering Failure Analysis* **105,** 1141–1153. doi:10.1016/j.engfailanal.2019.07.061. https://doi.org/10.1016/j.engfailanal.2019.07.061 (2019).
36. El-Sawy, K. & Moore, I. D. Parametric study for buckling of liners: effect of liner geometry and imperfections. *Proceedings of the Conference on Trenchless Pipeline Projects,* 416–423. doi:10.1061/9780784402443.052 (1997).
37. Madryas, C. & Szot, A. Structural sensitivity of circular sewer liners to geometrical imperfections. *Tunnelling and Underground Space Technology* **18,** 421–434. doi:https://doi.org/10.1016/S0886-7798(03)00065-8 (2003).
38. Jeyapalan, J. K. Unified design method for most no-dig rehabilitation liners. *Pipelines 2001: Advances in Pipeline Engineering and Construction - Proceedings of the Pipeline 2001 Conference* **107,** 717–721. doi:10.1061/40574(2001)79 (2004).
39. El-Sawy, K. M. & Sweedan, A. M. Effect of local wavy imperfections on the elastic stability of cylindrical liners subjected to external uniform pressure. *Tunnelling and Underground Space Technology* **25,** 702–713. doi:10.1016/j.tust.2010.04.002. http://dx.doi.org/10.1016/j.tust.2010.04.002 (2010).
40. El-Sawy, K. M. & Sweedan, A. M. Elastic stability analysis of loosely fitted thin liners - A proposed simplified procedure and evaluation of existing solutions. *Tunnelling and Underground Space Technology* **25,** 689–701. doi:10.1016/j.tust.2010.04.007. http://dx.doi.org/10.1016/j.tust.2010.04.007 (2010).
41. Li, Z., Wang, L., Guo, Z. & Shu, H. Elastic buckling of cylindrical pipe linings with variable thickness encased in rigid host pipes. *Thin-Walled Structures* **51,** 10–19. doi:10.1016/j.tws.2011.11.003. http://dx.doi.org/10.1016/j.tws.2011.11.003 (2012).
42. Thépot, O. Structural Design of Close-Fit Liners in Fractured Rigid Circular or Non-Circular Gravity Pipes. *Journal of Pipeline Systems Engineering and Practice* **12.** doi:https://doi.org/10.1061/(ASCE)PS.1949-1204.000052 (2021).
43. Khan, S. & Dobson, C. *Trouble Shooting for Trenchless Liner Installation During Sewer Line Rehabilitation* in *Proceedings of the Water Environment Federation* **1** (Sacramento, California, 2006), 5420–5435. doi:10.2175/193864706783763192.

44. Das, S., Bayat, A., Gay, L., Salimi, M. & Matthews, J. A comprehensive review on the challenges of cured-in-place pipe (CIPP) installations. *J. Water Supply: Res. Technol. - AQUA* **65,** 583–596. doi:10.2166/aqua.2016.119 (2016).
45. Ji, H. W., Yoo, S. S., Kim, J. & Koo, D. D. The mechanical properties of high strength reinforced Cured-in-Place Pipe (CIPP) liner composites for urbanwater infrastructure rehabilitation. *Water (Switzerland)* **10,** 1–12. doi:10.3390/w10080983 (2018).
46. Ji, H. W., Koo, D. D. & Kang, J. H. Short-and long-term structural characterization of cured-in-place pipe liner with reinforced glass fiber material. *International Journal of Environmental Research and Public Health* **17,** 1–15. doi:10.3390/ijerph17062073 (2020).
47. Yahong, Z. *et al.* Experiment and evaluation model of liner design for renewal of deteriorated reinforced concrete pipes utilizing cured-in-place-pipe technology. *Tunnelling and Underground Space Technology* **132.** doi:https://doi.org/10.1016/j.tust.2022.104866 (2023).
48. Gras-Travesset, F., Andreu Torras, A. & Pérez, M. A. Optimizing thickness for semi-structural CIPP liners in pressure pipes : A mathematical modeling approach. *Tunnelling and Underground Space Technology* **[Submitted** (2024).
49. Allouche, E. N., Bainbridge, K., Moore, I. D. & Council, H. C. Laboratory Examination of a Cured In Place Pressure Pipe Liner for Potable Water Distribution System. *North American Society for Trenchless Technology (NASTT)* **13689,** 1–10 (2005).
50. Jaganathan, A., Allouche, E. & Baumert, M. Experimental and numerical evaluation of the impact of folds on the pressure rating of CIPP liners. *Tunn. Undergr. Space Technol.* **22,** 666–678. doi:10.1016/j.tust.2006.11.007 (2007).
51. Ampiah, N., Fam, A. & Moore, I. D. *Wavy imperfections and the strength of cast-in-place pressure pipe liners* in *Proceedings of Pipelines Congress 2008 - Pipeline Asset Management: Maximizing Performance of Our Pipeline Infrastructure* **321** (2008). doi:10.1061/40994(321)54.
52. Ampiah, N., Fam, A. & Moore, I. D. Effect of Wrinkles on the Circumferential Strength of a Cast-in-Place Composite Polymer Liner Used in Retrofitting Pressure Pipes. *J. Mater. Civ. Eng.,* 1304–1314 (2010).
53. ASTM D2290. *Standard Test Method for Apparent Hoop Tensile Strength of Plastic or Reinforced Plastic Pipe, ASTM International, West Conshohocken, PA, 2022, URL www.astm.org*
54. Allouche, E. N., Shanghai, G., Baumert, M., Amobi, A. & Bainbridge, K. *The design and performance of pressure pipe liners under static and cyclic loading* in *Proceedings of Pipelines Congress 2008 - Pipeline Asset Management: Maximizing Performance of Our Pipeline Infrastructure* **321** (2008), 1–10. doi:10.1061/40994(321)38.
55. Brown, M. J., Moore, I. D. & Fam, A. Performance of a cured-in-place pressure pipe liner passing through a pipe section without structural integrity. *Tunnelling and Underground Space Technology* **42,** 87–95. doi:10.1016/j.tust.2014.01.005. http://dx.doi.org/10.1016/j.tust.2014.01.005 (2014).
56. Rajeev, P, Kodikara, J., Robert, D., Zeman, P. & Rajani, B. *Factors-contributing-to-large-diameter-water-pipe-falure* in (IWA, 2014), 9–14.

57. He, X. & Shawn, K. Mechanical performance of a pressure pipe CIPP liner with stress concentration effects associated with local defects. *Conference on Pipeline Engineering - Concepts in Harmony (PIPELINES),* 515–527 (2019).
58. Brown, M. J., Moore, I. D. & Fam, A. Analysis of a cured-in-place pressure pipe liner spanning circular voids. *Tunnelling and Underground Space Technology* **101,** 103424. doi:10.1016/j.tust.2020.103424. https://doi.org/10.1016/j.tust.2020.103424 (2020).
59. Adebola, T., Moore, I. & Hoult, N. Use of Optical Fibers to Investigate Strength Limit States for Pressure Pipe Liners Spanning across Circular Perforations. *Journal of Pipeline Systems Engineering and Practice.* doi:https://doi.org/10.1061/(ASCE)PS.1949-1204.0000523 (2021).
60. Shou, K. J. & Chen, B. C. Numerical analysis of the mechanical behaviors of pressurized underground pipelines rehabilitated by cured-in-place-pipe method. *Tunnelling and Underground Space Technology* **71,** 544–554. http://dx.doi.org/10.1016/j.tust.2017.11.005 (2018).
61. Shou, K. J. & Huang, C. C. Numerical analysis of straight and curved underground pipeline performance after rehabilitation by cured-in-place method. *Underground Space (China)* **5,** 30–42. doi:10.1016/j.undsp.2018.10.003. https://doi.org/10.1016/j.undsp.2018.10.003 (2020).
62. ASTM F2207-06. *Standard Specification for Cured-in-Place Pipe Lining System for Rehabilitation of Metallic Gas Pipe, ASTM International, West Conshohocken, PA, URL www.astm.org* 2019.
63. He, X. & Shawn, K. *Mechanical performance of a pressure pipe CIPP liner with stress concentration effects associated with local defects* in *Conference on Pipeline Engineering - Concepts in Harmony* (2019), 515–527.
64. Jeon, S. S., O'Rourke, T. D. & Neravali, A. N. Repetitive loading effects on cast iron pipelines with cast-in-place pipe lining systems. *Journal of Transportation Engineering* **130,** 692–705. doi:10.1061/(ASCE)0733-947X(2004)130:6(692) (2004).
65. Bouziou, D. *et al. Earthquake Response and Rehabilitation of Critical Lifelines* in *15th World Conference on Earthquake Engineering* (2012), Paper No. 511, 10 p.
66. Zhong, Z. *et al.* Seismic testing of critical lifelines rehabilitated with cured in place pipeline lining technology. *Journal of Earthquake Engineering* **18,** 964–985. doi:10.1080/13632469.2014.916632 (2014).
67. Zhong, Z., Aref, A. & Filiatrault, A. Seismic performance evaluation of buried pipelines retrofitted with cured-in-place pipe liner technology under near-fault ground motions. *Structures Congress 2015 - Proceedings of the 2015 Structures Congress,* 1903–1914. doi:10.1061/9780784479117.164 (2015).
68. Zhong, Z., Filiatrault, A. & Aref, A. Numerical simulation and seismic performance evaluation of buried pipelines rehabilitated with cured-in-place-pipe liner under seismic wave propagation. *Earthquake Engineering and Structural Dynamics* **46,** 811–829. doi:10.1002/eqe.2832 (2017).
69. Zhong, Z., Filiatrault, A. & Aref, A. Experimental performance evaluation of pipelines rehabilitated with cured-in-place pipe liner under earthquake transient ground deformations. *Journal of Infrastructure Systems* **23.** doi:10.1061/(ASCE)IS.1943-555X.0000326 (2017).
70. Argyrou, C., Bouziou, D., O'Rourke, T. D. & Stewart, H. E. Retrofitting pipelines with cured-in-place linings for earthquake-induced ground deformations. *Soil Dynamics and*

Earthquake Engineering **115,** 156–168. doi:10.1016/j.soildyn.2018.07.015. https://doi.org/10.1016/j.soildyn.2018.07.015 (2018).

71. Argyrou, C., O'Rourke, T. D., Stewart, H. E. & Wham, B. P. Large-Scale Fault Rupture Tests on Pipelines Reinforced with Cured-in-Place Linings. *J geotech geoenviron.* **145,** 1–11. doi:10.1061/(ASCE)GT.1943-5606.0002018. (2019).
72. Fang, H., Yang, K., Li, B., He, H. & Xue, B. Parameter Analysis of Wall Thickness of Cured-in-Place Pipe Linings for Semistructured Rehabilitation of Concrete Drainage Pipe. *Mathematical Problems in Engineering* **2020.** doi:10.1155/2020/5271027 (2020).
73. Yang, K. *et al.* Full-scale experimental investigation of the mechanical characteristics of corroded buried concrete pipes after cured-in-place-pipe rehabilitation. *Tunnelling and Underground Space Technology* **117,** 104153. https://doi.org/10.1016/j.tust.2021.104153 (2021).
74. Hsu, J.-M. & Shou, K.-J. Numerical analysis of the mechanical behavior of separated joints in underground pipelines rehabilitated by cured-in-place pipes. *Tunnelling and Underground Space Technology.* doi:https://doi.org/10.1016/j.tust.2022.104520 (2022).
75. Yang, K., Fang, H., Zhang, X., Li, B. & Hu, Q. Investigation of mechanical properties of corroded concrete pipes after cured-in-place-pipe (CIPP) rehabilitation under multi-field coupling. *Tunnelling and Underground Space Technology* **128.** doi:10.1016/j.tust.2022.104656 (2022).
76. Kiriella, S. *et al.* Lateral deformation behaviour of structural internal replacement pipe repair systems. *Composite Structures* **319,** 117144. doi:10.1016/j.compstruct.2023.117144. https://doi.org/10.1016/j.compstruct.2023.117144 (2023).
77. Zhai, K. & Moore, I. Axial stresses in pressure pipe liners spanning joints with initial gap, opening as a result of differential ground movements. *Tunnelling and Underground Space Technology* **133,** 104965. doi:https://doi.org/10.1016/j.tust.2022.104965 (2023).
78. Jaganathan, A. P. & Kodali, S. An electromagnetic sensor to locate service laterals during the trenchless lateral reinstatement. *Tunnelling and Underground Space Technology* **83,** 18–26. doi:10.1016/j.tust.2018.09.006. https://doi.org/10.1016/j.tust.2018.09.006 (2019).
79. Selvakumar, A., Kampbell, E., Downey, D. & Condit, W. Quality assurance and quality control practices for rehabilitation of sewer and water mains. *Urban Water Journal* **9,** 211–222. doi:10.1080/1573062X.2011.652134 (2012).
80. Allouche, E. *et al.* A pilot study for retrospective evaluation of cured-in-place pipe (CIPP) rehabilitation of municipal gravity sewers. *Tunnelling and Underground Space Technology* **39,** 82–93. doi:10.1016/j.tust.2012.02.002. http://dx.doi.org/10.1016/j.tust.2012.02.002 (2014).
81. Cigler, O., Kubečka, K. & Waldstein, P. Quality Assurance of CIPP Liners According EN ISO 11296-4. *Applied Mechanics and Materials* **752-753,** 1339–1342. doi:10.4028/www.scientific.net/amm.752-753.1339 (2015).
82. Adebola, T. O., Hoult, N. & Moore, I. D. Distributed Strain Sensing to Study a Composite Liner for Cast Iron Water Pipe Rehabilitation. *Journal of Testing and Evaluation* **48,** 20170497. doi:10.1520/jte20170497 (2020).

83. Gras-Travesset, F., Andreu Torras, A. & Pérez, M. A. A novel test procedure to assess the performance of composite cured-in-place-pipe liners for rehabilitation of water pressure pipes. *Case Studies in Construction Materials* **19.** doi:10.1016/j.cscm.2023.e02381 (2023).
84. Suresh, G. & Jayakumari, L. S. Analyzing the mechanical behavior of E-glass fibre-reinforced interpenetrating polymer network composite pipe. *Journal of Composite Materials* **50,** 3053–3061. doi:10.1177/0021998315615408 (2016).
85. Kara, M., Kirici, M. & Cagan, S. C. Effects of the Number of Fatigue Cycles on the Hoop Tensile Strength of Glass Fiber/Epoxy Composite Pipes. *Journal of Failure Analysis and Prevention* **19,** 1181–1186. doi:10.1007/s11668-019-00720-z. https://doi.org/10.1007/s11668-019-00720-z (2019).
86. Lee, S., Kim, S. H., Kim, S., Choi, J. & Choi, H. J. Hoop tensile strength of tubular carbon fiber reinforced silicon carbide matrix composites. *Ceramics International* **44,** 17087–17093. doi:10.1016/j.ceramint.2018.06.157. https://doi.org/10.1016/j.ceramint.2018.06.157 (2018).
87. Hudson, J. A., Cardenas, H., Matthews, J. & Alam, S. Performance evaluation of deteriorated and rehabilitated corrugated metal pipe culverts using multiphysics simulation. *Tunnelling and Underground Space Technology* **131,** 104827. doi:10.1016/j.tust.2022.104827. https://doi.org/10.1016/j.tust.2022.104827 (2023).
88. Li, B. *et al.* Trenchless rehabilitation of sewage pipelines from the perspective of the whole technology chain: A state-of-the-art review. *Tunnelling and Underground Space Technology.* doi:https://doi.org/10.1016/j.tust.2023.105022 (2023).
89. El-Sawy, K. M. & Elshafei, A. L. Neural network for the estimation of the inelastic buckling pressure of loosely fitted liners used for rigid pipe rehabilitation. *Thin-Walled Structures* **41,** 785–800. doi:10.1016/S0263-8231(03)00024-7 (2003).
90. Xia, Y. *et al.* Analysis of flexural failure mechanism of ultraviolet cured-in-place-pipe materials for buried pipelines rehabilitation based on curing temperature monitoring. *Engineering Failure Analysis* **142.** doi:https://doi.org/10.1016/j.engfailanal.2022.106763 (2022).
91. Xia, Y., Zhang, C., Wang, C. & Liu, H. Prediction of bending strength of glass fiber reinforced methacrylate-based pipeline UV-CIPP rehabilitation materials based on machine learning. *Tunnelling and Underground Space Technology.* doi:https://doi.org/10.1016/j.tust.2023.105319 (2023).
92. Zhu, H., Wang, T., Wang, Y. & Li, V. C. Trenchless rehabilitation for concrete pipelines of water infrastructure: A review from the structural perspective. *Cem. Concr. Compos.* **123,** 104193. doi:10.1016/j.cemconcomp.2021.104193 (2021).
93. UNE-EN ISO 11298-4. *Sistemas de canalización en materiales plásticos para la renovación de redes de conducción de agua enterradas. Parte 4: Entubado continuo con tubo curado en obra, 2022, URL www.iso.org*
94. Selvakumar, A. & Matthews, J. C. Demonstration and Evaluation of Innovative Rehabilitation Technologies for Water Infrastructure Systems. *Journal of Pipeline Systems Engineering and Practice* **8,** 06017001. doi:10.1061/(asce)ps.1949-1204.0000268 (2017).
95. International Organization for Standardization ISO 5084. *Textiles — Determination of thickness of textiles and textile products* 1996.

96. ASTM D6775. *Standard Test Method for Breaking Strength and Elongation of Textile Webbing , Tape and Braided Material, ASTM International, West Conshohocken, PA, 2017, URL www.astm.org* 2017.
97. ASTM D1475. *Standard Test Method For Density of Liquid Coatings, Inks and Related Products, ASTM International, West Conshohocken, PA, 2020, URL www.astm.org* 2020.
98. ASTM E1131. *Standard Test Method for Compositional Analysis by Thermogravimetry, ASTM International, West Conshohocken, PA, 2020, URL www.astm.org* 2020.
99. ISO 11357-1. *Plastics - Differential scanning calorimetry (DSC) - Part 1: General principles, URL www.iso.org* 2023.
100. ISO 15040. Composites - Prepregs - Determination of gel time, URL www.iso.org (1999).
101. ASTM D638. *Standard Test Method for Tensile Properties of Plastics, ASTM International, West Conshohocken, PA, 2022, URL www.astm.org*
102. ASTM D790. *Standard Test Methods for Flexural Properties of Unreinforced and Reinforced Plastics and Electrical Insulating Materials, ASTM International, West Conshohocken, PA, 2017, URL www.astm.org* 2017. doi:10.1520/D0790-15E02..
103. ISO 178. *Plastics, Determination of flexural properties Plastics - Determination of flexural properties, URL www.iso.org* 2019.
104. ASTM D3567. *Standard Practice for Determining Dimensions of "Fiberglass" (Glass-Fiber- Reinforced Thermosetting Resin) Pipe and Fittings, ASTM International, West Conshohocken, PA, 2022, URL www.astm.org* 2022. doi:10.1520/D3567-97R11.2.
105. ASTM D5813. *Standard Specification for Cured-In-Place Thermosetting Resin Sewer Pipe, ASTM International, West Conshohocken, PA, 2018, URL www.astm.org* 2018. doi:10.1520/D5813-04R12.2.
106. ISO 3126. *Plastics piping systems - plastics components - Determination of the amounts of constituents using the gravimetric method, URL www.iso.org* 2005.
107. UNE-EN 805. *Water supply - Requirements for systems and components outside buildings, URL www.une.org* 2000.
108. ISO 10466. *Glass-reinforced thermosetting plastics (GRP) pipes - Test method to prove the resistance to initial ring deflection, URL www.iso.org* 2021.
109. ASTM D2412. *Standard Test Method for Determination of External Loading Characteristics of Plastic Pipe by Parallel-Plate Loading, ASTM International, West Conshohocken, PA, 2022, URL www.astm.org* 2021.
110. UNE-EN 1228. Plastics Piping Systems. Glass-Reinforced Thermosetting Plastics (GRP) Pipes. Determination Of Initial Specific Ring Stiffness, URL www.une.org (1996).
111. ISO 527-2. *Plásticos. Determinación de las propiedades en tracción. Parte 2: Condiciones de ensayo de plásticos para moldeo y extrusión.* 2012.
112. Abel, T. Laboratory tests and analysis of CIPP epoxy resin internal liners used in pipelines-part II: Comparative analysis with the use of the FEM and engineering algorithms. *Stud. Geotech. Mech.* **43,** 307–322. doi:10.2478/sgem-2021-0007 (2021).
113. Nurazzi, N. M. *et al.* A review on mechanical performance of hybrid natural fiber polymer composites for structural applications. *Polymers* **13,** 1–47. doi:10.3390/polym13132170 (2021).

114. Kamble, Z. & Behera, B. K. Sustainable hybrid composites reinforced with textile waste for construction and building applications. *Constr. Build. Mater.* **284,** 122800. doi:10 . 1016 / j . conbuildmat.2021.122800. https://doi.org/10.1016/j.conbuildmat.2021.122800 (2021).

115. Fan, W. *et al.* Fatigue behavior of the 3D orthogonal carbon/glass fibers hybrid composite under three-point bending load. *Mater. Des.* **183,** 108112. doi:10.1016/j.matdes.2019.108112. https://doi.org/10.1016/j.matdes.2019.108112 (2019).

116. Guijun, X., Rui, G. & Chenggao, L. Combined effects of sustained bending loading, water immersion and fiber hybrid mode on the mechanical properties of carbon/glass fiber reinforced polymer composite. *Compos. Struct.* **281,** 115060. doi:10.1016/j.compstruct.2021.115060 (2022).

117. AWW Committee Report. *Structural Classifications of Pressure Pipe Linings, Suggested Protocol for Product Classification* tech. rep. (2019), 44.

118. Campo, E. A. *Selection of Polymeric Materials: How to Select Design Properties from Different Standards* 1st Editio, 350 (William Andrew, 2008).

119. Genger, K. T. & Hammad, A. Street closure prediction based on the combined conditions of spatially collocated municipal infrastructure assets at the segment level. *Expert Systems with Applications.* doi:https://doi.org/10.1016/j.eswa.2023.119671 (2023).

120. Nie, P., Roccotelli, M., Fanti, M. P., Ming, Z. & Li, Z. Prediction of home energy consumption based on gradient boosting regression tree. *Energy Reports* **7,** 1246–1255. doi:10.1016/j.egyr.2021.02.006. https://doi.org/10.1016/j.egyr.2021.02.006 (2021).

121. Islam Khan, M. S., Islam, N., Uddin, J., Islam, S. & Nasir, M. K. Water quality prediction and classification based on principal component regression and gradient boosting classifier approach. *Journal of King Saud University - Computer and Information Sciences* **34,** 4773–4781. doi:10.1016/j.jksuci.2021.06.003. https://doi.org/10.1016/j.jksuci.2021.06.003 (2022).

122. Khan, I. M. & Yassir M., A. Robust extreme gradient boosting regression model for compressive strength prediction of blast furnace slag and fly ash concrete. *Materials Today Communications* (2023).